

Dissertation zur Erlangung des Doktorgrades  
der Fakultät für Chemie und Pharmazie  
der Ludwig-Maximilians-Universität München

# **TWO-DIMENSIONAL TRANSITION METAL OXIDE NANOSHEETS FOR NANOARCHITECTONICS**

Christian Ziegler  
aus  
München, Deutschland

2015

## **ERKLÄRUNG**

Diese Dissertation wurde im Sinne von § 7 der Promotionsordnung vom 28. November 2011 von Frau Prof. Dr. Bettina Lotsch betreut.

## **EIDESSTATTLICHE VERSICHERUNG**

Diese Dissertation wurde eigenständig und ohne unerlaubte Hilfe erarbeitet.

München, 25.10.2015

.....  
(Christian Ziegler)

Dissertation eingereicht am 27.10.2015

1. Gutachterin: Prof. Dr. Bettina V. Lotsch

2. Gutachterin: Prof. Dr. Christina Scheu

Mündliche Prüfung am 30.11.2015

## **ACKNOWLEDGMENTS**

This PhD journey would have not been possible without the help and company of many people, whom I would like to express my gratitude to in the following:

First of all, my biggest thanks goes to Prof. Bettina V. Lotsch and Prof. Christina Scheu who guided me through my PhD on equal terms. Thanks to you I had the opportunity to work on an unique topic in two amazing groups under a synergetic supervision. Bettina, you always promoted me and spurred my ambition to success. I wish you all the best for your future, you work(ed) hard for it and you deserve to get the best out of it. Tina, you were always there for me once things got complicated and I got stuck. You are the person that sees the good things in every situation and motivates one to carry on. Keep this spirit and a happy future for you, too.

Sincere thanks to Prof. Achim Hartschuh, Prof. Karlheinz Sünkel, Prof. Andreas Kornath and Prof. Konstantin Karaghiosoff for being part of the board of examiners.

Special thanks to Prof. Gianluigi Botton and his group at the McMaster University in Hamilton, Ontario, Canada who made me feel very welcome during my visit abroad. A big thanks to Matthieu Bugnet, you are a very patient and great microscopist who got the best out of my tricky samples.

Although we have never met in person, I would like to express my gratitude towards the collaborators Yaron Kauffmann, Prof. Wayne D. Kaplan and Prof. Peter Blaha who did a great job regarding the electronic structure of the calcium niobates.

Stephan Werner, you became my closest fellow during the PhD and a friend for lifetime. Despite the fact that you are a guitarist and horrible in keeping order, you made my labdays short and the after hours long. Our trio infernale would have not been complete without Sebastian Schneider! It is always nice to know that there are others just like oneself. A big watering can cheers to you, guys!

A little less extroverted, but not less lovable my "Schatz" Stephan Hug. Thanks for everything. At this point, I would like to send lots of love to Olaf Alberto von Mankowski and Linus Stegbauer who kept the vibes alive after the party crew finished.

Among all the guys, Teresa Dennenwaldt became the important female counterpart during my PhD, not just as the link to the Scheu group, but also as a friend. May the future bring a lot more exciting journeys and adventures to you. And the other sunshine from the Lotsch group, Annekathrin Ranft! Maybe we will really open a café in the near-future together.

My pal, Kulpreet S. Viridi, thanks for enriching my academic and my cultural life. It is always a pleasure to share thoughts with you.

With Daniel Weber I spent the last years in school, most of my academic studies and almost the entire time of my PhD. Thanks for traveling along this road together and best of luck for the last few meters!

Since I got a very time consuming topic, it would have not been possible to achieve such versatile results without the help of my students, from which many became colleagues and friends: Erika Mühlbauer (thanks for the help in the early trial and error phase), Pirmin „The Pi-Machine“ Ganter (thanks for your dedicated work), Tine Pösl (thanks for the patience with the Microfluidizer), Tanja Holzmann (thank you for taking care of the LBL robot;), Matthias Wörsching (thanks for the best work-life balance results), Arne Schwarze (I hope you carry on and will finish your studies!), Laura Kohout (thanks for the record in number of experiments per day), Kristina Peters (thanks to „Der Gerät“), Stephanie Linke (thanks for getting the organic chemistry started), Katarina Marković (thank you for all the perfect cross-sections), Maximilian Lamothe (thanks for executing RaZi), Michaela Oswald (thanks for trying LDHs and LREHs) and last but not least Anne Friedrichs (thanks for the silver stuff).

Furthermore, I got great support from many people of the FKF. Special thanks goes to Viola Duppel for her TEM investigations. I deeply appreciate your careful acquisition of all the data. Sorry for producing so many samples! Another special thanks to Claudia Kamella who produced the Pb-samples in a large scale and of course for the nice E-Mails and phone calls! Many thanks to the PC and UV-Vis guys and girls Filip Podjaski, Brian Tuffy and Katharina Schwinghammer, Bernhard Fenk for FIB preparation, Marie-Luise Schreiber for ICP-AES, IR and elemental analysis, Armin Schulz for Raman spectroscopy, Igor Moudrakovski for ssNMR, Mitsuharu Konuma for XPS and Christine Stefani for XRD measurements. And of course thanks to all the people of the Lotsch group in Stuttgart.

The same accounts for many people in Munich. Many thanks to Christian Minke for SEM-EDX investigations, Markus Döblinger for teaching me TEM, Steffen Schmidt for helping me regarding electron microscopy issues, Wolfgang Wünschheim for IT support, Thomas Miller for fixing instruments, R. Eicher for elemental analysis, Helmut Hartl and Jana Obel for ICP-AES analysis. Thanks a lot to the current and former Lotsch group members in Munich: Claudia Lermer, Kerstin Gottschling, Hendrik Schlomberg, Katalin Szendrei, Leo Diehl, Erik Flügel, Sebastian Junggeburth, Hongi Wang and Sebastian Zech. And of course to the Scheu group members: Anna Frank (thanks for the shelter and I still want that ring;), Christoph Heinzl (thanks for having good times at the TEM), Andreas Wisnet (1D, 2D, 3D), Angela Wochnik, Katharina Hengge, Ramona Hoffmann, Alexander Müller, Stefan Hieke, Stephan Gleich, Alena Folger and Sophia Betzler.

I hope I did not forget someone!



Thanks for the great working atmosphere to the people from my former lab D2.107: Martin Mangstl, Sebastian Johansson, Sebastian Schmiechen, Philipp Pust, Peter Wagatha, Jonas Häusler etc.; the people from my former term Gina Friedrichs, Erwin Wiesnmayer, Franziska Hummel, Dominik Baumann; and all the other guys and girls from the solid-state groups!

I had the pleasure to be part of the NIM graduate program, which financed the first half year of my PhD and supported my trip to Canada. Thanks for that and thanks to Peter Sonntag, Christoph Hohmann, Birgit Ziller, my student board buddies Isabella Almstätter, Ida Pavlichenko, Bernhard Fichtl and Fabian Ziegler, and all the other people I had the chance to get in contact with through NIM.

A special thanks goes to my GNTM girls Kathrin Schwinghammer and Veronika Werner. I am looking forward towards our next cooking sessions!

Another thanks to my lunch girls Ellen Broda and Claudia Szeibert and to all the people who visited me in the lab or the office, especially Elisabeth Heinemann and Isabel Müller.

Besides the scientific community, I would like to express my deepest gratitude to my best friends Astrid Seeberger and Matthias Mair and my girlfriend Karoline Herbich. Thanks for always being there for me! And of course to all my other friends who accompanied me during the PhD, you know who you are!

Last but not least a huge thanks to my family. Without your support this all would not have been possible!

*"Coal and diamonds, sand and computer chips, cancer and healthy tissue: throughout history, variations in the arrangement of atoms have distinguished the cheap from the cherished, the diseased from the healthy. Arranged one way, atoms make up soil, air, and water; arranged another, they make up ripe strawberries. Arranged one way, they make up homes and fresh air; arranged another they make up ash and smoke."*

**Kim Eric Drexler**

*"When the last tree is cut, the last fish is caught, and the last river is polluted; when to breathe the air is sickening, you will realize, too late, that wealth is not in bank accounts and that you can't eat money."*

**Alanis Obomsawin**

*"Ich bin meiner Weisheit überdrüssig, wie die Biene, die des Honigs zuviel gesammelt hat, ich bedarf der Hände, die sich ausstrecken. Ich möchte verschenken und austeilen, bis die Weisen unter den Menschen wieder einmal ihrer Torheit und die Armen wieder einmal ihres Reichtums froh geworden sind."*

**Friedrich Nietzsche**

## I LIST OF ABBREVIATIONS

2D/3D	Two/Three-dimensional
ADF	Annular dark-field
AFM	Atomic force microscopy
<i>Ami</i> <sup>+</sup>	1-Allyl-3-methylimidazolium
APS	(3-Aminopropyl)trimethoxysilane
APTES	(3-Aminopropyl)triethoxysilane
APW + lo	Augmented plane wave + local orbitals approach
at%	Atomic percent
AV	Aurivillius
BF	Bright-field
BFP	Back focal plane
BSE	Backscattered electrons
<i>c</i>	Concentration
<i>Ch</i> <sup>+</sup>	Choline
CSA	Chemical shift anisotropy
<i>d</i>	Diameter
DF	Dark-field
DFT	Density functional theory
DJ	Dion-Jacobson
DOS	Density of states
DRAM	High-density dynamic random access memory devices
<i>EA</i>	Ethylamine
EDX	Energy dispersive X-ray spectroscopy
EELS	Electron energy loss spectroscopy
EFG	Electric field gradient
e.g.	For example (Latin = <i>exempli gratia</i> )
EISA	Evaporation induced self-assembly
ELNES	Energy loss-near edge structure
<i>ES</i> <sup>-</sup>	Ethylbenzenesulfonate
ESD	Electrostatic self-assembly deposition
EtOH	Ethanol
<i>et al.</i>	And others (Latin = <i>Et alii</i> (masculine), <i>et aliae</i> (neuter), <i>et alia</i> (feminine))
EXELFS	Extended energy loss fine structure

FFT	Fast Fourier transform
FIB	Focused ion beam
FWHM	Full width at half maximum
g	Gram(s)
GW	Green's function based calculations
h	Hour(s)
HAADF	High-angle annular dark field
HRTEM	High-resolution transmission electron microscopy
ICDD	International Centre for Diffraction Data
ICP-AES	Inductively coupled plasma atomic emission spectroscopy
ICSD	The Inorganic Crystal Structure Database
i.e.	That is to say (Latin = id est)
IR	Infrared
L	Liter(s)
LB	Langmuir-Blodgett
LBL	Layer-by-layer
LDH	Layered double hydroxide
LREH	Layered rare-earth hydroxide
MAS	Magic angle spinning
mg	Milligram(s)
mL	Milliliters
Min.	Minute(s)
NSTC	National Science and Technology Council
PAH	Poly(allylamine hydrochloride)
PBE-GGA	Perdew, Burke, and Ernzerhof generalized gradient approximation
PCD	Pearson's Crystal Data - Crystal Structure Database for Inorganic Compounds
PDDA	Poly(diallyldimethylammonium chloride)
PDOS	Partial density of states
PEI	Polyethyleneimine
PPA	Phenylphosphonate
PS	Polystyrene
PSS	Poly(sodium styrene-4-sulfonate)
RP	Ruddlesden-Popper

rpm	Revolutions per minute
SAED	Selected area electron diffraction
SAM	Self-assembled monolayer
SAWS	Self-assembly on water surface
SDS	Sodium dodecyl sulfate
SE	Secondary electrons
SEM	Scanning electron microscopy
SNR	Signal-to-noise ratio
STEM	Scanning transmission electron microscopy
<i>TBA</i> <sup>+</sup>	Tetra- <i>n</i> -butylammonium
<i>TBP</i> <sup>+</sup>	Tetra- <i>n</i> -butylphosphonium
<i>TBS</i> <sup>+</sup>	Tri- <i>n</i> -butylsulfonium
TEM	Transmission Electron Microscopy
<i>Th</i> <sup>+</sup>	Thiocholine
TMO	Transition metal oxide
TB-mBJ	Tran-Blaha modified Becke Johnson potential
UHV	Ultrahigh vacuum
UV-Vis	Ultraviolet-visible
VEELS	Valence electron energy loss spectroscopy
VOCS	Variable offset cumulative spectra
XPS	X-ray photoelectron spectroscopy
XRD	X-ray diffraction
ZLP	Zero-loss peak

## **II TABLE OF CONTENTS**

<b>1 Introduction</b>	<b>1</b>
1.1 The Nanotechnology Age	1
1.2 Two-dimensional Nanosheets	3
1.3 Nanosheet-Based Heterostructures	9
1.4 Objectives	12
1.5 Bibliography	13
<b>2 Methods</b>	<b>16</b>
2.1 Powder X-Ray Diffraction	16
2.2 Elemental Analysis	17
2.2.1 Inductively Coupled Plasma and Atomic Emission Spectroscopy	17
2.2.2 CHNS Elemental Analysis	18
2.3 Electron Microscopy	19
2.3.1 Energy Dispersive X-Ray Spectroscopy	20
2.3.2 Electron Energy Loss Spectroscopy	21
2.3.3 Scanning Electron Microscopy	22
2.3.4 Transmission Electron Microscopy	24
2.4 X-Ray Photoelectron Spectroscopy	29
2.5 Atomic Force Microscopy	29
2.6 Infrared Spectroscopy	32
2.7 Raman Spectroscopy	33
2.8 UV-Vis Spectroscopy	34
2.9 Bibliography	36
<b>3 Two-dimensional Transition Metal Oxide Nanosheets</b>	<b>39</b>
3.1 Functional Engineering of Perovskite Nanosheets by Lead Substitution	39
3.1.1 Introduction	39
3.1.2 Results and Discussion	41
3.1.3 Conclusion	56
3.1.4 Bibliography	57
3.1.5 Supporting Information	58
3.2 Structural Investigations on New Nanosheet Phosphors	72
3.2.1 Introduction	72

3.2.2 Results and Discussion	75
3.2.3 Conclusion	88
3.2.4 Bibliography	88
3.2.5 Supporting Information	90
<b>3.3 Exfoliation of Silver Exchanged Layered Transition Metal Oxides with Bulky Organic Iodides</b>	<b>102</b>
3.3.1 Introduction	102
3.3.2 Results and Discussion	104
3.3.3 Conclusion	113
3.3.4 Bibliography	113
3.3.5 Supporting Information	115
<b>4 Nanosheet Based Heterostructures</b>	<b>123</b>
<b>4.1 Artificial Solids by Design: Assembly and Electron Microscopy Study of Nanosheet-Derived Heterostructures</b>	<b>123</b>
4.1.1 Introduction	124
4.1.2 Results and Discussion	125
4.1.3 Conclusion	137
4.1.4 Bibliography	138
4.1.5 Supporting Information	141
<b>4.2 Thermal Behavior of Layered Perovskite and Layered Double Hydroxide Heterostructures</b>	<b>148</b>
4.2.1 Introduction	148
4.2.2 Results and Discussion	150
4.2.3 Conclusion	158
4.2.4 Bibliography	158
4.2.5 Supporting Information	160
<b>4.3 Nanoarchitectonics of Calcium Niobate Nanosheets</b>	<b>165</b>
4.3.1 Introduction	165
4.3.2 Experimental Section	166
4.3.3 Results and Discussion	169
4.3.4 Conclusion	177
4.3.5 Bibliography	178

<b>5 Electronic Structure Investigations</b>	<b>180</b>
<b>5.1 Electronic Structure of <math>\text{KCa}_2\text{Nb}_3\text{O}_{10}</math> as Envisaged by Density Functional Theory and Valence Electron Energy Loss Spectroscopy</b>	<b>180</b>
5.1.1 Introduction	180
5.1.2 Computational and Experimental Methodology	181
5.1.3 Results and Discussion	184
5.1.4 Conclusions	196
5.1.5 Bibliography	197
<b>5.2 Band Gap Extraction From Individual Two-dimensional Perovskite Nanosheets using Valence Electron Energy Loss Spectroscopy</b>	<b>200</b>
5.2.1 Introduction	200
5.2.2 Experimental Section	203
5.2.3 Results and Discussion	204
5.2.4 Conclusion	215
5.2.5 Bibliography	216
<b>6 Summary</b>	<b>220</b>
<b>7 Conclusion and Outlook</b>	<b>223</b>
<b>8 Appendix</b>	<b>225</b>
8.1 List of Publications	225
8.2 Chapter Contributions	226
8.3 Conference Contributions	228
8.4 Curriculum Vitae	230



# 1 Introduction

## 1.1 The Nanotechnology Age

New technologies can revolutionize economy and society if society is willing to adopt the technology in question and if there is a broader national consensus that allows the new technology to spread and transform from its initial niche to mass application.<sup>1</sup> For an emerging technology, nanotechnology has made a significant economic impact in a relatively short period of time in diverse sectors ranging from semiconductor manufacturing, catalysts, medicine and agriculture to energy production, and can be considered one of the most important branches of technological development in the early 21<sup>st</sup> century.<sup>2</sup> As a research basis, nanotechnology initiatives were established in sixty countries all over the world between 2001 and 2004.<sup>1</sup> One detailed definition of the term nanotechnology was generated after consultation of experts in over 20 countries by the National Science and Technology Council (NSTC) in 1999: *“Nanotechnology is the ability to control and restructure the matter at the atomic and molecular levels in the range of approximately 1-100 nm, and exploiting the distinct properties and phenomena at that scale as compared to those associated with single atoms or molecules or bulk behavior. The aim is to create materials, devices, and systems with fundamentally new properties and functions by engineering their small structure. This is the ultimate frontier to economically change materials properties, and the most efficient length scale for manufacturing and molecular medicine. The same principles and tools are applicable to different areas of relevance and may help establish a unifying platform for science, engineering, and technology at the nanoscale. The transition from single atoms or molecules behavior to collective behavior of atomic and molecular assemblies is encountered in nature, and nanotechnology exploits this natural threshold.”*<sup>3</sup>

According to this definition, one may consider the engineering of nanostructures to create functional materials as the “holy grail” of nanotechnology. One rather recent class of materials has shown great potential to fulfill this goal, namely two-dimensional (2D) nanosheets. The term “nanosheets” was first used by Sasaki *et al.* to reflect the specific features of unilamellar titanium oxide layers with a thickness of around ~1 nm, a lateral size in the micrometer regime and an extremely high 2D anisotropy.<sup>4</sup> Henceforth “nanosheet” was adopted by the nanotechnology community to describe similar 2D structures. In the ideal case nanosheets consist of single monolayers, but they are often manifested as incompletely exfoliated flakes comprising a small number (<10) of stacked monolayers.<sup>5</sup>

Although 2D materials have a long history, it was the exfoliation of graphite that triggered a research fever due to the remarkable electronic and mechanical properties of isolated graphene nanosheets consisting of a flat monolayer of carbon atoms tightly packed into a 2D honeycomb lattice.<sup>6</sup> In 2004, the group around Geim and Novoselov were first to confirm the existence of substrate-free 2D carbon nanosheets which are amenable to nanodevice

fabrication.<sup>7</sup> An accomplishment for which Geim and Novoselov were awarded with the Nobel Prize in Physics in 2010. From then on, graphene has been proposed and widely explored for use in various applications, ranging from hybrid materials, energy conversion and storage systems, to next-generation electronic and optical devices, such as transistors, sensors, detectors, etc.<sup>8-9</sup> Nevertheless, graphene is a simple material composed of only one element, carbon, which somewhat limits its versatility.<sup>10</sup> A limit that will be overcome by new 2D nanosheets that offer a vast diversity of composition, structure, and functionality.

Figure 1.1 illustrates the arising research trend by plotting the number of publications referring to the keyword “nanosheet” for the last two decades applying SciFinder® as search engine. From the beginning in 1995 till 2003 there were only a few articles published. From 2004 onwards the number of articles started to roughly double each two years, so that in 2014 over 4800 articles dealt with the topic “nanosheets”. A trend that is expected to continue in the near future.

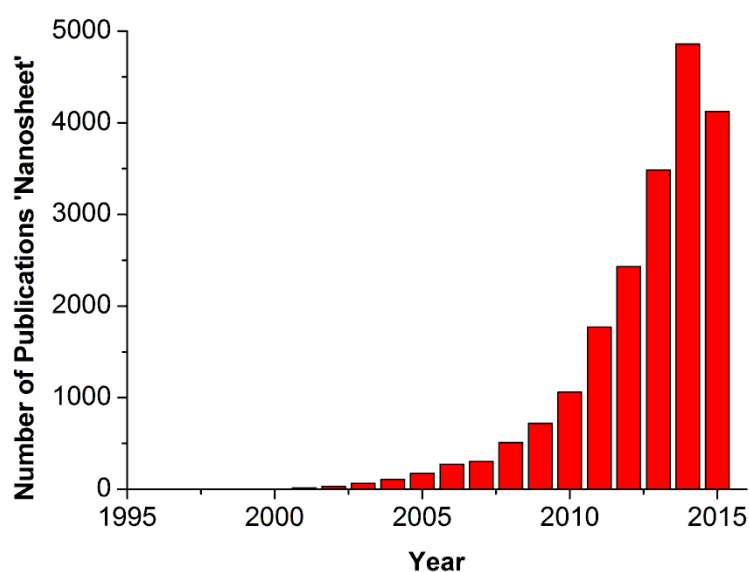


**Figure 1.1:** Number of publications containing the keyword “nanosheet” for the last two decades using SciFinder® as search engine, showing roughly a duplication of publications each two years (18.10.2015).

The present work deals with the synthesis and in-depth characterization of various 2D transition metal oxide (TMO) based nanosheets as well as their rearrangement as artificial solids. The following chapters will give a brief overview of layered bulk materials and their exfoliation into 2D nanosheets, with the focus on the compounds studied in this thesis. Several possibilities to utilize nanosheets as building blocks for the fabrication of new functional heterostructures are introduced. In the end, the objectives of this thesis are set with respect to the current research demands of nanotechnology.

## 1.2 Two-dimensional Nanosheets

A 2D material is defined as a material in which the atomic organization and bond strength along two dimensions are similar and much stronger than along a third dimension.<sup>11</sup> Besides graphite, there are manifold other layered materials that can be divided into two general groups, layered van der Waals solids and layered ionic solids. Layered van der Waals solids exhibit a crystal structure that features neutral layers of atoms or polyhedras with covalent or ionic bonding within the layer and van der Waals bonding between the layers. Graphite is the most prominent example of a layered van der Waals solid, but there are plenty of other examples like hexagonal boron nitride, layered transition metal dichalcogenides  $MX_2$  ( $M = \text{Mo, W, Ti, Zr, Hf, V, Nb, Ta, Re}$ ;  $X = \text{S, Se, Te}$ ) and other chalcogenides like  $\text{Bi}_2\text{Te}_3$ ,  $\text{Sb}_2\text{Te}_3$  and  $\beta\text{-FeSe}$ , to name a few.<sup>11-12</sup> In van der Waals solids weak interlayer energies of around 40-70 meV enable facile exfoliation by usage of for example the “Scotch tape” method or liquid exfoliation by dispersion of the solid in a solvent having the appropriate surface tension or intercalation of molecules/atoms and subsequent agitation (such as shear or ultrasonication) of the intercalated material.<sup>5, 11</sup>

On the contrary, layered ionic solids feature bulk crystal structures with charged polyhedral slabs that are interleaved with electropositive cations or electronegative anions.<sup>11</sup> Layered TMOs are the main group of compounds that form negatively charged nanosheets.<sup>13-14</sup> Its parental compounds are all constituted of negatively charged layers of corner- and/or edge-sharing  $\text{BO}_6$  ( $B = \text{Ti, Nb, Mn, Ta, W}$  etc.) octahedral units that are separated by cations or positively charged covalent networks, e.g. in the case of Aurivillius phases (AV) phases.  $\text{Cs}_{0.7}\text{Ti}_{1.825}\text{O}_4$ ,  $\text{KTiNbO}_5$ ,  $\text{K}_4\text{Nb}_6\text{O}_{17}$ ,  $\text{K}_{0.45}\text{MnO}_2$  or  $\text{Cs}_{6+x}\text{W}_{11}\text{O}_{36}$  are some prominent layered TMO precursors for subsequent exfoliation experiments.<sup>13-14</sup> Another major group of TMO oxides and also the central part of this work is the class of layered perovskites, which will be described in detail in the following.

All layered perovskites are based on the perovskite structure with the general formula  $\text{ABX}_3$ , where  $X$  is an anion and  $A$  and  $B$  are cations (Figure 1.2). Typically, the  $A$  cation is a large cation with low valency, e.g. an alkali or alkaline earth metal, and the  $B$  cation tends to be smaller and have a higher valency.  $X$  is usually O. Almost every element on the periodic table, aside from the noble gases, can be incorporated into the perovskite structure.<sup>15</sup> In the perovskite structure, the unit cell can be thought of as a 3D network of corner-sharing  $\text{BX}_6$  octahedra where the  $A$  cations sit in a cube out of 8  $\text{BX}_6$  octahedra.<sup>16</sup> Hence, within this structure the larger  $A$ -site cations are coordinated 12-fold by  $X$ , while the smaller  $B$ -site cations are coordinated 6-fold by  $X$ .

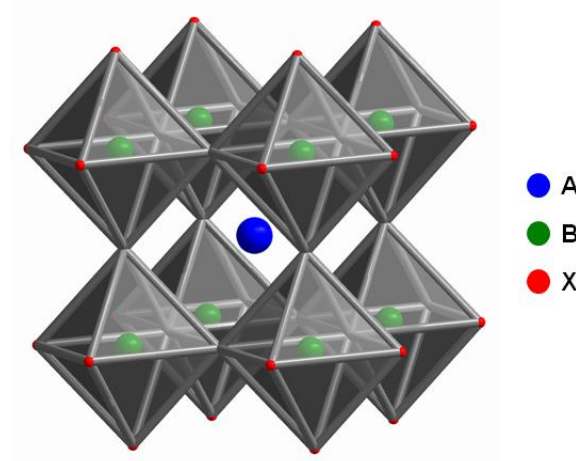


**Figure 1.2:** Polyhedral representation of the ternary perovskite structure  $ABX_3$ .

The ideal, undistorted structure is cubic and has the space group  $Pm\bar{3}m$ . For the aristotype, the size of the unit cell is determined by the  $A-X$  and  $B-X$  bond lengths,  $R_{A-X}$  and  $R_{B-X}$ , respectively. These distances are related by the Goldschmidt tolerance factor<sup>17</sup>:

$$\tau = \frac{R_{A-X}}{\sqrt{2}R_{B-X}} \quad (\text{Eq. 1.1})$$

When  $\tau \sim 0.9-1.0$ , the bond strain is minimized and the ideal geometry can be achieved. However, if  $\tau < 0.9$ , the  $A$  cation is too small for the cavity created for it by the  $BX_3$  network.<sup>18</sup> For  $\tau > 1.0$  a hexagonal structure is formed. As a consequence, distortions and tilts of the  $BX_6$  octahedra can arise in dependence of the present elements, that despite the composition itself can have a major contribution to the properties of the perovskites.<sup>19</sup>

In layered perovskites the perovskite motif is “infinite” in two dimensions, but interposed by cations or cationic structures in the third dimension. Hence, layered perovskites can be denoted by the generalized formula  $M_m[A_{n-1}B_nO_{3n+1}]$ , where  $A_{n-1}B_nO_{3n+1}$  represents the basic layer and  $M$  the interlayer cation or cationic structure.<sup>20</sup> The thickness of the perovskite layers is determined by the number of corner-sharing  $BO_6$  octahedra, which is defined by  $n$ . Layered perovskites can be divided into Dion-Jacobson (DJ), Ruddlesden-Popper (RP) and AV phases and are shown with representative examples in Figure 1.3.<sup>14, 20</sup>

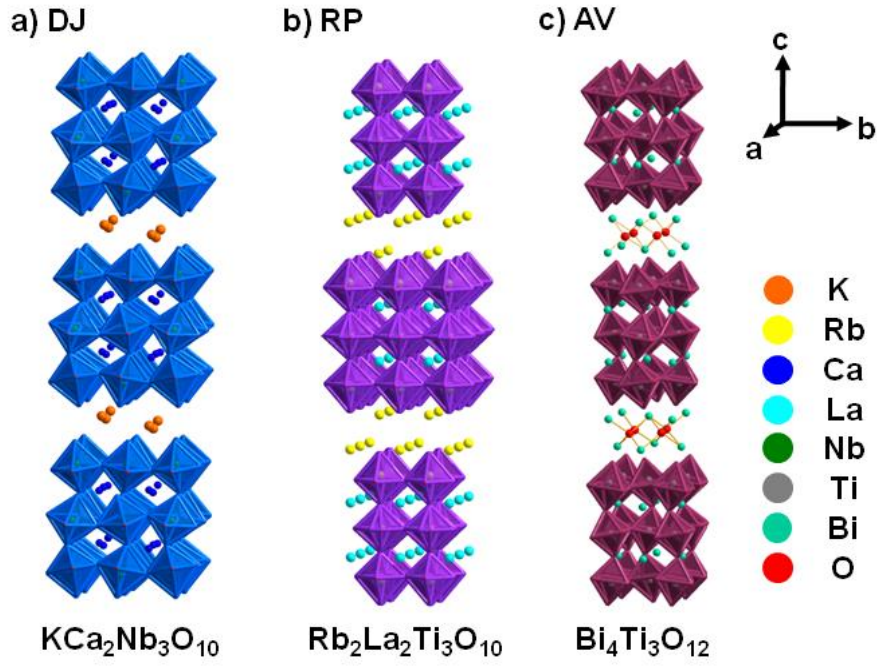


**Figure 1.3:** Schematic comparison of different layered perovskites with representative examples: a) Dion-Jacobson (DJ) phase  $\text{KCa}_2\text{Nb}_3\text{O}_{10}$ , b) Ruddlesden-Popper (RP) phase  $\text{Rb}_2\text{La}_2\text{Ti}_3\text{O}_{10}$  and Aurivillius (AV) phase  $\text{Bi}_4\text{Ti}_3\text{O}_{12}$ .

For the DJ series one monovalent interlayer cation  $M$  per formula unit separates the negatively charged  $[A_{n-1}B_n\text{O}_{3n+1}]^-$  perovskite slabs.  $M$  and  $A$  are usually alkali, alkaline earth or rare earth elements and  $B$  transition metals like niobium, tantalum or titanium. One of the most common and structurally characterized DJ representatives is  $\text{KCa}_2\text{Nb}_3\text{O}_{10}$ , which is also the central compound of this work.<sup>21</sup>  $\text{KCa}_2\text{Nb}_3\text{O}_{10}$  crystallizes in the monoclinic space group  $P2_1/m$  and is built up of corner sharing  $\text{NbO}_6$  octahedra.<sup>22</sup> The divalent  $\text{Ca}^{2+}$ -cations are filling the cavities resulting from eight corner-sharing  $\text{NbO}_6$  octahedra, whereas the monovalent potassium cations separate and link the individual anionic niobate layers. As one can see, the  $\text{NbO}_6$  octahedra are tilted with respect to each other. In general, the distortion is higher for the outer octahedra and is usually less for larger interlayer cations.<sup>23</sup> Equation 1.2 can be used to put these distortions in relation to each other:

$$\text{Octahedron distortion} = \frac{(\text{largest} - \text{smallest})B - O \text{ distance}}{\text{average } B - O \text{ distance}} \quad (\text{Eq. 1.2})$$

RP phases have two interlayer cations  $M_2$  per formula unit and thus twice the interlayer charge density compared to the DJ family.<sup>20</sup>  $\text{Rb}_2\text{La}_2\text{Ti}_3\text{O}_{10}$  is shown as a representative example.<sup>24</sup> In general, one  $A_{n-1}B_n\text{O}_{3n+1}$  perovskite structure block is embedded between two rock-salt structured  $MO$  layers.  $A$  cations show a cuboctahedral coordination, whereas the  $M$  cations have a nine-fold coordination in the interlayer. The unit cell of such RP phases is

elongated along the *c*-direction which leads to a distorted cubic unit cell of the pristine perovskite structure. In AV phases *M* is a covalent network built of  $(\text{Bi}_2\text{O}_2)^{2+}$  layers located between the 2D perovskite slabs  $[\text{A}_{n-1}\text{B}_n\text{O}_{3n+1}]^{2-}$ .<sup>20</sup>  $\text{Bi}_4\text{Ti}_3\text{O}_{12}$  is one prominent example for AV phases.<sup>25</sup>

As mentioned, the perovskite structure itself shows great flexibility in composition, which of course accounts for all types of layered perovskites, too. Thus, the incorporation of ions of different sizes and charges allows for subtle distortions that ease the bond strains created by e.g. size mismatch. Perovskites and layered perovskites are of great interest for the wide variety of properties that they exhibit, which are directly influenced by the structure, as subtle changes alter symmetry considerations, bond overlap, and band energy levels.<sup>18</sup> Despite these similarities, layered perovskites exhibit another useful feature: their cation-exchange property of the interlayer ions/structures. Ion-exchange and intercalation properties facilitate the process for chemically modifying the composition of the interlayer space at ambient temperature, while retaining the host slab units<sup>[20]</sup> - a unique characteristic that can be exploited for exfoliation of the layered perovskites into unilamellar nanosheets.

For layered TMOs a common 2-step exfoliation procedure is schematically shown for the example of  $\text{KCa}_2\text{Nb}_3\text{O}_{10}$  in Figure 1.4. In the first step the interlayer potassium cations are exchanged against protons *via* acid treatment and a solid Brønsted acid  $\text{HCa}_2\text{Nb}_3\text{O}_{10} \cdot x\text{H}_2\text{O}$  is achieved. In the second step, the protons are further exchanged against bulky organic cations such as tetra-*n*-butylammonium ( $\text{TBA}^+$ ) cations in aqueous basic solution to yield  $\text{TBA}_{1-y}\text{H}_y\text{Ca}_2\text{Nb}_3\text{O}_{10}$ . Note that bulky organic cations are usually too large to compensate the negative charge from one oxide unit cell and hence not every proton is exchanged.<sup>26</sup> Such exchange reactions are frequently accompanied by the introduction of large volumes of water, which leads to a decrease of interaction between oxide layers. A swollen phase is formed, that in the ideal case can be separated into individual perovskite layers by weak agitation like stirring, shaking or ultrasonication. One main driving force for this reaction is the neutralization of the protons by the hydroxide counterions of  $\text{TBA}^+$ . The degree of exfoliation along with the sheet quality are determined by certain factors, like composition, charge density, concentration and the nature of the exfoliating agent or solvent.<sup>14</sup>

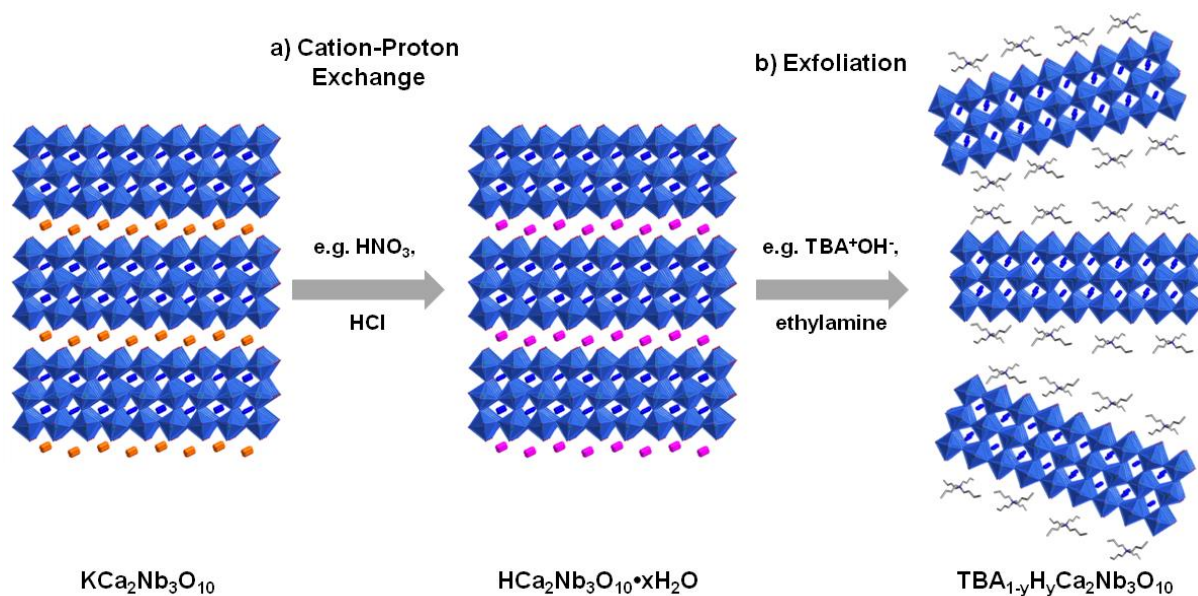


**Figure 1.4:** Common 2-step exfoliation procedure of layered transition metal oxides (TMO)s schematically drawn for the example of  $\text{KCa}_2\text{Nb}_3\text{O}_{10}$ . In step a) the cation is exchanged against a proton and subsequently against a bulky organic cation like tetra-*n*-butylammonium cation to yield individual nanosheets in step b).

Layered double hydroxides (LDHs) and layered rare-earth hydroxides (LREHs) are up to now the main compounds that form positively charged nanosheets, whereby only LDHs play a crucial role in this work. LDHs are basically derived from the Brucite structure ( $\text{Mg}(\text{OH})_2$ ) and exhibit the general formula  $[\text{M}^{2+}_{1-x}\text{M}^{3+}_x(\text{OH})_2]^{x+}[\text{A}^{n-}_{x/n}]^{x-} \cdot m\text{H}_2\text{O}$  (with  $\text{M}^{2+} = \text{Ca}^{2+}, \text{Mn}^{2+}, \text{Mg}^{2+}, \text{Zn}^{2+}, \text{Ni}^{2+}, \text{Co}^{2+}, \text{Fe}^{2+}$  etc. and  $\text{M}^{3+} = \text{Al}^{3+}, \text{Fe}^{3+}, \text{Cr}^{3+}, \text{Mn}^{3+}, \text{Ga}^{3+}, \text{Co}^{3+}, \text{Ni}^{3+}$  etc.).<sup>27</sup> Figure 1.5 shows a representative unit of the MgAl-LDH structure. LDHs are built of edge-sharing  $\text{M}^{2+}/\text{M}^{3+}(\text{OH})_6$  octahedra consisting of divalent and trivalent cations of similar ionic radii which are 6-fold coordinated by oxygen, forming infinite positively charged 2D Brucite-like sheets of  $[\text{M}^{2+}_{1-x}\text{M}^{3+}_x(\text{OH})_2]^{x+}$ . These sheets can be stacked together in the third dimension via hydrogen bonds among the functional hydroxyl groups of adjacent layers.<sup>28</sup> The positively charged framework built up of these sheets is a result of the partial substitution of  $\text{M}^{2+}$ -cations by  $\text{M}^{3+}$ -cations. In order to maintain charge neutrality and compensate the positive layer charge, negatively charged counter anions  $\text{A}^{n-}$  such as  $\text{SO}_4^{2-}$ ,  $\text{NO}_3^-$ ,  $\text{CO}_3^{2-}$ , halides or organic anions have to be intercalated between vicinal layers.<sup>27</sup> Attractive electrostatic interactions between the Brucite-like host layers and the intercalated guest anions as well as hydrogen bonds between the functional hydroxyl groups and interlayer water molecules contribute to a stabilization of the layered structure.<sup>13, 27</sup>



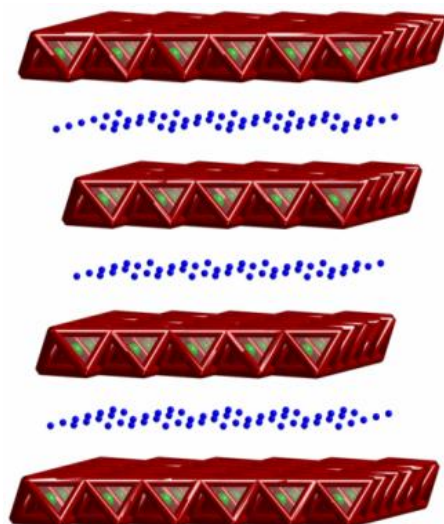


**Figure 1.5:** Polyhedral representation of the layered double hydroxide (LDH) structure.

LDHs can be synthesized in many different ways, whereas coprecipitation is one of the most commonly used methods.<sup>14</sup> Other methods are e.g. homogeneous precipitation or ion-exchange.<sup>14, 27</sup> Coprecipitation relies on the precipitation of two aqueous metal salt solutions of the desired divalent and trivalent ions in the form of the corresponding metal hydroxides under conditions of supersaturation at constant alkaline pH.<sup>13</sup> The strength of the electrostatic interaction between the host layers and the anion is determined by the characteristic properties of the anionic species. With decreasing size of the anion and simultaneously increasing charge the exchange of the anion is hindered due to its stronger electrostatic interactions within the lamellar composite suggesting that larger and lower charged ions facilitate the substitution process. The following sequence gives a general trend concerning the anion-exchangeability:  $\text{CO}_3^{2-} \gg \text{SO}_4^{2-} \gg \text{OH}^- > \text{F}^- > \text{Cl}^- > \text{Br}^- > \text{NO}_3^- > \text{I}^-$ . Thus, high exchangeability is expected if nitrate or halides are dissolved and the synthesis is performed under inert gas conditions in order to avoid the intercalation of carbonate from atmospheric  $\text{CO}_2$ .<sup>29</sup>

The exfoliation of LDHs is generally achieved by stabilizing solvents, e.g. the highly polar formamide, in order to overcome the attractive electrostatic forces between the cationic host layers and the charge balancing anions as well as the hydrogen bonds.<sup>30</sup> Additionally, incorporation of organophilic anions like amino acids, long-chain carboxylates, or other anionic surfactants into LDHs can further help to weaken the layer-to-layer interaction and facilitate swelling and exfoliation in the respective organic solvent.<sup>14</sup> Analogous to the exfoliating process of perovskites, the solvent is osmotically entering the interlayer gallery, interacting with the functional groups of the LDH, decreasing the electrostatic interaction between the host layers and the interlayer species and simultaneously causing an expansion of the crystal volume. Subsequent agitation like stirring, shaking or ultrasonication then leads to the final exfoliation into nanosheets.<sup>13</sup>



### 1.3 Nanosheet-Based Heterostructures

Nanosheets out of layered ionic solids are excellent candidates to be used as 2D building blocks for the controlled construction of various tailored 3D assemblies with superlattice-like arrangement at a molecular scale and sophisticated functionalities. The basic principles of these low-temperature assemblies date back to the 1990s, where the concepts of *Chimie Douce* were established.<sup>20, 31-32</sup> Mallouk and co-workers were among first to show “molecular beaker epitaxy” as solution-based counterpart to gas-phase molecular beam epitaxy.<sup>31</sup> They designed artificial solids that are inaccessible by thermodynamically driven, high-temperature solid-state synthesis pathways. This methodology was mainly extended by Sasaki and co-workers in the following years.<sup>10, 13-14</sup> To date, well-established assembling methods for the fabrication of 2D crystal-based multifunctional heterostructures, are flocculation, layer-by-layer (LbL) assembling techniques based on electrostatic sequential deposition (ESD) and the Langmuir-Blodgett method (LB) (Figure 1.6a-c). But also other traditional wet-processing film fabrication techniques like spin-coating or evaporation-induced self-assembly (EISA) (Figure 1.6d-e) can be used to create nanosheet-based heterostructures.

Flocculation might be considered the simplest method to combine different types of nanosheets (Figure 1.6a). In a general approach, the colloidal suspension of nanosheets is destabilized by the addition of either oppositely charged nanosheets or by addition of electrolytes like NaCl.<sup>13</sup> The advantages of such an approach are the speed as well as the amount of synthesized material, but the achieved heterostructures lack in terms of control over the layer structure, layer registry, and interfacial quality.<sup>33</sup> Some interesting examples are e.g. restacked solids composed of  $\text{Mg}_2\text{Al}(\text{OH})_6/\text{Ca}_2\text{Nb}_3\text{O}_{10}$ ,<sup>34</sup>  $\text{Ti}_{1.83}\text{O}_{0.17}/\text{Zn}_{0.69}\text{Cr}_{0.31}(\text{OH})_2$ ,<sup>35</sup> or  $(\text{Ho}_{0.096}\text{Yb}_{0.23}\text{Y}_{0.164})\text{Ca}_{1.76}\square_{0.24}\text{Nb}_3\text{O}_{10}\cdot 1.4\text{H}_2\text{O}$ .<sup>36</sup> The first example was also first to demonstrate the successful fabrication of a new type of inorganic sandwich structured materials between positively charged LDH nanosheets and negatively charged oxide nanosheets.<sup>34</sup> In the second example, the photocatalytic activity for visible light induced  $\text{O}_2$  generation and chemical stability of the resulting heterolayered nanohybrids in water was better than that of pristine Zn-Cr LDH itself.<sup>35</sup> In the last example a new upconversion material was designed by mixing rare-earth salts with calcium niobate nanosheets where  $\text{Ho}^{3+}$ ,  $\text{Yb}^{3+}$  and  $\text{Y}^{3+}$  act as photoactivator, sensitizer and space filler ions and the nanosheet as structural and thermal stabilizer.<sup>36</sup>

The ESD based LBL technique was used by Decher *et al.* to fabricate multilayer arrangements by alternately dipping a solid substrate in colloidal suspensions of oppositely charged nanoparticles or polyelectrolytes (Figure 1.6b).<sup>37-38</sup> Polyethylenimine (PEI) and Poly(diallyldimethylammoniumchloride) (PDDA) are typically used polymeric counterparts for the deposition and adsorption of multilayer films. This approach can be transferred to fabricate heterostructures out of oppositely charged nanosheets or a combination of

polyelectrolytes with nanosheets.<sup>13, 39</sup> The bottleneck of this approach is to achieve a dense monolayer packing for the first deposited layer. In most cases a pretreatment of the substrate with an organic polyelectrolyte of the opposite charge or self-assembled monolayers (SAMs) and a precise control of the pH is necessary in order to accomplish high surface coverage.<sup>40</sup> Afterwards, the LBL technique is a self-limiting process, as the adsorption of material stops, once the charge is compensated.<sup>33</sup> Extensive washing steps can be applied in between to remove excess material, so that control of the array on the nanometer scale is possible. For example, a  $(\text{Ca}_2\text{Nb}_3\text{O}_{10}/\text{PDDA}/\text{LaNb}_2\text{O}_7/\text{PDDA}/\text{Sr}_2\text{Nb}_3\text{O}_{10}/\text{PDDA}/\text{LaNb}_2\text{O}_7/\text{PDDA})_n$  mixed layered perovskite was synthesized by LBL deposition, which is not accessible by bulk synthesis.<sup>40</sup> Organic components can subsequently be decomposed by heat treatment or UV irradiation if the deposited nanosheets are photocatalytically active.<sup>41</sup> Examples of pure nanosheet based assemblies are  $(\text{Mg}_2\text{Al}(\text{OH})_6/\text{Ti}_{0.91}\text{O}_2)_n$  and  $(\text{Mg}_2\text{Al}(\text{OH})_6/\text{Ca}_2\text{Nb}_3\text{O}_{10})_n$  or  $(\text{Eu}(\text{OH})_{3-x}/\text{Ti}_{1.81}\text{O}_4)_n$ .<sup>34, 42</sup> In the latter, titanate nanosheets were used as an “antenna” for UV-light harvesting and europium nanosheets as an emissive layer due to a strong  $\text{Eu}^{3+}$  emission under UV irradiation.<sup>42</sup> Last but not least, multilayer films of only LDH nanosheets can typically be deposited with anionic poly(styrene 4-sulfonate) (PSS) as counter polyelectrolyte.<sup>43</sup>

In the LB deposition/transfer a compressed floating monolayer of nanosheets is transferred onto the substrate (Figure 1.6c). Thus, LB deposition is the current tool of choice to create high quality multilayer nanosheet films as the problem of a dense monolayer packing in ESD based experiments is overcome. Recent examples are an all-nanosheet capacitor out of  $(\text{Ru}_{0.95}\text{O}_2^{0.2-}/\text{Ca}_2\text{Nb}_3\text{O}_{10}^-/\text{Ru}_{0.95}\text{O}_2^{0.2-})$  where the ruthenium oxide sheets operate as electrodes and the calcium niobate sheets as dielectric block and  $(\text{LaNb}_2\text{O}_7^-/\text{Ca}_2\text{Nb}_3\text{O}_{10}^-)_n$  which shows a ferroelectric behavior despite the fact that both nanosheets are paraelectric.<sup>44-45</sup> However, the LB transfer is rather time consuming and the organic ligand has to be decomposed in order to enable deposition of the next layer. Thus, the LB approach can be considered an essential way to gather fundamental knowledge of nanosheet devices, but its setup has to be modified or transferred to other fabrication routes in order to match industrial needs.

Flocculation, LBL assembly and LB transfer are currently the three main pathways for fabrication of multilayer nanosheet heterostructures, however other wet processing methods like spin-coating (Figure 1.6d) or EISA (Figure 1.6e) can also be useful tools. E.g.,  $\text{TBA}_{1-y}\text{H}_y\text{Ca}_2\text{Nb}_3\text{O}_{10}$  nanosheets were spin-coated as a novel electron transport material in solution-processed multi-junction polymer solar cells.<sup>46</sup> Different niobate nanosheets derived from  $\text{K}_4\text{Nb}_6\text{O}_{17}$  were used to fabricate porous solids with EISA.<sup>47</sup>

Overall one can see a rapid development in the fabrication of heterostructures out of 2D nanosheets in the last decade, but there still remain many obstacles that need to and will be overcome in future.

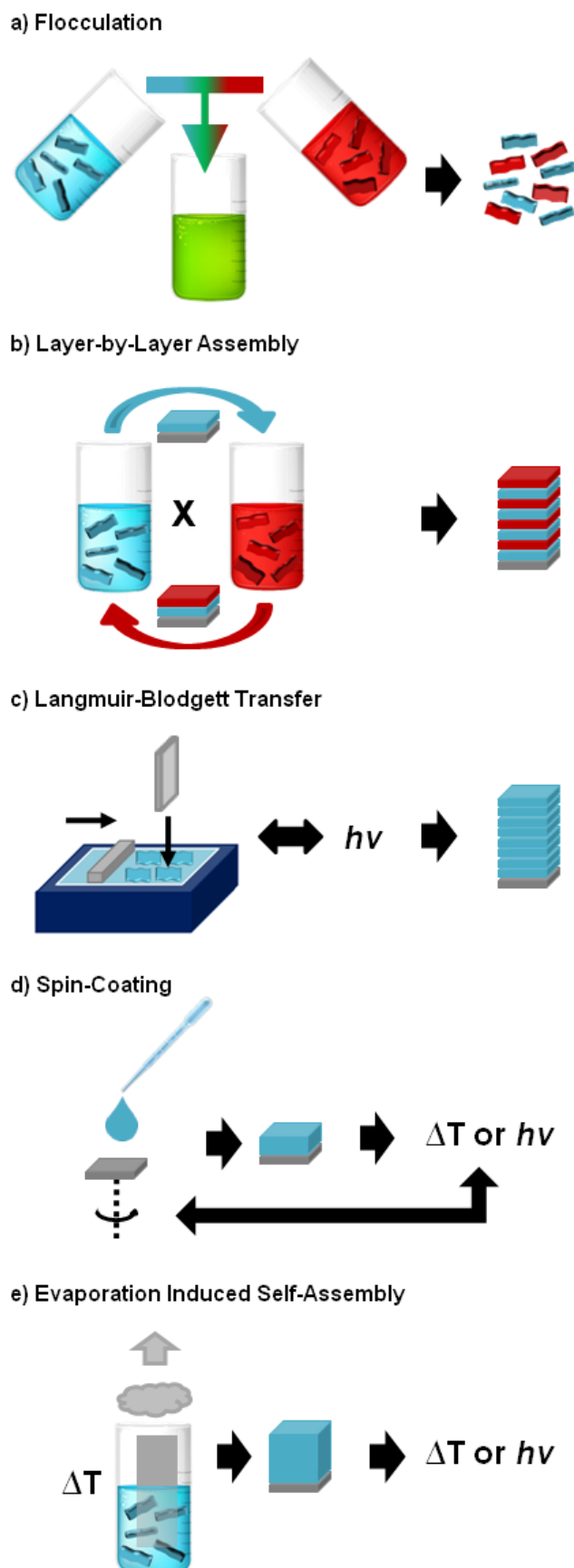


**Figure 1.6:** Schematic illustration of different wet-chemical assembly routes for heterostructures composed of nanosheets: a) flocculation, b) layer-by-layer (LBL) assembly, c) Langmuir-Blodgett (LB) transfer, d) spin-coating and e) evaporation induced self-assembly (EISA).

## 1.4 Objectives

One key challenge for the future of the fast expanding field of nanotechnology is the assembly of individual nanostructures into “composite materials by design”.<sup>48</sup> Thus, fabrication protocols need to be developed that allow for a flexible, automated, and scalable design of heterostructures, which are amenable to integration into the existing industrial schemes.<sup>33</sup> This goes along with the improvement of the current exfoliation pathways. The size, regular shape, purity and yield of nanosheets has to be drastically improved to allow for an industrial-scale production.<sup>5</sup> Sophisticated tuning of chemical composition and structure of the 2D nanosheets are an inevitable necessity in order to enable such fabrication protocols for the desired targeted functionality. Besides synthesis and exploration of properties, the in-depth analysis and hence understanding of nanomaterials is another factor that should not be underestimated in order to accomplish the transition from the realm of fundamental research to industrial applications. According to these requirements, the present dissertation is divided into three main chapters: two-dimensional transition metal oxide nanosheets (Chapter 3), nanosheet based heterostructures (Chapter 4) and electronic structure investigations (Chapter 5). In the following, the key objectives are described in more detail with respect to the general context above.

The development and expansion of a broad nanosheet library is the basis for the subsequent design of composite materials with manifold functionalities. Regarding water splitting Pb doping is a generic method of visible-light sensitization of layered TMOs for photochemical properties. In Chapter 3.1 we investigated the new solid solution  $\text{RbCa}_{2-x}\text{Pb}_x\text{Nb}_3\text{O}_{10}$  and derived nanosheets for this purpose. To impart TMOs with photoluminescent properties, rare-earth doping into layered TMOs is a tool of choice. Thus, in Chapter 3.2 we examined the series of  $\text{K}_{1-x}\text{Ca}_{2-x}\text{Ln}_x\text{Nb}_3\text{O}_{10}$  ( $\text{Ln}$  = lanthanide) compounds. New synthesis pathways are needed to extend the nanosheet library and improve nanosheet quality and yield. In Chapter 3.3, we established a new exfoliation route *via* an Ag exchange and subsequent exfoliation with a bulky organic iodide, following the Pearson acid base concept.

Recent literature focuses mainly on the fabrication of thin films, whereas information on the solution-based bottom-up fabrication of bulk materials is still lacking. This profound knowledge is key for future industrial scale-up productions. In Chapter 4.1, we show the fabrication of a 100 bilayer stack out of layered perovskite nanosheets and LDH nanosheets. In-depth transmission electron microscopy (TEM) coupled with energy-dispersive X-ray (EDX) spectroscopy and electron energy loss spectroscopy (EELS) is used to analyze the structure with state of the art tools. For future application of such heterostructures, many devices require high thermal stability, especially those in semiconductor industry, as well as smooth interfaces. We therefore analyzed the thermal behavior of fabricated hybrid stacks in Chapter 4.2. Another factor for consideration is that the function depends on parameters like

film thickness, porosity etc. Thus, we investigated several ways of exploiting the 2D nanosheet motif for the fabrication of various nanoscale morphologies in Chapter 4.3.

A driving force of nanotechnology is the difference between bulk material and nanomaterial. For example profound knowledge about the band-gap of the material as a function of the size is inevitable for many applications. Thus, we used valence electron energy loss spectroscopy (VEELS) to characterize bulk  $\text{KCa}_2\text{Nb}_3\text{O}_{10}$  (Chapter 5.1) as well as  $\text{TBA}_{1-y}\text{H}_y\text{Ca}_2\text{Nb}_3\text{O}_{10}$  nanosheets and derived the bandgap of individual TMO nanosheets by VEELS for the first time (Chapter 5.2).

## 1.5 Bibliography

- [1] A. Clunan, K. Rodine-Hardy, *Nanotechnology in a Globalized World: Strategic Assessments of an Emerging Technology*, **2014**.
- [2] H. Chen, M. C. Roco, J. Son, S. Jiang, C. A. Larson, Q. Gao, *J. Nanopart. Res.* **2013**, *15*, 1-21.
- [3] R. W. Siegel, E. Hu, M. C. Roco, D. M. Cox, H. Goronkin, *Nanostructure Science and Technology. A Worldwide Study*, DTIC Document, **1999**.
- [4] T. Sasaki, M. Watanabe, H. Hashizume, H. Yamada, H. Nakazawa, *J. Am. Chem. Soc.* **1996**, *118*, 8329-8335.
- [5] V. Nicolosi, M. Chhowalla, M. G. Kanatzidis, M. S. Strano, J. N. Coleman, *Science* **2013**, *340*.
- [6] A. K. Geim, *Science* **2009**, *324*, 1530-1534.
- [7] K. S. Novoselov, A. K. Geim, S. V. Morozov, D. Jiang, Y. Zhang, S. V. Dubonos, I. V. Grigorieva, A. A. Firsov, *Science* **2004**, *306*, 666-669.
- [8] K. S. Novoselov, V. I. Falko, L. Colombo, P. R. Gellert, M. G. Schwab, K. Kim, *Nature* **2012**, *490*, 192-200.
- [9] X. Huang, X. Qi, F. Boey, H. Zhang, *Chem. Soc. Rev.* **2012**, *41*, 666-686.
- [10] M. Osada, T. Sasaki, *Adv. Mater. (Weinheim, Ger.)* **2012**, *24*, 210-228.
- [11] S. Z. Butler, S. M. Hollen, L. Cao, Y. Cui, J. A. Gupta, H. R. Gutiérrez, T. F. Heinz, S. S. Hong, J. Huang, A. F. Ismach, E. Johnston-Halperin, M. Kuno, V. V. Plashnitsa, R. D. Robinson, R. S. Ruoff, S. Salahuddin, J. Shan, L. Shi, M. G. Spencer, M. Terrones, W. Windl, J. E. Goldberger, *ACS Nano* **2013**, *7*, 2898-2926.
- [12] P. Miro, M. Audiffred, T. Heine, *Chem. Soc. Rev.* **2014**, *43*, 6537-6554.
- [13] R. Ma, T. Sasaki, *Adv. Mater. (Weinheim, Ger.)* **2010**, *22*, 5082-5104.
- [14] R. Ma, T. Sasaki, *Acc. Chem. Res.* **2015**, *48*, 136-143.
- [15] D. G. Schlom, L.-Q. Chen, X. Pan, A. Schmehl, M. A. Zurbuchen, *J. Am. Ceram. Soc.* **2008**, *91*, 2429-2454.
- [16] K. S. Aleksandrov, V. V. Beznosikov, *Phys. Solid State* **1997**, *39*, 695-715.

- [17] V. M. Goldschmidt, *Naturwissenschaften* **1926**, *14*, 477-485.
- [18] M. C. Knapp, The Ohio State University **2006**.
- [19] A. M. Glazer, *Phase Transitions* **2011**, *84*, 405-420.
- [20] R. E. Schaak, T. E. Mallouk, *Chem. Mater.* **2002**, *14*, 1455-1471.
- [21] M. Dion, M. Ganne, M. Tournoux, *Mater. Res. Bull.* **1981**, *16*, 1429-1435.
- [22] T. Tokumitsu, K. Toda, T. Aoyagi, D. Sakuraba, K. Uematsu, M. Sato, *J. Ceram. Soc. Jpn.* **2006**, *114*, 795-797.
- [23] F. Lichtenberg, A. Herrnberger, K. Wiedenmann, *Prog. Solid State Chem.* **2008**, *36*, 253-387.
- [24] S.-H. Byeon, H.-J. Nam, *Chem. Mater.* **2000**, *12*, 1771-1778.
- [25] B. Aurivillius, *Arkiv for kemi* **1950**, *1*, 499-512.
- [26] H. Gao, S. Shori, X. Chen, H.-C. zur Loye, H. J. Ploehn, *J. Colloid Interface Sci.* **2013**, *392*, 226-236.
- [27] Q. Wang, D. O'Hare, *Chem. Rev. (Washington, DC, U. S.)* **2012**, *112*, 4124-4155.
- [28] A. I. Khan, D. O'Hare, *J. Mater. Chem.* **2002**, *12*, 3191-3198.
- [29] S. Carlino, *Solid State Ionics* **1997**, *98*, 73-84.
- [30] R. Ma, Z. Liu, L. Li, N. Iyi, T. Sasaki, *J. Mater. Chem.* **2006**, *16*, 3809-3813.
- [31] S. W. Keller, H.-N. Kim, T. E. Mallouk, *J. Am. Chem. Soc.* **1994**, *116*, 8817-8818.
- [32] G. Decher, J.-D. Hong, *Makromol. Chem., Macromol. Symp.* **1991**, *46*, 321-327.
- [33] B. V. Lotsch, *Annu. Rev. Mater. Res.* **2015**, *45*, 85-109.
- [34] L. Li, R. Ma, Y. Ebina, K. Fukuda, K. Takada, T. Sasaki, *J. Am. Chem. Soc.* **2007**, *129*, 8000-8007.
- [35] J. L. Gunjekar, T. W. Kim, H. N. Kim, I. Y. Kim, S.-J. Hwang, *J. Am. Chem. Soc.* **2011**, *133*, 14998-15007.
- [36] T. C. Ozawa, M. Onoda, N. Iyi, Y. Ebina, T. Sasaki, *J. Phys. Chem. C* **2014**, *118*, 1729-1738.
- [37] Y. Lvov, G. Decher, H. Moehwald, *Langmuir* **1993**, *9*, 481-486.
- [38] G. Decher, *Science* **1997**, *277*, 1232-1237.
- [39] R. Ma, T. Sasaki, *Annu. Rev. Mater. Res.* **2015**, *45*, 111-127.
- [40] R. E. Schaak, T. E. Mallouk, *Chem. Mater.* **2000**, *12*, 2513-2516.
- [41] T. Sasaki, Y. Ebina, K. Fukuda, T. Tanaka, M. Harada, M. Watanabe, *Chem. Mater.* **2002**, *14*, 3524-3530.
- [42] S. Ida, Y. Sonoda, K. Ikeue, Y. Matsumoto, *Chem. Commun. (Cambridge, U. K.)* **2010**, *46*, 877-879.
- [43] J. Han, Y. Dou, M. Wei, D. G. Evans, X. Duan, *Angew. Chem., Int. Ed. Engl.* **2010**, *49*, 2171-2174.

- [44] C. Wang, M. Osada, Y. Ebina, B.-W. Li, K. Akatsuka, K. Fukuda, W. Sugimoto, R. Ma, T. Sasaki, *ACS Nano* **2014**, 8, 2658-2666.
- [45] B.-W. Li, M. Osada, T. C. Ozawa, Y. Ebina, K. Akatsuka, R. Ma, H. Funakubo, T. Sasaki, *ACS Nano* **2010**, 4, 6673-6680.
- [46] L. Chang, M. A. Holmes, M. Waller, F. E. Osterloh, A. J. Moule, *J. Mater. Chem.* **2012**, 22, 20443-20450.
- [47] N. Miyamoto, K. Kuroda, *J. Colloid Interface Sci.* **2007**, 313, 369-373.
- [48] M. C. Roco, C. A. Mirkin, M. C. Hersam, *Nanotechnology research directions for societal needs in 2020: retrospective and outlook*, Vol. 1, Springer Science & Business Media, **2011**.

## 2 Methods

### 2.1 Powder X-Ray Diffraction

Powder X-ray diffraction (XRD) is a non destructive technique that allows to identify and characterize crystalline phases like layered TMOs regarding their lattice parameters, crystal structure, phase purity, crystallinity, orientation and particle size. A powder XRD diffractometer consists of an X-ray source, a sample stage, a detector and a way to vary the angle  $\theta$ .<sup>1</sup> Diffractometers can be operated either in transmission or in reflection geometry. X-rays are generated when matter like Cu or Ag is irradiated by a beam of high-energy electrons under vacuum conditions. The inner shell electrons of the material are excited to unoccupied states and emit X-rays or Auger electrons when they relax back to their ground state. These emissions are accompanied by “Bremsstrahlung” as a fraction of the incident electrons is slowed down in the Coulomb field of the atomic nucleus. The “Bremsstrahlung” and undesired emission lines are cut out by filters, monochromators or X-ray mirrors, before the resulting monochromatic X-rays are collimated and focused onto the specimen.

In a diffraction experiment, the incident X-rays must have wavelengths comparable to the spacings between atoms. The main target is to know the particular condition in which the scattered X-rays from atoms and the incident X-rays are completely in phase and reinforce each other to produce a detectable diffracted beam (Figure 2.1.1).<sup>1</sup> If the incident X-rays of wavelength  $\lambda$  impinge a crystal with a regular periodic array of atoms with interplanar spacing  $d$ , a diffracted beam of sufficient intensity is detected only when the Bragg’s law is fulfilled (Equation 2.1.1):<sup>2</sup>

$$2d \sin \theta = n\lambda \quad (\text{Eq. 2.1.1})$$

where the order of reflection  $n$  is an integer. The diffraction angle  $2\theta$  of any set of planes ( $hkl$ ) can be calculated combining the Bragg condition with the plane-spacing equations for the seven crystal systems, which relate the relationship among the distance of adjacent planes to Miller indices and lattice parameters for each crystal system.<sup>1</sup> On contrary, one can possibly determine an unknown crystal structure by measuring the diffraction angles and hence, relate the diffraction angles directly to the positions of atoms in the unit cell. In layered systems characteristic ( $00l$ ) reflections arise that correspond to the basal  $d$ -spacing resulting from the stacked layers. Compared to layered bulk materials, 2D nanosheets show only ( $hk0$ ) reflections, have a asymmetrical Warren-type peak profile and the peak position can be displaced with respect to the bulk material.<sup>3-4</sup>



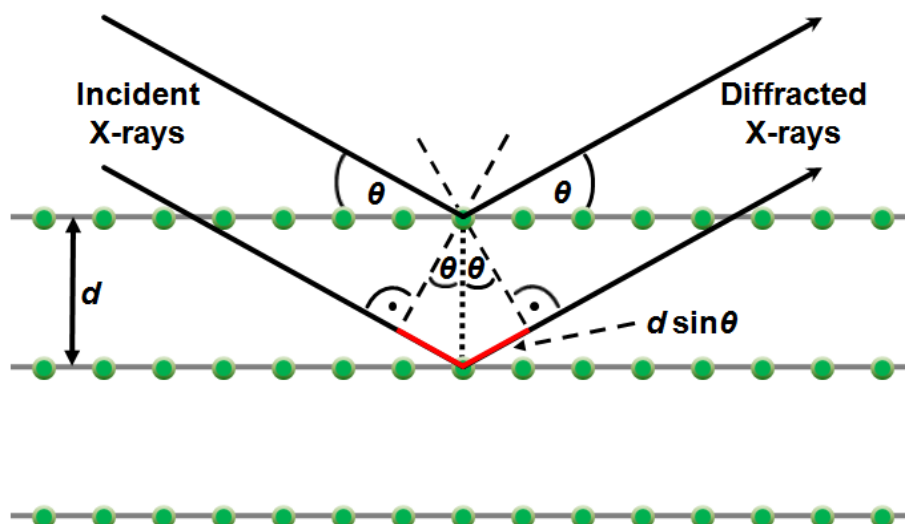


**Figure 2.1.1:** Schematic drawing of the Bragg condition. Two X-rays with characteristic wavelength  $\lambda$  are scattered at an angle  $\theta$  by atoms located at parallel lattice planes with distance  $d$  leading to a path difference  $2d \sin\theta$  shown in red.

In this thesis, XRD measurements were mainly used to monitor bulk precursors and intermediate cation-proton exchanged materials. XRD diffractograms were therefore analysed with the help of the software WINXPOW<sup>5-6</sup> and compared with the “International Centre for Diffraction Data” (ICDD)<sup>7</sup> database and the “Pearson's Crystal Data - Crystal Structure Database for Inorganic Compounds” (PCD)<sup>8</sup> and the “The Inorganic Crystal Structure Database” (ICSD)<sup>9</sup>. Furthermore, XRD was used to retrace structural changes in substitution experiments. In multilayer arrangements, XRD was performed to investigate the basal reflections.

In total, three different instruments were used. A Huber G670 Guinier Imaging Plate diffractometer (HUBER X-Ray Diffraction Equipment, Rimsting; Cu  $K_{\alpha 1}$ -radiation,  $\lambda = 154.051$  pm, Ge(111)-monochromator, external standard  $\text{SiO}_2$ ). A STOE Stadi P powder diffractometer in Debye–Scherrer-geometry (STOE & Cie GmbH, Darmstadt; Cu  $K_{\alpha 1}$  radiation,  $\lambda = 154.056$  pm, Ge(111)-monochromator, with a linear position sensitive detector). A Bruker D8 Advance diffractometer (Bruker, Billerica, Cu  $K_{\alpha 1}$  radiation,  $\lambda = 154.051$  pm) in Bragg Brentano geometry. All measurements were performed at room temperature. Daniel Weber (Chapter 3.1), Christine Stefani and Tanja Holzmann (Chapter 4.1) assisted in additional measurements.

## 2.2 Elemental Analysis

### 2.2.1 Inductively Coupled Plasma and Atomic Emission Spectroscopy

Inductively coupled plasma and atomic emission spectroscopy (ICP-AES) is a sensitive trace element analysis technique to determine which elements are present and at what

concentration<sup>10</sup> In general, excited atoms and ions can emit electromagnetic radiation at specific wavelengths peculiar to their chemical character as they return to ground state. For ICP-AES experiments, a plasma source is used to dissociate the sample into its constituent atoms/ions, exciting them to a higher energy level. A single, characteristic wavelength for each element is selected and the intensity of the emitted energy related to the amount of that element present in the sample. Thus, by detection of the emitted wavelengths and their intensities, it is possible to quantify the elemental composition of the given sample relative to a reference standard.<sup>10</sup>

In this thesis, ICP-AES was mainly used to ascertain a complete exchange of the layered bulk material interlayer cations against  $H^+$  or  $Ag^+$ , respectively. Moreover, chemical composition and impurities were investigated. Two ICP-AES systems were used. First, a Vista Pro ICP-AES spectrometer (Varian Inc., Darmstadt) where the characteristic wavelengths were separated with an Echelle-Polychromator and detected with a photomultiplier. Second, a VISTA RL CCD and ICP-AES analyzer system (Agilent Technologies, Waldbronn). Measurements were performed by Marie-Luise Schreiber (Chapter 3.1) and Helmut Hartl (Chapter 4.1).

### 2.2.2 CHNS Elemental Analysis

CHNS elemental analysis can provide a rapid determination of carbon, hydrogen, nitrogen and sulphur in various types of materials. In a combustion process carbon is converted to carbon dioxide; hydrogen to water, nitrogen to nitrogen (oxides) and sulphur to sulphur dioxide.<sup>11</sup> The desired combustion products are then separated and purified and their detection carried out, e.g. by gas chromatography and thermal conductivity measurements.<sup>11</sup> Calibration for each element by comparison to high purity micro-analytical standards is necessary for absolute quantification.

In this thesis, CHNS analysis was conducted to determine the amount of organic ligand surrounding inorganic nanosheets, e.g.  $TBA_{1-y}H_yCa_2Nb_3O_{10}$ . Therefore, unexfoliated material in colloidal suspensions was first removed at low centrifugation speeds and nanosheets subsequently isolated at high centrifugation speeds. The supernatant was removed and the nanosheet pellet dried before CHNS elemental analysis. Based on the mass fraction of ligand specific elements C, N and/or S the amount of ligand was determined and the amount of crystal water set on basis of the excess H. CHNS analysis was performed on an Elementar Vario EL (Elementar Analysensysteme, Hanau) by R. Eicher (Chapter 4.1).

## 2.3 Electron Microscopy

Electron microscopy today comprises a diversity of different techniques rather than just a single technique. These techniques offer unique possibilities to gain insights into structure, topology, morphology as well as composition of all kinds of materials. Manifold imaging and spectroscopic methods became indispensable tools for the characterization of specimens on an increasingly smaller size scale with the ultimate limit of a single atom. These profound possibilities are caused by the multitude of signals arising from the interaction of electrons with matter schematically depicted in Figure 2.3.1.<sup>12</sup> In general, one can distinguish between elastic and inelastic interactions.<sup>13</sup> In the former, no energy is transferred from the electron to the sample. This is the case, when the electron beam passes through the sample without any interaction and hence, no change in direction occurs. Another possibility is that electrons are deflected from their path by Coulomb interaction. In the case of scattering at the nucleus this can lead to backscattered electrons (BSE). However, for diffraction experiments the elastic scattering at the outer electron cloud is important. On contrary, analytical microscopy rather depends on the energy transfer of electrons to the specimen leading to different signals such as characteristic X-rays, Auger electrons, secondary electrons (SE), inelastically scattered electrons, plasmons, phonons etc.. In the following, main analytical methods like energy dispersive X-ray (EDX) spectroscopy and electron energy loss spectroscopy (EELS) will be explained in more detail before the basic principles of scanning electron microscopy (SEM) and transmission electron microscopy (TEM) will be evaluated.

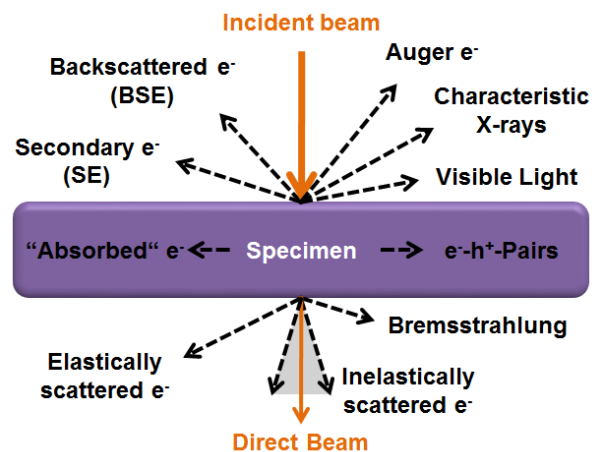


**Figure 2.3.1:** Schematic illustration of electron-matter interactions that can occur from the impact of an electron beam onto a specimen. No interaction (direct beam), elastically scattered electrons, backscattered electrons (BSE), inelastically scattered electrons, characteristic X-rays, Bremsstrahlung, Auger electrons, secondary electrons (SE), electron-hole pairs (cathodoluminescence), visible light, absorbance of electrons, as well as phonon and plasmon oscillations (not shown).

### 2.3.1 Energy Dispersive X-Ray Spectroscopy

EDX spectroscopy can be used in combination with SEM or TEM to determine the overall chemical composition of a sample or to analyze local differences in its composition. The generation of characteristic X-rays is visualized in Figure 2.3.2.<sup>13</sup> In the first step an atom is ionized by an energy transfer from the incident electron to an inner shell electron of the atom. The inner shell electron is either excited to an unoccupied level or ejected into the vacuum. In the second step, this arising vacancy is filled by an electron from a higher state, which can be accompanied by the emission of an X-ray quantum as a result of the surplus difference energy. Note that the emission of an Auger electron is an alternative process, where the excess energy is transferred to a further electron that subsequently gets ejected into the vacuum.<sup>13</sup>

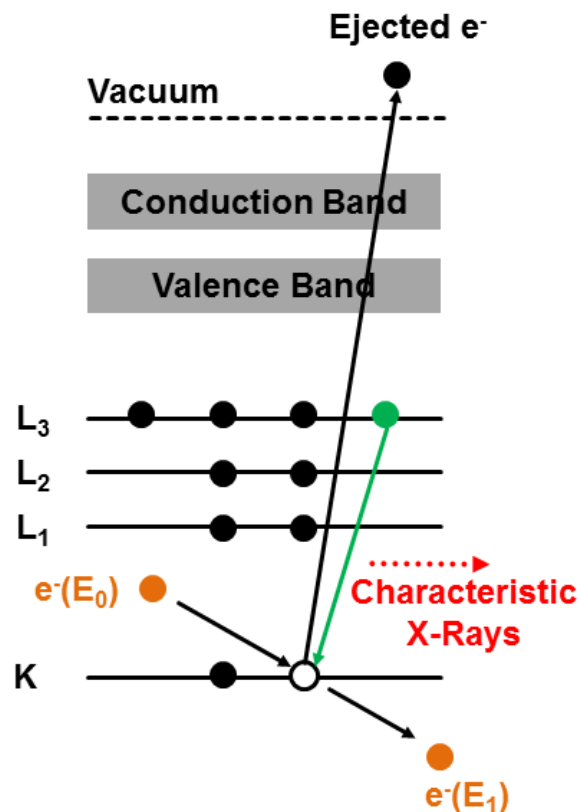


**Figure 2.3.2:** Scheme of characteristic X-ray generation. The incident electron transfers energy to an inner shell electron of an atom that gets ejected. The remaining vacancy is filled by an electron of a higher state. The energy difference is emitted in form of characteristic X-rays.

The emitted X-rays are characteristic for each element and can be used for quantitative analysis, especially for those with an atomic number  $Z > 13$ .<sup>12</sup> Below this threshold characteristic X-rays are low in energy and can easily be absorbed by the sample or the detector window. As different transitions can occur they are named after the electron shell from which the electron is excited (K, L, M) and the electron shell from which the

electron comes to fill the vacancy ( $\alpha$ ,  $\beta$ ,  $\gamma$ ). Quantitative EDX can be performed, e.g. by applying the Cliff-Lorimer equation (Equation 2.3.1):<sup>14</sup>

$$\frac{N_A}{N_B} = k_{AB} \frac{I_A}{I_B} \quad (\text{Eq. 2.3.1})$$

with  $N_A$  and  $N_B$  being the atomic% of element  $A$  and  $B$ ,  $I_A$  and  $I_B$  the measured intensity of the elements and  $k_{AB}$  being the Cliff-Lorimer factor. Note that first the unspecific background due to braking radiation (“Bremsstrahlung”) has to be subtracted, e.g. *via* the Kramer’s equation, and standards containing elements  $A$  and  $B$  should be used to obtain accurate values for the  $k_{AB}$  factor .<sup>15</sup>

### 2.3.2 Electron Energy Loss Spectroscopy

EELS is an analytical technique that measures the change in kinetic energy of electrons after their interaction with the sample and can give structural and chemical information with a spatial resolution down to the atomic level. Inelastic scattered electrons are separated in dependence of their energy with help of a magnetic prism and thus, detected as a function of their energy loss.<sup>16</sup> Figure 2.3.3 displays such an exemplary EEL spectrum. In the beginning the most dominant feature is visible, the zero loss peak (ZLP). It is related to all the elastically and quasielastically (i.e. vibrational- or phonon-) scattered electrons. Thus, for thin samples it is the most intense signal. The width of the ZLP, typically 0.2-2 eV, reflects mainly the energy distribution of the electron source and determines the overall spectral resolution. Adjacent to the ZLP the low loss region is found up to ~50 eV. The plasmon peaks are the dominant features in this region. Together with the ZLP the region can be used to determine the thickness of the sample. It is also referred to as valence electron energy loss spectrum (VEELS) as the excitations up to about 50 eV are predominantly caused by the excitations of the valence electrons.<sup>17</sup> From careful data acquisition it is possible to extract the band gap and information on the dielectric function of applicable materials in this region.<sup>12</sup> In the following core loss region the signal intensity drops rapidly and is mainly due to signals arising from e.g. plasmon tails and low energy edges.<sup>13</sup> Above the background well defined peaks can be found that belong to ionization edges that are characteristic for each element. The onset of such edges corresponds to the threshold energy that is necessary to excite an inner shell electron from its ground state to the lowest unoccupied level. Above threshold energy, not all further transitions are equally likely and for a crystal determined by the density of states (DOS) above the Fermi level.<sup>16</sup> This gives rise to the electron energy loss near edge structure (ELNES) that reflects the DOS and thus, gives information about the bonding state. Information about coordination and

interatomic distances can be obtained by evaluation of the extended energy loss fine structure (EXELFS).<sup>16</sup>

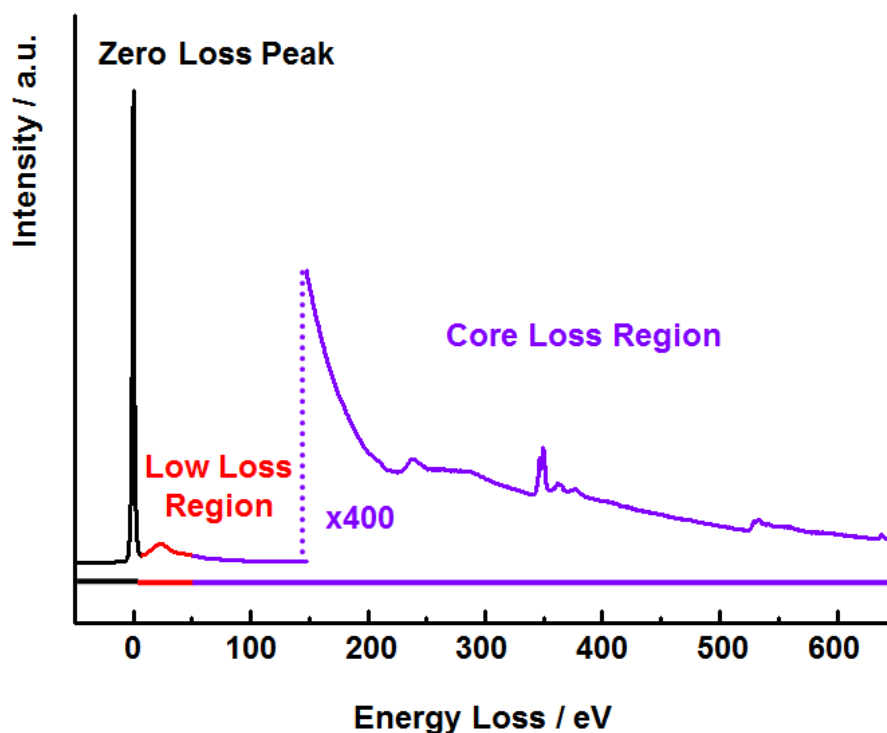


**Figure 2.3.3:** Exemplary EEL spectrum highlighting the essential three different regions: Zero loss peak, low loss and core loss region.

EELS and EDX can be regarded as complimentary analytical methods. In comparison, EELS has a higher energy resolution and can detect light elements, but needs thin samples and suffers from low intensities for edges at higher energy losses >1000 eV.

### 2.3.3 Scanning Electron Microscopy

SEM can be used to obtain information on the external morphology, namely size and shape of the investigated sample as well as its chemical composition when coupled with EDX spectroscopy. A schematic setup of a SEM is shown in Figure 2.3.4.<sup>18</sup> An electron gun, e.g. a thermionic gun, Schottky emitter or cold field emitter, emits electrons which are then accelerated to energies between 1-30 keV. A condenser lens system, the objective lens and various apertures are used to demagnify the electron beam to a diameter of 2–10 nm and scanning coils are used to scan the beam across the sample. The investigated samples have to be conductive to avoid charging effects due to electron trapping, therefore non-conductive samples are coated with thin layers of e.g. amorphous carbon or gold. The generated signals of each sample point are detected. Due to the small scattering angles, SEM micrographs have a large depth of field yielding

a characteristic three-dimensional appearance useful for understanding the surface structure of a sample.<sup>18</sup> SE with energies of a few eV arise from the upper layers (~50 nm) of the sample, are collected by an Everhart-Thornley detector and give information on the morphology. BSE are quasi-elastically scattered by the specimen and thus show energies close to the incident beam. They are detected with semiconductor devices and strongly depend on the atomic number. Thus, BSE can be used to determine element distribution within the sample. Generated X-rays provide information on the chemical composition as discussed in Chapter 2.3.1.

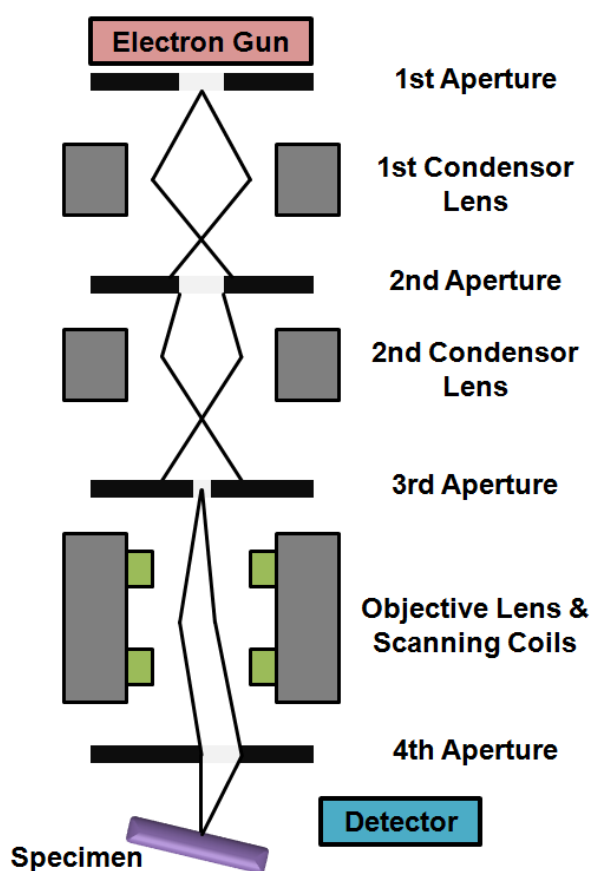


**Figure 2.3.4:** Schematic setup of a SEM. From the electron gun the beam is focused through a condenser and objective lens system. Scanning coils are used to move the beam across the sample and at each point various signals are recorded by special detectors.

In this thesis, SEM was used to investigate morphology and platelet-size of layered bulk-materials, cation-proton exchanged materials and restacked nanosheets. SEM measurements were performed on a JSM-6500F electron microscope (Co. JEOL Ltd., Tokyo) or a Vega TS 5130 MM (Tescan, Brno). All samples were sputter coated with carbon before investigation. Measurements were performed by Claudia Kamella (Chapter 3.1) and Christian Minke (Chapter 3.1-5.2).

### 2.3.4 Transmission Electron Microscopy

TEM can provide image resolution down to the sub-angstrom regime and additional analytical measurements can be performed making an impressive amount of information accessible. Besides TEMs exceptional image resolution, it is possible to characterize crystallographic phases and their orientation with diffraction experiments, generate elemental maps by using EDX or electron energy loss spectroscopy, and to acquire images highlighting elemental contrast.<sup>12</sup> Ultrathin samples along with a certain electron beam stability of the samples are a prerequisite for TEM investigations that are besides costs usually the bottleneck of the method. Samples investigated in this thesis were prepared in three different ways: As standard grid samples for bulk materials and nanosheets were used, while a lift-out technique or conventional cross-section sample preparation methods was applied for LBL deposited material.

In the first case, the solid sample is suspended in a solvent, ultrasonicated to reduce its size to electron transparency and the resulting suspension dropped onto a TEM grid (Cu, Au, etc.) that is covered by an amorphous lacey-carbon film. In the case of 2D nanosheets only dilution of the suspension is necessary.

The lift-out technique is performed in a focused ion beam (FIB) microscope.<sup>19</sup> At high beam currents a focused beam of ions, e.g. Ga, can be used for site specific sputtering or milling to prepare a TEM lamella. The region of interest is coated with a protective layer, e.g. Pt, before two trenches are milled next to this region. The central membrane between the two trenches is thinned and release cuts are introduced below the formed lamella. The lamella is then fixed on one side to a probe, cut off from the remaining connections, transferred to a carrier holder and thinned to electron transparency using a low current Ga beam.

Cross-sectional TEM samples were prepared as illustrated in Figure 2.3.5.<sup>20</sup> In the first step, two substrates are glued together with a two-component glue with the coated surfaces facing each other. The achieved “sandwich” structure is then cut down with a diamond wire saw so that it fits into a brass tube with a diameter of ~2 mm, where it is immobilized with a two-component glue. From this brass tube discs of ~200  $\mu\text{m}$  are cut off with the diamond wire saw, that are further thinned down to ~50  $\mu\text{m}$  by grinding. The thickness in the center of the disc is then reduced to 15  $\mu\text{m}$  with a dimpling wheel in combination with a diamond paste. In the final step, a precision ion polisher operated with two Ar ion beams removes wedge shape like remaining material until a hole forms in the middle of the sample. Right next to this hole, the sample is thin enough for TEM investigations, typically below 100 nm.



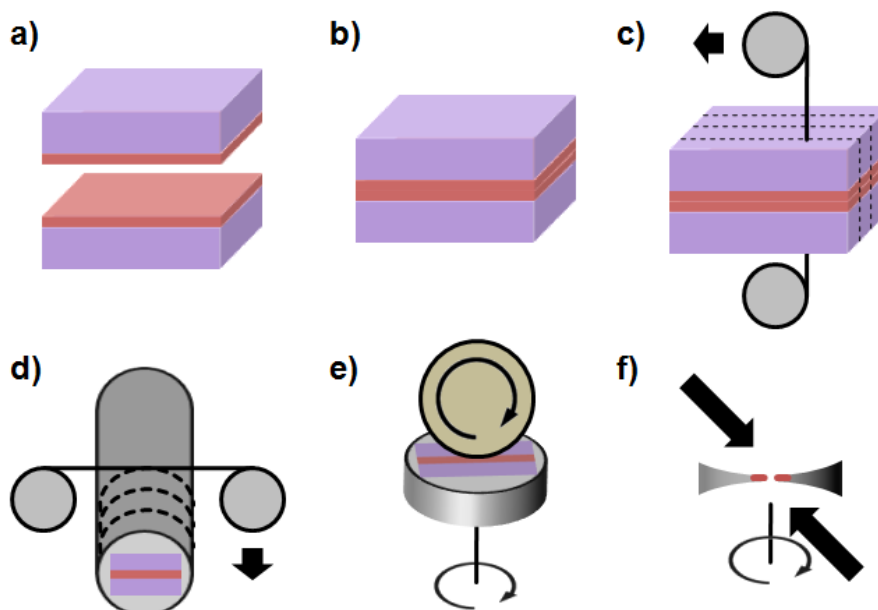


**Figure 2.3.5:** Illustration of different steps in TEM cross-sectional preparation: a)+b) gluing of two coated wafers into a “sandwich” structure; c) cutting of the “sandwich” into pieces that fit into d) a brass tube, where they are embedded in glue and further cut into discs that are grinded down to  $\sim 50\text{ }\mu\text{m}$ ; e) the inner part is further thinned with a dimple grinder and e) finalized with help of an ion polishing system.

In the TEM, high energetic electrons are transmitted through the specimen and the various interactions are used to form an image or diffraction pattern and to gain analytical information. The instrument itself can be divided into three components: the illumination system, the objective lens/stage, and the imaging system.<sup>12</sup> The role of the illumination system is to extract electrons from the gun and to transfer them through condensor lenses to the specimen. Depending on the mode the illumination can be either with a parallel beam or a convergent beam. While the former is used in conventional TEM imaging and selected area electron diffraction (SAED), the second is performed in scanning TEM (STEM) imaging and analytical experiments. In the center of the TEM the objective lens and the specimen stage are located and here the beam-specimen interactions take place. In the last part of the TEM, the imaging system magnifies and focuses the produced image or diffraction pattern on the viewing screen or detector, respectively.

Figure 2.3.6 describes basically the two operation modes of the conventional TEM: the diffraction mode and the imaging mode.<sup>12</sup> As one can see, the diffraction pattern and the image are simultaneously present. The objective lens forms a diffraction pattern in the back focal plane (BFP) with electrons scattered by the sample and combines them to a first image.<sup>21</sup> Controlled by the strength of the intermediate lens either the diffraction pattern or the image is produced on the viewing screen.

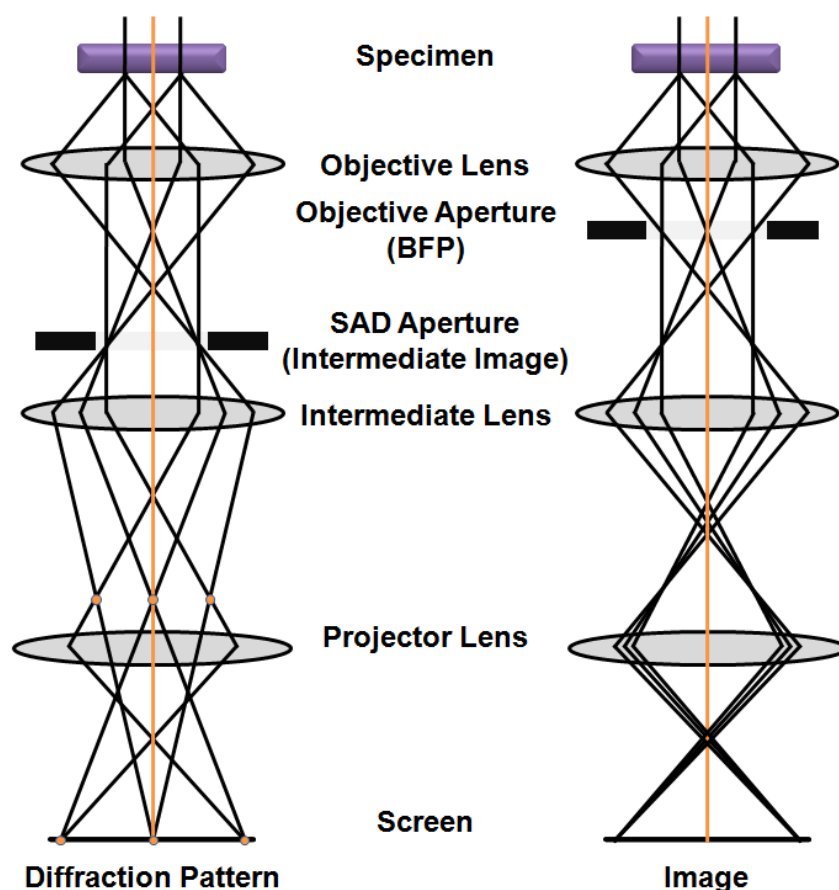


**Figure 2.3.6:** Schematic drawing of the two basic modes of conventional TEM and corresponding beam pathways: diffraction mode (left) and imaging mode (right).

For the diffraction mode the diffraction pattern can be confined to a selected area of the specimen by insertion of a SAD aperture into the image plane. In the imaging mode, positioning of an objective aperture at a specific location in the BFP can be used to select electrons that have been diffracted by a specific angle.<sup>12</sup> When the aperture is positioned to pass only the direct electron beam, a bright-field (BF) image is formed. As the contrast in conventional TEM is mainly due to diffraction contrast and mass-thickness contrast, strongly scattering regions of the specimen (heavy elements, large thickness) show a lower intensity in the BF images than weakly scattering regions (light elements, small thickness). When the aperture is positioned to pass only diffracted electrons at a certain angle, a dark-field (DF) image is formed, which can give useful information, e.g. about planar defects, stacking faults or particle size. Hence, combination of both imaging modes can be used to obtain complementary information on the sample. SAED diffraction experiments are applied to determine the lattice plane distances and the crystal structure.

The switchover from conventional TEM with a parallel beam to STEM with a convergent electron beam can be performed by a change in the illumination system.<sup>12</sup> The quality of STEM images is not affected by aberrations of the imaging lenses, but rather depends

on the size of the formed probe and hence is related directly to the quality in the illumination system. For each scanned position the scattered signal is measured and an image is formed point by point. Three different detectors are placed in dependence on the scattering angle  $\theta$  of the transmitted electrons with respect to the optical axis, so that complementary information of the specimen can be obtained (Figure 2.3.7): A BF detector with  $\theta < 10\text{-}25\text{ mrad}$ , an annular dark-field (ADF) detector with  $25 < \alpha < 50\text{ mrad}$  and a high angle annular dark-field (HAADF) detector with  $\beta > 75\text{ mrad}$ . In STEM it is possible to achieve spatial resolutions of  $< 0.1\text{ nm}$ . In addition analytical signals, like EDX and EELS, can be acquired with a high spatial resolution.

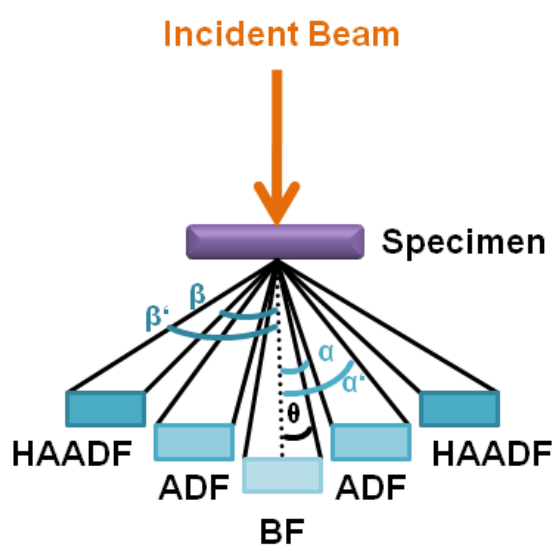


**Figure 2.3.7:** Schematic drawing of the various electron detectors in a STEM: BF- ( $\theta < 10\text{-}25\text{ mrad}$ ), ADF- ( $25 < \alpha < 50\text{ mrad}$ ) and HAADF ( $\beta > 75\text{ mrad}$ ) detector.

In this thesis, TEM in combination with related spectroscopies was the main analytical tool for various purposes. First of all, TEM in addition to XRD and Raman spectroscopy was used for structure determination of various “new” layered bulk materials. Second, TEM was critical for the evaluation of exfoliation products and further the extraction of 2D specific properties. Third, TEM allowed for in-depth characterization of heterostructures consisting of 2D nanosheets building blocks. Thus, several instruments were used in dependence of the purpose. An overview of all instruments is given in Table 2.3.1.

**Table 2.3.1:** Different TEMs used in this work, their specifications and their purposes.

<b>Microscope</b>	<b>Specifications</b>	<b>Purpose</b>
JEOL 2011 (JEOL Ltd., Tokyo)	LaB <sub>6</sub> cathode, 200 keV	Pre-Investigations
Philips CM30 ST (Royal Philips Electronics, Amsterdam)	LaB <sub>6</sub> cathode, 300 keV	Basic nanosheet and LBL characterization, SAED of bulk materials
FEI Titan 80-300 (S)TEM (FEI, Hillsboro)	Field emission gun, 80-300 keV EDAX Sapphire Si(Li) detector (EDAX, Mahwah) Model 3000 HAADF detector (Fischione Instruments, Export)	(HR)TEM, EDX and EELS of nanosheets and hybrid structures
FEI Titan 80-300 Cubed (STEM) (FEI, Hillsboro)	High brightness X-FEG, 80-300 keV Two C <sub>s</sub> correctors Gatan GIF (model 866) spectrometer	STEM, EDX and EELS of nanosheets and hybrid structures
FEI Titan 80-300 (S)TEM (FEI, Hillsboro)	Field emission gun, 80-300 keV C <sub>s</sub> corrector (imaging lens) Gatan UltraScan 1000 (2k × 2k) slow scan CCD	HRTEM of bulk materials
FEI Titan 80-300 (S)TEM (FEI, Hillsboro)	Field emission gun, 80-300 keV C <sub>s</sub> corrector (probe lens) Gatan UltraScan 1000 (2k × 2k) slow scan CCD Wien-type monochromator	STEM, EELS and EDX of bulk materials
FEI Titan 80-300 (S)TEM (FEI, Hillsboro)	Field emission gun, 80-300 keV 2k x 2k CCD Gatan Tridiem 866 energy filter Wien-type monochromator	STEM and VEELS on bulk materials and nanosheets

TEM measurements were performed by Viola Duppel (Chapter 3.1-4.3); Teresa Dennenwaldt, Marc Heggen, Juri Barthel, Anna Frank and Christina Scheu (Chapter 3.1); Matthieu Bugnet (Chapter 3.2/4.1); Kulpreet Viridi and Yaron Kauffmann (Chapter 5.1-5.2). Additional cross-section preparation were performed by Tanja Holzmann as well as Arne Schwarze (Chapter 4.1) and Katarina Markovic (Chapter 4.2-4.3). FIB samples were prepared by Bernhard Fenk (Chapter 4.3).

## 2.4 X-Ray Photoelectron Spectroscopy

X-ray photoelectron spectroscopy (XPS) allows for the detection of all elements except hydrogen and helium and their bonding states, with an information depth in the nanometer region. The basic components of a typical XPS instrument are an ultrahigh vacuum (UHV) based stainless steel chamber containing the sample stage, an electron energy analyzer and detection system, an X-ray source and an ion gun for sample cleaning and for depth profiling.<sup>22</sup> The chamber is connected to consoles with the electronics supply systems and the computer with the data acquisition and processing software on the outside. In XPS, the surface of a sample is irradiated with photons of characteristic energy, e.g. Mg  $K_{\alpha}$  radiation, which directly interact with core electrons of the sample atoms. Ionized states are created in the sample and photoelectrons (SE) are emitted with kinetic energies given approximately by the difference between the photon energy and the binding energy of the specific element.<sup>22</sup> This enables a fairly easy qualitative analysis of the samples, for example, by comparison with tabulated electron level energies and handbook spectra as each element will give rise to a characteristic set of peaks, but also quantitative analysis is possible. The exact binding energy of an electron depends on the level from which photoemission is occurring, the formal oxidation state of the atom and the local chemical and physical environment.

In this thesis, XPS was used to distinguish between  $Pb^{II}$  and  $Pb^{IV}$  species and to ensure that no reduction of  $Nb^V$  in the solid solution  $RbCa_{2-x}Pb_xNb_3O_{10}$  took place. Measurements were performed by Mitsuharu Konuma (Chapter 3.1).

## 2.5 Atomic Force Microscopy

Atomic force microscopy (AFM) is a method that measures forces between a tip and a sample and can be used to provide true 3D surface profiles. Additional information like optical or magnetic properties can be obtained by modification of the basic AFM setup. The key components of an AFM are shown in Figure 2.5.1.<sup>23</sup> A microcantilever scans across the sample in x, y direction, while the deflection is recorded by reflecting a laser on the back of the cantilever into a position sensitive photodiode. A feedback loop is used to keep the force, distance, amplitude etc. in z-direction constant with help of a piezoelectric transducer whilst the change in signal is recorded by the computer.

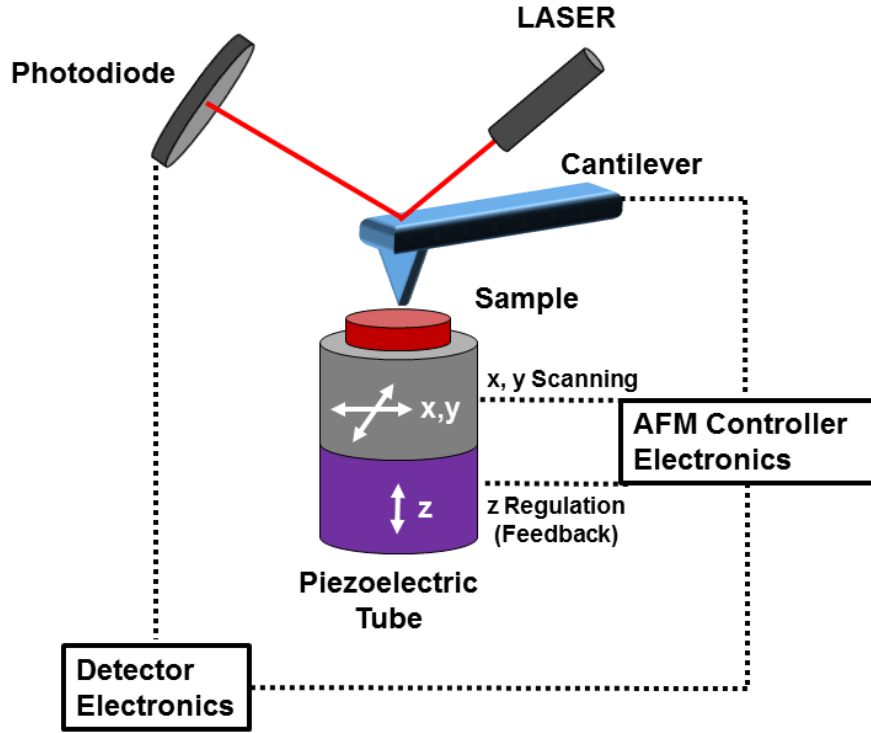


**Figure 2.5.1:** Schematic drawing of an AFM setup. A cantilever is scanned in  $x, y$  direction across the sample or vice versa, and the deflection of a laser beam at the back of the cantilever detected with a photodiode. Depending on the measurement the  $z$  height can be adjusted through a feedback loop.

The Lennard-Jones potential is a frequently used model potential to describe tip-sample interactions qualitatively. This potential describes the interaction between two neutral atoms and consists of a term describing the attractive part like the van der Waals interactions and a part describing the repulsive part like Pauli interactions (Equation 2.5.1):<sup>24-25</sup>

$$U_{LJ}(r) = 4U_0 \left[ \left( \frac{R_a}{r} \right)^{12} - \left( \frac{R_a}{r} \right)^6 \right] \quad (\text{Eq. 2.5.1})$$

where  $U_0$  is the depth of the potential well,  $r$  is the distance between the atoms, and  $R_a$  is the distance at which  $U_{LJ}(r)$  is zero. Hence, the attractive part is proportional to  $-1/r^6$  and the repulsive part to  $1/r^{12}$ . In the experiment the tip can be considered to have zero deflection when it is far from the sample surface. Attractive forces arise when the tip approaches the surface and when the tip is close enough a “snap-in” occurs, meaning the tip jumps into contact with the surface. Approaching the surface even further leads into the “repulsive” regime, i.e. the tip applies force to the sample and vice versa. Once the direction movement is reversed, the attractive forces become more dominant until

the point is reached when the cantilever snaps off. An AFM can be operated in three different imaging modes, each operating in different regimes: contact-mode, intermittent-contact-mode and noncontact-mode.<sup>23, 25-26</sup>

In the contact-mode the tip of the cantilever has a gentle contact with the sample surface and thus, operates in the repulsive regime. A very weak repulsion between atoms produces the probe offset and the feedback is used to control a fixed value, usually constant height or constant force mode. Whilst keeping the height constant different forces affect the cantilever and hence its bending, which renders the topographic images of the sample surface. In the constant force mode, the sample probe is lifted by the z-piezo so that no bending of the cantilever occurs and the topographic image is obtained by conversion of the z-piezo signal. Contact-mode is the fastest mode and has a better resolution than the other modes, but access force might damage the sample in cases for soft matter or the tip of the cantilever in cases of hard matter, respectively.

In the noncontact-mode detection is executed by using the long-range attraction (van der Waals forces) between the atoms. Modulation techniques like oscillation of the cantilever at its resonance frequency are required to increase the signal to noise ratio. The change of the oscillating frequency as well as the amplitude change is recorded during the scan and converted to produce a topographic image. One major drawback is the effect of a water film on the surface that drastically reduces the resolution. Thus, vacuum conditions are needed for the non-contact mode.

In tapping-mode, the probe repeatedly taps on the surface in a dynamic operating mode around the “zero-force” regime. The cantilever is oscillated near its resonance frequency and scanned across the sample with a micro-contact between the tip and the sample. The topographic image is generated by imaging the variation of the oscillating frequency due to the forces affecting the cantilever. Similar to the noncontact-mode a water film decreases the resolution.

In this thesis, AFM’s main purpose was to investigate nanosheet morphology as well as sheet height and indirectly the amount of ligand surrounding the nanosheets. Furthermore, nanosheet surface coverage in dependence of various parameters as well as the surfaces and heights of multilayer arrangements were analysed. AFM investigations were performed on a MFP-3D Stand alone AFM (Asylum Research, Santa Barbara). Additional measurements were performed by Arne Schwarze (Chapter 3.2) and Stephan Werner (Chapter 4.1).

## 2.6 Infrared Spectroscopy

Infrared (IR) spectroscopy is one of the most widely used and most important analytical methods in science in general. It allows to determine the structure or structural features of organic compounds and can also be useful to investigate characteristic vibrations in inorganic materials. The basic components of an IR spectrometer are the IR source, a beam splitter, a monochromator, a transducer, an analog to digital converter and a digital machine to quantify the readout.<sup>27</sup> IR spectroscopy is based on the interaction of electromagnetic radiation with the sample, in most cases in the form of absorption of energy from the incident beam. The absorption of IR light induces transitions between the vibrational energy levels. The first necessary condition for the sample to absorb IR light is that the sample must have a vibration during which the change in dipole moment with respect to distance is non-zero:<sup>28</sup>

$$\frac{\partial \mu}{\partial x} \neq 0 \quad (\text{Eq. 2.6.1})$$

with  $\partial \mu$  being the change in the dipole moment and  $\partial x$  being the change in bond distance. The second necessary condition for IR absorbance is that the energy of the light impinging the sample must be equal to a vibrational energy level difference within this sample.

In this thesis, IR spectroscopy was used to investigate the layered bulk material and its changes after cation-proton exchange as well as exfoliation. Special emphasis was laid to gain information on the ligands surrounding individual nanosheets. Characteristic vibrations for the main investigated compounds are listed in Table 2.6.1.<sup>29-31</sup> A Spectrum BX II FT-IR with ATR unit and Spectrum Two IR Spectrometer with ATR unit (both PerkinElmer, Waltham) were used. Additional IR measurements were performed bei Marie-Luise Schreiber (Chapter 3.1/4.1) and Stephan Werner (Chapter 4.1).

**Table 2.6.1:** Important IR bands for  $\text{KCa}_2\text{Nb}_3\text{O}_{10}$  and  $\text{TBA}_{1-y}\text{H}_y\text{Ca}_2\text{Nb}_3\text{O}_{10}$

$\sigma$ (cm <sup>-1</sup> )	Mode
~587	asym. Nb-O bridge
~771	sym. Nb-O bridge
~924	Nb-O term.
1370-1500	-C-H bend
1638	H-O-H bend
2800-3000	-C-H stretch
~3300	-O-H stretch



## 2.7 Raman Spectroscopy

Raman spectroscopy is very sensitive to the crystal structure and bond order of metal oxides and therefore is an effective method to obtain profound knowledge about structural features of layered perovskites, especially those regarding the interlayer gallery. The main components of a Raman system are a light source, optical components, such as lenses and mirrors, to focus the light onto a sample and collect the scattered light, a spectrometer and a detector.<sup>32</sup> In Raman spectroscopy UV, VIS or NIR laser emitting monochromatic light are used as radiation source that exhibit higher energy than the IR source, so that absorption of photons is impossible. Instead the incident light will excite the system to a high-energy state leading to scattering reactions when the system returns to the ground state. The simplest way of explaining the classical or spontaneous Raman effect is *via* an energy level diagram between a ground state  $n = 0$  and an excited state  $n = 1$  separated by the energy  $h\nu_M$ , where  $\nu_M$  is the frequency of the molecular vibration (Figure 2.7.1).<sup>28</sup> The incident light leads to a transition with energy  $h\nu_L$  to a virtual level, from which the system can return to the initial state in three different ways, by emission of light with frequencies  $\nu_L$ ,  $\nu_L - \nu_M$  and  $\nu_L + \nu_M$ . The transition that starts and finishes at the same vibrational energy level arises from elastic Rayleigh scattering. Stokes and anti-Stokes Raman scattering depict the shifts to lower and higher frequencies, respectively. At ambient conditions, most molecular vibrations are in the ground state and thus the Stokes Raman scattering is more intense and the one that is routinely studied.

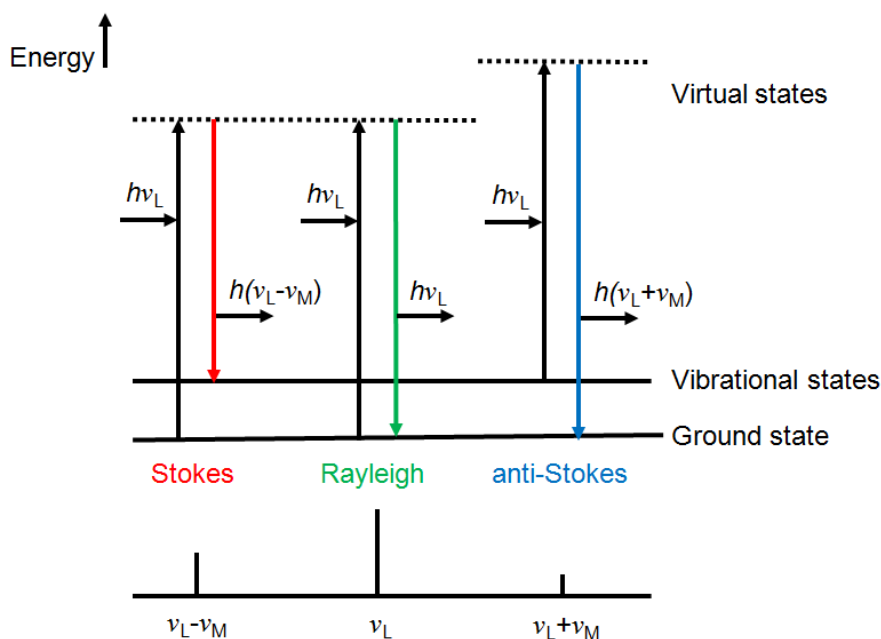


**Figure 2.7.1:** The energy level diagram showing the basic transitions involved in the spontaneous Raman scattering: Stokes, Rayleigh and anti-Stokes.

In contrast to IR spectroscopy a change of the polarization potential  $\alpha$  is necessary for a sample to exhibit a Raman effect.<sup>28</sup>

$$\frac{\partial \alpha}{\partial x} \neq 0 \quad (\text{Eq. 2.7.1})$$

with  $\partial \alpha$  being the change in the dipole moment and  $\partial x$  being the change in bond distance. Hence, Raman spectroscopy is a complementary technique to IR spectroscopy. In cases where a chemical compound exhibits a center of symmetry, certain normal vibrations will be only Raman active and certain normal vibrations will be only IR active. In cases where the normal modes are allowed in both techniques, bands that are strong in the Raman are usually weak in the IR, and vice versa.

In this thesis, Raman spectroscopy was primarily used to investigate structural changes in solid-solutions of layered TMOs. The Raman spectra were taken with a Typ V 010 labram single grating spectrometer (HORIBA Jobin Yvon GmbH, Bensheim), equipped with a double super razor edge filter and a peltier cooled CCD camera. Measurements were performed by Armin Schulz (Chapter 3.1).

## 2.8 UV-Vis Spectroscopy

Ultraviolet-visible light (UV-Vis) spectroscopy can provide information about electronic transitions occurring in the material by measurement of the light absorption as a function of wavelength. In the absorption measurement, the light intensity after traversal  $I(z)$  is related to the incident intensity  $I_0$ , the thickness  $z$  and the absorption coefficient  $\alpha_{abs}(\omega)$  according to the Beer-Lambert law (Equation 2.8.1):<sup>33</sup>

$$I(z) = I_0 e^{-\alpha_{abs}(\omega)z} \quad (\text{Eq. 2.8.1})$$

The absorption coefficient  $\alpha$ , is a materials property which defines the amount of light absorbed by it. The inverse of the absorption coefficient,  $\alpha^{-1}$ , can be imagined as the average distance traveled by a photon before it gets absorbed. On basis of such measurements, a detailed band gap analysis can be provided by plotting and fitting the absorption data. Equation 2.8.2 shows a relation presented by Tauc as well as Davis and Mott, that usually accounts for values of  $\alpha > 10^4 \text{ cm}^{-1}$ :<sup>34-35</sup>

$$(\alpha h\nu)^{1/n} = A(h\nu - E_g) \quad (\text{Eq. 2.8.2})$$

with  $h$  = Planck's constant,  $\nu$  = frequency of light,  $E_g$  = band gap and  $A$  = proportional constant.  $n$  can take values of 1/2 for a direct allowed transition, 3/2 for a direct forbidden transition, 2 for an indirect allowed transition and 3 for an indirect forbidden transition.

For solid samples like powders determination of an absorption coefficient in an absorption UV-Vis experiment can be inaccurate as the light will experience multiple passes through the sample due to reflection from the walls of the surrounding integrating sphere.<sup>36</sup> Thus, samples are usually measured in a diffuse reflectance configuration as shown in Figure 2.8.1. The various components that incident light can split into after interaction with the sample are visualized in this figure and their relation is depicted in Equation 2.8.3:<sup>37</sup>

$$I_0 = A\% + T + R_s + R_d + S \quad (\text{Eq. 2.8.3})$$

with  $A\%$  = absorbance,  $T$  = transmittance,  $R_s$  = specular reflectance,  $R_d$  = diffuse reflectance and  $S$  = forward scattering.

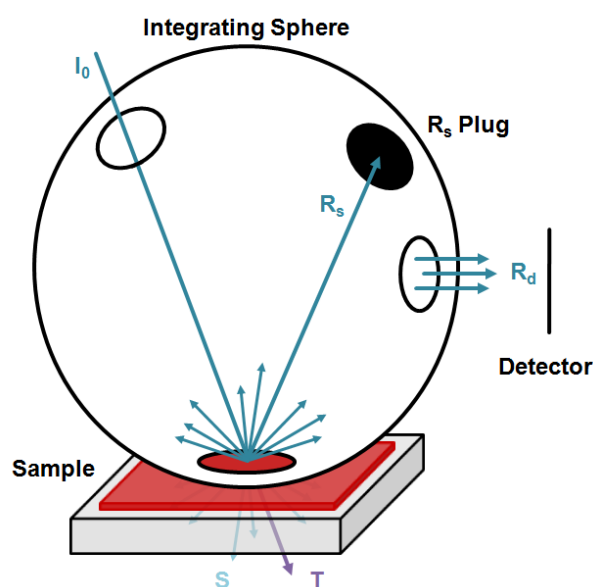


**Figure 2.8.1:** Schematic drawing of a UV-Vis diffuse reflectance configuration using an integrating sphere with a specular reflectance plug.

A typical integrating sphere has an input port connected to the light source, an output port connected to a signal meter that collects the diffusely reflected light, and an aperture against which the working or reference samples can be placed for measurement.<sup>36</sup> The inside of an integrating sphere is covered with a highly reflective material like  $\text{Ba}_2\text{SO}_4$ , which is effective over a large wavelength region of interest, and also serves as a nearly ideal Lambertian scatterer by distributing the light uniformly throughout the entire surface of the integrating sphere.<sup>36</sup> Note that specularly reflected light has not undergone an absorption process, and contains almost no information regarding electronic states within the material and thus

increases noise and decreases the accuracy of the measurement, respectively.<sup>37</sup> Thus, its contributions are usually minimized with help of a specular reflectance plug.<sup>36</sup> With this diffuse reflectance setup  $I = R_d$  can be measured and the Kubelka–Munk radiative transfer model quoted in Equation 2.8.4 be employed to extract the band gap:<sup>38</sup>

$$F(R) = \frac{(1 - R)^2}{2R} = \frac{\alpha}{s} \quad (\text{Eq. 2.8.4})$$

where  $F(R)$  is the Kubelka–Munk function,  $\alpha$  the absorption coefficient and  $s$  the scattering coefficient. If the scattering coefficient is assumed to be wavelength independent, then  $F(R)$  is proportional to  $\alpha$  and the Tauc plots can be made using  $F(R)$  in place of  $\alpha$ . For completeness it is emphasized at this point, that the optical band gap is not necessarily equal to the electronic band gap, which is defined as the energy difference between the valence band maximum and the conduction band minimum.<sup>36</sup>

In this thesis, diffuse UV-Vis spectroscopy was used to determine band gap of layered bulk materials, their cation-proton exchanged and isolated exfoliated nanosheets. Optical diffuse reflectance spectra of the bulk material and the nanosheet pellet were collected at room temperature with a Cary 5000 UV-Vis-NIR diffuse reflectance spectrometer (Agilent Technologies, Santa Clara) at a photometric range of 200-800 nm. Powders were prepared in a sample carrier with a quartz glass window at the edge of the integrating sphere with BaSO<sub>4</sub> as the optical standard. Kubelka–Munk spectra were calculated from the reflectance data. Measurements were performed by Brian Tuffy and Katharina Schwinghammer (Chapter 3.1/5.2).

## 2.9 Bibliography

- [1] C. Suryanarayana, M. G. Norton, *X-ray diffraction: a practical approach.*, Plenum Publishing Corporation, **1998**.
- [2] W. H. Bragg, W. L. Bragg, *Proc. R. Soc. London, Ser. A* **1913**, 88, 428-438.
- [3] D. Yang, R. F. Frindt, *J. Mater. Res.* **1996**, 11, 1733-1738.
- [4] R. A. Gordon, D. Yang, E. D. Crozier, D. T. Jiang, R. F. Frindt, *Phys. Rev. B* **2002**, 65, 125407.
- [5] W. SEARCH, *Vers. 2.08*, **2005**.
- [6] WINXPOW, *Vers. 2.12*, **2005**.
- [7] S. Kabekkodu, *International Centre for Diffraction Data (Database)*, Newtown Square, PA, USA, **2010**.
- [8] P. Villars, K. Cenzual, *Pearson's Crystal Data - Crystal Structure Database for Inorganic Compounds*, ASM International, Materials Park, Ohio, USA, **2009/2010**.

- [9] M. Hellenbrandt, *Crystallogr. Rev.* **2004**, 10, 17-22.
- [10] C. B. Boss, K. J. Fredeen, *Concepts, instrumentation and techniques in inductively coupled plasma optical emission spectrometry.*
- [11] M. Thompson, *AMC Technical Briefs* **2008**, 29, 1-2.
- [12] D. B. Williams, C. B. Carter, *Transmission Electron Microscopy: A Textbook for Materials Science*, Springer, **2009**.
- [13] F. Krumeich, *Properties of electrons, their interactions with matter and applications in electron microscopy*, **2011**.
- [14] G. Cliff, G. W. Lorimer, *J. Microsc.* **1975**, 103, 203-207.
- [15] H. A. Kramers, *Philosophical Magazine Series 6* **1923**, 46, 836-871.
- [16] R. Brydson, *Electron Energy Loss Spectroscopy*, BIOS Scientific Publishers, **2001**.
- [17] R. Egerton, *Electron Energy-Loss Spectroscopy in the Electron Microscope*, Springer US, **2012**.
- [18] D. Brandon, W. D. Kaplan, *Microstructural Characterization of Materials*, Wiley, **2013**.
- [19] J. Mayer, L. A. Giannuzzi, T. Kamino, J. Michael, *MRS Bullet.* **2007**, 32, 400-407.
- [20] A. Strecker, U. Salzberger, J. Mayer, *Prakt. Metall.* **1993**, 30, 482.
- [21] B. Fultz, J. M. Howe, *Transmission Electron Microscopy and Diffractometry of Materials*, Springer Berlin Heidelberg, **2012**.
- [22] S. Hofmann, *Auger- and X-Ray Photoelectron Spectroscopy in Materials Science: A User-Oriented Guide*, Springer Berlin Heidelberg, **2012**.
- [23] P. Eaton, P. West, *Atomic Force Microscopy*, OUP Oxford, **2010**.
- [24] J. E. Jones, *Proc. R. Soc. London, Ser. A* **1924**, 106, 463-477.
- [25] B. Voigtlaender, *Scanning Probe Microscopy: Atomic Force Microscopy and Scanning Tunneling Microscopy*, Springer Berlin Heidelberg, **2015**.
- [26] D. Shi, *Nanomaterials and Devices*, Elsevier Science, **2014**.
- [27] D. A. Skoog, F. J. Holler, S. R. Crouch, *Principles of Instrumental Analysis*, Thomson Brooks/Cole, **2007**.
- [28] S. Wartewig, *Basic Principles of Vibrational Spectroscopy*, Wiley-VCH Verlag GmbH & Co. KGaA, **2005**.
- [29] T. Sasaki, S. Nakano, S. Yamauchi, M. Watanabe, *Chem. Mater.* **1997**, 9, 602-608.
- [30] Y. Chen, X. Zhao, H. Ma, S. Ma, G. Huang, Y. Makita, X. Bai, X. Yang, *J. Solid State Chem.* **2008**, 181, 1684-1694.
- [31] S. Shori, P. J. Pellechia, H.-C. zur Loye, H. J. Ploehn, *J. Colloid Interface Sci.* **2015**, 437, 97-110.
- [32] J. R. Ferraro, K. Nakamoto, *Introductory Raman Spectroscopy*, Elsevier Science, **2012**.
- [33] M. Dresselhaus, *Solid State Physics Part II-Optical Properties of Solids*, **2001**.

- [34] E. A. Davis, N. F. Mott, *Philos. Mag.* **1970**, 22, 0903-0922.
- [35] D. L. Wood, J. Tauc, *Phys. Rev. B* **1972**, 5, 3144-3151.
- [36] Z. Chen, T. Deutsch, H. Dinh, K. Domen, K. Emery, A. Forman, N. Gaillard, R. Garland, C. Heske, T. Jaramillo, A. Kleiman-Shwarscstein, E. Miller, K. Takanabe, J. Turner, in *Photoelectrochemical Water Splitting*, Springer New York, **2013**, pp. 49-62.
- [37] J. M. Palmer, *Handbook of Optics* **1995**, 2, 25.11.
- [38] P. Kubelka, *J. Opt. Soc. Am.* **1948**, 38, 448-448.

## 3 Two-dimensional Transition Metal Oxide Nanosheets

### 3.1 Functional Engineering of Perovskite Nanosheets by Lead Substitution

Christian Ziegler, Daniel Weber, Teresa Dennenwaldt, Viola Duppel, Claudia Kamella, Filip Podjaski, Brian Tuffy, Igor Moudrakovski, Christina Scheu, Bettina V. Lotsch

*Manuscript to be submitted.*

**ABSTRACT:** Tuning the chemical composition and structure for targeted functionality in two-dimensional (2D) nanosheets has become a major objective in the rapidly growing area of 2D materials. In the context of photocatalysis, both miniaturization and extending the light absorption of UV active photocatalysts are major assets. Here, we bridge the gap between two photocatalytic systems known from literature to evolve  $H_2$  from water/methanol under UV –  $RbCa_2Nb_3O_{10}$  ( $E_g = 3.5$  eV) – and visible light irradiation –  $RbPb_2Nb_3O_{10}$  ( $E_g = 2.4$  eV) – by synthesizing the new solid solution  $RbCa_{2-x}Pb_xNb_3O_{10}$ . While the calcium niobate can easily be exfoliated into individual nanosheets *via* cation-proton exchange and subsequent treatment with tetra-*n*-butylammonium hydroxide (TBAOH), the lead niobate barely yields nanosheets. Spectroscopic and microscopic analysis suggest that this is caused by volatilization of Pb during synthesis, leading to a local 3D linkage of  $RbPb_2Nb_3O_{10}$  perovskite units with hypothetical Pb deficient ' $RbNb_3O_8$ ' units. On the one hand, this linkage progressively prevents exfoliation along with an increasing Pb content. On the other hand, introducing Pb into the perovskite blocks successively leads to band gap narrowing, thus gradually enhancing the light harvesting capability of the solid solution. Compromising this narrowing of the band gap with the possibility of exfoliation, visible light sensitized nanosheets can be engineered in good yield for an initial molar ratio of Ca:Pb  $\geq 1:1$ .

#### 3.1.1 Introduction

Over the past years, the development of renewable energy sources and their efficient utilization has become a hallmark of materials research.<sup>1-4</sup> Photocatalysts are not only able to decompose organic and inorganic pollutants but also to convert solar energy into chemical fuels by water splitting or  $CO_2$  reduction. Today, the quest for efficient visible light photocatalysts for solar water splitting has become one of the most important topics in photocatalysis research.

Layered transition metal oxides with  $d^0$  electron configuration (e.g.  $Ti^{IV}$ ,  $Nb^V$ ,  $Ta^V$  etc.) are promising candidates for overall water splitting. Among them, Dion-Jacobson (DJ) phases with the general formula  $M[A_{n-1}B_nO_{3n+1}]$  ( $M = H, Li, Na, K, Rb$  etc.,  $A = Ca, Sr, Pb, La$  etc.,  $B = Ti, Nb, Ta$  etc.), featuring layered perovskite blocks interleaved with alkali cations, have

attracted broad attention due to their excellent photocatalytic performance. 2D blocks composed of  $n$  corner-sharing  $\text{BO}_6$  octahedra form negatively charged  $[\text{A}_{n-1}\text{B}_n\text{O}_{3n+1}]^-$  layers that are stacked along the  $c$ -axis which are interleaved with exchangeable monovalent cations to retain electroneutrality. It has been reported that  $\text{KCa}_2\text{Nb}_3\text{O}_{10}$  has a high photocatalytic activity due to its unique layered structure, which can promote the separation of photogenerated electrons and holes across the layers due to its reduced symmetry.<sup>5</sup> However, the large band gap of  $\text{KCa}_2\text{Nb}_3\text{O}_{10}$  ( $E_g = 3.1\text{-}3.3$  eV) renders this material only moderately suitable for solar water splitting.<sup>6-8</sup> On the contrary, the structurally related  $\text{RbPb}_2\text{Nb}_3\text{O}_{10}$  was reported to evolve  $\text{H}_2$  from an aqueous methanol solution under visible irradiation.<sup>9-10</sup> The substitution of lead into layered perovskites was later on found to be a generic method of visible light sensitization for UV active materials.<sup>11</sup> According to band structure calculations, the conduction and valence bands of these compounds mostly consist of empty  $\text{Nb}4d$  and occupied  $\text{O}2p$  orbitals, respectively, whereby the  $\text{O}2p$  orbitals are hybridized with  $\text{Pb}6s$  orbitals. This causes an upward shift of the position of the valence band leading to a narrower band gap compared to the lead-free structures.<sup>11</sup>

To further improve the catalytic properties of these materials, nanostructuring has become a tool of choice as it increases the exposed surface area and shortens the transfer of photogenerated charge carriers to the surface. In a common approach, layered transition metal oxides are therefore converted into their protonic forms (e.g.  $\text{HCa}_2\text{Nb}_3\text{O}_{10}$ ) and subsequently exfoliated by neutralization of the interlayer protons and cation exchange, for example by  $\text{TBAOH}$  (e.g.  $\text{TBA}_{1-y}\text{H}_y\text{Ca}_2\text{Nb}_3\text{O}_{10}$ ,  $0 \leq y \leq 1$ ).<sup>12</sup> Introducing such bulky organic cations leads to a swelling of the interlayer gallery that is accompanied by the insertion of a large volume of water into the interlayer space. Individual nanosheets can then be separated with the aid of shear forces. *Osterloh* and co-workers have shown that in the case of  $\text{KCa}_2\text{Nb}_3\text{O}_{10}$ , exfoliation can lead to a 16-fold increase in  $\text{H}_2$  evolution and an 8-fold increase in  $\text{O}_2$  evolution.<sup>13</sup> On the contrary, it was shown that  $\text{RbPb}_2\text{Nb}_3\text{O}_{10}$  cannot be exfoliated under these mild conditions and high power ultrasonic treatment is necessary to accomplish exfoliation.<sup>14-15</sup> Such harsh conditions usually lead to low-quality nanosheets which are smaller in size and often suffer from defects.<sup>12, 16-17</sup>

In the present work, we report the full solid solution series  $\text{RbCa}_{2-x}\text{Pb}_x\text{Nb}_3\text{O}_{10}$  ( $x = 0, 0.5, 1, 1.5, 2$ ) and thus bridge the gap between the formerly known end members  $\text{RbCa}_2\text{Nb}_3\text{O}_{10}$  and  $\text{RbPb}_2\text{Nb}_3\text{O}_{10}$ . While the band gap gradually decreases with increasing Pb content the ability to exfoliate the material into nanosheets diminishes in the same direction. We reveal by a comprehensive spectroscopic and microscopic analysis that this is caused by local changes in the structure of parent  $\text{RbCa}_{2-x}\text{Pb}_x\text{Nb}_3\text{O}_{10}$  at higher Pb levels due to volatilization of Pb during synthesis. Thus, nanosheets showing improved solar absorption can be synthesized in good yield for  $x \leq 1$ , while at  $x > 1$ , exfoliation becomes inefficient.



### 3.1.2 Results and Discussion

**Bulk structure.** A representative structural unit of  $\text{RbCa}_2\text{Nb}_3\text{O}_{10}$  is displayed in Figure 3.1.1 a. The x-ray diffraction (XRD) patterns of  $\text{RbCa}_{2-x}\text{Pb}_x\text{Nb}_3\text{O}_{10}$  ( $x = 0, 0.5, 1.0, 1.5, 2.0$ ) are shown in Figure 3.1.1 b.  $\text{RbCa}_2\text{Nb}_3\text{O}_{10}$  was indexed on a tetragonal unit cell, space group  $P4/mmm$  (no. 123), with lattice parameters  $a = b = 3.863223(54) \text{ \AA}$  and  $c = 14.91398(25) \text{ \AA}$ , which is in accordance with data reported earlier ( $P4/mmm$ , ( $a = b = 3.85865(6) \text{ \AA}$  and  $c = 14.9108(3) \text{ \AA}$ )<sup>18</sup> or ( $a = b = 3.8662(5) \text{ \AA}$  and  $c = 14.9424(6) \text{ \AA}$ )<sup>19</sup>). The reflections of the solid solution members are gradually shifted towards lower  $2\theta$  with increasing Pb content, suggesting a homogeneous distribution of Ca and Pb throughout the structure. The observed shifts are in line with a lattice expansion due to the larger ionic radius of lead ( $r(\text{Pb}^{2+}) = 1.49 \text{ \AA}$ ) compared to calcium ( $r(\text{Ca}^{2+}) = 1.34 \text{ \AA}$ ).<sup>20</sup> However, subtle differences become apparent upon close inspection of the XRD pattern of the most Pb-rich material  $\text{RbPb}_2\text{Nb}_3\text{O}_{10}$ .

While indexing and simulating  $\text{RbPb}_2\text{Nb}_3\text{O}_{10}$  ( $a = b = 3.94 \text{ \AA}$  and  $c = 15.20 \text{ \AA}$ ) according to the  $P4/mmm$  structure shows good agreement for most reflections, the enlarged XRD pattern in Figure 3.1.1 c reveals additional reflections that become more apparent with higher Pb content.<sup>21</sup> In addition, a decrease in intensity pertaining to the (100), (004), (101) and (102) planes is apparent. Even more drastic changes are observed towards higher angles. Besides the first three unidentified reflections (marked with an asterisk in Figure 3.1.1 c), similar features are found in previously reported XRD patterns, which were indexed using a tetragonal unit cell with an orthorhombic distortion.<sup>10, 22</sup> An extensive search did not result in a satisfactory match of these additional reflections with any known structure of any possible combination of the elements Rb, Pb, Nb and O.

Likewise, the XRD patterns of the cation-proton exchanged forms are shown in Figure S3.1.1 and further support structural differences as well as differences in crystallinity between the Ca and Pb end members  $(\text{Rb,H})\text{Ca}_{2-x}\text{Pb}_x\text{Nb}_3\text{O}_{10}$ .<sup>23</sup> As will be shown by solid-state nuclear magnetic resonance (ssNMR) spectroscopy later, these reflections are not due to a distinct side phase, but caused by local changes in the structure of the parent layered perovskite.

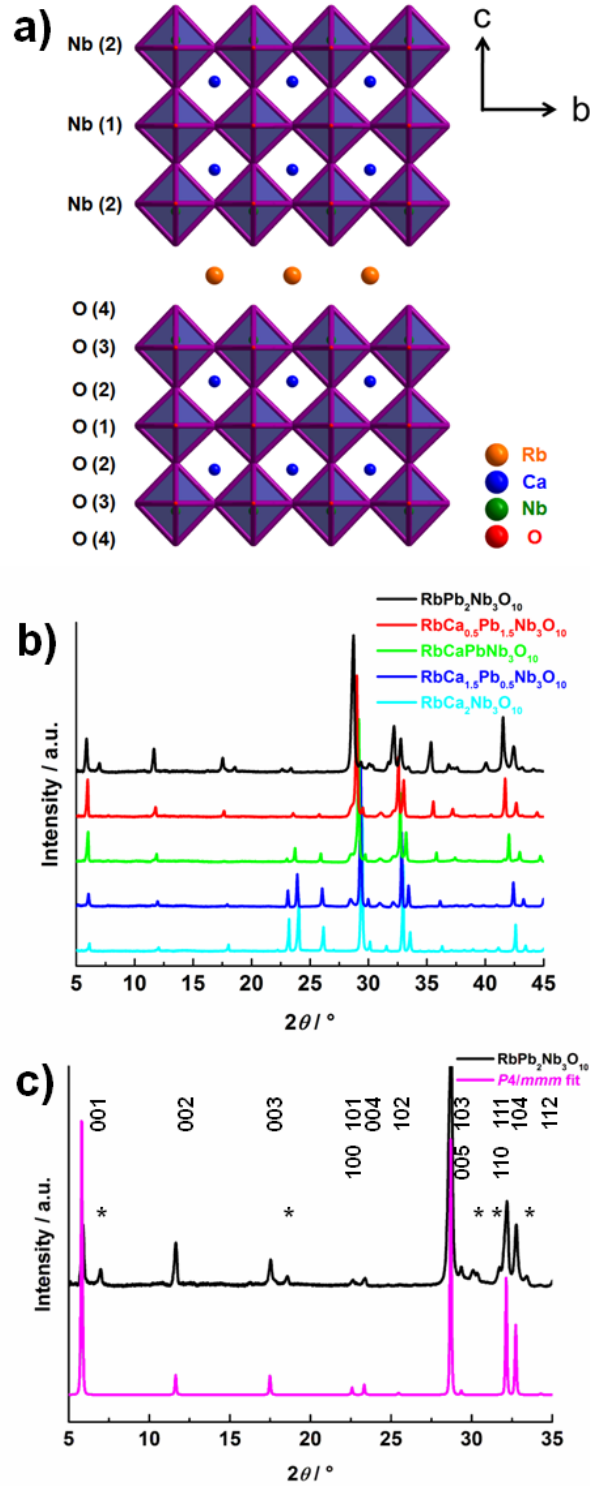


**Figure 3.1.1:** a) Representative structural unit of RbCa<sub>2</sub>Nb<sub>3</sub>O<sub>10</sub> (space group *P4/mmm*), viewing direction along *a* and the Nb and O positions labeled on the left side, b) XRD patterns of RbCa<sub>2-x</sub>Pb<sub>x</sub>Nb<sub>3</sub>O<sub>10</sub> (*x* = 0, 0.5, 1.0, 1.5, 2.0) and c) enlarged region from 5-35°2θ. RbPb<sub>2</sub>Nb<sub>3</sub>O<sub>10</sub> is tentatively indexed and fitted in *P4/mmm* (*a* = *b* = 3.94 Å and *c* = 15.20 Å) according to the literature.<sup>19</sup>,<sup>21</sup> Additional reflections are marked with an asterisk. Note that the intensity of the (100), (004), (101) and (102) reflections decreases with increasing lead content.

Inductively coupled plasma with atomic emission spectroscopy (ICP-AES) and energy dispersive X-ray spectroscopy (EDX) data were collected to quantify the emerging structural discrepancies upon introducing lead into the structure. As seen from ICP-AES data shown Table S3.1.1 the Rb and Ca content in  $\text{RbCa}_{2-x}\text{Pb}_x\text{Nb}_3\text{O}_{10}$ , the cation-exchanged form  $\text{HCa}_{2-x}\text{Pb}_x\text{Nb}_3\text{O}_{10}$  and the exfoliated nanosheets  $\text{TBA}_{1-y}\text{H}_y\text{Ca}_{2-x}\text{Pb}_x\text{Nb}_3\text{O}_{10}$  for  $x = 0, 0.5, 1.0, 1.5$  and  $2.0$  agrees well with the expected values and is the same - within the error margin - for the bulk and cation-proton exchanged material. Note that the values for nanosheets vary more significantly and will be discussed later. Notably, the Pb content never reaches the stoichiometric quantity, which is confirmed by EDX data (Table S3.1.2). The observed trend is visualized for the bulk material and the cation-proton exchanged form by plotting the observed vs theoretical stoichiometry of Pb and Ca, respectively, in Figure 3.1.2. The expected stoichiometry is visualized by a black line, whereas the experimental values are shown in red for the bulk phase and green for the cation-proton exchanged form. Whilst the Ca content stays within the tolerance limit and hence lies on the expected trendline, the Pb content decreases in average linearly with a factor of  $0.65x$  and lies below the trendline. Thus, the overall composition of the solid solution can be formulated as  $\text{RbCa}_{2-x}\text{Pb}_{0.65x}\text{Nb}_3\text{O}_{10-0.35x}$ , yielding e.g.  $\text{Rb}_3\text{Pb}_4\text{Nb}_9\text{O}_{28}$  for  $x = 2$ . For the sake of simplicity we will stick to the ideal stoichiometry  $\text{RbCa}_{2-x}\text{Pb}_x\text{Nb}_3\text{O}_{10}$  nomenclature in the following and refer to the actual composition if necessary.

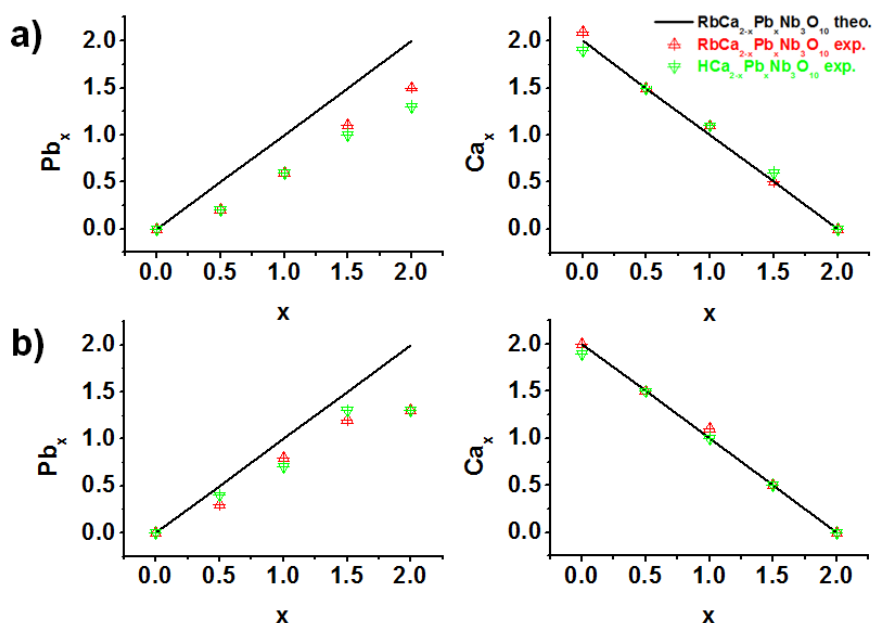


**Figure 3.1.2:** Theoretical expected Pb (left) and Ca (right) stoichiometry for  $\text{RbCa}_{2-x}\text{Pb}_x\text{Nb}_3\text{O}_{10}$  and  $\text{HCa}_{2-x}\text{Pb}_x\text{Nb}_3\text{O}_{10}$  plotted as black line against  $x = 0, 0.5, 1.0, 1.5, 2.0$  and the experimentally obtained values according to a) ICP-AES and b) EDX analysis shown as red triangle for the bulk and green triangle for the cation-proton exchanged material.

It is known that the high vapor pressure of lead oxide can be a limiting factor whilst heating at high temperatures.<sup>24</sup> Hence, PbO is most likely to volatilize to some extent under the synthesis conditions applied resulting in a substoichiometric Pb exchange for Ca, thus forcing the system to adopt a new structure.<sup>9</sup> The presence of Pb(IV) was excluded by means of X-ray photoelectron spectroscopy (XPS; Figure S3.1.2), which shows a Pb 4f<sub>7/2</sub> signal at 137.9 eV belonging to Pb(II).<sup>25</sup> This is expected since the synthesis of RbPb<sub>2</sub>Nb<sub>3</sub>O<sub>10</sub> was performed with PbO<sup>9-10</sup> or PbO<sub>2</sub><sup>14, 21</sup>, respectively, and PbO<sub>2</sub> decomposes to PbO + ½ O<sub>2</sub> above temperatures of 550 °C.<sup>26</sup> The Nb 3d<sub>5/2</sub> signal at 206.4 eV is uniform and close to the one obtained for calcium niobate Ca<sub>2</sub>Nb<sub>2</sub>O<sub>7</sub>.<sup>27</sup> Thus, the reduction of Nb(V) can be excluded. If we take the structural formation of tetragonal RbPb<sub>2</sub>Nb<sub>3</sub>O<sub>10</sub> as “host” for granted, the real obtained stoichiometry Rb<sub>3</sub>Pb<sub>4</sub>Nb<sub>9</sub>O<sub>28</sub> for  $x = 2$  can be rewritten as 2\*RbPb<sub>2</sub>Nb<sub>3</sub>O<sub>10</sub>•1\*\*RbNb<sub>3</sub>O<sub>8</sub>’, with ‘RbNb<sub>3</sub>O<sub>8</sub>’ being the hypothetical Pb deficient motif that is caused by local Pb volatilization. In an earlier study of the binary solid solution system Rb<sub>2</sub>O-Nb<sub>2</sub>O<sub>5</sub> RbNb<sub>3</sub>O<sub>8</sub> was reported to have hexagonal symmetry *P6<sub>3</sub>22* ( $a = 7.45$  Å and  $c = 7.66$  Å) and to melt incongruently above 964 °C.<sup>28</sup> Our attempts to synthesize ‘RbNb<sub>3</sub>O<sub>8</sub>’ by mixing stoichiometric amounts of Rb<sub>2</sub>CO<sub>3</sub> and Nb<sub>2</sub>O<sub>5</sub> and applying the same synthesis conditions as for the solid solution did not yield any phase pure material. Stoichiometric related KNb<sub>3</sub>O<sub>8</sub> was reported to crystallize in the orthorhombic space group *Cmcm* ( $a = 8.903(3)$  Å,  $b = 21.16(2)$  Å,  $c = 3.799(2)$ )<sup>29</sup> with a layered structure that can be exfoliated into Nb<sub>3</sub>O<sub>8</sub><sup>-</sup> nanosheets.<sup>30</sup> ICP and EDX data show that Rb<sup>+</sup> can be completely exchanged with H<sup>+</sup> and hence must maintain an interlayer position in a layered structure. As under given circumstances exfoliation of the cation-proton exchanged material is subsequently inhibited with increasing Pb content, the resulting structure must on the one hand retain the layered motif, but on the other hand form local intergrowth structures that break this 2D motif into a 3D linkage, as will be substantiated further based on transmission electron microscopy (TEM), Raman and ssNMR spectroscopy in the following.

Figure 3.1.3 shows overview TEM images where the layered structure of RbPb<sub>2</sub>Nb<sub>3</sub>O<sub>10</sub> is clearly visible. During the measurement, dark particles begin to form and separate from the structure as the material starts to decompose under electron beam irradiation. These particles are most likely PbO as is shown in Figure 3.1.3 c)+d), displaying a region with a crystalline particle which is highlighted in the HRTEM image. The  $d$ -spacings (2.86 Å and 1.86 Å) extracted by fast Fourier transform (FFT) match well with those corresponding to the (110) and (112) planes (2.83 Å and 1.89 Å, respectively) of Litharge (PbO) with *P4/mmm* structure. During further electron beam irradiation the particles become amorphous. Hence, all following experiments were taken with care to avoid or at least minimize decomposition of the pristine material under the electron beam.

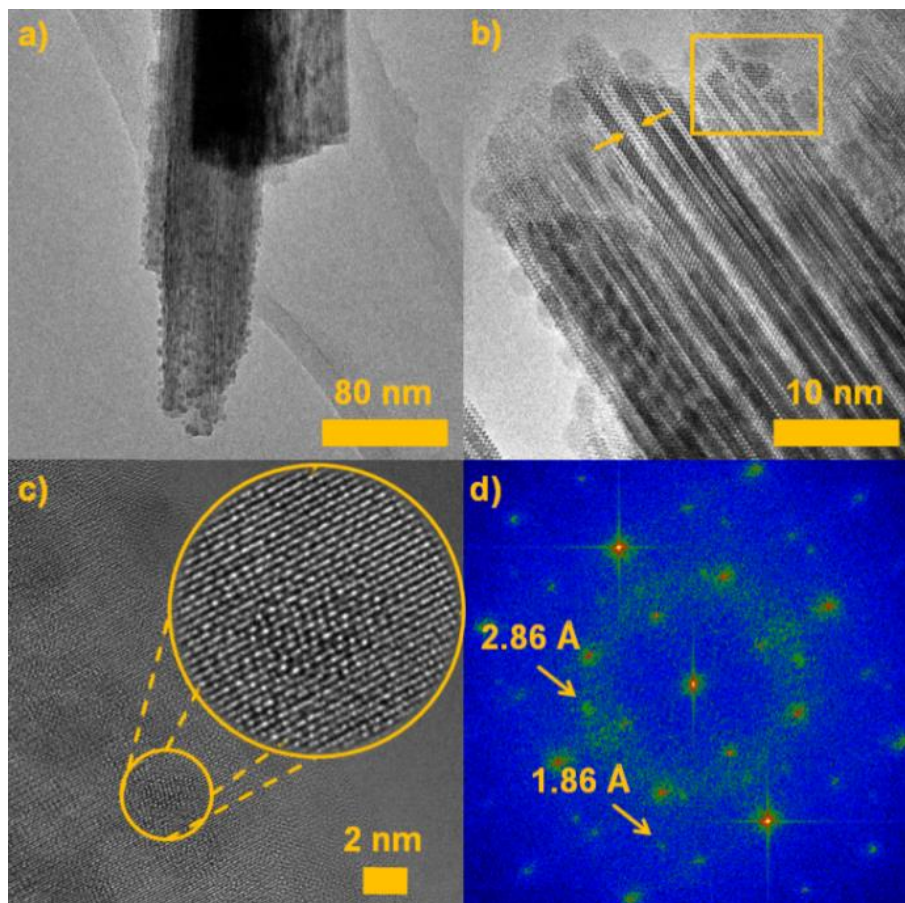


**Figure 3.1.3:** a) TEM overview image of  $\text{RbPb}_2\text{Nb}_3\text{O}_{10}$  where  $\text{PbO}$  particles are visible on its surface, b) TEM image of  $\text{RbPb}_2\text{Nb}_3\text{O}_{10}$  at higher magnification highlighting a possible change in the perovskite structure (orange arrows) and defects that might arise from local  $\text{Pb}$  deficiency (orange square), c) a region with a crystalline  $\text{PbO}$  particle and d) the corresponding FFT where the distances related to the particle are highlighted.

Simulated selected area electron diffraction (SAED) patterns of theoretically tetragonal  $\text{RbPb}_2\text{Nb}_3\text{O}_{10}$  ( $P4/mmm$  ( $a = b = 3.94 \text{ \AA}$  and  $c = 15.20 \text{ \AA}$ )) in comparison with the experimentally obtained patterns acquired along  $[100]$  and  $[001]$  directions of the  $\text{RbPb}_2\text{Nb}_3\text{O}_{10}$  lattice are shown in Figure 3.1.4. Along  $[100]$  we find a  $\text{RbPb}_2\text{Nb}_3\text{O}_{10}$  rich region that matches well with the simulated SAED pattern (Figure 3.1.4 b)). The green circle indicates reflections arising from polycrystalline  $\text{PbO}$  due to decomposition effects. For all other regions we found patterns that look similar to the one presented in Figure 3.1.4 c). Besides the  $\text{RbPb}_2\text{Nb}_3\text{O}_{10}$  lattice shown in black, another lattice attributed to hypothetical  $\text{Pb}$  deficient regions (yellow) becomes apparent with reflections that do not belong to tetragonal  $\text{RbPb}_2\text{Nb}_3\text{O}_{10}$  nor  $\text{PbO}$ . One axis of this region is oriented along the  $c$ -axis of  $\text{RbPb}_2\text{Nb}_3\text{O}_{10}$  and shows lattice parameters around  $4.23 \text{ \AA}$  ( $b^1$ ) and  $2.12 \text{ \AA}$  ( $b^2$ ) etc., which are obtained by dividing  $12.7 \text{ \AA}$  - found in the XRD pattern - by integers. Using the layered structure of  $\text{KNb}_3\text{O}_8$  as a basis, we chose  $b'$  as the axis related to the layer thickness of a hypothetical ' $\text{RbNb}_3\text{O}_8$ ' region. Note that the SAED reflections are very broad due to overlapping

reflections from both lattices as well as possible lattice strain between both domains. This is also seen in the broadening of the XRD reflections for increasing Pb content of the  $\text{RbCa}_{2-x}\text{Pb}_x\text{Nb}_3\text{O}_{10}$  system. Figure 3.1.4 e)+f) depict the orientation of the other two axes:  $c'$  runs along  $[110]$  of  $\text{RbPb}_2\text{Nb}_3\text{O}_{10}$  and forms an angle of  $90 \pm 4^\circ$  with  $a'$ . Hence the Pb deficient layer is rotated by  $45 \pm 4^\circ$  compared to the 2D perovskite layer of  $\text{RbCa}_{2-x}\text{Pb}_x\text{Nb}_3\text{O}_{10}$  and can have 4 different orientations. This becomes clear as in Figure 3.1.4 e) we only see  $a'$  reflections along one direction with different intensities and in Figure 3.1.4 f) we see these reflections also rotated by  $90^\circ$ . For  $a'$  we find integers dividing  $8.62 \text{ \AA}$  ( $a'1$ ) and for  $c'$   $5.45 \text{ \AA}$  ( $c'1$ ), that can also be related to the XRD pattern. These structural conditions highlight the existence of two different patterns, whereof the one related to ideal  $\text{RbPb}_2\text{Nb}_3\text{O}_{10}$  can exist on its own, but the Pb deficient region is only observed in combination of both motifs.

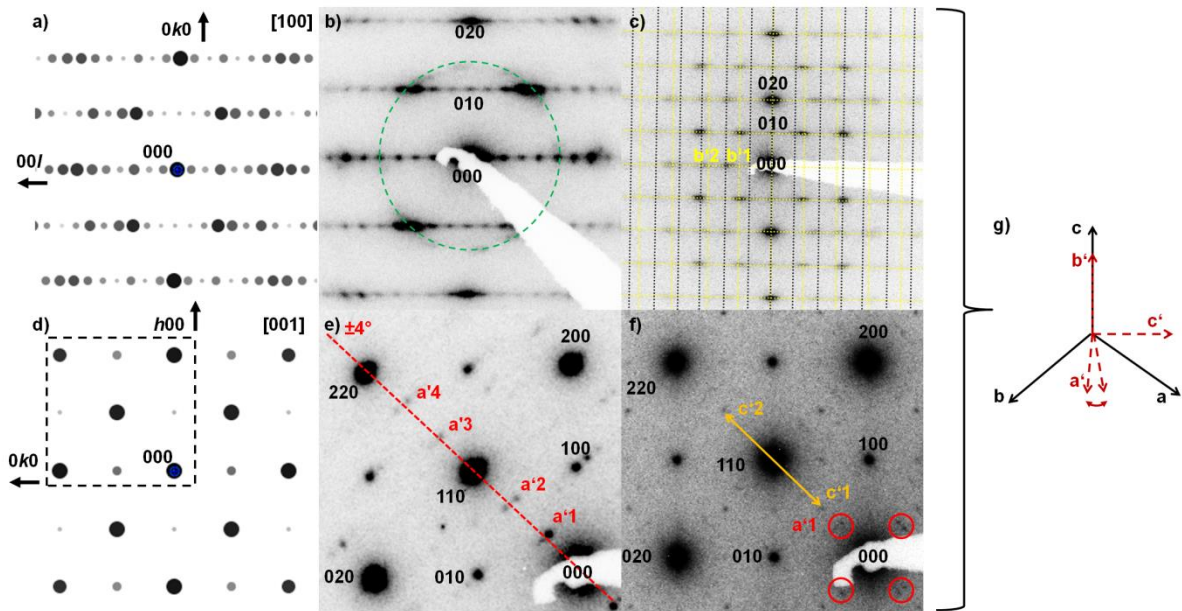


**Figure 3.1.4:** a) Simulated SAED pattern of  $\text{RbPb}_2\text{Nb}_3\text{O}_{10}$  along  $[100]$  viewing direction and b) corresponding experimental SAED pattern of a  $\text{RbPb}_2\text{Nb}_3\text{O}_{10}$  rich region where the green circle emphasizes polycrystalline reflections arising from  $\text{PbO}$ , and c) a common region where a second pattern belonging to a Pb deficient region is highlighted in yellow; d) simulated SAED pattern of  $\text{RbPb}_2\text{Nb}_3\text{O}_{10}$  along  $[001]$  and e) + f) corresponding experimental SAED patterns from an enlarged region of d) showing the two different axes of Pb deficient regions and their orientation with respect to the  $\text{RbPb}_2\text{Nb}_3\text{O}_{10}$ . g) Resulting relation between the coordinate systems of  $\text{RbPb}_2\text{Nb}_3\text{O}_{10}$  (black) and Pb deficient regions as inferred from the TEM/SAED analysis.

These findings are summarized in Figure 3.1.4 g).  $b'$  runs along  $c$  and forms a  $90^\circ$  angle with respect to  $a'$  and  $c'$ .  $c'$  is rotated by  $45^\circ$  against  $a$  and  $b$  and forms a  $90 \pm 4^\circ$  angle with  $a'$ . This is interpreted as the formation of an intergrowth structure along the stacking direction  $c$  of  $[\text{Pb}_2\text{Nb}_3\text{O}_{10}]^-$  where the Pb deficient layers can take 4 different orientations compared to



[Pb<sub>2</sub>Nb<sub>3</sub>O<sub>10</sub>]<sup>-</sup>. Hence, as  $\beta'$  is not 90° nor 120° a monoclinic symmetry for these regions arises. Such a distortion might be seen in Figure 3.1.3 b), highlighted by the orange arrows, and may also cause a partial breakup of the layered 2D character (orange circles in Figure 3.1.3 c). Unfortunately, decomposition of RbPb<sub>2</sub>Nb<sub>3</sub>O<sub>10</sub> in the electron beam limits detailed analysis by scanning TEM (STEM) coupled with electron energy loss spectroscopy (EELS) line-scans, which we previously used to characterize bottom-up assembled, structurally related [Ca<sub>2</sub>Nb<sub>3</sub>O<sub>10</sub>]<sup>-</sup>/[Mn<sub>2</sub>Al(OH)<sub>6</sub>]<sup>+</sup> hybrid stacks.<sup>31</sup>

As SAED patterns are taken from larger sample regions and their sizes are determined by the aperture size of the instrument capture region (ca. 100-150 nm), we used FFT of HRTEM images to analyze the two different regions in more detail. Representative HRTEM images of RbPb<sub>2</sub>Nb<sub>3</sub>O<sub>10</sub> in comparison with RbCa<sub>2</sub>Nb<sub>3</sub>O<sub>10</sub> and their corresponding reduced FFT images along [001] are shown in Figure S3.1.3. The 90° angle between the (100) and (010) planes of RbCa<sub>2</sub>Nb<sub>3</sub>O<sub>10</sub> clearly confirms its tetragonal structure. On the contrary, the angle of RbPb<sub>2</sub>Nb<sub>3</sub>O<sub>10</sub> varies around 91.3-92.3°, depending on the selected area and, hence, suggests lowering of the symmetry to a monoclinic structure. We interpret this finding as a tilting of the NbO<sub>6</sub> octahedra due to the lattice mismatch caused by the intergrowth of RbPb<sub>2</sub>Nb<sub>3</sub>O<sub>10</sub> and Pb deficient regions, which proves a homogeneous distribution of these domains on the nanoscale.

At this point it has to be mentioned that we tried to fit hypothetical 'RbNb<sub>3</sub>O<sub>8</sub>' on basis of the obtained lattice parameters and its relations according to orthorhombic KNb<sub>3</sub>O<sub>8</sub> or a lowered monoclinic symmetry, but did not succeed to match a phase explaining the additional reflections in the XRD. Thus, we envision Rb<sub>3</sub>Pb<sub>4</sub>Nb<sub>9</sub>O<sub>28</sub> to have tetragonal RbPb<sub>2</sub>Nb<sub>3</sub>O<sub>10</sub> domains that are 'randomly' 3D linked in Pb deficient regions.

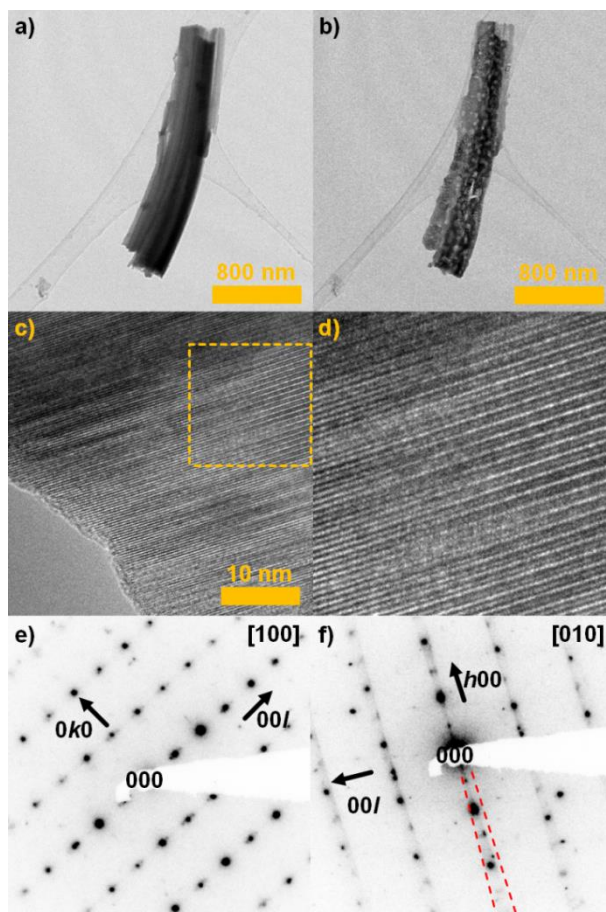
Since we were not able to synthesize 'RbNb<sub>3</sub>O<sub>8</sub>' under ambient conditions we tried to decompose RbPb<sub>2</sub>Nb<sub>3</sub>O<sub>10</sub> in the electron beam following the equation:



Figure 3.1.5 shows the investigated region before and after electron bombardment. EDX shows a transition from RbPb<sub>2</sub>Nb<sub>3</sub>O<sub>10</sub> to Rb<sub>0.8</sub>Nb<sub>3</sub>O<sub>8</sub> that in composition would be close to Pb deficient 'RbNb<sub>3</sub>O<sub>8</sub>' domains. Longer electron irradiation leads to further disintegration over Rb<sub>0.4</sub>Nb<sub>3</sub>O<sub>8</sub> to a niobium oxide in the end. Hence, a loss of Rb and Pb is observed similar to the one induced by heating in the performed solid state synthesis. Rubidium niobates with the obtained stoichiometries in decomposition experiments were published as orthorhombic for Rb<sub>0.105</sub>Nb<sub>0.379</sub>O<sub>z</sub>/Rb<sub>0.83</sub>Nb<sub>3</sub>O<sub>z</sub> ( $a = 12.991(4)$  Å,  $b = 7.5500(10)$  Å and  $c = 3.8978(8)$  Å) and tetragonal for Rb<sub>0.051</sub>Nb<sub>0.390</sub>O<sub>z</sub>/Rb<sub>0.39</sub>Nb<sub>3</sub>O<sub>z</sub> ( $a = 27.484(3)$  Å and  $c = 3.9656(4)$  Å) as part of a Rb<sub>2</sub>O-Nb<sub>2</sub>O<sub>5</sub> equilibria study, but do not match our lattice parameters.<sup>32</sup> We tried to stop

decomposition at  $\text{Rb}_{0.8}\text{Nb}_3\text{O}_8$  (Figure 3.1.5 c)+d)) and found regions that partly showed a layered structure similar to the one seen in Figure 3.1.3 b).

SAED patterns of  $\text{Rb}_{0.8}\text{Nb}_3\text{O}_8$  displayed in Figure 3.1.5 e)+f) show similar, yet slightly larger lattice parameters which may be related to the lower Rb amount present. It is interesting to note the spreading of the reflections along the  $a'$  axis (highlighted by the red line) is similarly to the ones observed in Figure 3.1.4 e). Thus,  $\text{Rb}_{0.8}\text{Nb}_3\text{O}_8$  may be structural related to Pb deficient intergrowth regions.



**Figure 3.1.5:** TEM images of a)  $\text{RbPb}_2\text{Nb}_3\text{O}_{10}$  before and b)  $\text{Rb}_{0.8}\text{Nb}_3\text{O}_8$  after electron irradiation, with c) representative HRTEM image of  $\text{Rb}_{0.8}\text{Nb}_3\text{O}_8$  where the orange square is shown enlarged in d) and SAED patterns of  $\text{Rb}_{0.8}\text{Nb}_3\text{O}_8$  are shown along e)  $[100]$  and f)  $[010]$  directions.

It is worth noting that along with the loss of Pb for increasing  $x$  in  $\text{RbCa}_{2-x}\text{Pb}_x\text{Nb}_3\text{O}_{10}$  and  $\text{HCa}_{2-x}\text{Pb}_x\text{Nb}_3\text{O}_{10}$  an increase in crystal size of both, the bulk and cation-proton exchanged materials is observed. The SEM images of  $\text{RbCa}_{2-x}\text{Pb}_x\text{Nb}_3\text{O}_{10}$  and their cation-exchanged form  $\text{HCa}_{2-x}\text{Pb}_x\text{Nb}_3\text{O}_{10}$  ( $x = 0, 0.5, 1.0, 1.5, 2.0$ ) show plate-like morphology (Figure S3.1.4), where the size of the platelets increases from around 1-2  $\mu\text{m}$  for the pure Ca compound ( $x = 0$ ) by one order of magnitude to around 10  $\mu\text{m}$  for the pure Pb ( $x = 2$ ) compound. This is in contradiction with the XRD data where the full width at half maximum (FWHM) of the



related XRD reflections get significantly broader with higher Pb content, pointing towards smaller crystallites. Thus, the broadening must be due to strain or a structural disorder caused by a 3D linkage of the 2D layered structure.

The Raman spectra of  $\text{RbCa}_{2-x}\text{Pb}_x\text{Nb}_3\text{O}_{10}$  and  $\text{HCa}_{2-x}\text{Pb}_x\text{Nb}_3\text{O}_{10}$  ( $x = 0, 0.5, 1.0, 1.5, 2.0$ ) are given in Figure 3.1.6 and the corresponding Raman frequencies, labeled (1)-(5) and (1H)-(5H), respectively, are listed in Table S3.1.3. The labeling of the Nb and O positions is given in Figure 3.1.1 a) and additional information to the following assignments provided in the Supporting Information (Chapter 3.1.5). The top images in Figure 3.1.6 a)+b) directly compare the Raman spectra of the end members  $\text{RbCa}_2\text{Nb}_3\text{O}_{10}$  and  $\text{RbPb}_2\text{Nb}_3\text{O}_{10}$  on the left, as well as  $\text{HCa}_2\text{Nb}_3\text{O}_{10}$  and  $\text{HPb}_2\text{Nb}_3\text{O}_{10}$  on the right, while the enlarged Raman spectra in the middle and on the bottom show the changes of Raman bands for all investigated solid solutions (Figure 3.1.6 c)+f)). Proceeding from  $\text{RbCa}_2\text{Nb}_3\text{O}_{10}$  to  $\text{RbPb}_2\text{Nb}_3\text{O}_{10}$  most Raman bands shift towards lower wavenumbers, but some Raman bands maintain their position and additionally new features appear and others disappear steadily.

Starting with the most prominent band (1.1) around  $930\text{ cm}^{-1}$  for  $\text{RbCa}_{2-x}\text{Pb}_x\text{Nb}_3\text{O}_{10}$  ( $x = 0, 0.5, 1.0, 1.5, 2.0$ ), this band is related to the symmetrical stretch vibration of Nb(2)-O(4) and is characteristic for layered perovskites compared to regular perovskites.<sup>33</sup> For  $\text{RbCa}_2\text{Nb}_3\text{O}_{10}$  one sharp band is found since all Nb(2)-O(4) positions are equal. With increase of the Pb content the Raman band (1.1) splits first into two and later into two-three bands (1.1), (1.2), (1.3), where the most intense band is still located around  $930\text{ cm}^{-1}$ , but the other ones are shifted towards lower wavenumbers. This means that instead of one terminal Nb(2)-O(4) position at least two other terminal Nb-O positions are present in  $\text{RbPb}_2\text{Nb}_3\text{O}_{10}$  with a longer and hence weaker Nb-O bond. Integration of the area under (1.1):(1.2):(1.3) gives a ratio of 64%:24%:12% showing that roughly 2/3 of the terminal Nb(2)-O(4) positions in  $\text{RbPb}_2\text{Nb}_3\text{O}_{10}$  are maintained, whereas 1/3 are modified. This matches with our scenario where we have a theoretical ratio of two different motifs  $2^*\text{RbPb}_2\text{Nb}_3\text{O}_{10}$  to  $1^*\text{RbNb}_3\text{O}_8$ . Further, this modification is accompanied by a change of the Rb-O-Nb linkage as known from literature.<sup>34-36</sup> Where Raman band (1.1) is related to a tilted Rb-O-Nb linkage in the tetragonal layered perovskite structure, the bands (1.2) and (1.3) related to the Pb deficient regions evolve towards a linear Rb-O-Nb linkage.

Proceeding with Raman band (2) which is located around  $761\text{ cm}^{-1}$  for  $\text{RbCa}_2\text{Nb}_3\text{O}_{10}$ , this band is related to the slightly distorted inner Nb(1)O<sub>6</sub> octahedra. Increasing the Pb content for the solid-solution  $\text{RbCa}_{2-x}\text{Pb}_x\text{Nb}_3\text{O}_{10}$  ( $x = 0, 0.5, 1.0, 1.5, 2.0$ ) we find a reversal of the  $I(1)/I(2)$  ratio from 2:1 via 1.4:1 to 1:1 to 1:1.6 to 1:2.1 for  $\text{RbPb}_2\text{Nb}_3\text{O}_{10}$  in the end. This trend suggests that more outer octahedra compared to the inner ones are present with higher Pb content, which is in agreement with the ssNMR data shown afterwards. Instead of corner

sharing  $\text{NbO}_6$  octahedra in the triple perovskite layer, hypothetical  $[\text{Nb}_3\text{O}_8]^-$  layers might show corner and edge sharing octahedra like the ones found in  $\text{KNb}_3\text{O}_8$  that cause this reversal. The position of Raman band (2H) for  $\text{HCa}_{2-x}\text{Pb}_x\text{Nb}_3\text{O}_{10}$  ( $x = 0, 0.5, 1.0, 1.5, 2.0$ ) stays nearly the same compared to their bulk counterpart as can be seen in Table S3.1.3. Accordingly, the vibration is not influenced by manipulation of the interlayer and belongs to the inner  $\text{Nb}(1)\text{O}_6$  octahedra. With increase of the lead content (2H) splits into two vibrational modes and bands become less distinguishable - which also arises from the overlap with (3H)-(5H) – which is not clearly observed for the bulk material. This points towards a lowering in symmetry, that might be due to the formation of two different kinds of inner octahedra, one in  $[\text{Pb}_2\text{Nb}_3\text{O}_{10}]^-$  and one in formal  $[\text{Nb}_3\text{O}_8]^-$ . This is further underlined by Raman band (3), which we attribute to the  $\text{Nb}(2)\text{O}_6$  inner octahedra. Similar to Raman band (2) a split into two bands is observed.

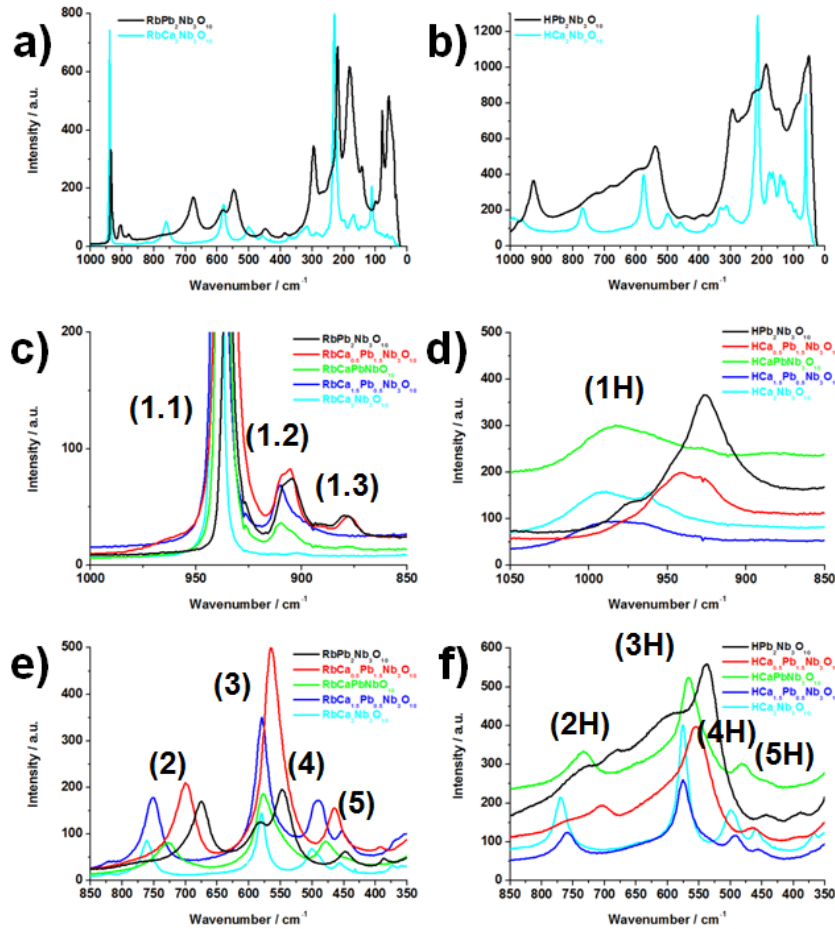


**Figure 3.1.6:** Raman spectra of a)  $\text{RbCa}_{2-x}\text{Pb}_x\text{Nb}_3\text{O}_{10}$  and b)  $\text{HCa}_{2-x}\text{Pb}_x\text{Nb}_3\text{O}_{10}$  for  $x = 0$  (black) and  $x = 2$  (cyan), and c)-f) close-ups of different regions for  $x = 0, 0.5$  (red),  $1.0$  (green),  $1.5$  (blue),  $2.0$ . The labeling (1)-(5) corresponds to characteristic vibrational modes for the bulk and (1H)-(5H) to corresponding modes after cation-proton exchange.

For completeness of the shown analysis complementary IR spectra and discussion are given in the Supporting Information (Figure S3.1.5) underlying the same trend as observed for Raman spectroscopy.

In Figure S3.1.6  $^{93}\text{Nb}$  ssNMR spectra in the series of  $\text{RbCa}_{2-x}\text{Pb}_x\text{Nb}_3\text{O}_{10}$  ( $x = 0, 0.5, 1.0, 1.5, 2.0$ ) are shown. The spectrum of the parent  $\text{RbCa}_2\text{Nb}_3\text{O}_{10}$  shows a well defined quadrupolar pattern that could be fit by two Nb environments with a relative ratio 1:2. Both sites possess close to axial electric field gradient (EFG) tensors, while the magnitudes of the EFGs interactions with the quadrupole moments of the Nb atoms are substantially different. The more abundant site demonstrates a quadrupolar coupling constant  $C_Q = 42.2$  MHz, asymmetry parameter  $\eta_Q = 0.0$ , and isotropic chemical shift  $\delta_{\text{iso}} = -1050 \pm 50$  ppm. The less abundant site has almost three times larger  $C_Q = 114.2$  MHz,  $\eta_Q = 0.1$ , and isotropic chemical shift  $\delta_{\text{iso}} = -1070 \pm 50$  ppm. Both sites have similar chemical shifts, indicating similar oxygen environments. The larger magnitude of the quadrupolar interactions together with the lower population of the second site is in agreement with the crystal structure of the material and the local symmetry of the site Nb(1).<sup>18</sup> The fact that both sites have the asymmetry parameters close to zero is an indication that the sites have local symmetry that include an axis of the third or higher order.

We note, that only quadrupolar interactions are accounted in our fit, and a possible contribution from the chemical shift anisotropy (CSA) has been completely ignored. While it was previously demonstrated that the CSA can contribute in the  $^{93}\text{Nb}$  spectra of structurally similar  $\text{RbSr}_2\text{Nb}_3\text{O}_{10}$ , this contribution at the moderate magnetic field of 9.4 T is relatively minor compared to dominant quadrupolar interaction.<sup>37</sup>

The  $^{93}\text{Nb}$  spectrum of the material with the largest concentration of lead is also composed of two signals, with the magnitude of the quadrupolar interactions for the site Nb(1) significantly diminished, and for the site Nb(2) remaining almost unchanged. Our attempt to improve resolution with the magic angle spinning (MAS) resulted only in a partially resolved signal, and precluded obtaining more accurate chemical shifts and relative occupancies of Nb sites. One can conclude, however, that the site with the smaller quadrupolar interaction ( $C_Q = 34.8$  MHz,  $\eta_Q = 0.1$ ,  $\delta_{\text{iso}} = -1144 \pm 50$  ppm), is also less abundant than the second site ( $C_Q = 45.3$  MHz,  $\eta_Q = 0.1$ ,  $\delta_{\text{iso}} = -1060 \pm 50$  ppm).

$^{93}\text{Nb}$  NMR spectra of the materials with intermedium concentrations of lead show a gradual transformation of the parent lead-free materials with no apparent indication of neither changing of the structural type (at least on the local level), nor formation of any foreign phases. Maintaining of the structural type on the local level is reflected primarily in preserving two distinct Nb sites, both possessing a higher than 2-fold rotational axis.

$^{207}\text{Pb}$  solid state NMR spectra of  $\text{RbCa}_{2-x}\text{Pb}_x\text{Nb}_3\text{O}_{10}$  ( $x = 0.5, 1.0, 1.5, 2.0$ ) are shown in Figure S3.1.7. Overall, the observed isotropic shifts are well within the range expected for

$\text{Pb}^{2+}$  ions 8-coordinated to oxygen atoms, which points towards a change of coordination from formerly 12-coordinated  $\text{Ca}^{2+}$  ions.<sup>38-39</sup> At  $x = 0.5$  and  $1.0$ , the spectra are similar, and reminiscent of the axial anisotropy of the chemical shift with a substantial broadening due to the distribution of the chemical shift. The latter effectively prevents any appreciable signal narrowing by the MAS. Broadening of the signals in these materials due to the chemical shift distribution is not too surprising, as  $^{207}\text{Pb}$  is known for rather high sensitivity of the chemical shift to the local disorder. The isotropic chemical shifts  $\delta_{\text{iso}}$  and the axially of the CSA tensor  $\delta = (\delta_{33} - \delta_{\text{iso}})$  for  $x = 0.5$  and  $1.0$  are  $-2390 \pm 40$  and  $-2410 \pm 40$  ppm, and  $366 \pm 30$  ppm and  $199 \pm 30$  ppm, respectively, with the anisotropy of the CSA tensor  $\eta_{\text{CS}} = (\delta_{22} - \delta_{11})/(\delta_{33} - \delta_{\text{iso}})$  assumed to be 0 in both cases. The spectrum at  $x = 1.5$  still shows axial anisotropy ( $\eta_{\text{CS}} = 0$ ) and is broadened to about the same extent as previously. Two other parameters are slightly reduced:  $\delta_{\text{iso}} = -2320 \pm 30$  ppm,  $\delta = 160$  ppm.

For stoichiometric  $\text{RbPb}_2\text{Nb}_3\text{O}_{10}$  in  $P4/mmm$  space group, an axially anisotropic  $^{207}\text{Pb}$  spectrum is expected. The anisotropy in the spectrum of the material with  $x = 2.0$ , however, is visibly a non-axial:  $\delta_{\text{iso}} = -2100$  ppm,  $\delta = -410$  ppm,  $\eta_{\text{CS}} = 0.8$ . This suggests a breakage of the local  $\text{C}_4$  symmetry at the Pb sites, and perhaps is an indication of the  $\text{RbNb}_3\text{O}_8$  linkages and the overall deficit of lead in the structure.

Akin to the  $^{93}\text{Nb}$  data, the  $^{207}\text{Pb}$  NMR confirms the preservation of the original structural type and homogeneous distribution of the lead throughout the lattice without formation of additional phases. Preservation of the axial symmetry of the chemical shift tensor up to  $x = 1.5$  is an indication of the lead atoms placement into the vacant Ca positions of the lattice.

At this point we like to recall some important findings from the applied analysis methods, before a final structure model will be proposed on the additional information of the exfoliation results. First of all, instead of 2 distinct phases we deal with an local intergrowth structure that for an extreme hypothetical case can be thought of  $2^*\text{RbPb}_2\text{Nb}_3\text{O}_{10} \cdot 1^*\text{RbNb}_3\text{O}_8$ . Second, according to TEM analysis there exist either  $\text{RbPb}_2\text{Nb}_3\text{O}_{10}$  or intergrowth regions.

**Exfoliation.** With these structural insights in mind, exfoliation was performed by treatment of cation-proton exchanged materials with  $\text{TBAOH}$  in aqueous solution. Figure S3.1.8 shows a photograph of colloidal suspensions of  $\text{TBA}_{1-y}\text{H}_y\text{Ca}_{2-x}\text{Pb}_x\text{Nb}_3\text{O}_{10}$  nanosheets after removal of non-exfoliated material by centrifugation. Dense suspensions are obtained up to  $x \leq 1$ , while above this composition rather clear solutions occur. Figure 3.1.7 depicts AFM images and the corresponding height profiles of dried  $\text{TBA}_{1-y}\text{H}_y\text{Ca}_{2-x}\text{Pb}_x\text{Nb}_3\text{O}_{10}$  suspensions on a Si substrate along with TEM images and corresponding SAED patterns of dried suspensions on a lacey carbon grid. For  $x \leq 1$  a large number of essentially unilamellar nanosheets with a height of  $\approx 2.6 \pm 0.1$  nm are formed with a lateral range of  $0.5\text{-}2\text{ }\mu\text{m}$  per edge. For a

concentrated suspension with  $x = 1.5$  only few nanosheets with similar dimensions are found in the AFM, whereas plenty of nanosheets are observed in the TEM. For  $\text{RbPb}_2\text{Nb}_3\text{O}_{10}$  even after concentration of the suspension no nanosheets were observed in the AFM and only single nanosheets are visible in the TEM.

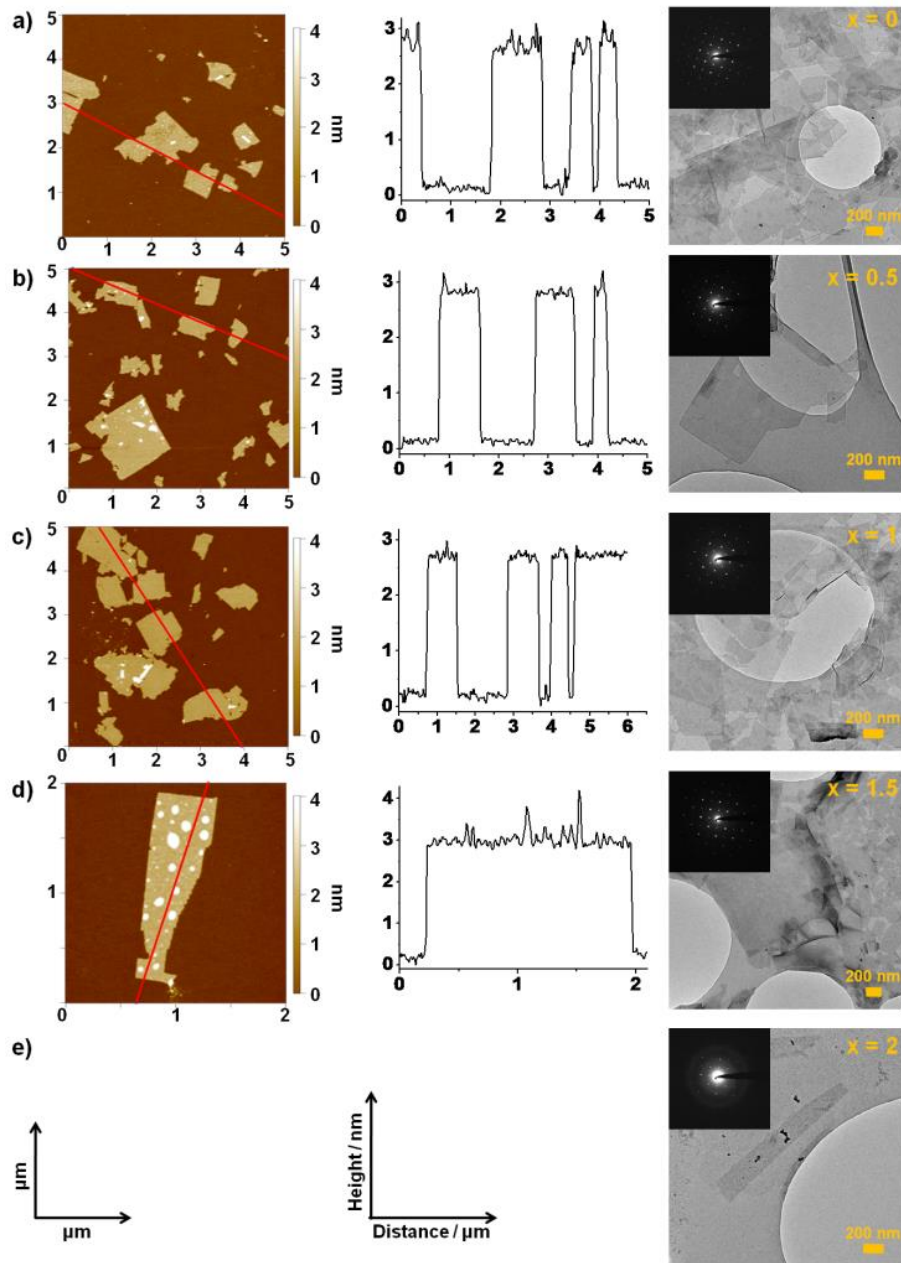


**Figure 3.1.7:** AFM images (left) with corresponding height profiles (middle) and TEM images with corresponding SAED patterns as inset (right) of  $\text{TBA}_{1-y}\text{H}_y\text{Ca}_{2-x}\text{Pb}_x\text{Nb}_3\text{O}_{10}$  nanosheets  $x =$  a) 0, b) 0.5, c) 1.0 and d) 1.5. Note that for  $x = 2.0$  no nanosheets were found in the AFM.

Thus, the amount of exfoliated nanosheets is decreasing with increasing Pb content. The height of the nanosheets is slightly higher than their crystallographic thickness of an ideal  $[\text{Ca}_{2-x}\text{Pb}_x\text{Nb}_3\text{O}_{10}]^-$  perovskite layer ( $\sim 1.5$  nm), since AFM measurements were carried out

under ambient conditions and are affected by  $TBA^+/H^+$  as well as water adsorption.<sup>31</sup> As expected, we did not find any evidence in the AFM for nanosheets with a different height that would point towards exfoliation of  $[Nb_3O_8]^-$  nanosheets (~1.2 nm) and hence, relate the obtained nanosheets to the solid solution  $TBA_{1-y}H_yCa_{2-x}Pb_xNb_3O_{10}$  without Pb deficient 3D linkage. This is further supported by the  $d$ -values obtained by SAED listed in Table S3.1.4. Nanosheet lattices stay approximately the same within the limit of error and do not point towards a different structure.

ICP-AES data obtained from a nanosheet pellet, thus averaging over a larger volume, show the same trend as discussed earlier for the bulk and cation-proton-exchange materials. On the contrary, TEM-EDX data show significant variations for different nanosheet regions. We focus on  $x = 1.0, 1.5$  of  $TBA_{1-y}H_yCa_{2-x}Pb_xNb_3O_{10}$  where a bunch of overlapping nanosheets were measured (Figure 3.1.7 c)+d)), as the EDX signal is too low in intensity for individual nanosheet of  $TBA_{1-y}H_yPb_2Nb_3O_{10}$  due to the rapid disintegration under electron bombardment. Niobate nanosheets always had Pb incorporated along with Ca, proving the successful solid solution. On one region we also found pure lead niobate, but with a 1:3.8 ratio of Pb:Nb. Thus, overall distribution of Ca and Pb is homogeneous but can be locally differ, which might be caused by volatilization effects. As expected, we did not find any region where possible  $[Nb_3O_8]^-$  nanosheets were present. Figure S3.1.9 shows an EDX map of a particle of uncentrifuged  $TBA_{1-y}H_yPb_2Nb_3O_{10}$  nanosheets where Pb M, Nb L $\alpha$  and O K $\alpha$  peaks point towards a homogeneous distribution of all elements within the particle. The average composition of  $(TBA_{1-y}H_y)_3Pb_{3.4}Nb_9O_z$  is close to the one for the bulk and cation-proton exchanged forms. Thus, this further proves that instead of exfoliation,  $[Pb_2Nb_3O_{10}]^-$  and Pb deficient regions form an intergrowth with strong interactions between the layers, that can not be separated under the given synthesis conditions.

Based on the combination of all analysis information obtained Figure 3.1.9 displays a structural model for  $RbPb_2Nb_3O_{10}$ . The actual composition is  $Rb_3Pb_4Nb_9O_{28}$  that can be written as  $2 \cdot RbPb_2Nb_3O_{10} \cdot 1 \cdot 'RbNb_3O_8'$  for an edge case. Instead of the ideal  $P4/mmm$  structure shown in Figure 3.1.8 a) local loss of Pb during the synthesis causes the formation of Pb deficient regions ' $RbNb_3O_8$ ' denoted as B shown in Figure 3.1.8 b). These regions having a monoclinic symmetry, are rotated  $45 \pm 4^\circ$  against the parent tetragonal perovskite layers A, show more linear terminal Nb-O-Rb angles (Figure 3.1.8 c)+d)) and cause the additional reflections found in the XRD. Note that ssNMR suggests no overall change of the symmetry further pointing towards local effects. TEM-SAED investigations support this finding as Pb-deficient layers only exist along with the perovskite layers and cannot be exfoliated. Thus, the Pb loss must lead to a more or less directed 3D linkage of the layers as shown in Figure 3.1.8 e) and the composition of these layers might be more accurately pictured somewhere between  $RbPb_2Nb_3O_{10}$  and ' $RbNb_3O_8$ '.

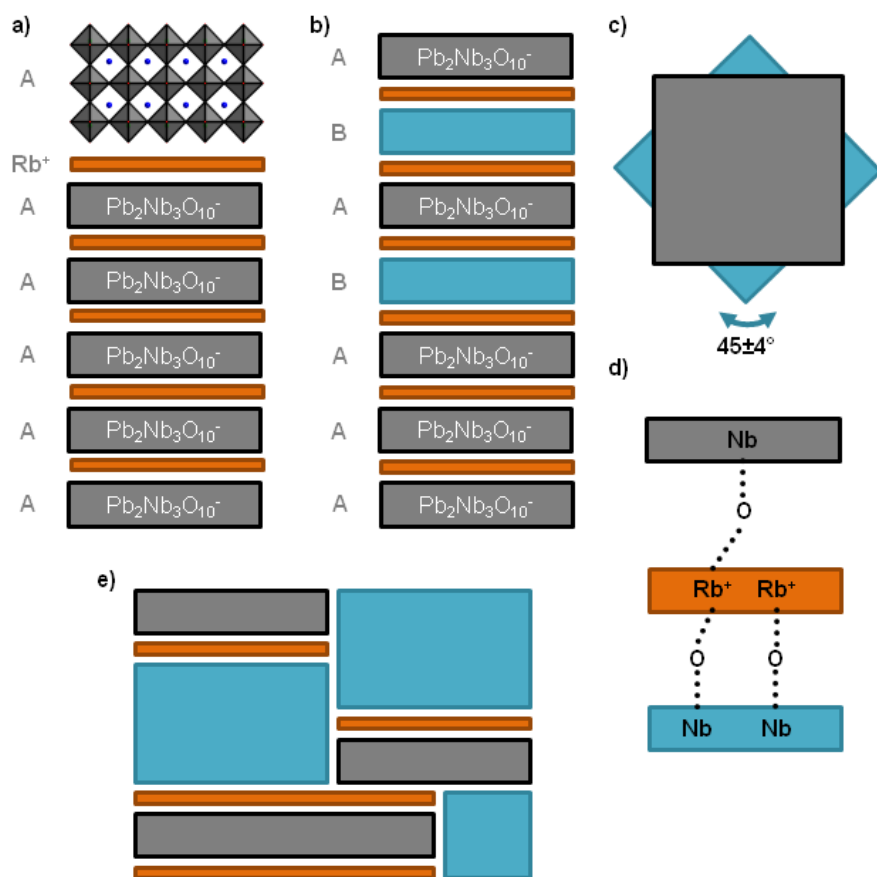


**Figure 3.1.8:** Structural model for  $\text{RbCa}_{2-x}\text{Pb}_x\text{Nb}_3\text{O}_{10}$  for  $x=2$  derived from a) ideal tetragonal structure of  $\text{RbPb}_2\text{Nb}_3\text{O}_{10}$ . Local Pb volatilization leads to b) formation of Pb deficient regions B, that form c) an angle of  $45 \pm 4^\circ$  with the parent  $[\text{Pb}_2\text{Nb}_3\text{O}_{10}]^-$  layer A along the stacking direction. This causes d) a change of the Nb-O-Rb angle and can be pictured as e) a 3D linkage of Pb deficient regions B with the  $[\text{Pb}_2\text{Nb}_3\text{O}_{10}]^-$  layers A.

Figure S3.1.10 shows UV-VIS spectra of  $(\text{Rb,H})\text{Ca}_{2-x}\text{Pb}_x\text{Nb}_3\text{O}_{10}$  for  $x=0, 0.5, 1.0, 1.5, 2.0$  and  $\text{TBA}_{1-y}\text{H}_y\text{Ca}_{2-x}\text{Pb}_x\text{Nb}_3\text{O}_{10}$  for  $x=0, 0.5, 1.5$ , as too few nanosheets were obtained for  $x=2$ . Introduction of Pb into the structure leads to a rapid red-shift for all materials. We extracted the optical band gaps ( $E_g$ ) based on the Kubelka–Munk remission function  $F(R) = (1-R)^2/2R$  ( $R$  = reflectance) and linear extrapolation of Tauc plots, plotting  $F(R)^{1/n}$  against  $h\nu$ , using  $n = 1/2$  for a direct semiconductor.<sup>8, 40</sup> A summary is listed in Table 3.1.1. The band gap decreases about 1 eV down from  $\sim 3.5$  eV to  $\sim 2.5$  eV for all materials as Pb is introduced into the perovskite blocks. Interestingly, the minimum is found for  $\text{RbCa}_{0.5}\text{Pb}_{1.5}\text{Nb}_3\text{O}_{10}$  with  $2.4 \pm 0.1$  eV rather than for pure  $\text{RbPb}_2\text{Nb}_3\text{O}_{10}$ . This anomaly may be due to the higher amount of the Pb deficient phase.

**Table 3.1.1:** Band gap of  $\text{RbCa}_{2-x}\text{Pb}_x\text{Nb}_3\text{O}_{10}$ ,  $\text{HCa}_{2-x}\text{Pb}_x\text{Nb}_3\text{O}_{10}$  and  $\text{TBA}_{1-y}\text{H}_y\text{Ca}_{2-x}\text{Pb}_x\text{Nb}_3\text{O}_{10}$  for  $x = \text{a) } 0, \text{ b) } 0.5, \text{ c) } 1.0, \text{ d) } 1.5 \text{ and e) } x = 2.0$  given in eV with an error of  $\pm 0.1$  eV for the bulk and cation-proton exchanged form and  $\pm 0.2$  eV for the nanosheets

Theoretical Formula	Rb	H	$\text{TBA}_{1-y}\text{H}_y$
$\text{MCa}_2\text{Pb}_0\text{Nb}_3\text{O}_{10}$	3.5	3.5	3.4
$\text{MCa}_{1.5}\text{Pb}_{0.5}\text{Nb}_3\text{O}_{10}$	2.5	2.7	2.6
$\text{MCaPbNb}_3\text{O}_{10}$	2.5	2.6	2.5
$\text{MCa}_{0.5}\text{Pb}_{1.5}\text{Nb}_3\text{O}_{10}$	2.3	2.5	-*
$\text{MCa}_0\text{Pb}_2\text{Nb}_3\text{O}_{10}$	2.4	2.6	-*

\* Amount of nanosheets too small for measurement

### 3.1.3 Conclusion

In conclusion, we have demonstrated the existence of solid solution  $\text{RbCa}_{2-x}\text{Pb}_x\text{Nb}_3\text{O}_{10}$ . For increasing Pb content local Pb volatilization leads to a change in structure that for  $x = 2$  can be in an edge case formulated as  $2^*\text{RbPb}_2\text{Nb}_3\text{O}_{10} \cdot 1^*\text{RbNb}_3\text{O}_8$ . ‘ $\text{RbNb}_3\text{O}_8$ ’ cannot be synthesized applying the same synthesis protocol using  $\text{Rb}_2\text{CO}_3$  and  $\text{Nb}_2\text{O}_5$  as precursors. Neither is it possible to exfoliate the pure lead niobate. Thus, the Pb deficient layers seem to three dimensionally link  $[(\text{Ca,Pb})_2\text{Nb}_3\text{O}_{10}]^-$  layers thereby exhibiting a composition somewhere between  $\text{RbPb}_2\text{Nb}_3\text{O}_{10}$  and ‘ $\text{RbNb}_3\text{O}_8$ ’ as we have demonstrated by in depth TEM, Raman and ssNMR characterization. SAED showed that these layers are stacked along the c-axis of the perovskite and are rotated by an angle of  $45 \pm 4^\circ$  with respect to the host layer. As already a slight substitution of Pb for Ca leads to a significant decrease in the band gap, we found  $\text{TBA}_{1-y}\text{H}_y\text{CaPbNb}_3\text{O}_{10}$  nanosheets to be the best compromise between a minimized band gap and a good yield of high quality nanosheets.

**ACKNOWLEDGMENTS:** This work was supported by the cluster of excellence Nanosystems Initiative Munich (NIM), the Fonds der Chemischen Industrie (FCI) and the Center for Nanoscience (CeNS). We gratefully acknowledge M.-L. Schreiber for IR and ICP-AES measurements, M. Konuma for XPS measurements, A. Schulz for Raman spectroscopy, A. Frank for additional SAED tilt experiments, J. Barthel for HRTEM measurements and M. Heggen for EDX maps.



### 3.1.4 Bibliography

- [1] N. S. Lewis, D. G. Nocera, *Proc. Natl. Acad. Sci.* **2006**, *103*, 15729-15735.
- [2] A. Kudo, Y. Miseki, *Chem. Soc. Rev.* **2009**, *38*, 253-278.
- [3] X. Chen, S. Shen, L. Guo, S. S. Mao, *Chem. Rev. (Washington, DC, U. S.)* **2010**, *110*, 6503-6570.
- [4] F. E. Osterloh, *Chem. Soc. Rev.* **2013**, *42*, 2294-2320.
- [5] E. M. Sabio, M. Chi, N. D. Browning, F. E. Osterloh, *Langmuir* **2010**, *26*, 7254-7261.
- [6] K. Domen, J. Yoshimura, T. Sekine, A. Tanaka, T. Onishi, *Catal. Lett.* **1990**, *4*, 339-343.
- [7] O. C. Compton, E. C. Carroll, J. Y. Kim, D. S. Larsen, F. E. Osterloh, *J. Phys. Chem. C* **2007**, *111*, 14589-14592.
- [8] K. S. Viridi, Y. Kauffmann, C. Ziegler, P. Ganter, B. V. Lotsch, W. D. Kaplan, P. Blaha, C. Scheu, *Phys. Rev. B* **2013**, *87*, 115108.
- [9] J. Yoshimura, Y. Ebina, J. Kondo, K. Domen, A. Tanaka, *J. Phys. Chem.* **1993**, *97*, 1970-1973.
- [10] Y. Hu, J. Shi, L. Guo, *Appl. Catal., A* **2013**, *468*, 403-409.
- [11] H. G. Kim, O. S. Becker, J. S. Jang, S. M. Ji, P. H. Borse, J. S. Lee, *J. Solid State Chem.* **2006**, *179*, 1214-1218.
- [12] R. Ma, T. Sasaki, *Acc. Chem. Res.* **2015**, *48*, 136-143.
- [13] E. M. Sabio, R. L. Chamousis, N. D. Browning, F. E. Osterloh, *J. Phys. Chem. C* **2012**, *116*, 3161-3170.
- [14] M. Fang, C. H. Kim, G. B. Saupe, H.-N. Kim, C. C. Waraksa, T. Miwa, A. Fujishima, T. E. Mallouk, *Chem. Mater.* **1999**, *11*, 1526-1532.
- [15] Y. Hu, L. Guo, *ChemCatChem* **2015**, *7*, 584-587.
- [16] M. Osada, T. Sasaki, *Adv. Mater. (Weinheim, Ger.)* **2012**, *24*, 210-228.
- [17] V. Nicolosi, M. Chhowalla, M. G. Kanatzidis, M. S. Strano, J. N. Coleman, *Science* **2013**, *340*.
- [18] Z.-H. Liang, K.-B. Tang, Q.-W. Chen, H.-G. Zheng, *Acta Crystallogr., Sect. E: Struct. Rep. Online* **2009**, *65*, i44-i44.
- [19] T. A. Kodenkandath, A. S. Kumbhar, W. L. Zhou, J. B. Wiley, *Inorg. Chem.* **2001**, *40*, 710-714.
- [20] R. Shannon, *Acta Crystallogr., Sect. A* **1976**, *32*, 751-767.
- [21] M. A. Subramanian, J. Gopalakrishnan, A. W. Sleight, *Mater. Res. Bull.* **1988**, *23*, 837-842.
- [22] S.-J. K. Young-Sik Hong, *Bull. Korean Chem. Soc.* **1996**, *17*, 730-736.
- [23] Y. Chen, X. Zhao, H. Ma, S. Ma, G. Huang, Y. Makita, X. Bai, X. Yang, *J. Solid State Chem.* **2008**, *181*, 1684-1694.

- [24] S. Royer, D. Duprez, F. Can, X. Courtois, C. Batiot-Dupeyrat, S. Laassiri, H. Alamdari, *Chem. Rev. (Washington, DC, U. S.)* **2014**, 114, 10292-10368.
- [25] J. A. Taylor, D. L. Perry, *J. Vac. Sci. Technol., A* **1984**, 2, 771-774.
- [26] A. F. Holleman, E. Wiberg, *Lehrbuch der Anorganischen Chemie, Vol. 101*, Walter de Gruyter, Berlin, **1995**.
- [27] M. K. Bahl, *J. Phys. Chem. Solids* **1975**, 36, 485-491.
- [28] P. N. Iyer, A. J. Smith, *Acta Crystallogr., Sect. B* **1971**, 27, 731-734.
- [29] M. Gasperin, *Acta Crystallogr., Sect. B* **1982**, 38, 2024-2026.
- [30] A. Takagaki, D. Lu, J. N. Kondo, M. Hara, S. Hayashi, K. Domen, *Chem. Mater.* **2005**, 17, 2487-2489.
- [31] C. Ziegler, S. Werner, M. Bugnet, M. Wörsching, V. Duppel, G. A. Botton, C. Scheu, B. V. Lotsch, *Chem. Mater.* **2013**, 25, 4892-4900.
- [32] D. B. Minor, R. S. Roth, H. S. Parker, W. S. Brower, *J. Res. Natl. Bur. Stand.* **1977**, 82, 151-165.
- [33] J. M. Jehng, I. E. Wachs, *Chem. Mater.* **1991**, 3, 100-107.
- [34] H. J. Kim, S.-H. Byeon, H. Yun, *Bull. Korean Chem. Soc.* **2001**, 22, 298-302.
- [35] S.-H. Byeon, H.-J. Nam, *Chem. Mater.* **2000**, 12, 1771-1778.
- [36] S.-H. Byeon, S.-O. Lee, H. Kim, *J. Solid State Chem.* **1997**, 130, 110-116.
- [37] X. Wang, J. Adhikari, L. J. Smith, *J. Phys. Chem. C* **2009**, 113, 17548-17559.
- [38] F. Fayon, I. Farnan, C. Bessada, J. Coutures, D. Massiot, J. P. Coutures, *J. Am. Chem. Soc.* **1997**, 119, 6837-6843.
- [39] O. Dmitrenko, S. Bai, P. A. Beckmann, S. van Bramer, A. J. Vega, C. Dybowski, *J. Phys. Chem. A* **2008**, 112, 3046-3052.
- [40] S. P. Tandon, J. P. Gupta, *Phys. Status Solidi B* **1970**, 38, 363-367.

### 3.1.5 Supporting Information

#### EXPERIMENTAL PROCEDURES:

RbCa<sub>2-x</sub>Pb<sub>x</sub>Nb<sub>3</sub>O<sub>10</sub> ( $x = 0, 0.5, 1.0, 1.5, 2.0$ ) was synthesized similar to common solid state synthesis routes.<sup>1-3</sup> Rb<sub>2</sub>CO<sub>3</sub> (99%, Acros Organics), Nb<sub>2</sub>O<sub>5</sub> (99.5%, Alfa Aesar), CaCO<sub>3</sub> (99+%, Sigma-Aldrich) and/or PbO (99.9+%, Acros Organics) were mixed in a molar ratio according to the stoichiometric ratio of RbCa<sub>2-x</sub>Pb<sub>x</sub>Nb<sub>3</sub>O<sub>10</sub> and fired up to 1000°C for 32 h with one intermediate grinding step in between. 10% excess of Rb<sub>2</sub>CO<sub>3</sub> was added for the compensation of volatilization losses. Cation-proton exchange was achieved by stirring the bulk material in 5 M HNO<sub>3</sub> for at least 5 days with several renewals of the acid to ensure complete exchange. The washed and dried at 100°C HCa<sub>2-x</sub>Pb<sub>x</sub>Nb<sub>3</sub>O<sub>10</sub> was dispersed in a molar ratio of 1:1 with tetra-*n*-butylammonium hydroxide (TBAOH) 30-hydrate (Sigma-

Aldrich) in an aqueous solution and stirred for 3-4 weeks to achieve exfoliation. In order to analyze the exfoliated nanosheets  $TBA_{1-y}H_yCa_{2-x}Pb_xNb_3O_{10}$  the colloidal suspension was centrifuged using a bench top centrifuge Sigma 3-30K (Sigma Laborzentrifugen, Osterode). Unexfoliated material was removed at a centrifugation speed of 3000 rpm for 30 min and the supernatant either directly used for analysis or further processed. To isolate the nanosheets the supernatant was centrifuged at a speed of 25000 rpm for another 30 min, the remaining aqueous solution removed and the pellet dried at 60°C.

#### **CHARACTERIZATION:**

**XRD.** Powder X-ray diffraction (XRD) patterns were recorded on a STOE Stadi P powder diffractometer in Debye–Scherrer-geometry at 298 K utilizing Cu-K $\alpha_1$  radiation ( $k = 154.056$  pm) with a Ge(111)-monochromator with a linear position sensitive detector.

**ICP-AES.** Inductively coupled plasma atomic emission spectroscopy (ICP-AES) was analyzed with a Vista Pro ICP-AES spectrometer. The characteristic wavelengths were separated with an Echelle-Polychromator (Varian, Darmstadt) and detected with a photomultiplier.

**SEM-EDX.** Crystalline precursors and the nanosheet pellet were analyzed by scanning electron microscopy (SEM) coupled with energy dispersive X-ray spectroscopy (EDX) on a Vega TS 5130 MM (Tescan, Brno) using a Si/Li detector (Oxford Instruments, Abingdon) and a JSM-6500F electron microscope (JEOL Ltd., Tokyo) equipped with a 7418 EDX detector (Oxford Instruments, Abingdon).

**XPS.** X-ray photoelectron spectroscopy (XPS) was done on an Axis Ultra (Kratos Analytical, Manchester) X-ray photoelectron spectrometer with an Al anode (Al K $\alpha$  radiation,  $h\nu = 1486.58$  eV, energy resolution  $\sim 0.1$  eV). The binding energy scale was calibrated using the C 1s peak at 284.800 eV.

**TEM-EDX.** Transmission electron microscopy (TEM) samples were prepared either by suspending the pestle powder in ethanol or diluting of the colloidal suspension of nanosheets and dropping the suspension onto a copper or gold grid coated with a lacey and holey carbon film, respectively. For TEM analysis, which were performed at 300 kV, the grid was mounted on a double tilt holder with a maximum tilt angle of 30°. High-resolution TEM (HRTEM) investigations were conducted on a FEI Titan 80-300 keV TEM equipped with a field emission gun, an imaging spherical aberration corrector element leading to sub Ångström resolution and a Gatan UltraScan 1000 (2k × 2k) slow scan charged coupled device camera system. Scanning TEM (STEM) were done on a FEI Titan 80-300 keV TEM equipped with a field emission gun, a probe spherical aberration corrector element along with an electron monochromator, leading to a sub Ångström resolution, a post column energy filter system and a Gatan UltraScan 1000 (2k × 2k) slow scan charged coupled device camera system. A Philips CM30 ST microscope (300 keV, LaB $_6$  cathode, CS = 1.15 mm,

Royal Philips Electronics, Amsterdam) was used for imaging of nanosheets and determining their elemental composition *via* EDX measurements. Overall, TEM investigations were performed with a total of about 40 particles being analyzed.

**Raman.** The Raman spectra were taken with a Typ V 010 LabRAM single grating spectrometer (HORIBA Jobin Yvon GmbH, Bensheim), equipped with a double super razor edge filter and a Peltier cooled CCD camera. Spectra are taken in quasi-backscattering geometry using the linearly polarized 456.9 nm line of a diode laser with power less than 1 mW, focused to a 2  $\mu\text{m}$  spot through a 100x microscope objective on to the top surface of the sample. The resolution of the spectrometer (grating 1800 L mm<sup>-1</sup>) is 1 wavenumber (cm<sup>-1</sup>).

**IR.** Infrared (IR) spectroscopy was measured on a Spectrum Two IR Spectrometer with an attenuated total reflectance unit (PerkinElmer, Waltham).

**ssNMR.** Solid state nuclear magnetic resonance (ssNMR) measurements of <sup>1</sup>H, <sup>93</sup>Nb and <sup>207</sup>Pb were performed on a Bruker Avance III 400 MHz instrument (B<sub>0</sub>=9.4 T), at resonance frequencies of 400.1, 97.96 and 83.71 MHz, respectively. Double channel Bruker 2.5 and 4 mm magic angle spinning (MAS) probes were used for <sup>207</sup>Pb experiments. Stationary <sup>93</sup>Nb measurements were performed on a double-channel 5 mm solenoid probe from NMR Service. The chemical shifts of <sup>207</sup>Pb are externally referenced to the signals of tetramethyllead (Pb(CH<sub>3</sub>)<sub>4</sub>). <sup>93</sup>Nb NMR chemical shifts were referenced to a saturated solution of K[NbCl<sub>6</sub>] in acetonitrile (absolute frequency ratio 24.476 170 %).<sup>4</sup> A total of 1200 scans were acquired for <sup>207</sup>Pb to achieve an acceptable signal-to-noise ratio. Stationary <sup>93</sup>Nb NMR data were acquired as variable offset cumulative spectra (VOCS) using a ( $\pi/2$ – $\pi$ – $\pi/2$ )-quadrupolar-echo pulse sequence with 0.8  $\mu\text{s}$  RF pulses and 50  $\mu\text{s}$  echo delays.<sup>5</sup> Each spectrum is a sum of ten sub-spectra acquired in equal frequency offsets of 100 kHz, with 128 scans per offset. Analytical simulations of experimental spectra were carried out with the Bruker TopSpin 3.2 Lineshape Analysis Tool and WinFit simulation package.<sup>6</sup>

**AFM.** Atomic force microscopy (AFM) measurements were performed on a MFP-3D Stand alone AFM (Asylum Research, Santa Barbara). Tapping-mode was applied using OMCL-AC160TS-R3 (Olympus, Tokyo) cantilevers with a resonant frequency of 300 kHz. For topography measurements of the nanosheets the colloidal suspension after centrifugation at 3000 rpm was dropped on to a silicon wafer with (100) orientation (Silchem, Freiberg) for 15–30 min before the wafer was dried in an N<sub>2</sub> flow.

**UV-VIS.** Optical diffuse reflectance spectra of the bulk material and the nanosheet pellet were collected at room temperature with a Cary 5000 UV-Vis-NIR diffuse reflectance spectrometer (Agilent Technologies, Santa Clara) at a photometric range of 200–800 nm. Powders were prepared in a sample carrier with a quartz glass window at the edge of the integrating sphere with BaSO<sub>4</sub> as the optical standard. Kubelka–Munk spectra were calculated from the reflectance data.

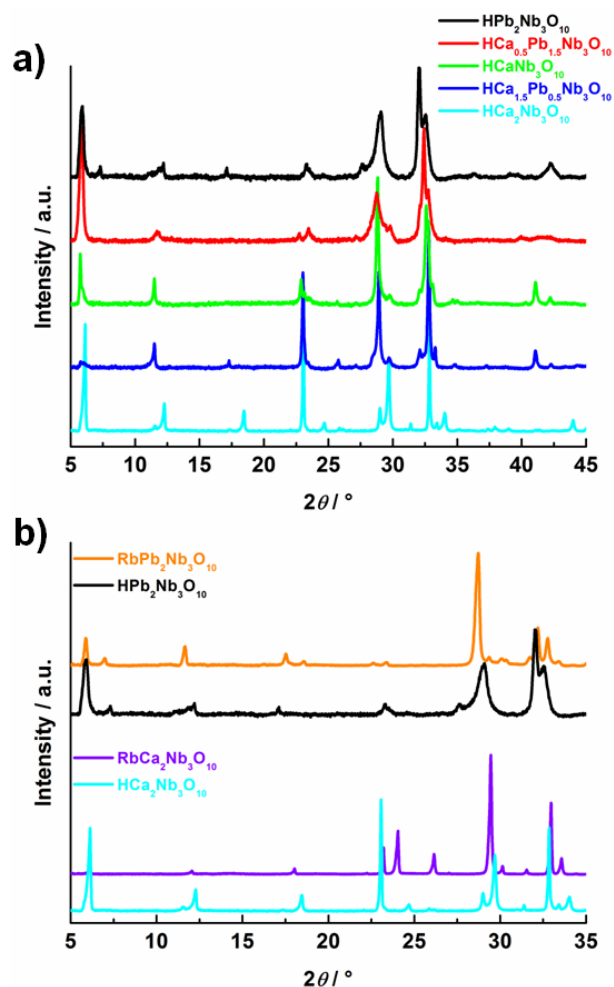


**Figure S3.1.1:** a) XRD pattern of  $\text{HCa}_{2-x}\text{Pb}_x\text{Nb}_3\text{O}_{10}$  ( $x = 0, 0.5, 1.0, 1.5, 2.0$ ) and b) enlarged region from  $5$ - $35^\circ 2\theta$  comparing the bulk material of endmembers with their cation-proton exchanged forms.

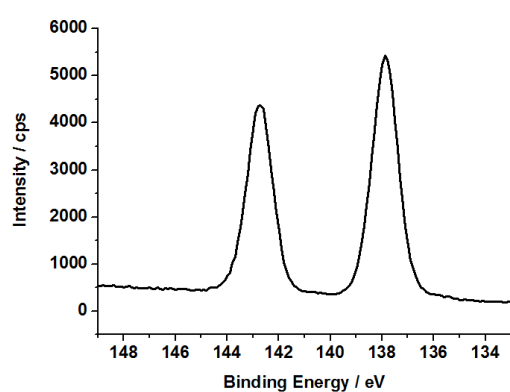


**Figure S3.1.2:** XPS spectrum of  $\text{RbPb}_2\text{Nb}_3\text{O}_{10}$  showing the  $\text{Pb } 4f_{5/2}$  and  $\text{Pb } 4f_{7/2}$  peaks for  $\text{Pb}^{\text{II}}$  species.

**Table S3.1.1:** ICP-AES data for weighted samples  $\text{RbCa}_{2-x}\text{Pb}_x\text{Nb}_3\text{O}_{10}$ , their cation-proton exchanged forms  $\text{HCa}_{2-x}\text{Pb}_x\text{Nb}_3\text{O}_{10}$  and the separated nanosheets  $\text{TBA}_{1-y}\text{HyCa}_{2-x}\text{Pb}_x\text{Nb}_3\text{O}_{10}$  with  $x = 0, 0.5, 1.0, 1.5, 2.0$ . The theoretical expected formula is listed along with the analytical values given in wt% as average of 2-4 measurements, as well as the resulting experimental formula.

Theoretical Formula	Rb	Ca	Pb	Nb	Experimental Formula
$\text{RbCa}_2\text{Nb}_3\text{O}_{10}$	13.3	13.21	-	46.18	$\text{Rb}_{0.9}\text{Ca}_{2.0}\text{Pb}_{0.0}\text{Nb}_3\text{O}_z$
$\text{HCa}_2\text{Nb}_3\text{O}_{10}^a$	-	14.39	-	53.50	$\text{HyCa}_{1.9}\text{Pb}_{0.0}\text{Nb}_3\text{O}_z$
$\text{TBA}_{1-y}\text{HyCa}_2\text{Nb}_3\text{O}_{10}^a$	-	12.86	-	42.08	$\text{TBA}_{1-y}\text{HyCa}_{2.1}\text{Pb}_{0.0}\text{Nb}_3\text{O}_z$
$\text{RbCa}_{1.5}\text{Pb}_{0.5}\text{Nb}_3\text{O}_{10}$	12.55	9.55	9.17	45.34	$\text{Rb}_{0.9}\text{Ca}_{1.5}\text{Pb}_{0.3}\text{Nb}_3\text{O}_z$
$\text{HCa}_{1.5}\text{Pb}_{0.5}\text{Nb}_3\text{O}_{10}^a$	-	9.89	12.08	45.84	$\text{HyCa}_{1.5}\text{Pb}_{0.4}\text{Nb}_3\text{O}_z$
$\text{TBA}_{1-y}\text{HyCa}_{1.5}\text{Pb}_{0.5}\text{Nb}_3\text{O}_{10}^a$	-	10.38	7.36	41.18	$\text{TBA}_{1-y}\text{HyCa}_{1.8}\text{Pb}_{0.3}\text{Nb}_3\text{O}_z$
$\text{RbCaPbNb}_3\text{O}_{10}$	10.93	6.55	23.10	40.33	$\text{Rb}_{0.9}\text{Ca}_{1.1}\text{Pb}_{0.8}\text{Nb}_3\text{O}_z$
$\text{HCaPbNb}_3\text{O}_{10}^a$	-	6.15	22.48	44.95	$\text{HyCa}_{1.0}\text{Pb}_{0.7}\text{Nb}_3\text{O}_z$
$\text{TBA}_{1-y}\text{HyCaPbNb}_3\text{O}_{10}^a$	-	6.51	19.22	36.26	$\text{TBA}_{1-y}\text{HyCa}_{1.3}\text{Pb}_{0.7}\text{Nb}_3\text{O}_z$
$\text{RbCa}_{0.5}\text{Pb}_{1.5}\text{Nb}_3\text{O}_{10}$	9.71	2.55	32.17	35.14	$\text{Rb}_{0.9}\text{Ca}_{0.5}\text{Pb}_{1.2}\text{Nb}_3\text{O}_z$
$\text{HCa}_{0.5}\text{Pb}_{1.5}\text{Nb}_3\text{O}_{10}^a$	-	2.87	35.82	37.42	$\text{HyCa}_{0.5}\text{Pb}_{1.3}\text{Nb}_3\text{O}_z$
$\text{TBA}_{1-y}\text{HyCa}_{0.5}\text{Pb}_{1.5}\text{Nb}_3\text{O}_{10}^a$	-	2.46	25.15	32.72	$\text{TBA}_{1-y}\text{HyCa}_{0.5}\text{Pb}_{1.1}\text{Nb}_3\text{O}_z$
$\text{RbPb}_2\text{Nb}_3\text{O}_{10}$	9.80	-	32.72	33.32	$\text{RbCa}_{0.0}\text{Pb}_{1.3}\text{Nb}_3\text{O}_z$
$\text{HPb}_2\text{Nb}_3\text{O}_{10}^a$	-	-	35.94	38.10	$\text{HyCa}_{0.0}\text{Pb}_{1.3}\text{Nb}_3\text{O}_z$
$\text{TBA}_{1-y}\text{HyPb}_2\text{Nb}_3\text{O}_{10}^a$	-	-	32.82	34.11	$\text{TBA}_{1-y}\text{HyCa}_{0.0}\text{Pb}_{1.3}\text{Nb}_3\text{O}_z$

<sup>a</sup> Note that neither the H and O content, nor the amount of  $\text{TBA}^+$  can be determined *via* ICP-AES

**Table S3.1.2:** EDX data for weighted samples  $\text{RbCa}_{2-x}\text{Pb}_x\text{Nb}_3\text{O}_{10}$ , their cation-proton exchanged forms  $\text{HCa}_{2-x}\text{Pb}_x\text{Nb}_3\text{O}_{10}$  both conducted on the SEM-EDX and for the separated nanosheets  $\text{TBA}_{1-y}\text{H}_y\text{Ca}_{2-x}\text{Pb}_x\text{Nb}_3\text{O}_{10}$  conducted on the TEM-EDX with  $x = 0, 0.5, 1.0, 1.5, 2.0$ . The theoretical expected formula is listed along with the analytical values given in at% as average of at least 3 measurements, as well as the resulting experimental formula.

Theoretical Formula	Rb	Ca	Pb	Nb	O	Experimental Formula
$\text{RbCa}_2\text{Nb}_3\text{O}_{10}$	6.66	12.60	-	18.17	62.57	$\text{Rb}_{1.1}\text{Ca}_{2.1}\text{Pb}_{0.0}\text{Nb}_3\text{O}_{10.3}$
$\text{HCa}_2\text{Nb}_3\text{O}_{10}^{\text{a}}$	0.2	11.20	-	18.27	70.33	$\text{H}_y\text{Ca}_{1.9}\text{Pb}_{0.0}\text{Nb}_3\text{O}_{11.5}$
$\text{TBA}_{1-y}\text{H}_y\text{-Ca}_2\text{Nb}_3\text{O}_{10}^{\text{a}}$	-	10.74	-	24.77	64.49	$\text{TBA}_{1-y}\text{H}_y\text{-Ca}_{1.3}\text{Pb}_{0.0}\text{Nb}_3\text{O}_{7.80}$
$\text{RbCa}_{1.5}\text{Pb}_{0.5}\text{Nb}_3\text{O}_{10}$	6.84	8.39	1.32	16.52	66.93	$\text{Rb}_{1.2}\text{Ca}_{1.5}\text{Pb}_{0.2}\text{Nb}_3\text{O}_{12.2}$
$\text{HCa}_{1.5}\text{Pb}_{0.5}\text{Nb}_3\text{O}_{10}^*$	-	8.41	1.11	16.55	73.93	$\text{H}_y\text{Ca}_{1.5}\text{Pb}_{0.2}\text{Nb}_3\text{O}_{13.4}$
$\text{TBA}_{1-y}\text{H}_y\text{-Ca}_{1.5}\text{Pb}_{0.5}\text{Nb}_3\text{O}_{10}^{\text{a}}$	-	9.02	3.17	27.68	60.13	$\text{TBA}_{1-y}\text{H}_y\text{-Ca}_{1.0}\text{Pb}_{0.3}\text{Nb}_3\text{O}_{6.50}$
$\text{RbCaPbNb}_3\text{O}_{10}$	6.25	6.32	3.52	16.76	67.15	$\text{Rb}_{1.1}\text{Ca}_{1.1}\text{Pb}_{0.6}\text{Nb}_3\text{O}_{12.0}$
$\text{HCaPbNb}_3\text{O}_{10}^{\text{a}}$	-	6.96	3.50	18.37	71.17	$\text{H}_y\text{Ca}_{1.1}\text{Pb}_{0.6}\text{Nb}_3\text{O}_{11.6}$
$\text{TBA}_{1-y}\text{H}_y\text{-CaPbNb}_3\text{O}_{10}^{\text{a}}$	-	5.78	4.06	20.87	69.29	$\text{TBA}_{1-y}\text{H}_y\text{-Ca}_{0.8}\text{Pb}_{0.6}\text{Nb}_3\text{O}_{10}$
$\text{RbCa}_{0.5}\text{Pb}_{1.5}\text{Nb}_3\text{O}_{10}$	6.64	2.70	5.85	16.09	68.72	$\text{Rb}_{1.2}\text{Ca}_{0.5}\text{Pb}_{1.1}\text{Nb}_3\text{O}_{12.8}$
$\text{HCa}_{0.5}\text{Pb}_{1.5}\text{Nb}_3\text{O}_{10}^{\text{a}}$	-	3.32	5.97	17.87	72.84	$\text{H}_y\text{Ca}_{0.6}\text{Pb}_{1.0}\text{Nb}_3\text{O}_{12.2}$
$\text{TBA}_{1-y}\text{H}_y\text{-Ca}_{0.5}\text{Pb}_{1.5}\text{Nb}_3\text{O}_{10}^{\text{a}}$	-	1.31	1.67	10.60	86.42	$\text{TBA}_{1-y}\text{H}_y\text{-Ca}_{0.4}\text{Pb}_{0.5}\text{Nb}_3\text{O}_{24.5}$
$\text{RbPb}_2\text{Nb}_3\text{O}_{10}$	6.88	-	8.93	17.57	66.62	$\text{Rb}_{1.2}\text{Ca}_{0.0}\text{Pb}_{1.5}\text{Nb}_3\text{O}_{11.4}$
$\text{HPb}_2\text{Nb}_3\text{O}_{10}^{\text{a}}$	-	-	8.52	19.60	71.88	$\text{H}_y\text{Ca}_{0.0}\text{Pb}_{1.3}\text{Nb}_3\text{O}_{11.0}$
$\text{TBA}_{1-y}\text{H}_y\text{-Pb}_2\text{Nb}_3\text{O}_{10}^{\text{a,b}}$	-	-	-	-	-	-

<sup>a</sup> Note that neither the H, nor the amount of  $\text{TBA}^+$  can be determined *via* EDX

<sup>b</sup> Due to the lack of material EDX yielded too less counts for element identification

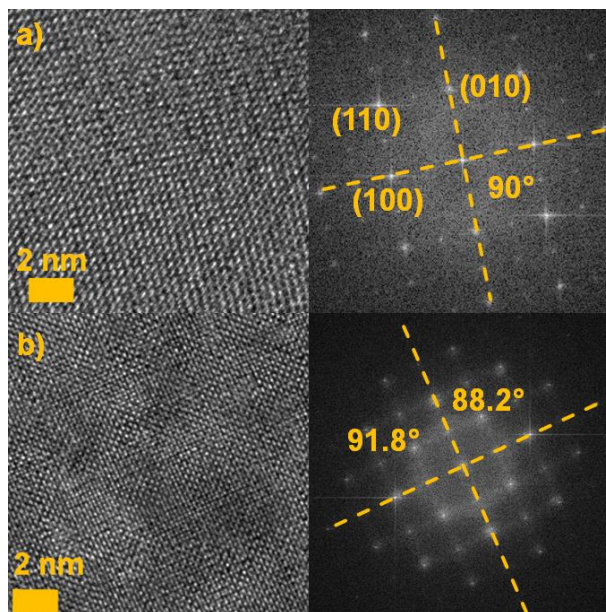


**Figure S3.1.3:** HRTEM images and corresponding FFTs of a) RbCa<sub>2</sub>Nb<sub>3</sub>O<sub>10</sub> and b) RbPb<sub>2</sub>Nb<sub>3</sub>O<sub>10</sub>.

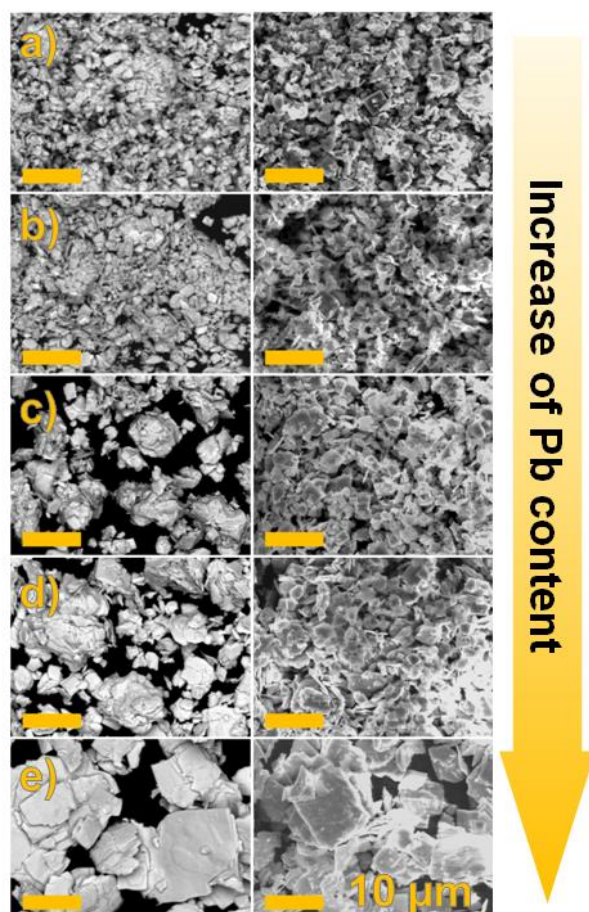


**Figure S3.1.4:** SEM images of RbCa<sub>2-x</sub>Pb<sub>x</sub>Nb<sub>3</sub>O<sub>10</sub> (right) and cation-proton exchanged HCa<sub>2-x</sub>Pb<sub>x</sub>Nb<sub>3</sub>O<sub>10</sub> (left) for x = a) 0, b) 0.5, c) 1.0, d) 1.5 and e) 2.0 showing larger platelets with increasing Pb content.



**Table S3.1.3:** Maxima of vibrational Raman bands found for  $\text{RbCa}_{2-x}\text{Pb}_x\text{Nb}_3\text{O}_{10}$  (1)-(5) and corresponding  $\text{HCa}_{2-x}\text{Pb}_x\text{Nb}_3\text{O}_{10}$  (1H)-(5H) in the region of  $1050\text{-}350\text{ cm}^{-1}$  with  $x = 0, 0.5, 1.0, 1.5, 2.0$ . All frequencies are given in  $\text{cm}^{-1}$ .

	$x = 0$	$x = 0.5$	$x = 1.0$	$x = 1.5$	$x = 2.0$
(1.1)	940	939	937	937	936
(1.2)	-	910	910	905	904
(1.3)	-	-	878	878	878
(1H)	990/961	987	983/928	977/942	973/926
(2)	761	751	728	700	674
(2H)	770	759	733	704	725/679
(3)	580	579	577	565	582/547
(3H)	575	575	567	555	593/537
(4)	501	490	479	465	448
(4H)	499	491	481	464	442
(5)	457	453	391	391	387
(5H)	459	456	438	395	388

Raman data is shown in Figure 3.1.6 and Table S3.1.3 and evaluated in the main manuscript. Additional information is given in the following. The assignment of the vibrational modes of our material is based on a comprehensive Raman study of several niobium oxides by Jehng and Wachs.<sup>7</sup> We further refer to systematic studies by Byeon and co-workers<sup>8-10</sup> dealing with the structurally related  $\text{A}_2\text{La}_2\text{Ti}_3\text{O}_{10}$  ( $M = \text{Li, Na, K, Rb}$ ) and their relation to  $\text{ACa}_2\text{Nb}_3\text{O}_{10}$  ( $A = \text{Na, K, Rb, Cs}$ ), including a detailed investigation of the solid solutions between the end members of both, and a normal coordinate analysis of Nozaki *et al.*<sup>11</sup>

Associated Raman bands (1.1) for  $\text{ACa}_2\text{Nb}_3\text{O}_{10}$  ( $A = \text{Na, K, Rb, Cs}$ ) as well as the ones for  $\text{CsM}_2\text{Nb}_3\text{O}_{10}$  ( $M = \text{Ca, Sr, Ba}$ ), regardless of the change of  $A$  or  $M$ , were reported to maintain their position since the A-O-Nb linkage is not influenced by cation substitution.<sup>9-10</sup> On the contrary, moving from  $\text{RbLa}_{2-x}\text{Ca}_x\text{Ti}_{2-x}\text{Nb}_{1+x}\text{O}_{10}$  ( $2 \geq x \geq 0$ ) to  $\text{Rb}_{2-x}\text{La}_2\text{Ti}_{3-x}\text{Nb}_x\text{O}_{10}$  ( $1 \geq x \geq 0$ ), a shift of Raman band (1.1) from  $\sim 930\text{ cm}^{-1}$  down to  $867\text{ cm}^{-1}$  is observed because of a structurally introduced linear Rb-Ti-O linkage.<sup>10</sup> The bands at  $904\text{ cm}^{-1}$  (1.2) and  $878\text{ cm}^{-1}$  (1.3) fall in between these two boundaries. Hence, the additional intergrowth phase evolves towards a linear Rb-O-Nb linkage. If a Pb deficient  $[\text{Nb}_3\text{O}_8]^-$  motif is integrated in four different orientations in the perovskite matrix, this seems to be the reason for the split of Raman band (1.1).

Cation-proton exchange of  $\text{RbCa}_{2-x}\text{Pb}_x\text{Nb}_3\text{O}_{10}$  ( $x = 0, 0.5, 1.0, 1.5, 2.0$ ) has a direct influence on the Raman band (1.1) due to association of the proton with the terminal oxygen atoms.<sup>7</sup> Hence, a broadening as well as a shift and a splitting of the Raman band is observed for (1H) of  $\text{HCa}_2\text{Nb}_3\text{O}_{10}$ . Consequently, we also observe a shift and broadening of (1.2) and (1.3) for  $\text{RbPb}_2\text{Nb}_3\text{O}_{10}$  after the cation-proton exchange proving that vibrations (1.2) and (1.3) belong

to terminal Nb=O vibrations. Instead of several split bands a broad reflection with two shoulders becomes apparent.

Regarding Raman Band (2) Jehng and Wachs determined between inner and outer NbO<sub>6</sub> octahedra by taking the ratio of the integrated Raman intensity of the bands  $I(1)/I(2)$ . They found a 2:1 ratio reflecting the ratio of inner to outer octahedra as can be seen in Figure 3.1.1 a).<sup>7</sup> For RbCa<sub>2-x</sub>Pb<sub>x</sub>Nb<sub>3</sub>O<sub>10</sub> the Raman band is shifted towards 674 cm<sup>-1</sup> and the overlap with Raman band (3)-(5) as well as a shoulder at higher wavenumbers becomes a major issue and makes integrating challenging. We used a Voigt function to fit the Raman bands as it accounts Doppler (Gaussian) and Stark (Lorentz) broadening of the line profiles. Nevertheless, for a proper fit of the Voigt function neighboring Raman bands should be sufficiently separated. Hence, the given ratios given in the main manuscript are interpreted rather as trend than absolute values.

For Raman band (3) around 580 cm<sup>-1</sup> there are contrary opinions whether this vibration is associated with the highly distorted Nb(2)O<sub>6</sub> outer octahedra or the slightly distorted Nb(1)O<sub>6</sub> inner octahedra. Byeon *et al.* assigned the Raman band to the outer octahedral, deriving their interpretation from the comparison of ALaNb<sub>2</sub>O<sub>7</sub> (A = Na, K, Rb, Cs), having only highly distorted outer octahedral, and ACa<sub>2</sub>Nb<sub>3</sub>O<sub>10</sub>. For ALaNb<sub>2</sub>O<sub>7</sub> Raman band (2) was not observed, whereas Raman band (3) was present in both. Hence, they concluded that it must belong to the Nb(2)O<sub>6</sub> outer octahedra.<sup>9</sup> Jehng and Wachs linked the Raman band to the inner octahedra due to the area ratio of the bands compared to each other.<sup>7</sup> This is further supported by the normal coordinate analysis of Nozaki *et al.*<sup>11</sup> We attributed Raman band (3) to the Nb(2)O<sub>6</sub> inner octahedra, since Raman band (3H) does not show any significant shift after cation-proton exchange

Raman bands (4), (5) and (4H), (5H), respectively, seem to belong to the inner octahedra, too. Since they are less intense, no additional information was maintained from analysis of these vibrational modes.

IR absorption spectra of RbCa<sub>2-x</sub>Pb<sub>x</sub>Nb<sub>3</sub>O<sub>10</sub> and HCa<sub>2-x</sub>Pb<sub>x</sub>Nb<sub>3</sub>O<sub>10</sub> (x = 0, 0.5, 1.0, 1.5, 2.0) are shown in Figure S3.1.5. IR spectroscopy is complementary to Raman spectroscopy and can also give structural insights. For example phase transitions in BaTiO<sub>3</sub> and related materials like LiNbO<sub>3</sub> and KNbO<sub>3</sub> was probed with IR spectroscopy.<sup>12</sup> To the best of our knowledge IR spectroscopy has not been applied to probe structural changes in Dion Jacobson phases until now. Only exchange of interlayer ions against organic cations or bases was monitored *via* IR spectroscopy.<sup>13</sup> Hence, little is known about the investigated and related systems. On the basis of Raman spectroscopy we find similar characteristics in the IR spectra. A strong band around 910 cm<sup>-1</sup> for RbCa<sub>2</sub>Nb<sub>3</sub>O<sub>10</sub> (930 cm<sup>-1</sup> in Raman) splits into 3-4 bands for RbPb<sub>2</sub>Nb<sub>3</sub>O<sub>10</sub>. A new band at 797 cm<sup>-1</sup> is found that might belong to a

vibrational mode where O(2) and O(4) move in the opposite direction than the O(3)s. This mode was reported to be Raman active by Nozaki *et al.* but is barely seen in the Raman spectra.<sup>11</sup> 765 cm<sup>-1</sup> (761 cm<sup>-1</sup> in Raman) as well as the band around 797 cm<sup>-1</sup> disappear with increasing lead content and seem to become inactive for IR spectroscopy. Hence, a change in structure is indicated. Vibrations at 567 cm<sup>-1</sup> and 537 cm<sup>-1</sup> most likely belong to Raman bands (3) and (4), whereas two new bands are found at 476 cm<sup>-1</sup> and 454 cm<sup>-1</sup>. When exchanging Rb<sup>+</sup> against H<sup>+</sup> the vibrational mode at 910 cm<sup>-1</sup> is largely influenced since the Nb(2)-O(4) stretching mode is largely dependent on the interlayer ion. Vibrational modes at lower wavenumbers are as well found at the approximately same position. Similar to Raman spectroscopy IR spectra become less distinguishable with increasing lead content for the cation-proton exchanged form.

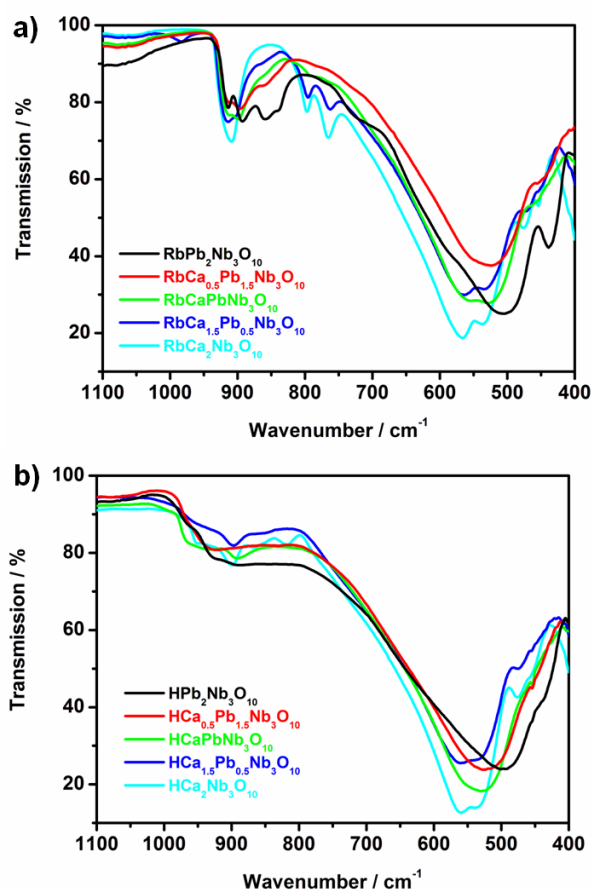


**Figure S3.1.5:** IR absorption spectra of a) RbCa<sub>2-x</sub>Pb<sub>x</sub>Nb<sub>3</sub>O<sub>10</sub> and b) HCa<sub>2-x</sub>Pb<sub>x</sub>Nb<sub>3</sub>O<sub>10</sub> with  $x = 0, 0.5, 1.0, 1.5$  and  $2.0$ .

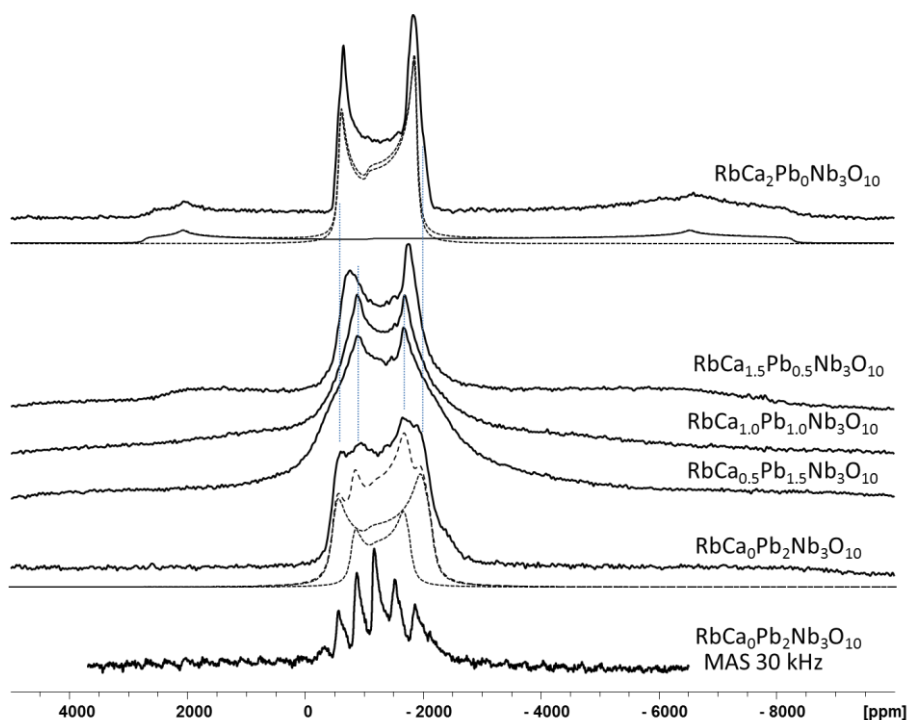


**Figure S3.1.6:** Experimental  $^{93}\text{Nb}$  solid state NMR spectra of the series  $\text{RbCa}_{2-x}\text{Pb}_x\text{Nb}_3\text{O}_{10}$  ( $x = 0, 0.5, 1.0, 1.5, 2.0$ ) acquired with VOCS (10 offsets) and MAS (only for  $\text{RbCa}_0\text{Pb}_2\text{Nb}_3\text{O}_{10}$ , bottom spectrum), shown with corresponding simulations. The vertical dotted lines only for guiding an eye, and point into singularities of the two Nb sites in the lead loaded materials.

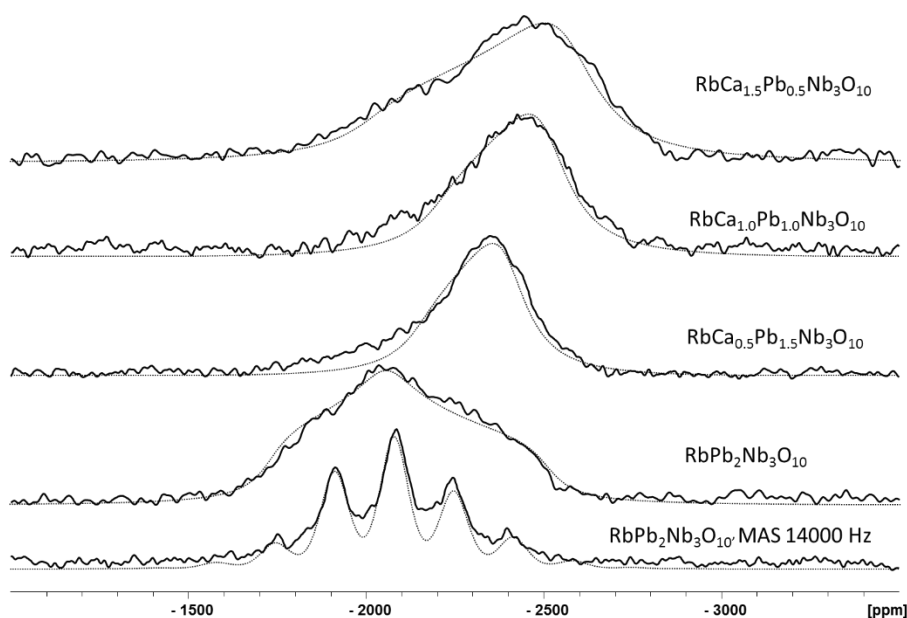


**Figure S3.1.7:** Experimental  $^{207}\text{Pb}$  solid state NMR spectra of the series  $\text{RbCa}_{2-x}\text{Pb}_x\text{Nb}_3\text{O}_{10}$  ( $x = 0, 0.5, 1.0, 1.5, 2.0$ ) acquired with Hahn-echo and MAS (only for  $\text{RbCa}_0\text{Pb}_2\text{Nb}_3\text{O}_{10}$ , bottom spectrum), shown with corresponding simulations.

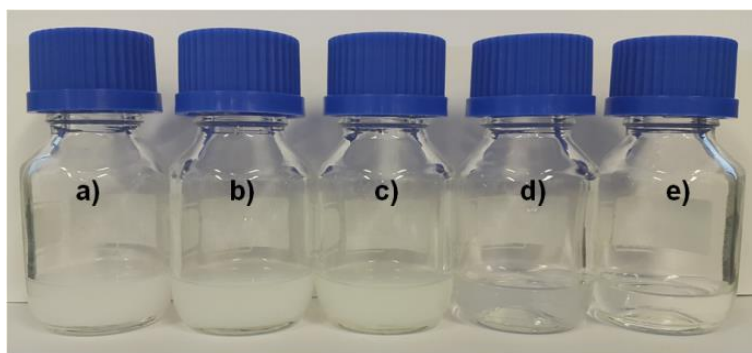


**Figure S3.1.8:** Image of colloidal suspensions of  $TBA_{1-y}HyCa_{2-x}Pb_xNb_3O_{10}$  after centrifugation at 3000 rpm for  $x =$  a) 0, b) 0.5, c) 1.0, d) 1.5 and e) 2.0.

**Table S3.1.4:** Several lattice parameters for  $TBA_{1-y}HyCa_{2-x}Pb_xNb_3O_{10}$  nanosheets and angle between directions as average out of 3-5 SAED patterns

Theoretical Formula	A	B	C	D	E
$TBA_{1-y}HyCa_2Pb_0Nb_3O_{10}$	3.79 Å	2.68 Å	1.90 Å	1.70 Å	1.34 Å
$TBA_{1-y}HyCa_{1.5}Pb_{0.5}Nb_3O_{10}$	3.80 Å	2.70 Å	1.91 Å	1.70 Å	1.35 Å
$TBA_{1-y}HyCaPbNb_3O_{10}$	3.84 Å	2.70 Å	1.93 Å	1.72 Å	1.36 Å
$TBA_{1-y}HyCa_{0.5}Pb_{1.5}Nb_3O_{10}$	3.84 Å	2.72 Å	1.93 Å	1.72 Å	1.36 Å
$TBA_{1-y}HyCa_0Pb_2Nb_3O_{10}$	3.82 Å	2.71 Å	1.91 Å	1.71 Å	1.35 Å

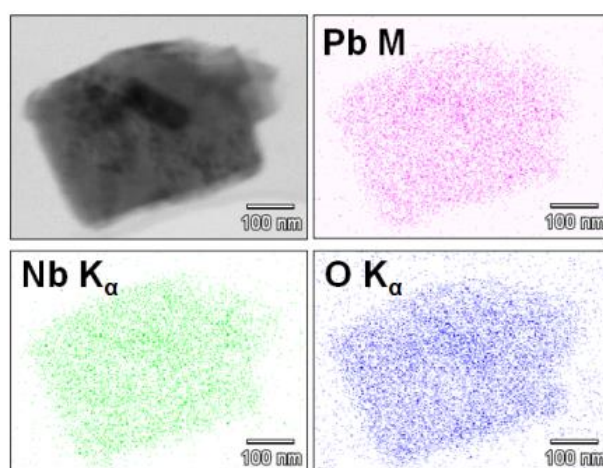


**Figure S3.1.9:** EDX mapping of a  $TBA_{1-y}HyRb_2Nb_3O_{10}$  nanosheets showing homogeneous distribution of all elements. Pb M, Nb K $_{\alpha}$  and O K $_{\alpha}$  were measured.

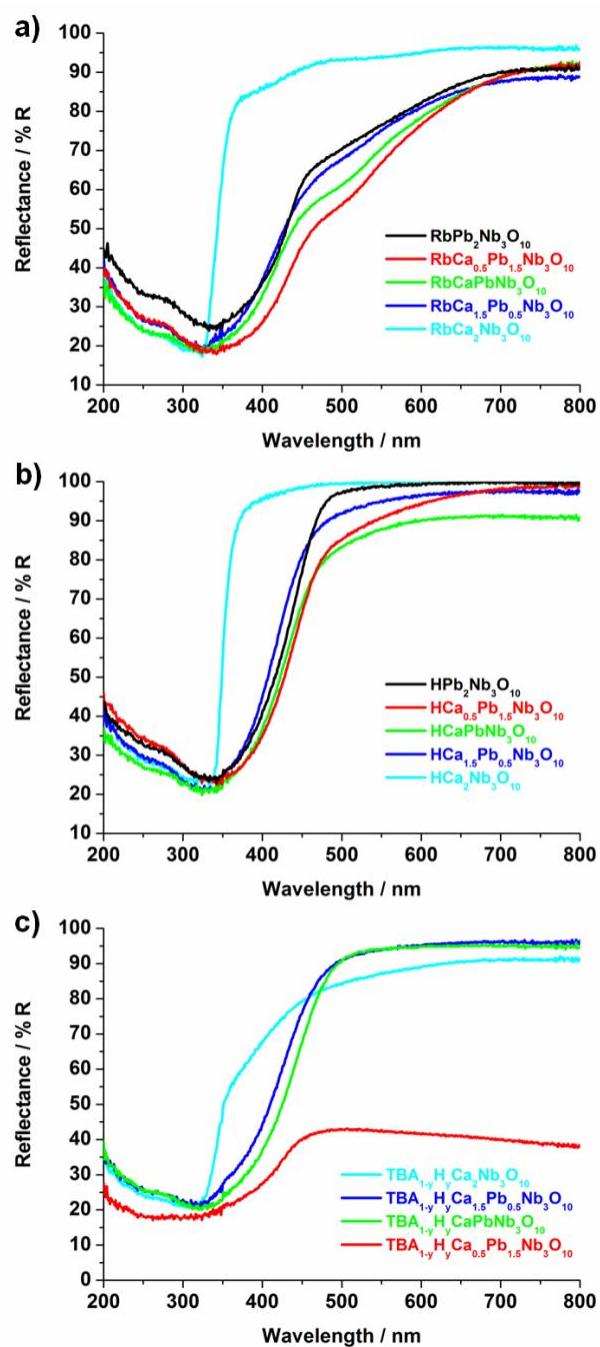


**Figure S3.1.10:** UV-VIS spectra of a)  $\text{RbCa}_{2-x}\text{Pb}_x\text{Nb}_3\text{O}_{10}$  b)  $\text{HCa}_{2-x}\text{Pb}_x\text{Nb}_3\text{O}_{10}$  and c)  $\text{TBA}_{1-y}\text{H}_y\text{Ca}_{2-x}\text{Pb}_x\text{Nb}_3\text{O}_{10}$  for  $x =$  a) 0, b) 0.5, c) 1.0, d) 1.5 and e)  $x = 2.0$ .

- [1] M. Dion, M. Ganne, M. Tournoux, *Mater. Res. Bull.* **1981**, 16, 1429-1435.
- [2] J. Yoshimura, Y. Ebina, J. Kondo, K. Domen, A. Tanaka, *J. Phys. Chem.* **1993**, 97, 1970-1973.
- [3] Y. Hu, J. Shi, L. Guo, *Appl. Catal., A* **2013**, 468, 403-409.
- [4] R. K. Harris, E. D. Becker, S. M. Cabral De Menezes, P. Granger, R. E. Hoffman, K. W. Zilm, *Solid State Nucl. Magn. Reson.* **2008**, 33, 41-56.
- [5] D. Massiot, I. Farnan, N. Gautier, D. Trumeau, A. Trokiner, J. P. Coutures, *Solid State Nucl. Magn. Reson.* **1995**, 4, 241-248.
- [6] B. Alonso, J.-O. Durand, B. Bujoli, Z. Gan, G. Hoatson, *Magn. Reson. Chem* **2002**, 40, 70-76.
- [7] J. M. Jehng, I. E. Wachs, *Chem. Mater.* **1991**, 3, 100-107.
- [8] S.-H. Byeon, S.-O. Lee, H. Kim, *J. Solid State Chem.* **1997**, 130, 110-116.
- [9] S.-H. Byeon, H.-J. Nam, *Chem. Mater.* **2000**, 12, 1771-1778.
- [10] H. J. Kim, S.-H. Byeon, H. Yun, *Bull. Korean Chem. Soc.* **2001**, 22, 298-302.
- [11] R. Nozaki, J. N. Kondo, C. Hirose, K. Domen, A. Wada, Y. Morioka, *J. Phys. Chem. B* **2001**, 105, 7950-7953.
- [12] J. T. Last, *Physical Review* **1957**, 105, 1740-1750.
- [13] A. Shimada, Y. Yoneyama, S. Tahara, P. H. Mutin, Y. Sugahara, *Chem. Mater.* **2009**, 21, 4155-4162.

## 3.2 Structural Investigations on New Niobate Nanosheet Phosphors

Christian Ziegler, Laura Kohout, Stephanie Linke, Matthieu Bugnet, Viola Duppel,  
Gianluigi A. Botton, Christina Scheu, Bettina V. Lotsch

*Unpublished results.*

**ABSTRACT:** Luminescent nanosheets with high photoactivator concentration are promising candidates for optical devices because of their two-dimensional (2D) morphology, an efficient host to activator energy transfer, and their high luminescence intensities. Here, we systematically investigated a series of Dion-Jacobson (DJ) type  $K_{1-x}Ca_{2-x}Ln_xNb_3O_{10}$  ( $x = 0.05, 0.25, 0.50, 0.75$ ;  $Ln = La, Pr, Nd, Sm, Eu, Gd, Dy, Ho, Er, Tm, Yb$ ) layered perovskites, where the intrananosheet photoactivator concentration can be tuned by increasing levels of rare earth dopant. Exfoliation *via* a cation-proton exchange and subsequent treatment with tetra-*n*-butylammonium hydroxide (TBAOH) showed that only up to 20 at% of the rare earth ions can be incorporated into the host matrices during bulk synthesis. These findings also hold for the structurally similar  $Rb_{1-x}Sr_{2-x}Ln_xNb_3O_{10}$  ( $Ln = La, Eu, Er$ ) where 10 at% rare earth ions can be incorporated. Consequently, the structural evolution of  $K_{1-x}Ca_{2-x}Ln_xNb_3O_{10}$  is evaluated for the  $Eu^{3+}$  series and a possible miscibility gap is proposed.  $Eu^{3+}$ ,  $Sm^{3+}$  and mixed valence  $Pr^{3+/4+}$  containing nanosheets showed red,  $Dy^{3+}$  containing yellow and  $Er^{3+}$  modified materials green emission under excitation at  $\lambda = 366$  nm, and are therefore promising candidates for nanosheet-based lightning applications.

### 3.2.1 Introduction

In the last decade, nanosheet-based phosphors exfoliated from (doped) layered transition metal oxides (TMOs) opened up a field in the design of new types of phosphor materials.<sup>1-9</sup> With a height around ~1 nm and a lateral size in the micrometer-regime, nanosheets offer a unique 2D morphology that has certain advantages over that of their bulk counterparts.<sup>10-11</sup> For example, their large surface area enables nanosheets to efficiently absorb excitation energy and relatively high concentrations of photoactivators can be incorporated into a 2D host without diminishment of emission intensity by cross relaxation processes.<sup>3, 5, 7</sup> Additionally, several studies showed that photoluminescence emissions from rare earth photoactivated TMO nanosheets are rather dominated by host excitation than by direct rare earth photoactivator excitation.<sup>10</sup> Hence, the optimum excitation wavelength can be exclusively adjusted by an appropriate choice of host material for intended applications. Table 3.2.1 lists, to the best of our knowledge, all layered TMO-based photoluminescent nanosheets that have been synthesized up to now. Besides the blue emitting



$EA_{1.12}Bi_{0.16}Sr_{0.75}Ta_2O_7$ <sup>1</sup> ( $EA$  = ethylamine) which exhibits photoluminescence itself, all other nanosheets show photoluminescence due to the insertion of rare earth ions. A green emission is found for the compounds doped with  $Tb^{3+}$ , whereas red emissions are obtained by inserting  $Eu^{3+}$  or  $Sm^{3+}$  into the nanosheet host.  $EA_2Gd_{1.4}Eu_{0.6}Ti_3O_{10}$  nanosheets are an interesting example for an energy transfer cascade from the Ti-O network of the nanosheet to  $Gd^{3+}$  and then to  $Eu^{3+}$ , yielding a higher luminescence intensity of the phosphor and further extend the possibilities of material design.<sup>4</sup>

**Table 3.2.1:** Overview of layered bulk TMO based phosphors that have been exfoliated into photoluminescent nanosheets either with  $EA$  or  $TBAOH$  as exfoliation agent.

<b>Red Phosphors</b>	$KLa_{0.90}Eu_{0.05}Nb_2O_7$ to $TBALa_{0.90}Eu_{0.05}Nb_2O_7$ <sup>2</sup> $Li_2Eu_{0.56}Ta_2O_7$ to $TBA_2Eu_{0.56}Ta_2O_7$ <sup>3</sup> $KLa_{0.95}Eu_{0.05}Nb_2O_7$ , $RbLa_{0.95}Eu_{0.05}Ta_2O_7$ , $K_2Ln_{1.9}Eu_{0.1}Ti_3O_{10}$ ( $Ln = La, Tb$ ) and $K_2Gd_{2-x}Eu_xTi_3O_{10}$ ( $x = 0, 0.02, 0.04, 0.1, 0.2, 0.6, 1, 2$ ) all to $EA$ -TMOs <sup>4</sup> $K(K_{1.5}Eu_{0.5})Ta_3O_{10}$ to $TBA(K_{1.5}Eu_{0.5})Ta_3O_{10}$ <sup>5</sup> $KLa_{0.90}Sm_{0.05}Nb_2O_7$ to $TBALa_{0.90}Sm_{0.05}Nb_2O_7$ <sup>6</sup> $Li_2La_{2/3-x}Eu_xTa_2O_7$ to $TBA_2La_{2/3-x}Eu_xTa_2O_7$ <sup>7</sup>
<b>Green Phosphors</b>	$RbLa_{1-x}Tb_xTa_2O_7$ ( $x = 0.01, 0.05, 0.30, 0.50, 1.00$ ) to $EALa_{1-x}Tb_xTa_2O_7$ <sup>4</sup> $CsCa_{2-x}Tb_xTa_3O_{10}$ ( $x = 0.001-0.1$ ) to $TBACa_{2-x}Tb_xTa_3O_{10}$ <sup>9</sup>
<b>Blue Phosphors</b>	$Bi_2SrTa_2O_9$ to $EA_{1.12}Bi_{0.16}Sr_{0.75}Ta_2O_7$ <sup>1</sup> $KLa_{0.90}Dy_{0.05}Nb_2O_7$ to $TBALa_{0.90}Dy_{0.05}Nb_2O_7$ <sup>8</sup>

These options can be further extended by the most intriguing property of nanosheets, the possibility to use them as building blocks for the fabrication of hybrid materials with tailor-made properties based on their assembly *via* various layer-by-layer (LBL) techniques.<sup>10-11</sup> Such and related approaches allow to overcome thermodynamic constraints due to the high temperatures usually used for solid-state synthesis and, hence, open up pathways to new functional materials.<sup>10-11</sup> In a typical experiment a colloidal suspension of negatively charged nanosheets, e.g.  $Ti_{0.91}O_2^-$ ,  $Ti_4O_9^{2-}$ ,  $Nb_6O_{17}^{4-}$  etc., are either flocculated with dissolved rare earth ions or stacked in a LBL fashion by dipping a substrate alternately into both suspensions/solutions.<sup>12-17</sup> This rather straightforward procedure was recently used to fabricate a new upconversion material by flocculation of calcium niobate with rare earth salts yielding  $(Ho_{0.096}Yb_{0.23}Y_{0.164})Ca_{1.76}\square_{0.24}Nb_3O_{10} \cdot 1.4H_2O$  ( $\square$  = vacancy) where  $Ho^{3+}$ ,  $Yb^{3+}$  and  $Y^{3+}$  act as photoactivator, sensitizer and space filler ions and the nanosheet as structural and thermal stabilizer.<sup>18</sup>

Above all these versatile pathways, it is possible to monitor the local atomic configuration for thin TMO-based nanosheets and to correlate e.g. concentration-based quenching effects to structural arrangements. Recently, Ida and co-workers determined the photofunctional centers in  $TBACa_{2-x}Tb_xTa_3O_{10}$  with the help of high-angle annular dark-field scanning

transmission electron microscopy (HAADF-STEM) and found that no concentration-based quenching was observed even for centers lying in close proximity to each other.<sup>9</sup> Thus, nanosheets can play a crucial role in order to understand fundamental properties of light-energy-converting materials, which demonstrates the need for extension of the currently restricted nanosheet library.

Our study focuses on the synthesis, rare earth doping and substitution, subsequent exfoliation and structural evaluation of one of the most prominent bulk materials for the fabrication of oxide nanosheets,  $\text{KCa}_2\text{Nb}_3\text{O}_{10}$ .<sup>19</sup> First studies of doping  $\text{La}^{3+}$  and  $\text{Eu}^{3+}$  into  $\text{KCa}_2\text{Nb}_3\text{O}_{10}$  and its cation-proton exchanged form  $\text{HCa}_2\text{Nb}_3\text{O}_{10}$  revealed that both systems are excellent hosts for these photoactivators.<sup>20-21</sup> Secondly, it was reported that  $\text{K}_{1-x}\text{Ca}_{2-x}\text{La}_x\text{Nb}_3\text{O}_{10}$  is a layered perovskite series with variable inter- (K) and intralayer (La) cation density, thus enabling the tuning of the rare earth element to an optimal photoactivator concentration within the host.<sup>22</sup> A schematic drawing of both end-members is shown in Figure 3.2.1.

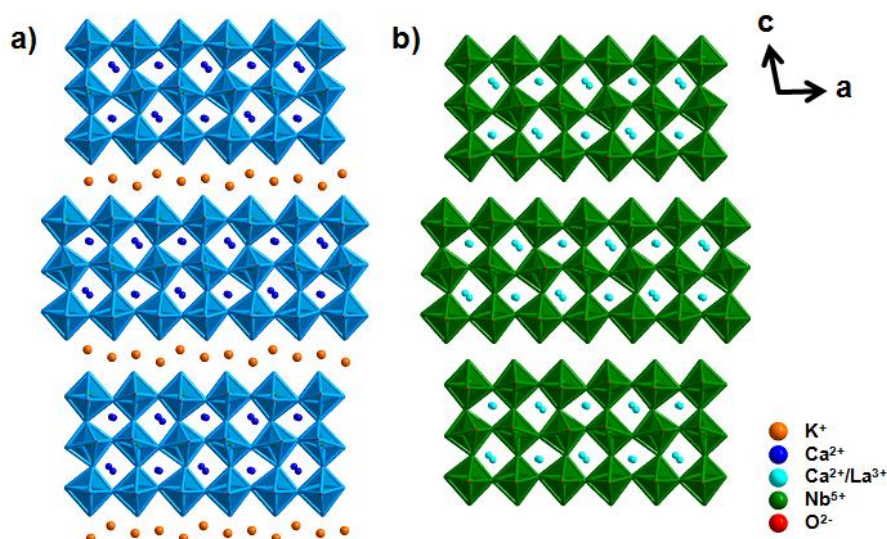


**Figure 3.2.1:** Schematic representation of end-members of  $\text{K}_{1-x}\text{Ca}_{2-x}\text{Ln}_x\text{Nb}_3\text{O}_{10}$  series: a)  $\text{KCa}_2\text{Nb}_3\text{O}_{10}$  and b)  $\text{CaLnNb}_3\text{O}_{10}$ .

$\text{KCa}_2\text{Nb}_3\text{O}_{10}$  has a monoclinic structure with space group  $P2_1/m$  as determined by neutron diffraction experiments.<sup>23</sup>  $\text{CaLaNb}_3\text{O}_{10}$  has been described as orthorhombic similar to the results of an early X-ray diffraction (XRD) structure refinement of  $\text{KCa}_2\text{Nb}_3\text{O}_{10}$  without specification of the space group.<sup>22</sup> Note that for the sake of simplicity a monoclinic cell instead of the assumed orthorhombic structure for  $\text{CaLaNb}_3\text{O}_{10}$  is shown in Figure 3.2.1. Within the  $\text{K}_{1-x}\text{Ca}_{2-x}\text{Ln}_x\text{Nb}_3\text{O}_{10}$  series, the  $\text{Ln}^{3+}$  ions can, in principle, replace the  $\text{K}^+$  ions located in the interlayer region as well as the  $\text{Ca}^{2+}$  located at the A position of the perovskite layer. It is found that that  $\text{Ln}^{3+}$  exchanges for the A position and, hence, decreases the

perovskite layer charge density successively with increasing  $x$ . In terms of structure, this means that in  $\text{KCa}_2\text{Nb}_3\text{O}_{10}$  and  $\text{LaCaNb}_3\text{O}_{10}$  the adjacent triple perovskite layer blocks are stacked with a displacement by  $a/2$  along the  $[110]$  direction and are bonded by weak van der Waals forces.<sup>21</sup> In contrast to literature reports, our findings indicate that a homogeneous perovskite series with variable interlayer cation density does not occur and provide evidence that only up to 20 at% rare earth element content can be incorporated into the  $[\text{Ca}_2\text{Nb}_3\text{O}_{10}]^-$  layers, decreasing the interlayer charge by 20% yielding  $\text{A}_{0.8}\text{Ln}_{0.2}\text{Ca}_{1.8}\text{Nb}_3\text{O}_{10}$  ( $A = \text{K, H, TBA}$ ) at maximum. Still, Eu, Sm, Pr, Dy and Er doped materials seem to be good photoactivators for niobate-based nanosheet phosphors. This finding also holds for the structurally similar  $\text{A}_{1-x}\text{Sr}_{2-x}\text{Ln}_x\text{Nb}_3\text{O}_{10}$  ( $A = \text{Rb, H, TBA, Ln} = \text{La, Eu, Er}$ ) system, where a maximum photoactivator concentration of 10 at% was observed for that case.

### 3.2.2 Results and Discussion

Figure 3.2.2 displays the XRD patterns for  $\text{K}_{1-x}\text{Ca}_{2-x}\text{Eu}_x\text{Nb}_3\text{O}_{10}$  ( $x = 0.05, 0.25, 0.50, 0.75$ ) in comparison with standard cards of  $\text{KCa}_2\text{Nb}_3\text{O}_{10}$ <sup>23</sup> and  $\text{CaLaNb}_3\text{O}_{10}$ <sup>22</sup>. For the sake of simplicity, we first comprehensively investigate the series  $\text{A}_{1-x}\text{Ca}_{2-x}\text{Eu}_x\text{Nb}_3\text{O}_{10}$  ( $A = \text{K, H, TBA}$ ) and subsequently discuss structural similarities and differences between distinct rare earth elements of the  $\text{A}_{1-x}\text{Ca}_{2-x}\text{Ln}_x\text{Nb}_3\text{O}_{10}$  ( $x = 0.05, 0.25, 0.50, 0.75, A = \text{K, H, TBA; Ln} = \text{La, Pr, Nd, Sm, Eu, Gd, Dy, Ho, Er, Tm, Yb}$ ) series (Figure S3.2.1-S3.2.4). The  $\text{Eu}^{3+}$  series was chosen because the bulk material is known to show the characteristic red emission of the  $\text{Eu}^{3+}$  ions due to an energy transfer between the host material and the  $\text{Eu}^{3+}$  dopant, whereas exfoliation into luminescent nanosheets has to the best of our knowledge not been reported yet.<sup>20</sup> Additional XRD data of the La series is evaluated in more detail as this is the only series where structural data of the end-members  $\text{KCa}_2\text{Nb}_3\text{O}_{10}$ <sup>23</sup> and  $\text{CaLaNb}_3\text{O}_{10}$ <sup>22</sup> were published before. XRD patterns of  $\text{K}_{1-x}\text{Ca}_{2-x}\text{La}_x\text{Nb}_3\text{O}_{10}$  ( $x = 0.05, 0.25, 0.50, 0.75$ ) are shown in Figure 3.2.3. As can be seen, the monoclinic  $P2_1/m$  structure of the parent compound  $\text{KCa}_2\text{Nb}_3\text{O}_{10}$  is almost maintained for  $x = 0.05$ .<sup>23</sup> Nevertheless, additional reflections - mainly the one at  $21^\circ 2\theta$  - become apparent. Bizeto *et al.* attributed this to minor structural modifications due to the rare earth dopant.<sup>20</sup> We find, however, that these reflections can also be due to the second prominent  $(211)$  reflection plane (and higher orders) of  $\text{Ca}_2\text{Nb}_2\text{O}_7$ , as most of the  $\text{Ca}_2\text{Nb}_2\text{O}_7$  reflections overlay with those from  $\text{KCa}_2\text{Nb}_3\text{O}_{10}$  and minor intense reflections vanish in the background.<sup>24</sup> With increasing rare earth content, the intensity of  $\text{KCa}_2\text{Nb}_3\text{O}_{10}$ -related reflections decreases, and new reflections arise and/or should shift towards the positions of the reflections of  $\text{CaLaNb}_3\text{O}_{10}$ , which is partly the case. Note that we did not synthesize the  $\text{CaLnNb}_3\text{O}_{10}$  end-members as the main goal was to investigate nanosheets derived from the interlayer exchange of  $\text{K}^+$  and subsequent exfoliation with the bulky organic cation  $\text{TBA}^+$ , which is not possible for the end-members.

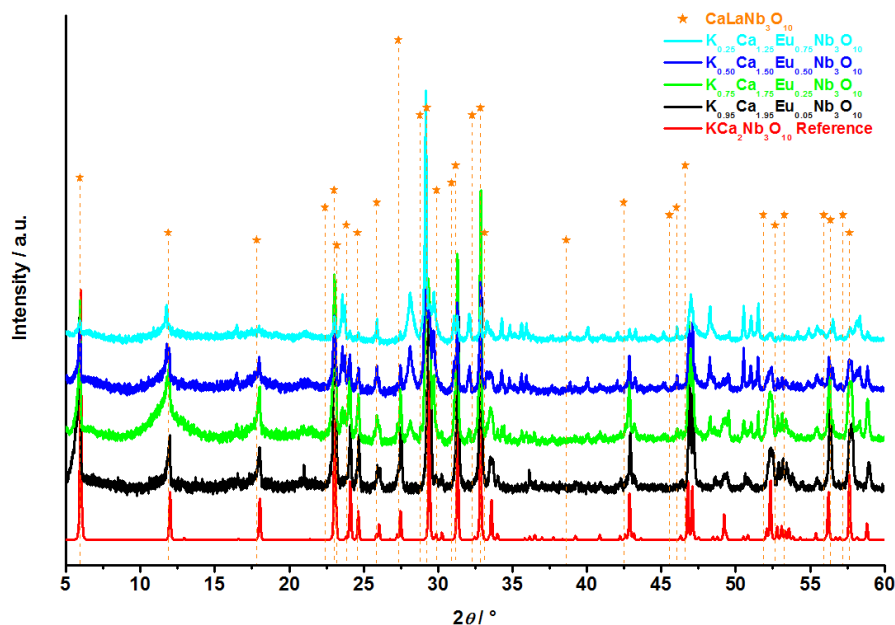


**Figure 3.2.2:** XRD patterns of  $K_{1-x}Ca_{2-x}Eu_xNb_3O_{10}$  ( $x = 0.05, 0.25, 0.50, 0.75$ ) in comparison with reference end-members  $KCa_2Nb_3O_{10}$  and  $CaLaNb_3O_{10}$ .<sup>22-23</sup>

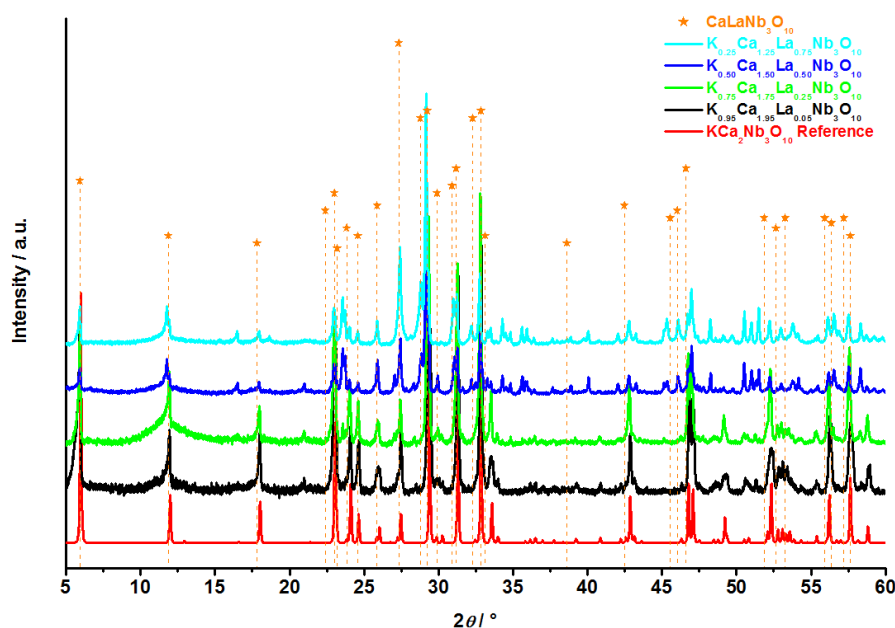


**Figure 3.2.3:** XRD patterns of  $K_{1-x}Ca_{2-x}La_xNb_3O_{10}$  ( $x = 0.05, 0.25, 0.50, 0.75$ ) in comparison with reference end-members  $KCa_2Nb_3O_{10}$  and  $CaLaNb_3O_{10}$ .<sup>22-23</sup>

Figure 3.2.4 highlights the XRD patterns of the more highly substituted  $K_{0.25}Ca_{1.25}La_{0.75}Nb_3O_{10}$  and  $K_{0.25}Ca_{1.25}Eu_{0.75}Nb_3O_{10}$  compared to  $KCa_2Nb_3O_{10}$ <sup>23</sup> and  $CaNb_2O_6$ <sup>25</sup>. The resulting rare earth containing  $K_{0.25}Ca_{1.25}Ln_{0.75}Nb_3O_{10}$  compounds can be described as a phase mixture consisting of  $KCa_2Nb_3O_{10}$ ,  $CaNb_2O_6$  and at least one additional phase that might be related to a rare earth containing compound (orange arrows). Neither

$\text{Ln}_2\text{O}_3$  reported as impurity phase by Huang *et al.*, nor  $\text{LnNbO}_4$  or other rare earth containing references of various databases matched these reflections.<sup>21</sup> As the reaction progress was not complete, we used various temperatures between 1100-1300°C for the  $\text{K}_{1-x}\text{Ca}_{2-x}\text{La}_x\text{Nb}_3\text{O}_{10}$  synthesis as suggested in the literature, and around 1200°C where we obtained phase pure  $\text{KCa}_2\text{Nb}_3\text{O}_{10}$ .<sup>20-22, 26</sup> For lower temperatures the formation of  $\text{Ca}_2\text{Nb}_2\text{O}_7$  was favored, whereas for higher temperatures  $\text{CaNb}_2\text{O}_6$  was observed as side phase. For none of the applied temperature profiles we obtained any phase-pure doped material and hence have no evidence of a homogeneous formation of a solid solution of the  $\text{A}_{1-x}\text{Ca}_{2-x}\text{Ln}_x\text{Nb}_3\text{O}_{10}$  series under these synthesis conditions.

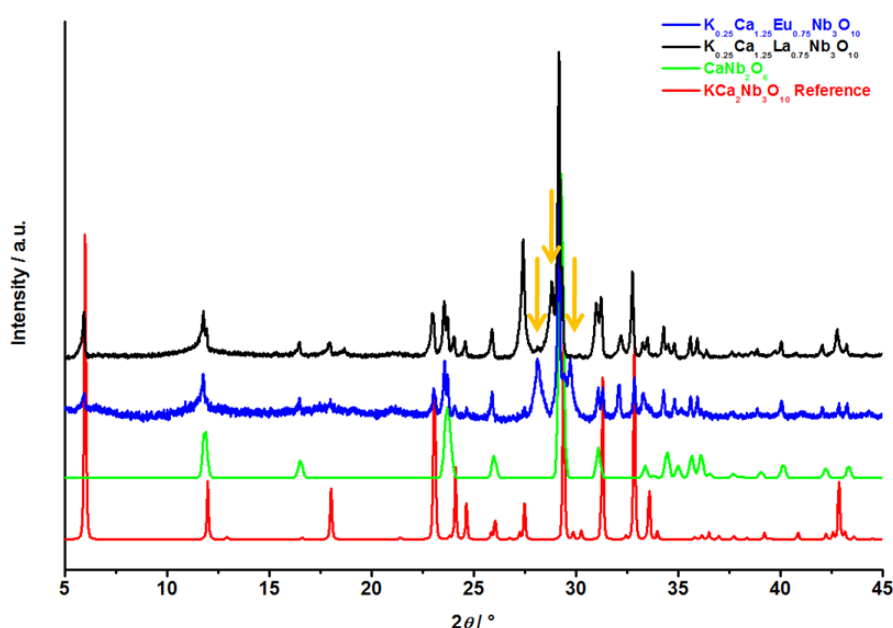


**Figure 3.2.4:** XRD patterns of  $\text{K}_{0.25}\text{Ca}_{1.25}\text{La}_{0.75}\text{Nb}_3\text{O}_{10}$  and  $\text{K}_{0.25}\text{Ca}_{1.25}\text{Eu}_{0.75}\text{Nb}_3\text{O}_{10}$  in comparison with the standard cards of  $\text{KCa}_2\text{Nb}_3\text{O}_{10}$  and  $\text{CaNb}_2\text{O}_{10}$ . Additional reflections are marked with an orange arrow.<sup>23, 25</sup>

SEM-EDX measurements were conducted to evaluate the chemical homogeneity of the reaction products in more detail. SEM images for  $\text{K}_{1-x}\text{Ca}_{2-x}\text{Eu}_x\text{Nb}_3\text{O}_{10}$ , its proton-exchanged form and dried nanosheets are shown in Figure 3.2.5. Images of  $\text{A}_{1-x}\text{Ca}_{2-x}\text{La}_x\text{Nb}_3\text{O}_{10}$  are displayed in Figure S3.2.5. Both series show the expected plate-like shape for all doping degrees. The dimension of the platelets is around 10  $\mu\text{m}$  and no other morphology is observed. The same is the case for the cation-proton exchanged forms. Thus, occurring side phases seem also to exhibit the plate-like morphology. Exfoliated nanosheets form rather large aggregates with dimensions of 30-100  $\mu\text{m}$  as they restack whilst drying. In the following EDX data was taken as average from larger aggregates as no distinction of different phases due to the morphology was possible.

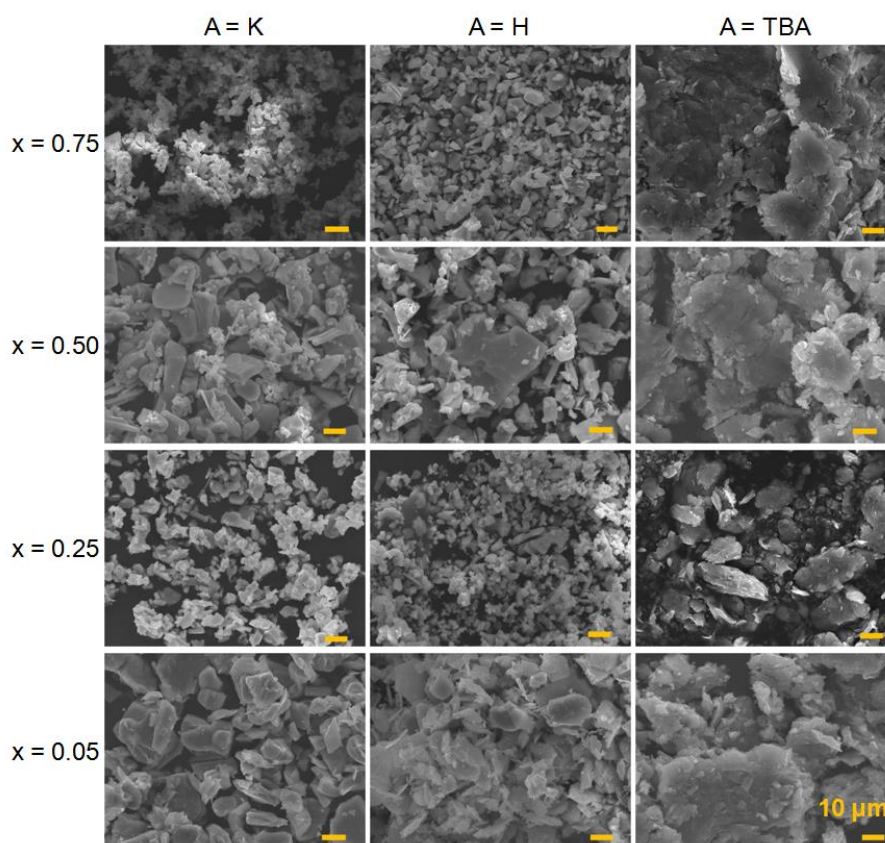


**Figure 3.2.5:** SEM images of  $A_{1-x}Ca_{2-x}Eu_xNb_3O_{10}$  ( $A = K, H, TBA, x = 0.05, 0.25, 0.50, 0.75$ ), showing plate-like morphology for all samples.

Corresponding EDX data for the  $Eu^{3+}$  series is listed in Table 3.2.2. For all other rare earth substituted  $A_{1-x}Ca_{2-x}Ln_xNb_3O_{10}$  samples the values can be found in Table S3.2.1-S3.2.4 and will be discussed further below. Stoichiometric ratios of bulk  $K_{1-x}Ca_{2-x}Eu_xNb_3O_{10}$  samples match well within the measurement uncertainties for lower substitution degrees, while a lack of  $Eu^{3+}$  is observed for higher substitution degrees. Still, the trend of decreasing  $K^+$  and  $Ca^{2+}$  and increasing  $Eu^{3+}$  is obvious. This is different for the cation-proton exchanged forms that show in average a high loss in the  $Eu^{3+}$  content with increasing  $x$  compared to the bulk material. This might be related to degradation of the material due to acid treatment. Either way,  $K^+$  ions of all samples can be completely removed or exchanged against protons  $H^+$  during acid treatment with three renewals of the acid. Sometimes a fourth or fifth treatment is necessary in order to complete the exchange, hence minor  $K^+$  contents can still be present in some cases. As will be shown below, all cation-proton exchanged  $H_{1-x}Ca_{2-x}Eu_xNb_3O_{10}$  samples can be exfoliated into nanosheets due to intercalation of  $TBA^+$  ions into the interlayer region of the perovskites in aqueous solution.

EDX measurements for nanosheet samples were conducted in three different ways. First, non-exfoliated material was removed by centrifugation at low speeds. The residue was washed, dried and investigated *via* SEM-EDX measurements. Secondly, the obtained



colloidal suspension was dropped onto a lacey carbon-coated TEM grid and individual nanosheets were studied in the TEM. Last, a nanosheet pellet from the colloidal suspension was collected at high centrifugation speed, dried, washed and also analyzed with SEM-EDX. An important observation is the fact that the amount of isolated material became less with increasing  $x$ . As one can see from all three measurements, the rare earth content in the nanosheets becomes similar to the cation-proton exchanged form significantly lower for higher substitution degrees and seems to have a maximum of about 20 at% in total. Especially TEM-EDX measurements of individual nanosheets did not give any hint for a higher rare earth content in the substituted nanosheets and only shows minimal deviation from the given average value.

**Table 3.2.2:** EDX measurements of  $K_{0.95}Ca_{1.95}Eu_{0.05}Nb_3O_{10}$ ,  $K_{0.75}Ca_{1.75}Eu_{0.25}Nb_3O_{10}$ ,  $K_{0.5}Ca_{1.5}Eu_{0.5}Nb_3O_{10}$ ,  $K_{0.25}Ca_{1.25}Eu_{0.75}Nb_3O_{10}$ , their cation-proton exchanged and exfoliated forms given in at%; r = residue after centrifugation at 3000 rpm, c = nanosheets after centrifugation at 20000 rpm, t = nanosheets measured in the TEM; at% values are average values of three EDX measurements.

Theoretical formula	K [%]	Eu [%]	Ca [%]	Nb [%]	O [%]	Experimental formula
$K_{0.95}Ca_{1.95}Eu_{0.05}Nb_3O_{10}$	4.32	8.00	0.22	13.42	74.04	$K_{0.96}Ca_{1.79}Eu_{0.05}Nb_{3.00}O_{16.9}$
$H_{0.95}Ca_{1.95}Eu_{0.05}Nb_3O_{10}$	-	19.29	0.29	18.15	71.27	$Ca_{1.72}Eu_{0.05}Nb_{3.00}O_{11.9}$
$Ca_{1.95}Eu_{0.05}Nb_3O_{10}^{0.95-} r$	-	11.79	0.25	16.61	70.15	$Ca_{2.14}Eu_{0.05}Nb_{3.00}O_{12.94}$
$Ca_{1.95}Eu_{0.05}Nb_3O_{10}^{0.95-} c$	-	13.34	0.37	20.50	65.79	$Ca_{1.95}Eu_{0.05}Nb_{3.00}O_{9.71}$
$K_{0.75}Ca_{1.75}Eu_{0.25}Nb_3O_{10}$	3.27	0.56	8.33	15.7	71.6	$K_{0.64}Ca_{1.60}Eu_{0.11}Nb_{3.00}O_{13.7}$
$H_{0.75}Ca_{1.75}Eu_{0.25}Nb_3O_{10}$	-	1.20	6.40	13.2	79.2	$Ca_{1.46}Eu_{0.27}Nb_{3.00}O_{18.0}$
$Ca_{1.75}Eu_{0.25}Nb_3O_{10}^{0.75-} r$	-	0.87	6.59	14.6	78.0	$Ca_{1.35}Eu_{0.18}Nb_{3.00}O_{16.0}$
$Ca_{1.75}Eu_{0.25}Nb_3O_{10}^{0.75-} c$	0.10	0.60	10.4	17.0	71.4	$K_{0.02}Ca_{1.84}Eu_{0.11}Nb_{3.00}O_{12.6}$
$K_{0.5}Ca_{1.5}Eu_{0.5}Nb_3O_{10}$	2.37	0.70	6.85	13.7	76.3	$K_{0.58}Ca_{1.52}Eu_{0.17}Nb_{3.00}O_{17.1}$
$H_{0.5}Ca_{1.5}Eu_{0.5}Nb_3O_{10}$	-	0.71	8.40	13.6	77.3	$Ca_{1.88}Eu_{0.16}Nb_{3.00}O_{17.1}$
$Ca_{1.5}Eu_{0.5}Nb_3O_{10}^{0.5-} r$	0.09	0.88	8.94	15.5	74.6	$K_{0.01}Ca_{1.72}Eu_{0.17}Nb_{3.00}O_{15.3}$
$Ca_{1.5}Eu_{0.5}Nb_3O_{10}^{0.5-} c$	0.15	0.58	10.4	17.0	71.6	$K_{0.03}Ca_{1.83}Eu_{0.10}Nb_{3.00}O_{12.7}$
$Ca_{1.5}Eu_{0.5}Nb_3O_{10}^{0.5-} t$	-	1.10	10.3	23.2	65.4	$Ca_{1.33}Eu_{0.14}Nb_{3.00}O_{8.5}$
$K_{0.25}Ca_{1.25}Eu_{0.75}Nb_3O_{10}$	1.47	1.73	5.93	13.6	77.3	$K_{0.28}Ca_{1.29}Eu_{0.38}Nb_{3.00}O_{17.7}$
$H_{0.25}Ca_{1.25}Eu_{0.75}Nb_3O_{10}$	-	0.47	8.30	15.2	76.0	$Ca_{1.65}Eu_{0.09}Nb_{3.00}O_{15.2}$
$Ca_{1.25}Eu_{0.75}Nb_3O_{10}^{0.25-} r$	-	0.49	6.96	11.9	80.3	$Ca_{1.75}Eu_{0.12}Nb_{3.00}O_{20.3}$
$Ca_{1.25}Eu_{0.75}Nb_3O_{10}^{0.25-} c$	-	0.59	9.94	16.2	72.1	$Ca_{1.84}Eu_{0.10}Nb_{3.00}O_{13.7}$
$Ca_{1.25}Eu_{0.75}Nb_3O_{10}^{0.25-} t$	1.00	0.50	8.00	13.0	77.5	$K_{0.23}Ca_{1.84}Eu_{0.19}Nb_{3.00}O_{17.9}$

There are two explanations for this observation. First, a certain layer-charge might be required in order to ion exchange and intercalate  $TBA^+$  cations. Second, substitution of  $Ln^{3+}$  ions into the  $KCa_2Nb_3O_{10}$  host is only possible up to a certain amount before a miscibility gap arises. Thus, we may infer that the obtained overall composition encompasses the following

known compounds, as we have already seen the existence of both  $\text{KCa}_2\text{Nb}_3\text{O}_{10}$  and  $\text{CaNb}_2\text{O}_6$ -related compounds in the XRD data:

$$x = 0.25: \quad \text{K}_3\text{Ca}_7\text{LnNb}_{12}\text{O}_{40} = 3 \text{KCa}_2\text{Nb}_3\text{O}_{10}:\text{Ln}_y + \text{CaNb}_2\text{O}_6:\text{Ln}_z + ' \text{Ln}_{1-y-z}\text{NbO}_4 ' \quad (\text{Eq. 3.2.1})$$

$$x = 0.50: \quad \text{KCa}_3\text{LnNb}_6\text{O}_{20} = \text{KCa}_2\text{Nb}_3\text{O}_{10}:\text{Ln}_y + \text{CaNb}_2\text{O}_6:\text{Ln}_z + ' \text{Ln}_{1-y-z}\text{NbO}_4 ' \quad (\text{Eq. 3.2.2})$$

$$x = 0.75: \quad \text{KCa}_5\text{Ln}_3\text{Nb}_{12}\text{O}_{40} = \text{KCa}_2\text{Nb}_3\text{O}_{10}:\text{Ln}_y + 3 \text{CaNb}_2\text{O}_6:\text{Ln}_z + 3' \text{Ln}_{1-y-z}\text{NbO}_4 ' \quad (\text{Eq. 3.2.3})$$

Rare earth ortho-niobates  $\text{LnNbO}_4$  are materials with a fergusonite structure that changes into a scheelite structure.<sup>27</sup> At this point we cannot give clear evidence on the formation of these phases on the basis of XRD analysis as the reflections of the standard cards do not match the experimental reflections exactly. Nevertheless, this finding is supported by the analysis of the residue. As the rare earth content of the residue is only slightly higher than the one of the individual nanosheets, this means that some rare earth containing compound must have been disintegrated and dissolved due to the acid-treatment or while switching to the highly basic environment in the exfoliation process. As the residue consists mainly of non-exfoliated material, the rare earth elements might be incorporated into  $\text{CaNb}_2\text{O}_6$  or  $\text{LnNbO}_4$ .<sup>28</sup> Note that the sum of  $\text{CaNb}_2\text{O}_6$  and  $\text{LnNbO}_4$  yields the end-member  $\text{CaLnNb}_3\text{O}_{10}$  of  $\text{K}_{1-x}\text{Ca}_{2-x}\text{Ln}_x\text{Nb}_3\text{O}_{10}$  series for  $x = 1$ , which is further pointing towards a miscibility gap.

Figure 3.2.6 shows photographs of the colloidal suspensions of  $\text{TBA}_{1-x}\text{Ca}_{2-x}\text{Eu}_x\text{Nb}_3\text{O}_{10}$ . The one with the lowest  $\text{Eu}^{3+}$  concentration is apparently more concentrated in terms of exfoliated material than those with higher  $\text{Eu}^{3+}$  concentrations. Since the possible side-phases  $\text{CaNb}_2\text{O}_6$  and  $\text{LnNbO}_4$  have no layered structure, less material for exfoliation is available for higher  $x$  decreasing the amount of nanosheets present in suspension. For increased  $\text{Eu}^{3+}$  content no clear difference is distinguishable by the eye due to the strong light scattering property of the nanosheets.

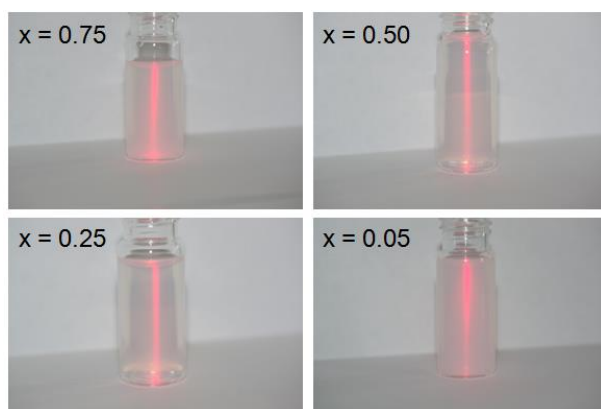


**Figure 3.2.6:** Photographs of colloidal suspensions and the resulting Tyndall effect of the exfoliated compounds  $\text{TBA}_{1-x}\text{Ca}_{2-x}\text{Eu}_x\text{Nb}_3\text{O}_{10}$  illuminated by laser light.



AFM images and corresponding height profiles for the  $\text{Eu}^{3+}$  nanosheet series are displayed in Figure 3.2.7. All samples yielded unilamellar nanosheets of dimensions up to  $1\ \mu\text{m}$  length and heights between 2.4–2.8 nm; only  $\text{TBA}_{0.95}\text{Ca}_{1.95}\text{Eu}_{0.05}\text{Nb}_3\text{O}_{10}$  gave larger sheets with a lower height around 2.0 nm. Nanosheets are generally thicker compared to the theoretical height of an individual perovskite layer due to the attached ligand and ambient water.<sup>4</sup> We have previously shown that the amount of ligand is determined by a  $\text{H}^+ - \text{TBA}^+$  exchange reaction depending on the *TBAOH* concentration (see Chapter 4.1).<sup>29</sup> The more precise sum formula would therefore be  $(\text{TBA}_{1-y}\text{H}_y)_{1-x}\text{Ca}_{2-x}\text{Ln}_x\text{Nb}_3\text{O}_{10}$ , where *y* can be tuned by the concentration of the aqueous colloidal suspension. Thus, samples with less exfoliateable material available would likely show a comparably higher *TBAOH* concentration, yielding slightly thicker nanosheets in the AFM because of the more densely packed *TBA* attached to the nanosheet surface. Another possibility would be a change in the acidity of the perovskite layers that leads to a higher attachment of ligands with increasing lanthanoide content.

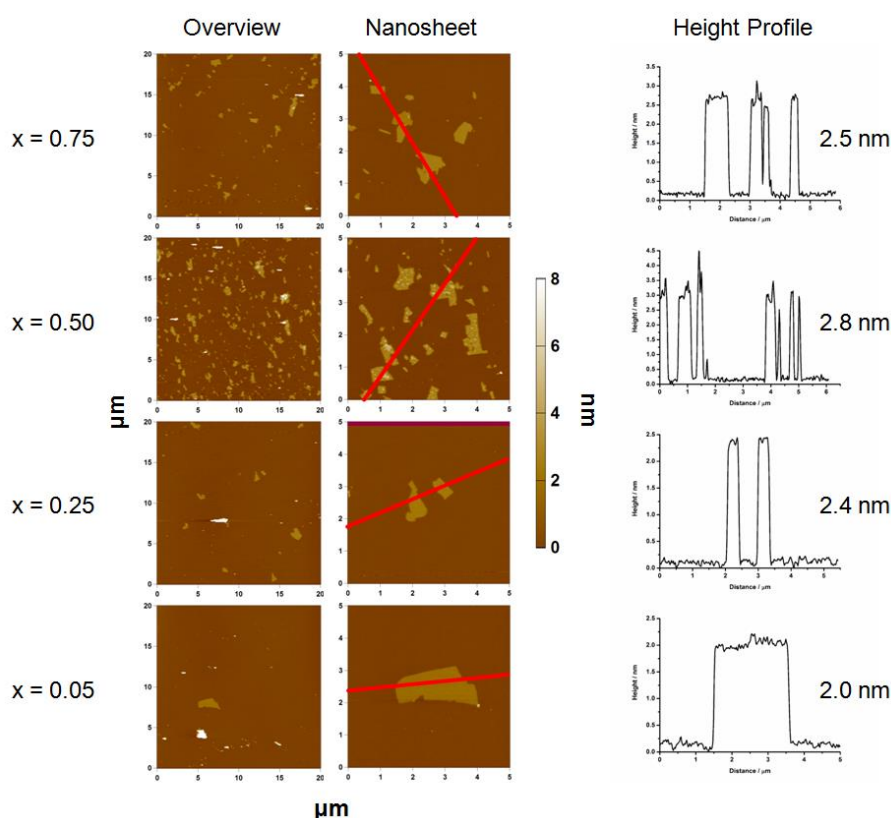


**Figure 3.2.7:** AFM overview images, as well as images of individual nanosheets and corresponding height profiles of the exfoliated compounds  $\text{TBA}_{1-x}\text{Ca}_{2-x}\text{Eu}_x\text{Nb}_3\text{O}_{10}$ .

TEM images of  $\text{TBA}_{0.95}\text{Ca}_{1.95}\text{Eu}_{0.05}\text{Nb}_3\text{O}_{10}$  versus  $\text{TBA}_{0.50}\text{Ca}_{1.50}\text{Eu}_{0.50}\text{Nb}_3\text{O}_{10}$  are shown in Figure 3.2.8. Again, nanosheets for the  $x = 0.05$  compound seem to be larger and less fragmented. At higher magnification dark spots on the nanosheets become visible. One may assume that these spots arise due to the contrast of more strongly diffracting  $\text{Eu}^{3+}$  ions, but

in fact they arise from a Cu impurity attached to the nanosheet. Figure S3.2.6 shows a STEM-EELS line scan where the signal for the Cu  $L_{2,3}$  edge at 931 eV and 951 eV is extracted. The EEL spectra were recorded on a free-standing sheet in the middle of a TEM grid cavity, so that contributions of the Cu grid can be neglected. Also, the intensity of the Cu signal was higher in the middle of the particle than between both particles. Thus, the impurity likely stems from Cu dissolved from the TEM Cu grid which we used for sample preparation, since no Cu was detected in SEM-EDX measurements for bulk, cation-proton exchanged materials and centrifuged nanosheets. Note that on top of the Cu  $L_{2,3}$  edge the Eu  $M_{4,5}$  edge at 1131 eV and 1161 eV, respectively, is visible. Hence, rare earth elements seem to be homogeneously distributed throughout the nanosheet and no possibly luminescent particles are attached to the surface.

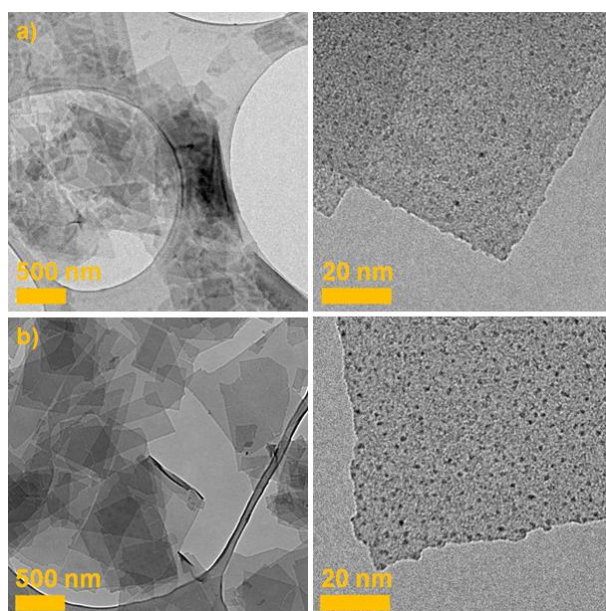


**Figure 3.2.8:** TEM images of a)  $TBA_{0.95}Ca_{1.95}Eu_{0.05}Nb_3O_{10}$  and b)  $TBA_{0.50}Ca_{1.50}Eu_{0.50}Nb_3O_{10}$  at different magnifications.

Figure 3.2.9 shows STEM images and EELS box measurement for three different  $TBA_{0.50}Ca_{1.50}Ln_{0.50}Nb_3O_{10}$  ( $Ln = La, Eu, Er$ ) nanosheets. The extracted rare earth  $M_{4,5}$  edges are shown next to the STEM image where the area of the EEL spectrum is marked with an orange box. As one can see, the white lines of La  $M_{4,5}$  at 832 eV and 849 eV are clearly visible for a single-sheet as the edge is not overlaid with the following Cu  $L_{2,3}$  edge arising from an impurity attached to the sheet. This is different to the Eu  $M_{4,5}$  edge at 1131 eV and 1161 eV, as well as the Er  $M_{4,5}$  edge at 1409 eV and 1453 eV, which suffer from the Cu  $L_{2,3}$  edge-induced background and the general decrease in intensity due to the lower ionization cross sections at higher energies. For both signals the  $M_4$  edge is barely visible. Hence, larger areas or regions of double-triple-sheets are necessary to obtain a signal. This can also be related to the fact that only a maximum of 20 at% lanthanide ions can be incorporated into

the nanosheet and thus, the signal weakening the signal. Nevertheless, the substituted rare earth elements seem to be homogeneously integrated into the nanosheet rather than being attached to the surface or forming regions or clusters with higher and lower dopant levels, respectively. This is in line with the XRD and AFM results.

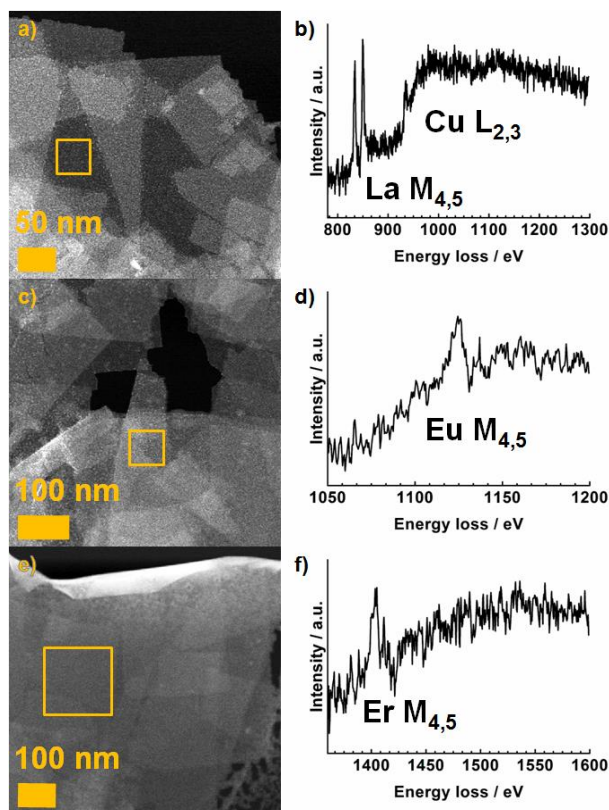


**Figure 3.2.9:** STEM images of a)  $TBA_{0.50}Ca_{1.50}La_{0.50}Nb_3O_{10}$ , c)  $TBA_{0.50}Ca_{1.50}Eu_{0.50}Nb_3O_{10}$ , e)  $TBA_{0.50}Ca_{1.50}Er_{0.50}Nb_3O_{10}$  nanosheets with the area of the performed EELS scan (orange square) highlighted, and the corresponding extracted rare earth  $M_{4,5}$  edges for b) La, d) Eu and f) Er.

Figure 3.2.10 compares photographs of  $A_{1-x}Ca_{2-x}Eu_xNb_3O_{10}$  ( $A = K, H, TBA, x = 0.05, 0.25, 0.50, 0.75$ ) under UV excitation at  $\lambda = 366$  nm. All samples show the characteristic red emission of the  $Eu^{3+}$  ions. The intensities of the potassium-containing and cation-proton exchanged bulk materials are similar and much stronger than those of the precipitated nanosheets. This can be rationalized as follows: First, non-layered materials might also exhibit luminescence, for example,  $CaNb_2O_6:Ln^{3+}$  is known as photoluminescent material.<sup>28</sup> Thus, the luminescence intensity of impurity phases might be stronger than the one of doped perovskites. Secondly, much more substance was available for the measurements of the parent compounds. The luminescence of the nanosheets is fairly homogeneous, only for  $TBA_{0.5}Ca_{1.5}Eu_{0.5}Nb_3O_{10}$  the larger part of the sample does not seem to exhibit any photoluminescence and may belong to undoped  $Ca_2Nb_3O_{10}$ . Further TEM-EDX experiments would be necessary to prove this assumption. The above results suggest that  $Eu^{3+}$ -substituted  $TBA_{1-x}Ca_{2-x}Eu_xNb_3O_{10}$  seems to be a suitable material for further luminescence studies.

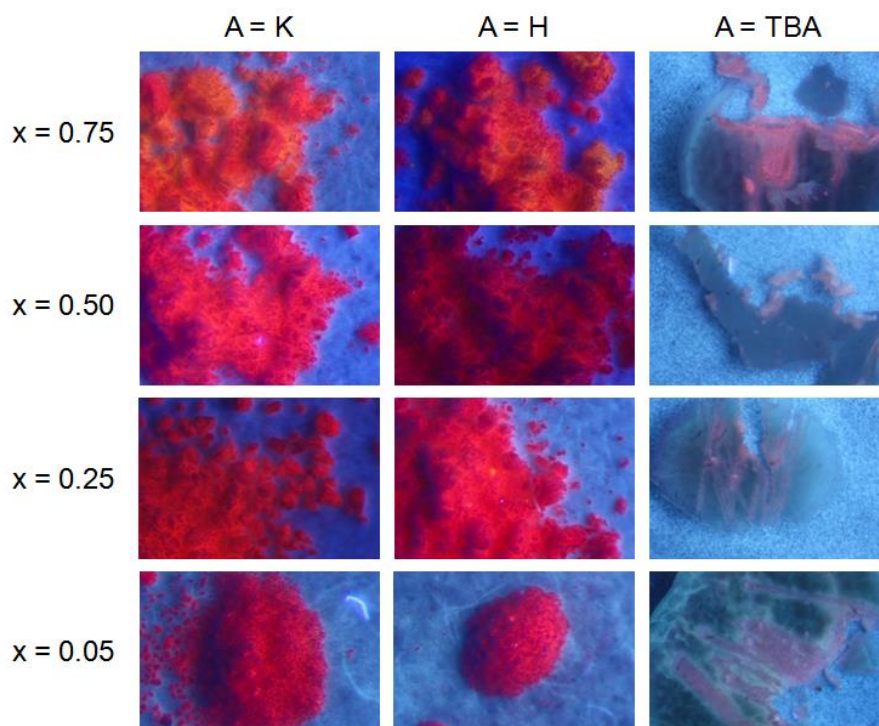


**Figure 3.2.10:** Luminescence photographs of  $A_{1-x}Ca_{2-x}Eu_xNb_3O_{10}$  ( $A = K, H, TBA, x = 0.05, 0.25, 0.50, 0.75$ ) under UV irradiation at  $\lambda = 366$  nm.

So far mainly the  $Eu^{3+}$  series was evaluated. According to XRD, SEM-EDX and AFM measurements most of the  $A_{1-x}Ca_{2-x}Ln_xNb_3O_{10}$  ( $x = 0.05, 0.25, 0.50, 0.75$ ;  $A = K, H, TBA$ ;  $Ln = La, Pr, Nd, Sm, Gd, Dy, Ho, Er, Tm, Yb$ ) samples followed a similar trend concerning structure, chemical composition and photoluminescent properties. Figure S3.2.1-S3.2.4 displays the XRD patterns of all materials including  $Eu^{3+}$  for different rare earth contents  $x$ . As can be seen from XRD data all lanthanide ions can be incorporated into the monoclinic host  $KCa_2Nb_3O_{10}$ . The inset in Figure S3.2.1 shows a close-up of the evolution of the reflections of the  $(001)$  plane for the  $x = 0.05$  series as a function of the type of rare earth cation. The reflections shift towards lower  $2\theta$  values upon substitution of the larger  $La^{3+}$  (1.36 Å) for the smaller  $Ca^{2+}$  (1.34 Å) site and then back to higher  $2\theta$  values due to the lanthanide contraction.<sup>30</sup> On the contrary, the reflection at  $21^\circ 2\theta$  is only present in some cases and does not shift, and hence may in fact belong to a  $Ca_2Nb_2O_7$  impurity as mentioned earlier. For increasing  $x$  the evolution of the XRD patterns is similar to those discussed for  $Eu^{3+}$  versus  $La^{3+}$ , while only mixed valence  $Pr^{3+/4+}$  and the smaller  $Tm^{3+}$  and  $Yb^{3+}$  substituted samples show greater divergence. The reason for these deviations might be the mixed valence precursor  $Pr_6O_{11}$  for  $Pr^{3+/4+}$  on the one hand as quadrivalent ions do not substitute as good as trivalent in the investigated system, and the size of  $Tm^{3+}$  and  $Yb^{3+}$  on the other side. EDX data of  $K_{1-x}Ca_{2-x}Ln_xNb_3O_{10}$  and acid treated materials are listed in Table S3.2.1-S3.2.4. Doping with low amounts of rare earth leads to the successful incorporation into the host lattice and all materials can be exfoliated, while a higher substitution degree leads to



inhomogeneous samples as detected by the XRD. These results are in good agreement with those for the  $\text{Eu}^{3+}$  series. Thus, not all exfoliated materials were centrifuged for further analysis.

Despite the trend of a limited solid solution range for  $\text{A}_{1-x}\text{Ca}_{2-x}\text{Ln}_x\text{Nb}_3\text{O}_{10}$ , some of the doped materials still exhibit notable luminescence properties. The  $\text{Sm}^{3+}$  and  $\text{Pr}^{3+/4+}$  materials show red emissions, whereas  $\text{Dy}^{3+}$  compounds exhibit a rather yellow one.  $\text{Er}^{3+}$  materials yield an intense green photoluminescence. Photographs under UV irradiation for the respective bulk materials can be seen in Figure 3.2.11.

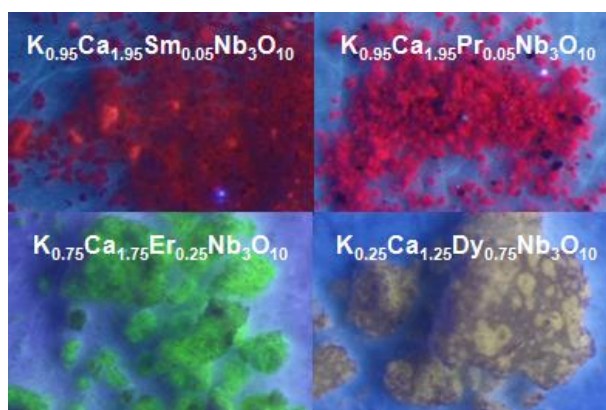


**Figure 3.2.11:** Luminescence photographs of various  $\text{K}_{1-x}\text{Ca}_{2-x}\text{Ln}_x\text{Nb}_3\text{O}_{10}$  bulk materials under UV irradiation at  $\lambda = 366 \text{ nm}$ .

Since substitution within the  $\text{A}_{1-x}\text{Ca}_{2-x}\text{Ln}_x\text{Nb}_3\text{O}_{10}$  crystal structure seems to be limited, we investigated also the structurally similar compounds  $\text{K}_{1-x}\text{Sr}_{2-x}\text{Ln}_x\text{Nb}_3\text{O}_{10}$  and  $\text{Rb}_{1-x}\text{Sr}_{2-x}\text{Ln}_x\text{Nb}_3\text{O}_{10}$  with larger  $\text{Sr}^{2+}$  ions on the A site of the perovskite lattice in order to achieve a complete solid solution with tunable photoactivator concentration. Again, reaction temperatures of  $1100\text{--}1300^\circ\text{C}$  were used to synthesize homogeneous samples. All K containing samples showed a very inhomogeneous distribution of elements and the formation of different phases according to XRD and SEM-EDX analysis. The reason might be that the small  $\text{K}^+$  may lead to too high lattice distortions of the larger Sr containing perovskite lattice.<sup>31</sup> We therefore continued with the Rb containing samples which showed identical XRD patterns in the synthesis temperature range of  $1200\text{--}1300^\circ\text{C}$ . Figure 3.2.12 shows the XRD patterns for a  $\text{Rb}_{0.5}\text{Sr}_{1.5}\text{Ln}_{0.5}\text{Nb}_3\text{O}_{10}$  ( $\text{Ln} = \text{La}, \text{Eu}, \text{Er}$ ) compound compared to  $\text{RbSr}_2\text{Nb}_3\text{O}_{10}$ <sup>32</sup> and  $\text{SrNb}_2\text{O}_6$ <sup>33</sup>. The  $\text{RbSr}_2\text{Nb}_3\text{O}_{10}$  reflections are in agreement with the literature and shift as a function of the lanthanide ion; also, additional reflections become apparent. These do not belong to  $\text{SrNb}_2\text{O}_6$  and hence do not follow the same trend as for the Ca analogue. Nevertheless, these reflections again suggest the presence of a side phase, and no homogeneous series of  $\text{Rb}_{1-x}\text{Sr}_{2-x}\text{Ln}_x\text{Nb}_3\text{O}_{10}$  could be obtained.

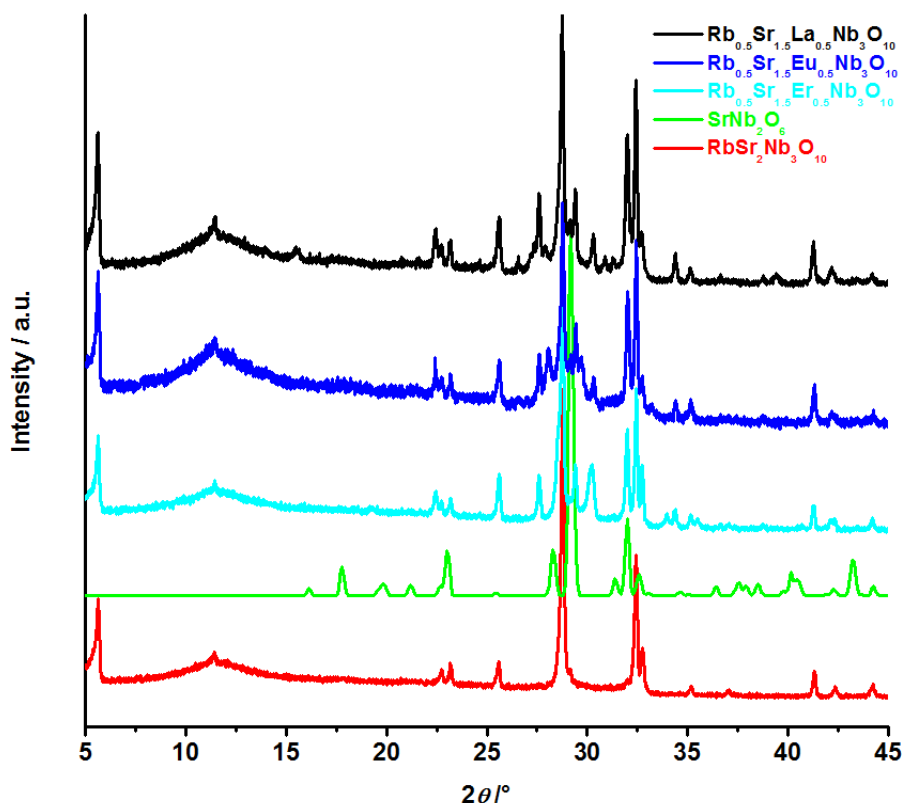


**Figure 3.2.12:** XRD patterns of  $\text{Rb}_{0.5}\text{Sr}_{1.5}\text{Ln}_{0.5}\text{Nb}_3\text{O}_{10}$  ( $\text{Ln} = \text{La}, \text{Eu}, \text{Er}$ ) in comparison with standard cards of  $\text{RbSr}_2\text{Nb}_3\text{O}_{10}$  and  $\text{SrNb}_2\text{O}_6$ .<sup>32-33</sup>

Figure S3.2.7 displays SEM images for  $\text{A}_{0.5}\text{Sr}_{1.5}\text{Eu}_{0.5}\text{Nb}_3\text{O}_{10}$ , showing the expected plate-like morphology. With around  $10\ \mu\text{m}$  their size is similar to those of the Ca analogues. Table 3.2.3 lists the corresponding EDX measurements. The composition  $\text{Rb}_{0.36}\text{Sr}_{0.91}\text{Eu}_{0.78}\text{Nb}_{3.00}\text{O}_{15.4}$  suggests the formation of a different composition with increased Eu and decreased Rb and Sr content, with an inhomogeneous mixture of compounds. Acid treatment and exfoliation leads to nanosheets with a composition close to that of the Ca analogue, showing that only 10 at% of  $\text{Eu}^{3+}$  can be substituted into a  $\text{Sr}_2\text{Nb}_3\text{O}_{10}^-$  host.

**Table 3.2.3:** EDX measurements of  $\text{Rb}_{0.50}\text{Sr}_{1.50}\text{Eu}_{0.50}\text{Nb}_3\text{O}_{10}$ , and its cation-proton exchanged as well as exfoliated forms given in at%; at% values are average values of three EDX measurements.

Theoretical formula	Rb [%]	Eu [%]	Sr [%]	Nb [%]	O [%]	Experimental formula
$\text{Rb}_{0.5}\text{Sr}_{1.5}\text{Eu}_{0.5}\text{Nb}_3\text{O}_{10}$	1.75	4.43	3.78	14.5	74.9	$\text{Rb}_{0.36}\text{Sr}_{0.91}\text{Eu}_{0.78}\text{Nb}_{3.00}\text{O}_{15.4}$
$\text{H}_{0.5}\text{Sr}_{1.5}\text{Eu}_{0.5}\text{Nb}_3\text{O}_{10}$	0.00	9.13	0.53	16.3	71.3	$\text{Rb}_{0.00}\text{Sr}_{1.67}\text{Eu}_{0.09}\text{Nb}_{3.00}\text{O}_{15.4}$
$\text{Sr}_{1.5}\text{Eu}_{0.5}\text{Nb}_3\text{O}_{10}^{0.50-}$	0.00	9.73	0.62	17.4	72.1	$\text{Rb}_{0.00}\text{Sr}_{1.67}\text{Eu}_{0.10}\text{Nb}_{3.00}\text{O}_{12.4}$

AFM images and individual height profiles of the obtained nanosheets are depicted in Figure 3.2.13 for  $\text{TBA}_{0.5}\text{Sr}_{1.5}\text{Eu}_{0.5}\text{Nb}_3\text{O}_{10}$  and  $\text{TBA}_{0.5}\text{Sr}_{1.5}\text{Er}_{0.5}\text{Nb}_3\text{O}_{10}$ . The sheets are fairly

large in size (around 2  $\mu\text{m}$ ) and larger in height due to the larger  $\text{Sr}^{2+}$  ion as well as a denser packed  $\text{TBA}^+$  ligand shell.

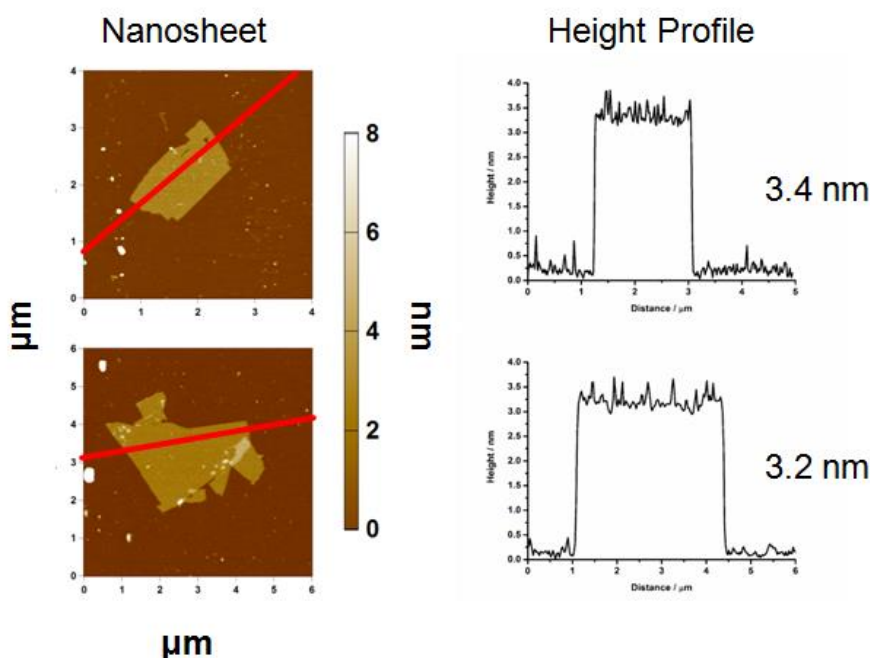


**Figure 3.2.13:** AFM images of individual  $\text{TBA}_{0.5}\text{Sr}_{1.5}\text{Eu}_{0.5}\text{Nb}_3\text{O}_{10}$  (top) and  $\text{TBA}_{0.5}\text{Sr}_{1.5}\text{Er}_{0.5}\text{Nb}_3\text{O}_{10}$  (bottom) nanosheets and the corresponding height profiles.

Luminescence photographs of  $\text{Rb}_{0.5}\text{Sr}_{1.5}\text{Eu}_{0.5}\text{Nb}_3\text{O}_{10}$ ,  $\text{Rb}_{0.5}\text{Sr}_{1.5}\text{Er}_{0.5}\text{Nb}_3\text{O}_{10}$  and  $\text{TBA}_{0.5}\text{Sr}_{1.5}\text{Er}_{0.5}\text{Nb}_3\text{O}_{10}$  are depicted in Figure 3.2.14, showing the red and green emissions of  $\text{Eu}^{3+}$  and  $\text{Er}^{3+}$  samples. The amount of  $\text{TBA}_{0.5}\text{Sr}_{1.5}\text{Eu}_{0.5}\text{Nb}_3\text{O}_{10}$  nanosheets was too little for a photograph. In comparison, the Sr samples are less intense than their Ca counterparts. This might be due to the lower photoactivator concentration in the strontium niobate perovskite host and for bulk materials also be caused by the absence of photoluminescent impurity phases.

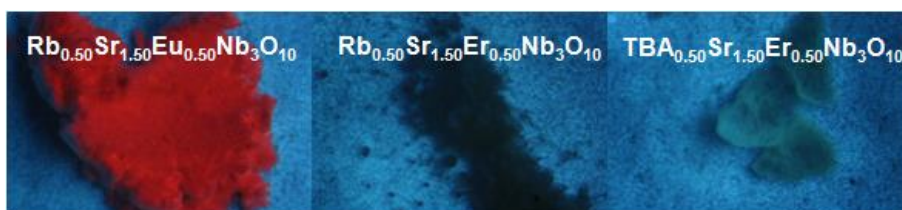


**Figure 3.2.14:** Luminescence photographs of various  $\text{A}_{1-x}\text{Sr}_{2-x}\text{Ln}_x\text{Nb}_3\text{O}_{10}$  bulk materials under UV irradiation at  $\lambda = 366 \text{ nm}$ .

### 3.2.3 Conclusion

In the present study, we systematically investigated the layered perovskites  $K_{1-x}Ca_{2-x}Ln_xNb_3O_{10}$  ( $x = 0.05, 0.25, 0.50, 0.75$ ;  $Ln = La, Pr, Nd, Sm, Eu, Gd, Dy, Ho, Er, Tm, Yb$ ), where the La series is reported in the literature to possess a variable interlayer cation density due to the homogeneous and aliovalent replacement of  $K^+$  and  $Ca^{2+}$  ions by  $Ln^{3+}$  ions. In reproducing these samples, XRD measurements suggest that instead  $CaNb_2O_6$  and another rare earth containing compound for increasing  $x$  is formed along with  $KCa_2Nb_3O_{10}$  at various synthesis temperatures. SEM- and TEM-EDX measurements revealed that only up to 20 at% rare earth ions can be incorporated into the  $KCa_2Nb_3O_{10}$  systems, yielding a maximum of  $K_{0.8}Ca_{1.8}Ln_{0.2}Nb_3O_{10}$  before a miscibility gap arises. Exfoliation of these rare earth containing parent compounds gives rise to nanosheets that show red emissions in case of  $Eu^{3+}$ ,  $Sm^{3+}$ ,  $Pr^{3+/4+}$ , green emissions for  $Er^{3+}$ , and yellow emissions for  $Dy^{3+}$  under excitation at  $\lambda = 366\text{nm}$ . A similar scenario was obtained for  $Rb_{1-x}Sr_{2-x}Ln_xNb_3O_{10}$  ( $x = 0.50$ ,  $Ln = La, Eu, Er$ ), yielding nanosheets with a maximum uptake of 10 at% rare earth ions and correspondingly lower emission intensity.

### 3.2.4 Bibliography

- [1] S. Ida, C. Ogata, U. Unal, K. Izawa, T. Inoue, O. Altuntasoglu, Y. Matsumoto, *J. Am. Chem. Soc.* **2007**, *129*, 8956-8957.
- [2] T. C. Ozawa, K. Fukuda, K. Akatsuka, Y. Ebina, T. Sasaki, *Chem. Mater.* **2007**, *19*, 6575-6580.
- [3] T. C. Ozawa, K. Fukuda, K. Akatsuka, Y. Ebina, T. Sasaki, K. Kurashima, K. Kosuda, *J. Phys. Chem. C* **2008**, *112*, 1312-1315.
- [4] S. Ida, C. Ogata, M. Eguchi, W. J. Youngblood, T. E. Mallouk, Y. Matsumoto, *J. Am. Chem. Soc.* **2008**, *130*, 7052-7059.
- [5] T. C. Ozawa, K. Fukuda, K. Akatsuka, Y. Ebina, T. Sasaki, K. Kurashima, K. Kosuda, *J. Phys. Chem. C* **2008**, *112*, 17115-17120.
- [6] T. C. Ozawa, K. Fukuda, K. Akatsuka, Y. Ebina, K. Kurashima, T. Sasaki, *J. Phys. Chem. C* **2009**, *113*, 8735-8742.
- [7] C. O. Tadashi, F. Katsutoshi, E. Yasuo, K. Kosuke, S. Akira, M. Yuichi, K. Keiji, S. Takayoshi, *Sci. Technol. Adv. Mater.* **2011**, *12*, 044601.
- [8] L.-M. Fu, B.-Z. Lin, Y.-L. Chan, O. Zhang, B. Li, H. Qu, *J. Alloys Compd.* **2012**, *525*, 14-21.
- [9] S. Ida, S. Koga, T. Daio, H. Hagiwara, T. Ishihara, *Angew. Chem., Int. Ed. Engl.* **2014**, *53*, 13078-13082.
- [10] R. Ma, T. Sasaki, *Adv. Mater. (Weinheim, Ger.)* **2010**, *22*, 5082-5104.
- [11] R. Ma, T. Sasaki, *Acc. Chem. Res.* **2015**, *48*, 136-143.



- [12] H. Xin, R. Ma, L. Wang, Y. Ebina, K. Takada, T. Sasaki, *Appl. Phys. Lett.* **2004**, *85*, 4187-4189.
- [13] Y. Matsumoto, U. Unal, Y. Kimura, S. Ohashi, K. Izawa, *J. Phys. Chem. B* **2005**, *109*, 12748-12754.
- [14] S. Ida, K. Araki, U. Unal, K. Izawa, O. Altuntasoglu, C. Ogata, Y. Matsumoto, *Chem. Commun. (Cambridge, U. K.)* **2006**, 3619-3621.
- [15] S. Ida, U. Unal, K. Izawa, O. Altuntasoglu, C. Ogata, T. Inoue, K. Shimogawa, Y. Matsumoto, *J. Phys. Chem. B* **2006**, *110*, 23881-23887.
- [16] S. Ida, C. Ogata, T. Inoue, K. Izawa, U. Unal, O. Altuntasoglu, Y. Matsumoto, *Chem. Lett.* **2007**, *36*, 158-159.
- [17] S. Ida, U. Unal, K. Izawa, C. Ogata, T. Inoue, Y. Matsumoto, *Mol. Cryst. Liq. Cryst.* **2007**, *470*, 393-402.
- [18] T. C. Ozawa, M. Onoda, N. Iyi, Y. Ebina, T. Sasaki, *J. Phys. Chem. C* **2014**, *118*, 1729-1738.
- [19] M. A. Bizeto, A. L. Shiguihara, V. R. L. Constantino, *J. Mater. Chem.* **2009**, *19*, 2512-2525.
- [20] M. A. Bizeto, V. R. L. Constantino, H. F. Brito, *J. Alloys Compd.* **2000**, *311*, 159-168.
- [21] Y. Huang, Y. Xie, L. Fan, Y. Li, Y. Wei, J. Lin, J. Wu, *Int. J. Hydrogen Energy* **2008**, *33*, 6432-6438.
- [22] S. Uma, J. Gopalakrishnan, *J. Solid State Chem.* **1993**, *102*, 332-339.
- [23] T. Tokumitsu, K. Toda, T. Aoyagi, D. Sakuraba, K. Uematsu, M. Sato, *J. Ceram. Soc. Jpn.* **2006**, *114*, 795-797.
- [24] K. Scheunemann, H. Müller-Buschbaum, *J. Inorg. Nucl. Chem.* **1974**, *36*, 1965-1970.
- [25] J. P. Cummings, S. H. Simonsen, *Am. Mineral.* **1970**, *55*, 90-97.
- [26] K. S. Virdi, Y. Kauffmann, C. Ziegler, P. Ganter, B. V. Lotsch, W. D. Kaplan, P. Blaha, C. Scheu, *Phys. Rev. B* **2013**, *87*, 115108.
- [27] V. Trunov, L. Kinzhibalo, *Phys.-Dokl.* **1982**, *27*, 185.
- [28] K. Li, X. Liu, Y. Zhang, X. Li, H. Lian, J. Lin, *Inorg. Chem.* **2015**, *54*, 323-333.
- [29] C. Ziegler, S. Werner, M. Bugnet, M. Wörsching, V. Duppel, G. A. Botton, C. Scheu, B. V. Lotsch, *Chem. Mater.* **2013**, *25*, 4892-4900.
- [30] R. Shannon, *Acta Crystallogr., Sect. A* **1976**, *32*, 751-767.
- [31] R. E. Schaak, T. E. Mallouk, *Chem. Mater.* **2002**, *14*, 1455-1471.
- [32] V. Thangadurai, P. Schmid-Beurmann, W. Weppner, *J. Solid State Chem.* **2001**, *158*, 279-289.
- [33] B. O. Marinder, P.-L. Wang, P.-E. Werner, *Acta Chem. Scand.* **1986**, *40a*, 467-475.

### 3.2.5 Supporting Information

#### EXPERIMENTAL PROCEDURES:

**Chemicals.** All chemicals and solvents were purchased from commercial suppliers and used without further purification: Potassium carbonate ( $K_2CO_3$ , Merck KGaA, >99%), rubidium carbonate ( $Rb_2CO_3$ , Alfa Aesar, 99.8%), calcium carbonate ( $CaCO_3$ , Grüssing, 99%), strontium carbonate ( $SrCO_3$ , Merck KGaA, 99%), niobium(V) oxide ( $Nb_2O_5$ , Alfa Aesar, 99.5%), lanthanide(III) oxides ( $Ln_2O_3$ ,  $Ln = La, Nd, Sm, Eu, Gd, Dy, Ho, Er, Tm, Yb$ , Alfa Aesar, 99.9%), praseodymium(III;IV) oxide ( $Pr_6O_{11}$ , Alfa Aesar, 99.9%) and tetra-*n*-butylammonium hydroxide (*TBAOH*,  $[CH_3(CH_2)_3]_4NOH \cdot 30 H_2O$ , Sigma-Aldrich, 98%). Deionized water was used throughout all synthesis procedures.

**Bulk synthesis.** Layered bulk materials  $K_{1-x}Ca_{2-x}Ln_xNb_3O_{10}$  ( $x = 0.05, 0.25, 0.50, 0.75$ ;  $Ln = La, Pr, Nd, Sm, Eu, Gd, Dy, Ho, Er, Tm, Yb$ ) and  $(K,Rb)_{1-x}Sr_{2-x}Ln_xNb_3O_{10}$  ( $x = 0.50$ ;  $Ln = La, Eu, Er$ ) were synthesized according to protocols modified from those reported in the literature.<sup>1-4</sup> In general,  $A_2CO_3$  ( $A = K, Rb$ ),  $BCO_3$  ( $B = Ca, Sr$ ) and  $Nb_2O_5$  were mixed with the respective lanthanide oxide in a stoichiometric ratio depending on the lanthanide content  $x$ . 20 at% excess of the alkaline carbonate was added to compensate for evaporation losses during heating. The mixture was thoroughly grinded and fired up to temperatures between 1100-1300°C in an alumina crucible. The final product was washed with deionized water and dried at room temperature or 100°C.

**Cation-proton exchange.** The cation-proton exchange was carried out by stirring the as-prepared bulk materials in 5M aqueous  $HNO_3$  solution for 5–6 days at room temperature. To ensure complete exchange of all alkaline-ions with protons, the acid was replaced several times. After the reaction was complete, the products were filtered, washed with a small amount of distilled water, and dried at room temperature.

**Exfoliation.** After cation-proton exchange, exfoliation was performed with two different exfoliation reagents. 250 mg of the cation-proton exchanged solid products were admixed with a 1:1 molecular ratio with *TBAOH* in 40 mL aqueous solution and shaken for 3 weeks with an orbital shaker at RT. To remove non-exfoliated material, all suspensions were centrifuged at 3000 rpm for 30 min. The supernatants were collected and used for atomic force microscopy (AFM) and transmission electron microscopy (TEM) measurements. To isolate nanosheets for further investigations, the supernatants were centrifuged at 20000 rpm for 30 min and the isolated nanosheets dried at RT.

**CHARACTERIZATION:**

X-ray diffraction (XRD) analysis, scanning electron microscopy (SEM) coupled with energy-dispersive X-ray (EDX) analysis, AFM and TEM coupled with EDX spectroscopy and electron energy loss spectroscopy (EELS) were used to monitor starting and intermediate compounds as well as the obtained nanosheets.

**XRD.** XRD data of powders were collected using a Huber G670 (Huber, Rimsting; Cu  $K_{\alpha 1}$ -radiation,  $\lambda = 154.051$  pm, Ge(111)-monochromator, external standard  $\text{SiO}_2$ ) Guinier Imaging Plate diffractometer.

**SEM-EDX.** SEM was conducted on a JSM-6500F electron microscope (JEOL Ltd., Tokyo). The microscope was equipped with a 7418 EDX detector (Oxford Instruments, Abingdon).

**AFM.** AFM measurements were performed on a MFP-3D stand alone AFM (Asylum Research, Santa Barbara). Tapping-mode was applied using OMCL-AC160TS-R3 (Olympus, Tokio) cantilevers with a resonant frequency of 300 kHz.

**TEM-EDX.** For TEM characterization a Philips CM30 ST microscope (300 kV,  $\text{LaB}_6$  cathode,  $C_s = 1.15$  mm, Royal Philips Electronics, Amsterdam), a FEI Titan 80-300 (300 kV, field emission gun, FEI, Hillsboro) equipped with an EDAX Sapphire Si(Li) detector (EDAX, Eindhoven) and a FEI Titan 80-300 Cubed (S)TEM (300 kV, high intensity X-FEG, FEI, Hillsboro) equipped with two aberration correctors for the probe and the image forming lenses and a Gatan GIF (model 866) spectrometer were used.

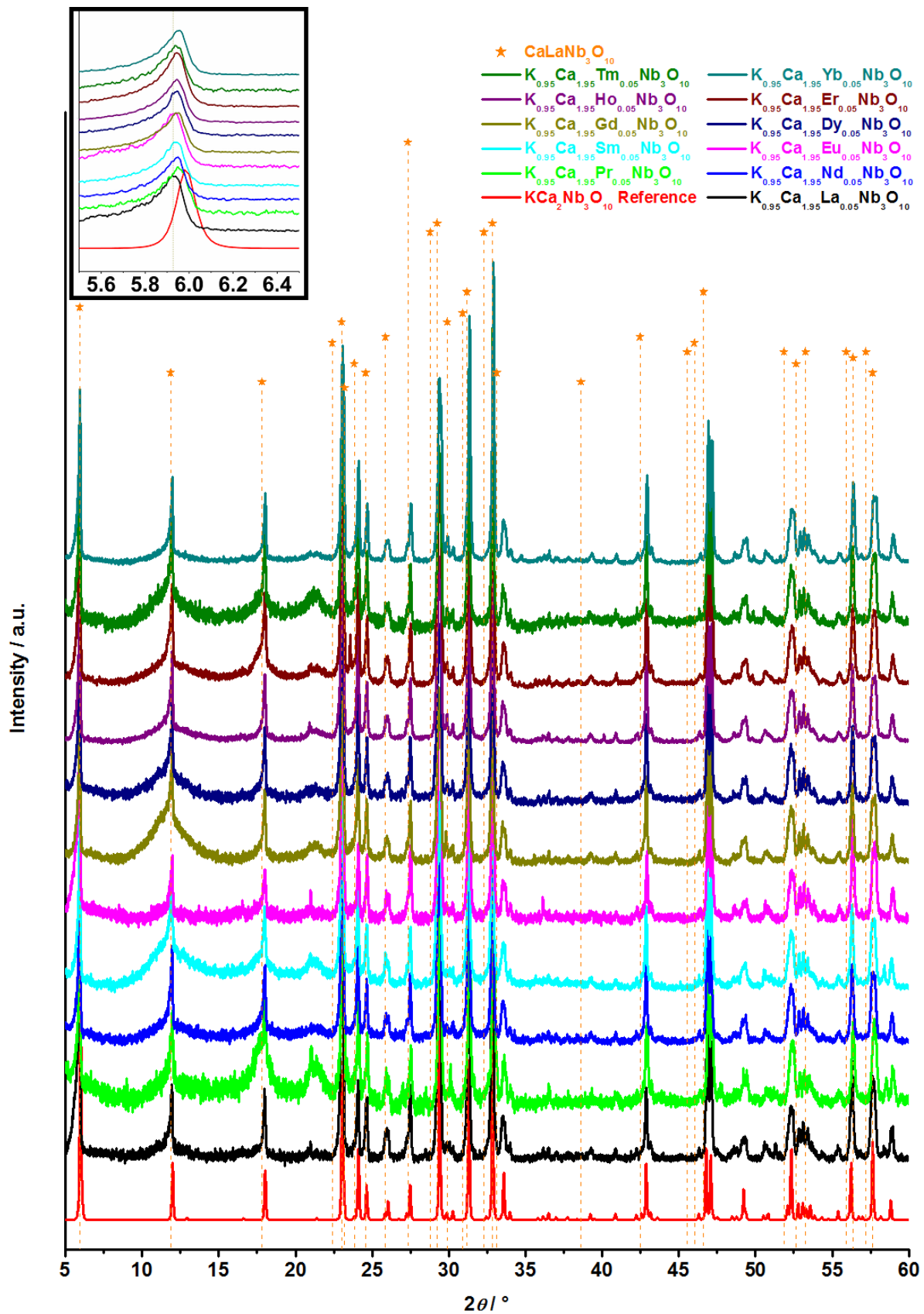


**Figure S3.2.1:** XRD patterns of  $K_{0.95}Ca_{1.95}Ln_{0.05}Nb_3O_{10}$  ( $Ln = La, Pr, Nd, Sm, Eu, Gd, Dy, Ho, Er, Tm, Yb$ ) in comparison with the reference end-members  $KCa_2Nb_3O_{10}$  and  $CaLaNb_3O_{10}$ . The inset shows a close-up of the region around the reflections belonging to the  $(001)$  plane.<sup>1,5</sup>

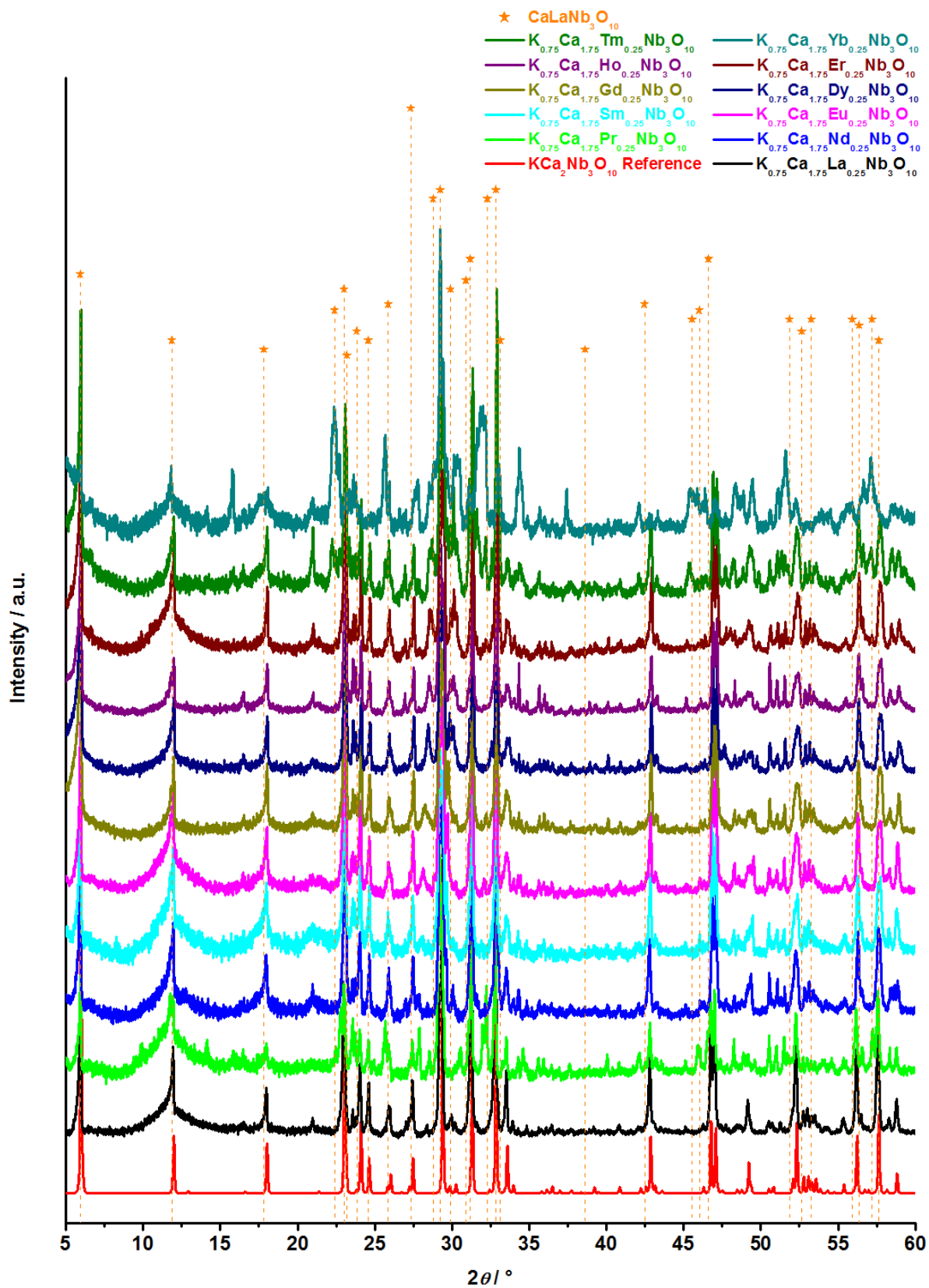


**Figure S3.2.2:** XRD patterns of  $K_{0.75}Ca_{1.75}Ln_{0.25}Nb_3O_{10}$  ( $Ln = La, Pr, Nd, Sm, Eu, Gd, Dy, Ho, Er, Tm, Yb$ ) in comparison with the reference end-members  $KCa_2Nb_3O_{10}$  and  $CaLaNb_3O_{10}$ .<sup>1, 5</sup>

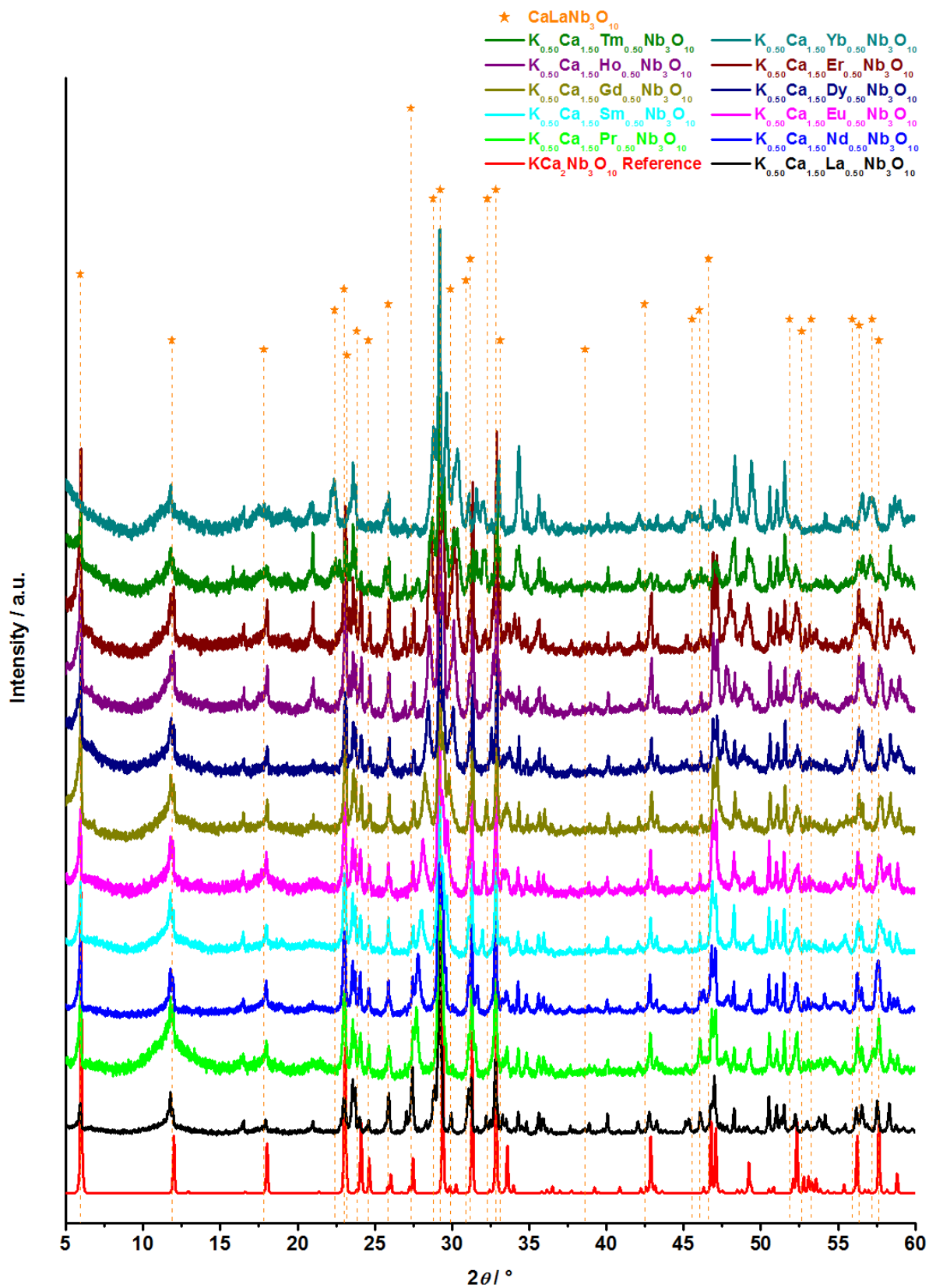


**Figure S3.2.3:** XRD patterns of  $\text{K}_{0.50}\text{Ca}_{1.50}\text{Ln}_{0.50}\text{Nb}_3\text{O}_{10}$  ( $\text{Ln} = \text{La}, \text{Pr}, \text{Nd}, \text{Sm}, \text{Eu}, \text{Gd}, \text{Dy}, \text{Ho}, \text{Er}, \text{Tm}, \text{Yb}$ ) in comparison with the reference end-members  $\text{KCa}_2\text{Nb}_3\text{O}_{10}$  and  $\text{CaLaNb}_3\text{O}_{10}$ .<sup>1, 5</sup>

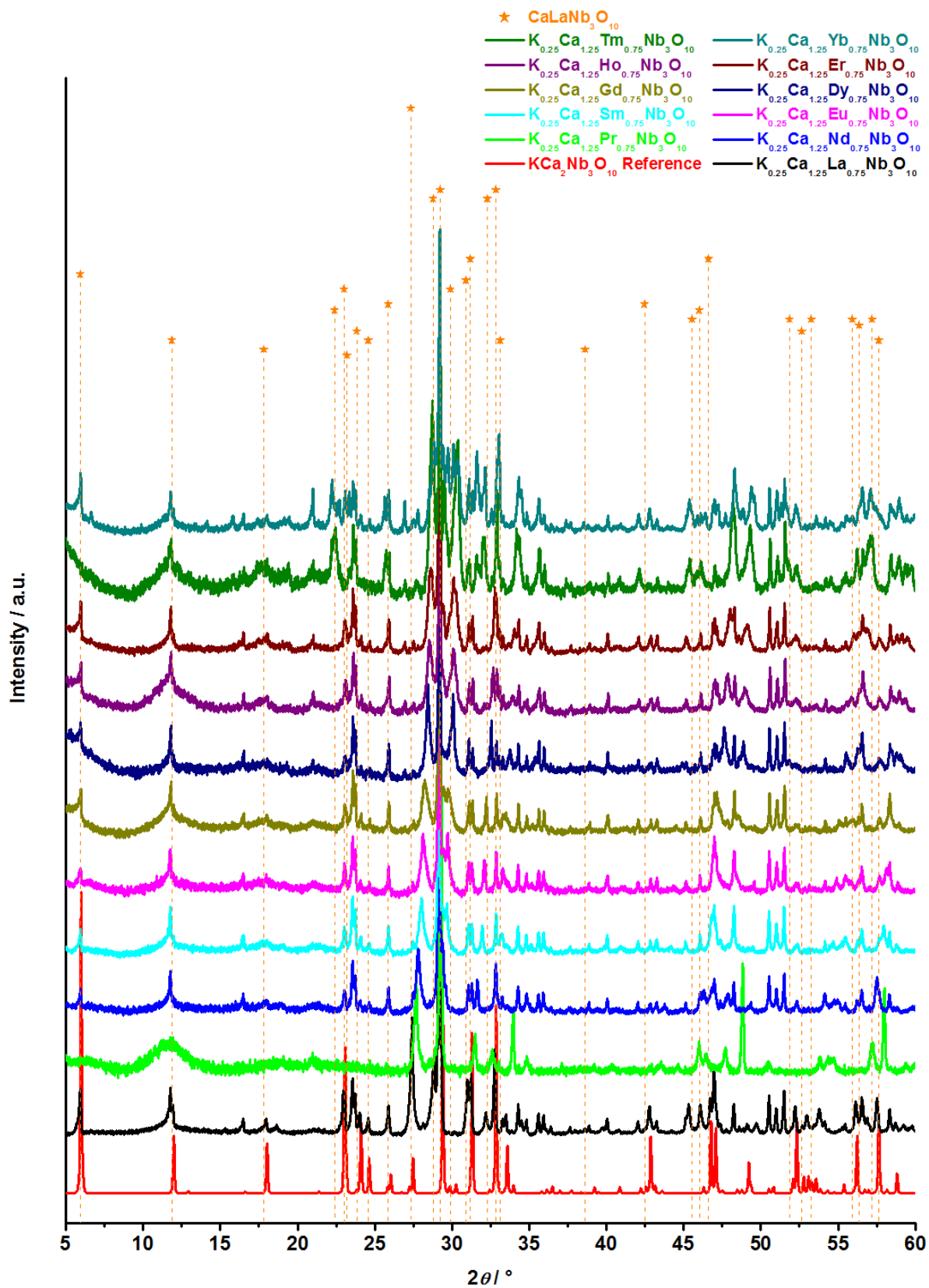


**Figure S3.2.4:** XRD patterns of  $K_{0.25}Ca_{1.25}Ln_{0.75}Nb_3O_{10}$  ( $Ln = La, Pr, Nd, Sm, Eu, Gd, Dy, Ho, Er, Tm, Yb$ ) in comparison with the reference end-members  $KCa_2Nb_3O_{10}$  and  $CaLaNb_3O_{10}$ .<sup>1, 5</sup>

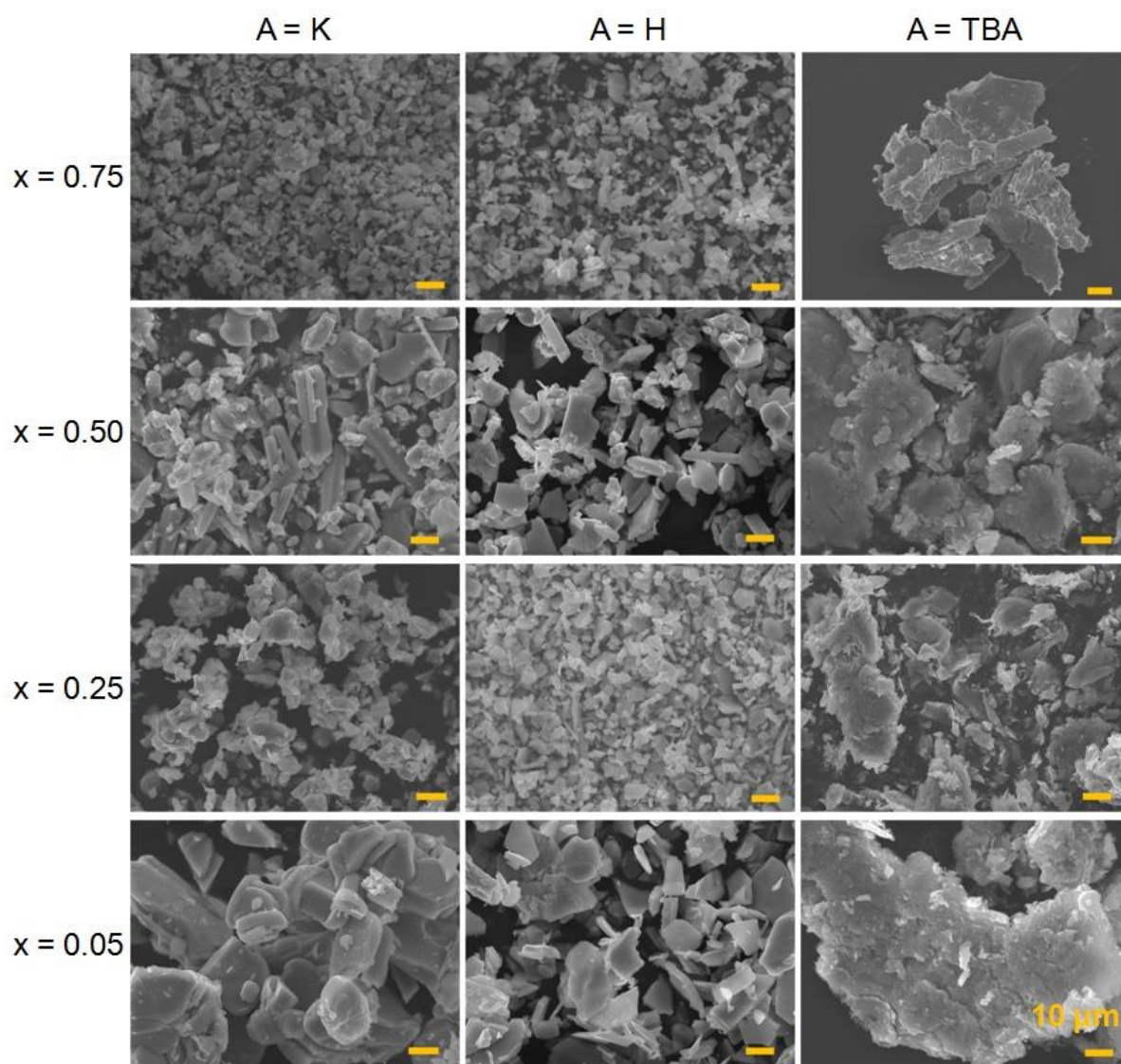


**Figure S3.2.5:** SEM images of  $A_{1-x}Ca_{2-x}La_xNb_3O_{10}$  ( $A = K, H, TBA, x = 0.05, 0.25, 0.50, 0.75$ ) showing plate-like morphologies for all samples.



**Table S3.2.1:** EDX measurements of  $K_{0.95}Ca_{1.95}Ln_{0.05}Nb_3O_{10}$ ,  $H_{0.95}Ca_{1.95}Ln_{0.05}Nb_3O_{10}$  and  $Ca_{1.95}Ln_{0.05}Nb_3O_{10}^{0.95-}$  nanosheets ( $Ln = La, Pr, Nd, Sm, Gd, Tb, Dy, Ho, Er, Tm, Yb$ ) given in at%. at% values are average values of three EDX measurements.

Theoretical formula	K [%]	Ca [%]	Ln [%]	Nb [%]	O [%]	Experimental formula
$K_{0.95}Ca_{1.95}La_{0.05}Nb_3O_{10}$	4.91	9.33	0.24	15.12	70.4	$K_{0.97}Ca_{1.85}La_{0.05}Nb_{3.00}O_{14.0}$
$H_{0.95}Ca_{1.95}La_{0.05}Nb_3O_{10}$	-	9.77	0.25	15.83	74.2	$Ca_{1.85}La_{0.05}Nb_{3.00}O_{14.1}$
$Ca_{1.95}La_{0.05}Nb_3O_{10}^{0.95-}$	-	10.17	0.23	16.15	73.5	$Ca_{1.89}La_{0.04}Nb_{3.00}O_{13.7}$
$K_{0.95}Ca_{1.95}Pr_{0.05}Nb_3O_{10}$	3.49	8.09	0.36	12.5	75.6	$K_{0.84}Ca_{1.94}Pr_{0.09}Nb_{3.00}O_{18.5}$
$K_{0.95}Ca_{1.95}Nd_{0.05}Nb_3O_{10}$	5.02	8.16	0.21	13.4	73.8	$K_{0.95}Ca_{1.82}Nd_{0.05}Nb_{3.00}O_{16.7}$
$H_{0.95}Ca_{1.95}Nd_{0.05}Nb_3O_{10}$	-	8.20	0.20	13.5	78.1	$Ca_{1.82}Nd_{0.04}Nb_{3.00}O_{17.5}$
$Ca_{1.95}Nd_{0.05}Nb_3O_{10}^{0.95-}$	-	10.2	0.27	16.1	73.4	$Ca_{1.89}Nd_{0.05}Nb_{3.00}O_{14.0}$
$K_{0.95}Ca_{1.95}Sm_{0.05}Nb_3O_{10}$	4.82	9.10	0.22	14.8	71.1	$K_{0.98}Ca_{1.83}Sm_{0.04}Nb_{3.00}O_{14.6}$
$H_{0.95}Ca_{1.95}Sm_{0.05}Nb_3O_{10}$	-	12.0	0.26	19.1	68.6	$Ca_{1.87}Sm_{0.04}Nb_{3.00}O_{10.9}$
$Ca_{1.95}Sm_{0.05}Nb_3O_{10}^{0.95-}$	-	12.1	0.33	18.5	69.1	$Ca_{1.96}Sm_{0.05}Nb_{3.00}O_{11.2}$
$K_{0.95}Ca_{1.95}Gd_{0.05}Nb_3O_{10}$	0.15	8.17	0.19	13.3	74.1	$K_{1.01}Ca_{1.84}Gd_{0.04}Nb_{3.00}O_{16.8}$
$H_{0.95}Ca_{1.95}Gd_{0.05}Nb_3O_{10}$	-	9.69	0.27	15.73	74.31	$Ca_{1.85}Gd_{0.05}Nb_{3.00}O_{14.2}$
$Ca_{1.95}Gd_{0.05}Nb_3O_{10}^{0.95-}$	-	10.8	0.27	17.2	71.6	$Ca_{1.88}Gd_{0.05}Nb_{3.00}O_{12.7}$
$K_{0.95}Ca_{1.95}Tb_{0.05}Nb_3O_{10}$	-	8.88	0.28	11.6	76.0	$Ca_{2.31}Tb_{0.42}Nb_{3.00}O_{19.7}$
$H_{0.95}Ca_{1.95}Tb_{0.05}Nb_3O_{10}$	-	7.60	0.34	13.0	78.4	$Ca_{1.75}Tb_{0.08}Nb_{3.00}O_{18.1}$
$Ca_{1.95}Tb_{0.05}Nb_3O_{10}^{0.95-}$	-	13.2	0.58	20.5	65.7	$Ca_{1.93}Tb_{0.08}Nb_{3.00}O_{9.62}$
$K_{0.95}Ca_{1.95}Dy_{0.05}Nb_3O_{10}$	3.86	9.19	0.21	15.0	70.7	$K_{0.98}Ca_{1.84}Dy_{0.04}Nb_{3.00}O_{14.5}$
$H_{0.95}Ca_{1.95}Dy_{0.05}Nb_3O_{10}$	-	9.04	0.25	14.8	75.9	$Ca_{1.83}Dy_{0.05}Nb_{3.00}O_{15.4}$
$Ca_{1.95}Dy_{0.05}Nb_3O_{10}^{0.95-}$	-	11.6	0.29	18.1	69.8	$Ca_{1.92}Dy_{0.05}Nb_{3.00}O_{11.7}$
$K_{0.95}Ca_{1.95}Ho_{0.05}Nb_3O_{10}$	3.86	7.35	0.18	12.1	76.5	$K_{0.95}Ca_{1.81}Ho_{0.05}Nb_{3.00}O_{20.0}$
$H_{0.95}Ca_{1.95}Ho_{0.05}Nb_3O_{10}$	-	11.6	0.28	18.3	69.8	$Ca_{1.91}Ho_{0.05}Nb_{3.00}O_{11.5}$
$Ca_{1.95}Ho_{0.05}Nb_3O_{10}^{0.95-}$	-	10.8	0.23	17.2	71.8	$Ca_{1.88}Ho_{0.04}Nb_{3.00}O_{12.6}$
$K_{0.95}Ca_{1.95}Er_{0.05}Nb_3O_{10}$	5.02	9.22	0.10	15.0	70.7	$K_{1.19}Ca_{1.84}Er_{0.02}Nb_{3.00}O_{16.6}$
$H_{0.95}Ca_{1.95}Er_{0.05}Nb_3O_{10}$	-	10.2	0.45	16.3	73.2	$Ca_{1.88}Er_{0.03}Nb_{3.00}O_{13.5}$
$Ca_{1.95}Er_{0.05}Nb_3O_{10}^{0.95-}$	-	12.5	0.28	18.9	68.4	$Ca_{1.97}Er_{0.04}Nb_{3.00}O_{11.5}$
$K_{0.95}Ca_{1.95}Tm_{0.05}Nb_3O_{10}$	4.82	0.91	0.24	14.6	71.2	$K_{0.97}Ca_{1.85}Tm_{0.05}Nb_{3.00}O_{14.6}$
$H_{0.95}Ca_{1.95}Tm_{0.05}Nb_3O_{10}$	-	8.48	0.28	14.1	77.1	$Ca_{1.80}Tm_{0.06}Nb_{3.00}O_{17.0}$
$Ca_{1.95}Tm_{0.05}Nb_3O_{10}^{0.95-}$	-	10.1	0.26	16.2	73.4	$Ca_{1.88}Tm_{0.05}Nb_{3.00}O_{13.6}$
$K_{0.95}Ca_{1.95}Yb_{0.05}Nb_3O_{10}$	0.15	9.93	0.20	12.8	64.4	$K_{0.04}Ca_{2.36}Yb_{0.05}Nb_{3.00}O_{15.2}$
$H_{0.95}Ca_{1.95}Yb_{0.05}Nb_3O_{10}$	-	10.2	0.24	16.3	73.3	$Ca_{1.87}Yb_{0.04}Nb_{3.00}O_{13.6}$
$Ca_{1.95}Yb_{0.05}Nb_3O_{10}^{0.95-}$	-	11.9	0.28	18.2	69.7	$Ca_{1.96}Yb_{0.05}Nb_{3.00}O_{11.6}$

**Table S3.2.2:** EDX measurements of  $K_{0.75}Ca_{1.75}Ln_{0.25}Nb_3O_{10}$  and  $H_{0.75}Ca_{1.75}Ln_{0.25}Nb_3O_{10}$  nanosheets ( $Ln = La, Pr, Nd, Sm, Gd, Tb, Dy, Ho, Er, Tm, Yb$ ) given in at%. at% values are average values of three EDX measurements.

Theoretical formula	K [%]	Ca [%]	Ln [%]	Nb [%]	O [%]	Experimental formula
$K_{0.75}Ca_{1.75}La_{0.25}Nb_3O_{10}$	5.44	8.94	1.15	16.4	68.0	$K_{1.00}Ca_{1.64}La_{0.21}Nb_{3.00}O_{12.5}$
$H_{0.75}Ca_{1.75}La_{0.25}Nb_3O_{10}$	-	10.1	1.30	15.8	72.83	$Ca_{1.90}La_{0.25}Nb_{3.00}O_{14.1}$
$K_{0.75}Ca_{1.75}Pr_{0.25}Nb_3O_{10}$	3.31	5.37	0.93	12.9	77.5	$K_{0.78}Ca_{1.24}Pr_{0.22}Nb_{3.00}O_{19.5}$
$H_{0.75}Ca_{1.75}Pr_{0.25}Nb_3O_{10}$	1.77	5.33	1.33	14.5	77.1	$K_{0.37}Ca_{1.11}Pr_{0.28}Nb_{3.00}O_{16.1}$
$K_{0.75}Ca_{1.75}Nd_{0.25}Nb_3O_{10}$	4.71	8.61	0.91	14.9	70.9	$K_{0.94}Ca_{1.72}Nd_{0.18}Nb_{3.00}O_{17.7}$
$H_{0.75}Ca_{1.75}Nd_{0.25}Nb_3O_{10}$	-	8.55	0.86	14.9	75.7	$Ca_{1.70}Nd_{0.17}Nb_{3.00}O_{15.8}$
$K_{0.75}Ca_{1.75}Sm_{0.25}Nb_3O_{10}$	3.28	8.25	0.57	15.3	72.4	$K_{0.65}Ca_{1.29}Sm_{0.11}Nb_{3.00}O_{14.2}$
$H_{0.75}Ca_{1.75}Sm_{0.25}Nb_3O_{10}$	-	7.95	0.56	14.5	76.9	$Ca_{1.64}Sm_{0.12}Nb_{3.00}O_{15.8}$
$K_{0.75}Ca_{1.75}Gd_{0.25}Nb_3O_{10}$	5.08	9.24	0.68	15.6	69.4	$K_{0.98}Ca_{1.52}Gd_{0.13}Nb_{3.00}O_{13.7}$
$H_{0.75}Ca_{1.75}Gd_{0.25}Nb_3O_{10}$	-	8.20	0.73	14.7	76.4	$Ca_{1.68}Gd_{0.15}Nb_{3.00}O_{16.3}$
$K_{0.75}Ca_{1.75}Dy_{0.25}Nb_3O_{10}$	3.54	7.42	0.58	31.1	75.3	$K_{0.81}Ca_{1.69}Dy_{0.13}Nb_{3.00}O_{17.4}$
$H_{0.75}Ca_{1.75}Dy_{0.25}Nb_3O_{10}$	-	8.98	0.74	15.0	75.2	$Ca_{1.80}Dy_{0.15}Nb_{3.00}O_{15.4}$
$K_{0.75}Ca_{1.75}Ho_{0.25}Nb_3O_{10}$	3.39	5.41	0.64	11.7	78.9	$K_{0.87}Ca_{1.37}Ho_{0.17}Nb_{3.00}O_{20.4}$
$H_{0.75}Ca_{1.75}Ho_{0.25}Nb_3O_{10}$	-	8.98	0.35	16.2	74.5	$Ca_{1.69}Ho_{0.07}Nb_{3.00}O_{15.1}$
$K_{0.75}Ca_{1.75}Er_{0.25}Nb_3O_{10}$	1.47	7.58	0.26	15.6	75.1	$K_{0.35}Ca_{1.47}Er_{0.06}Nb_{3.00}O_{14.9}$
$H_{0.75}Ca_{1.75}Er_{0.25}Nb_3O_{10}$	-	10.1	0.32	16.5	72.9	$Ca_{1.84}Er_{0.05}Nb_{3.00}O_{13.4}$
$K_{0.75}Ca_{1.75}Tm_{0.25}Nb_3O_{10}$	2.47	8.56	0.62	12.52	75.8	$K_{0.60}Ca_{1.72}Tm_{0.15}Nb_{3.00}O_{18.2}$
$H_{0.75}Ca_{1.75}Tm_{0.25}Nb_3O_{10}$	-	7.72	1.34	13.4	77.5	$Ca_{1.63}Tm_{0.63}Nb_{3.00}O_{14.3}$
$K_{0.75}Ca_{1.75}Yb_{0.25}Nb_3O_{10}$	5.94	3.36	0.51	14.4	75.8	$K_{1.27}Ca_{0.69}Yb_{0.10}Nb_{3.00}O_{16.2}$
$H_{0.75}Ca_{1.75}Yb_{0.25}Nb_3O_{10}$	3.59	4.65	1.32	16.1	74.3	$K_{0.64}Ca_{0.90}Yb_{0.24}Nb_{3.00}O_{14.0}$

**Table S3.2.3:** EDX measurements of  $K_{0.50}Ca_{1.50}Ln_{0.50}Nb_3O_{10}$  and  $H_{0.50}Ca_{1.50}Ln_{0.50}Nb_3O_{10}$  nanosheets ( $Ln = La, Pr, Nd, Sm, Gd, Tb, Dy, Ho, Er, Tm, Yb$ ) given in at%. at% values are average values of three EDX measurements.

Theoretical formula	K [%]	Ca [%]	Ln [%]	Nb [%]	O [%]	Experimental formula
$K_{0.5}Ca_{1.5}La_{0.5}Nb_3O_{10}$	2.87	7.65	1.49	13.0	75.1	$K_{0.69}Ca_{1.76}La_{0.34}Nb_{3.00}O_{17.5}$
$H_{0.5}Ca_{1.5}TLa_{0.5}Nb_3O_{10}$	-	8.50	1.83	15.0	74.7	$Ca_{1.71}La_{0.40}Nb_{3.00}O_{15.0}$
$K_{0.5}Ca_{1.5}Pr_{0.5}Nb_3O_{10}$	4.40	6.36	1.26	14.7	73.3	$K_{0.90}Ca_{1.31}Pr_{0.26}Nb_{3.00}O_{14.5}$
$H_{0.5}Ca_{1.5}Pr_{0.5}Nb_3O_{10}$	-	7.13	1.21	5.48	76.9	$Ca_{1.45}Pr_{0.24}Nb_{3.00}O_{15.8}$
$K_{0.5}Ca_{1.5}Nd_{0.5}Nb_3O_{10}$	3.03	7.66	0.98	15.0	73.4	$K_{0.62}Ca_{1.54}Nd_{0.20}Nb_{3.00}O_{14.8}$
$H_{0.5}Ca_{1.5}Nd_{0.5}Nb_3O_{10}$	0.07	6.80	0.72	14.4	78.0	$K_{0.01}Ca_{1.42}Nd_{0.20}Nb_{3.00}O_{16.3}$
$K_{0.5}Ca_{1.5}Sm_{0.5}Nb_3O_{10}$	1.34	6.52	0.62	13.6	77.9	$K_{0.28}Ca_{1.43}Sm_{0.14}Nb_{3.00}O_{17.3}$
$H_{0.5}Ca_{1.5}Sm_{0.5}Nb_3O_{10}$	-	5.77	0.58	12.3	81.4	$Ca_{1.42}Sm_{0.15}Nb_{3.00}O_{20.1}$
$K_{0.5}Ca_{1.5}Gd_{0.5}Nb_3O_{10}$	4.03	7.94	0.79	13.8	73.4	$K_{0.86}Ca_{1.70}Gd_{0.18}Nb_{3.00}O_{16.6}$
$H_{0.5}Ca_{1.5}Gd_{0.5}Nb_3O_{10}$	-	7.13	1.12	15.8	77.0	$Ca_{1.46}Gd_{0.24}Nb_{3.00}O_{16.2}$
$K_{0.5}Ca_{1.5}Dy_{0.5}Nb_3O_{10}$	2.70	7.99	0.67	15.3	73.3	$K_{0.61}Ca_{1.07}Dy_{0.14}Nb_{3.00}O_{15.0}$
$H_{0.5}Ca_{1.5}Dy_{0.5}Nb_3O_{10}$	-	9.21	0.79	16.5	73.5	$Ca_{1.65}Dy_{0.14}Nb_{3.00}O_{14.0}$
$K_{0.5}Ca_{1.5}Ho_{0.5}Nb_3O_{10}$	4.14	5.32	0.68	13.3	76.7	$K_{0.93}Ca_{1.65}Ho_{0.14}Nb_{3.00}O_{17.7}$
$H_{0.5}Ca_{1.5}Ho_{0.5}Nb_3O_{10}$	0.25	9.03	0.90	15.2	74.6	$K_{0.05}Ca_{1.78}Ho_{0.17}Nb_{3.00}O_{14.7}$
$K_{0.5}Ca_{1.5}Er_{0.5}Nb_3O_{10}$	2.86	7.05	4.89	15.1	70.07	$K_{0.52}Ca_{1.36}Er_{1.07}Nb_{3.00}O_{14.7}$
$H_{0.5}Ca_{1.5}Er_{0.5}Nb_3O_{10}$	-	8.79	0.34	14.3	76.7	$Ca_{1.82}Er_{0.07}Nb_{3.00}O_{16.7}$
$K_{0.5}Ca_{1.5}Tm_{0.5}Nb_3O_{10}$	5.41	5.01	0.74	15.7	73.2	$K_{1.03}Ca_{1.11}Tm_{0.15}Nb_{3.00}O_{14.1}$
$H_{0.5}Ca_{1.5}Tm_{0.5}Nb_3O_{10}$	-	10.5	0.96	15.7	72.9	$Ca_{2.02}Tm_{0.19}Nb_{3.00}O_{14.2}$
$K_{0.5}Ca_{1.5}Yb_{0.5}Nb_3O_{10}$	1.21	4.13	3.72	16.1	75.5	$K_{0.26}Ca_{0.47}Yb_{0.69}Nb_{3.00}O_{14.7}$
$H_{0.5}Ca_{1.5}Yb_{0.5}Nb_3O_{10}$	3.43	2.50	0.51	17.4	76.2	$K_{0.55}Ca_{0.49}Yb_{0.09}Nb_{3.00}O_{13.4}$

**Table S3.2.4:** EDX measurements of  $K_{0.25}Ca_{1.25}Ln_{0.75}Nb_3O_{10}$  and  $H_{0.25}Ca_{1.25}Ln_{0.75}Nb_3O_{10}$  nanosheets ( $Ln = La, Pr, Nd, Sm, Gd, Tb, Dy, Ho, Er, Tm, Yb$ ) given in at%. at% values are average values of three EDX measurements.

Theoretical formula	K [%]	Ca [%]	Ln [%]	Nb [%]	O [%]	Experimental formula
$K_{0.25}Ca_{1.25}La_{0.75}Nb_3O_{10}$	1.78	6.14	1.52	14.2	76.2	$K_{0.38}Ca_{1.30}La_{0.33}Nb_{3.00}O_{16.4}$
$H_{0.25}Ca_{1.25}La_{0.75}Nb_3O_{10}$	-	5.52	0.92	13.0	80.6	$Ca_{1.27}La_{0.22}Nb_{3.00}O_{19.0}$
$K_{0.25}Ca_{1.25}Pr_{0.75}Nb_3O_{10}$	-	5.28	5.87	10.3	78.4	$Ca_{1.52}Pr_{1.72}Nb_{3.00}O_{16.3}$
$K_{0.25}Ca_{1.25}Nd_{0.75}Nb_3O_{10}$	-	7.62	0.94	16.8	74.6	$Ca_{1.35}Nd_{0.17}Nb_{3.00}O_{13.4}$
$H_{0.25}Ca_{1.25}Nd_{0.75}Nb_3O_{10}$	-	6.45	0.73	14.4	78.5	$Ca_{1.35}Nd_{0.16}Nb_{3.00}O_{16.8}$
$K_{0.25}Ca_{1.25}Sm_{0.75}Nb_3O_{10}$	3.08	6.77	1.57	13.4	75.0	$K_{0.70}Ca_{1.52}Sm_{0.35}Nb_{3.00}O_{16.9}$
$H_{0.25}Ca_{1.25}Sm_{0.75}Nb_3O_{10}$	-	6.74	2.08	14.1	77.0	$Ca_{1.39}Sm_{0.47}Nb_{3.00}O_{16.8}$
$K_{0.25}Ca_{1.25}Gd_{0.75}Nb_3O_{10}$	0.08	4.07	2.81	11.9	81.2	$K_{0.02}Ca_{1.37}Gd_{0.07}Nb_{3.00}O_{19.4}$
$H_{0.25}Ca_{1.25}Gd_{0.75}Nb_3O_{10}$	-	6.74	2.08	14.1	77.0	$Ca_{1.43}Gd_{0.24}Nb_{3.00}O_{18.7}$
$K_{0.25}Ca_{1.25}Dy_{0.75}Nb_3O_{10}$	1.42	8.40	0.87	17.87	71.1	$K_{0.27}Ca_{1.16}Dy_{0.21}Nb_{3.00}O_{12.2}$
$H_{0.25}Ca_{1.25}Dy_{0.75}Nb_3O_{10}$	-	5.17	1.85	12.0	81.0	$Ca_{1.29}Dy_{0.48}Nb_{3.00}O_{20.5}$
$K_{0.25}Ca_{1.25}Ho_{0.75}Nb_3O_{10}$	0.09	6.18	0.89	14.3	78.9	$K_{0.02}Ca_{1.30}Ho_{0.19}Nb_{3.00}O_{16.8}$
$H_{0.25}Ca_{1.25}Ho_{0.75}Nb_3O_{10}$	-	5.08	8.04	17.9	68.9	$Ca_{0.72}Ho_{1.57}Nb_{3.00}O_{12.2}$
$K_{0.25}Ca_{1.25}Er_{0.75}Nb_3O_{10}$	0.40	3.13	7.16	13.1	75.7	$K_{0.23}Ca_{0.43}Er_{1.56}Nb_{3.00}O_{18.3}$
$H_{0.25}Ca_{1.25}Er_{0.75}Nb_3O_{10}$	-	6.74	1.85	14.7	76.7	$Ca_{1.37}Er_{0.40}Nb_{3.00}O_{16.1}$
$K_{0.25}Ca_{1.25}Tm_{0.75}Nb_3O_{10}$	-	11.8	4.46	10.2	73.5	$Ca_{3.73}Tm_{1.24}Nb_{3.00}O_{21.7}$
$H_{0.25}Ca_{1.25}Tm_{0.75}Nb_3O_{10}$	3.06	1.53	0.48	18.5	78.2	$K_{0.22}Ca_{0.36}Tm_{0.09}Nb_{3.00}O_{13.7}$
$K_{0.25}Ca_{1.25}Yb_{0.75}Nb_3O_{10}$	5.07	3.57	1.17	16.3	73.9	$K_{0.93}Ca_{0.66}Yb_{0.22}Nb_{3.00}O_{13.6}$
$H_{0.25}Ca_{1.25}Yb_{0.75}Nb_3O_{10}$	-	6.69	0.78	13.6	78.9	$Ca_{1.48}Yb_{0.17}Nb_{3.00}O_{17.5}$

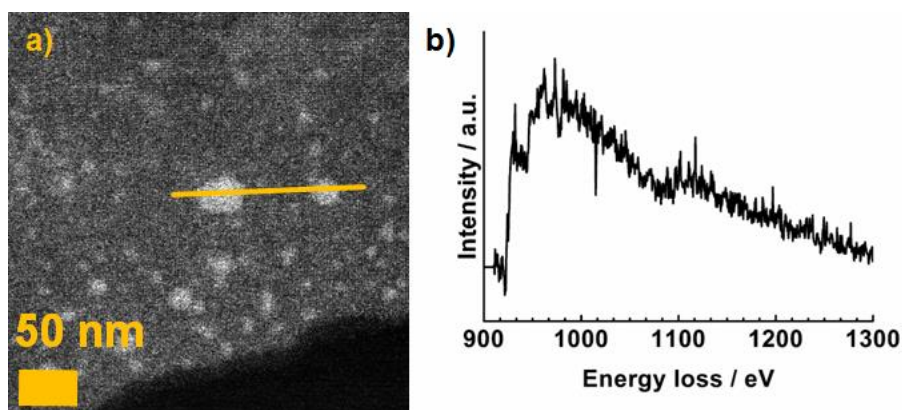


**Figure S3.2.6:** a) STEM image of a  $TBA_{0.25}Ca_{1.25}Eu_{0.75}Nb_3O_{10}$  nanosheet and EELS line scan (orange bar), and b) corresponding extracted Cu  $L_{2,3}$  edge based on the EELS line scan showing that bright particles belong to a copper impurity.

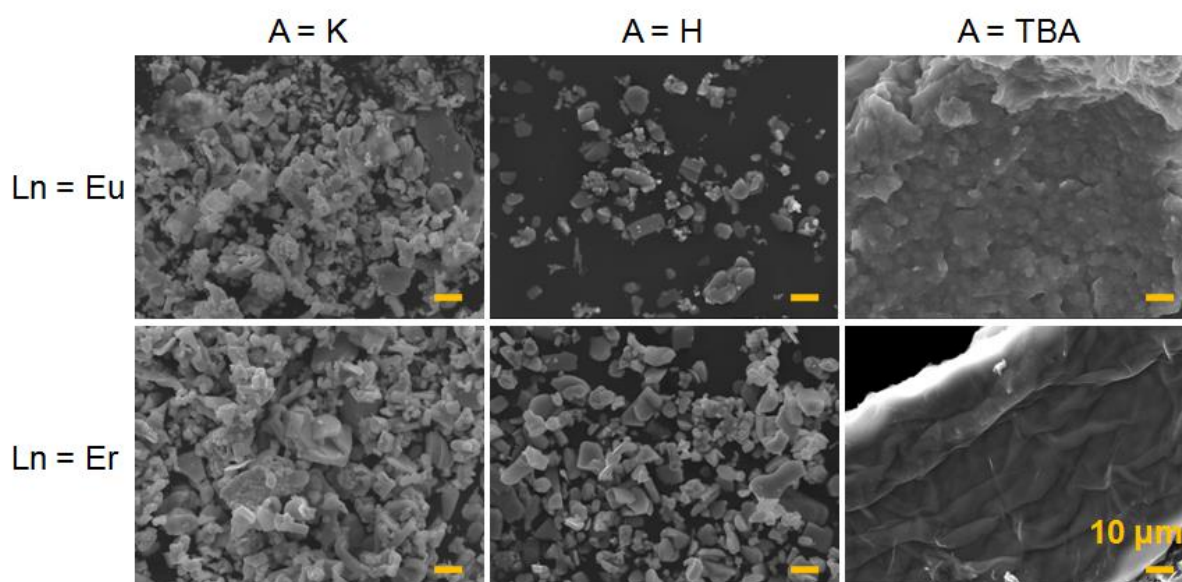


**Figure S3.2.7:** SEM images of  $A_{0.5}Sr_{1.5}Ln_{0.5}Nb_3O_{10}$  ( $A = K, H, TBA, Ln = Eu, Er$ ) showing plate-like morphologies for all samples.

#### BIBLIOGRAPHY:

- [1] S. Uma, J. Gopalakrishnan, *J. Solid State Chem.* **1993**, 102, 332-339.
- [2] M. A. Bizeto, V. R. L. Constantino, H. F. Brito, *J. Alloys Compd.* **2000**, 311, 159-168.
- [3] K. Domen, J. Yoshimura, T. Sekine, A. Tanaka, T. Onishi, *Catal. Lett.* **1990**, 4, 339-343.
- [4] V. Thangadurai, P. Schmid-Beurmann, W. Weppner, *J. Solid State Chem.* **2001**, 158, 279-289.
- [5] T. Tokumitsu, K. Toda, T. Aoyagi, D. Sakuraba, K. Uematsu, M. Sato, *J. Ceram. Soc. Jpn.* **2006**, 114, 795-797.

### 3.3 Exfoliation of Silver Exchanged Layered Transition Metal Oxides with Bulky Organic Iodides

Christian Ziegler, Pirmin Ganter, Anne Friedrichs, Viola Duppel, Christina Scheu,  
Bettina V. Lotsch

*Manuscript to be submitted.*

**ABSTRACT:** Layered transition metal oxide (TMO) nanosheets have emerged as one of the most promising classes of two-dimensional (2D) materials in the post-graphene area due to their diversity in composition, structure, and functionality. Improving and extending exfoliation pathways is currently one key requirement for the posterior fabrication of functional devices utilizing nanosheets as principal components. Here, we present a new exfoliation route on the examples of Dion-Jacobson (DJ) type layered perovskites  $\text{KLaNb}_2\text{O}_7$  and  $\text{KCa}_2\text{Nb}_3\text{O}_{10}$  that allows for a simple introduction of organic ligands with functional groups into the intergallery space and, subsequently, attachment to the nanosheet surface during the exfoliation process. Interlayer cation-silver exchange of the bulk materials and subsequent treatment with bulky organic iodides in an aqueous medium under weak agitation forces leads to the formation of unilamellar nanosheets. The silver based route yields nanosheets that are similar in quality compared to those achieved through the commonly applied route *via* a cation-proton exchange and subsequent treatment with organic bases, but beyond that allows for an enormous extension of the applicable exfoliation reagents. Thus, it was possible to attach choline, thiocholine and 1-allyl-3-methylimidazolium ligands with functional hydroxyl groups, thiol groups or a double bond, respectively, to the nanosheet. Preliminary investigations on various tantalate nanosheets show that the silver based route can be extended to other layered systems and can act as complementary pathway to the proton based route.

#### 3.3.1 Introduction

Topochemical reactions are considered to be the toolbox of solid-state chemists, while mostly relying on the kinetic control of product phases under low-temperature conditions rather than on the thermodynamically controlled product formation under high-temperature conditions. Although still limited compared to the large library of organic reactions, topochemical reactions have made some astonishing progress within the last decades. Focusing on layered TMOs and especially layered perovskites, (de)intercalation, layer extraction or construction, pillaring, substitution, ion exchange and grafting reactions have become a tool of choice to manipulate crystalline lattices and hence, direct properties into a

certain direction.<sup>1-3</sup> The ultimate goal is the establishment of a reaction library that allows for the rational design of new targeted compounds with specific properties and their utilization in fields like catalysis, optics, superconductivity and many others. While the listed topochemical modifications mostly deal with the retention of crystalline integrity, exfoliation of layered TMOs offers another promising approach to amplify the existing toolbox. Exfoliation denotes the separation of layered materials into individual 2D nanosheets with heights around 1 nm and a lateral size up to a few micrometers. The nanosheets themselves show intriguing properties due to their enhanced surface and quantum-confinement effects, and in addition can serve as building blocks for the fabrication of tailor-made devices.<sup>4-6</sup>

In a typical two-step route, interlayer ions of layered TMOs are first exchanged against protons and the obtained solid acid is further reacted with bulky organic bases, usually quarternary ammonium hydroxides like tetra-*n*-butylammonium hydroxide ( $TBA^+OH^-$ ). Exfoliation is then facilitated for the appropriate reagent ratio and mechanical forces like shaking or stirring. Single layers of Ti-, Mn-, Nb-, Ta-, Mo-, Ru-, and W oxides as well as sheets of several perovskites have been separated from bulk samples through this procedure.<sup>4-7</sup> In this ion-exchange based exfoliation route, a chemical intercalant is always required that assists in the separation of layers, compensates the charge and hampers the reassembly of the bulk lamellar material. Thus, TMO nanosheets can be seen as combination of an inorganic nanosheet with an organic ligand.

Up to now, the main focus in the literature is based on the exfoliation of new materials and the exploration of their properties, which is mainly related to the inorganic part of the nanosheets. On the contrary, less is known on the chemical manipulation based on the organic part attached to the TMO nanosheets. Recently, Shori *et al.* showed that phenylphosphonate (PPA) can be directly grafted onto the hydroxyl groups of exfoliated calcium niobate nanosheets.<sup>8</sup> Kim *et al.* have shown that (3-aminopropyl)trimethoxysilane (APS) can be coupled onto the hydroxyl groups of  $TBACa_2Nb_3O_{10}$  nanosheets and that the functional amino-group can further be utilized to bind oleic acid-ligated magnetic  $Fe_3O_4$  clusters.<sup>9</sup> This approach was further extended to bind citrate-stabilized Pt and  $IrO_2$  particles to the APS-functionalized nanosheets.<sup>10</sup> Another approach was performed by Mochizuki *et al.* where octylamine was intercalated into a layered tungstate  $H_2W_2O_7$  as well as a layered titanate  $H_xTi_{2-x/4}\square_{x/4}O_4$ . The titanate was further reacted with allyltrimethoxysilane to immobilize alkene groups, and the tungstate was hybridized with 3-mercaptopropyltrimethoxysilane to insert thiol groups.<sup>11</sup> After exfoliation of the materials *via* ultrasonication, a thiol-ene click reaction was performed between the two “functional” nanosheets. This approach was used for tuning the interlayer distances by varying the chain-length of organic ligands as well as subsequent intercalation of cationic dyes like rhodamine B into the hybrid materials.<sup>12-13</sup> These examples indicate the feasibility of

combining organic with inorganic synthesis protocols, though a general approach for introducing of functional ligands on the nanosheet surface without post-modification of the nanosheet is still missing.

Here, we present a new exfoliation pathway based on the cation-silver exchange of layered bulk materials and the subsequent addition of bulky organic iodides that allows for introducing ligands with various functional groups.<sup>14</sup> Through electron microscopy and atomic force microscopy (AFM) we show on the example of  $\text{KLaNb}_2\text{O}_7$ ,  $\text{KCa}_2\text{Nb}_3\text{O}_{10}$  and various other layered materials that nanosheets similar in quality to those of the commonly performed cation-proton exchanged route can be obtained. For the first time we used choline, thiocholine and 1-allyl-3-methylimidazolium as organic ligands to introduce hydroxyl groups, thiol groups or double bonds, respectively, onto the inorganic nanosheets. We believe that this new exfoliation pathway further narrows the gap between organic and inorganic synthesis protocols and can be interpreted in terms of the Pearson acid base concept, which may help to gain fundamental knowledge of the required driving forces to establish exfoliation for a specific system in the near future.

### 3.3.2 Results and Discussion

Powder X-ray diffraction (XRD) patterns of  $\text{KLaNb}_2\text{O}_7$ ,  $\text{KCa}_2\text{Nb}_3\text{O}_{10}$  and their cation-silver exchanged forms are shown in Figure 3.3.1, those for their cation-proton exchanged forms in Figure S3.3.1.  $\text{KLaNb}_2\text{O}_7$  and  $\text{KCa}_2\text{Nb}_3\text{O}_{10}$  are DJ type layered perovskites that crystallize in space group  $C222$  (No. 21) or  $P2_1/m$  (No. 11), respectively.<sup>15-16</sup> They consist of a 2D double or triple perovskite layer of corner-sharing  $\text{NbO}_6$  octahedra with La or Ca located in the intralayer A sites and K in the interlayer region, which separates the perovskite blocks along the stacking direction  $c$ . Both precursors were synthesized similar to routes known from literature and match well with the reported structures.<sup>15-16</sup> The same accounts for the cation-proton exchanged materials  $\text{HLaNb}_2\text{O}_7$  ( $P4/m$ , No. 83),  $\text{HCa}_2\text{Nb}_3\text{O}_{10}$  ( $P4/mbm$ , No. 127) and cation-silver exchanged  $\text{AgLaNb}_2\text{O}_7$  ( $I4_1/acd$ , No. 142).<sup>17-19</sup> Additionally, EDX data show the expected atomic ratios of incorporated elements listed in Table S3.3.1. The layered motif is kept for all of the exchanged materials, only differences in size of the introduced ions can either lead to a distortion of the  $\text{NbO}_6$  octahedra or a shift of the perovskite layers with respect to each other, thus altering the overall symmetry.  $\text{AgCa}_2\text{Nb}_3\text{O}_{10}$  is the only compound whose structure has not yet been determined, but has been part of a recent study of Boltersdorf and Maggard.<sup>20</sup> Similar to their findings we observe with energy dispersive X-ray (EDX) spectroscopy and inductively coupled plasma - atomic emission spectroscopy (ICP-AES) that the interlayer cations can be completely replaced by Ag (Table S3.3.1 and Table S3.3.2), while the XRD pattern exhibits a lower degree in crystallinity compared to the bulk material (Figure 3.3.1 c). Boltersdorf and Maggard related the  $\text{AgCa}_2\text{Nb}_3\text{O}_{10}$  structure to



layered  $\text{Ag}_{1.1}\text{Ca}_{0.9}[\text{Ca}_{0.6}\text{Ag}_{0.9}\text{Nb}_3\text{O}_{10}]$ , where Ag(I) and Ca(II) ions occupy both interlayer and intralayer positions.<sup>21</sup> As we will show later through exfoliation experiments, EDX data of calcium niobate nanosheets do not give any evidence for the presence of Ag within the nanosheets and show the expected composition related to  $[\text{Ca}_2\text{Nb}_3\text{O}_{10}]^-$  perovskite blocks. Thus, we reason that the cation-silver exchange most likely leads to structural changes similar to the ones observed for the ion-exchange reactions described above. In the case of  $\text{AgCa}_2\text{Nb}_3\text{O}_{10}$  this change causes the near-extinction of the (00 $\ell$ ) reflections and compared to the bulk material a general shift of the reflections towards higher angles, which is most likely caused by the smaller ionic radii of  $\text{Ag}^+$  compared to  $\text{K}^+$ . Some additional reflections e.g. around 37 and 61° 2 $\theta$  appear, that do not match any known phases out of the participating elements in the ICSD database and are hence also be attributed to  $\text{AgCa}_2\text{Nb}_3\text{O}_{10}$ .

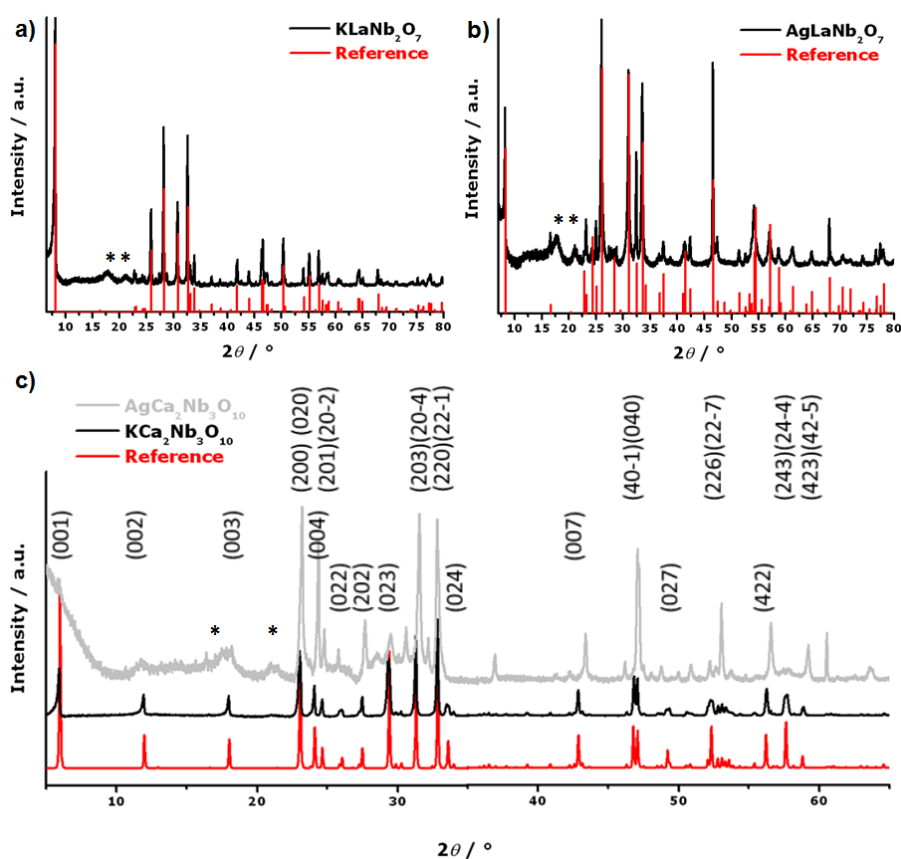


**Figure 3.3.1:** XRD patterns of a)  $\text{KLaNb}_2\text{O}_7$ , b)  $\text{AgLaNb}_2\text{O}_7$  and c)  $\text{KCa}_2\text{Nb}_3\text{O}_{10}$  and  $\text{AgCa}_2\text{Nb}_3\text{O}_{10}$  in comparison with the respective simulated powder patterns taken from the ICSD database.<sup>15-16, 19</sup> Note that the broad reflections around 18°2 $\theta$  and 23°2 $\theta$  marked with an asterisk are due to the polyester mounting foil in the XRD setup.

An overview and comparison of the exfoliation experiments conducted with  $\text{KLaNb}_2\text{O}_7$  is displayed in Figure 3.3.2. For separation and exfoliation of the 2D perovskite layers into individual nanosheets the ion-exchange capability of the layered perovskites is a crucial

requirement.<sup>2, 7</sup> In the most common approach depicted in Figure 3.3.2 a) a cation-proton exchange of the interlayer ions yields the “protonated” form  $\text{HLaNb}_2\text{O}_7$  that is further treated with bulky organic bases like *TBAOH* to achieve exfoliation. One main driving force of this reaction interpreted on the basis of the Pearson’s concept of “hard and soft acids and bases” (HSAB) is the acid-base reaction of a relatively “hard” proton  $\text{H}^+$  with a “hard” hydroxide  $\text{OH}^-$ , which is accompanied by the insertion of the bulky organic cation and simultaneous formation of water.<sup>7, 14</sup> This leads to the separation of the perovskite layers to an extent that mechanical agitation like shaking or stirring results in exfoliation of the material. Based on Pearson’s concept we hypothesized that the Lewis acid-base reaction of “soft”  $\text{Ag}^+$  with “soft”  $\text{I}^-$  contained in various ligands (Figure 3.3.2 b)) may likewise present an effective driving force for the exfoliation of layered materials.<sup>14</sup>

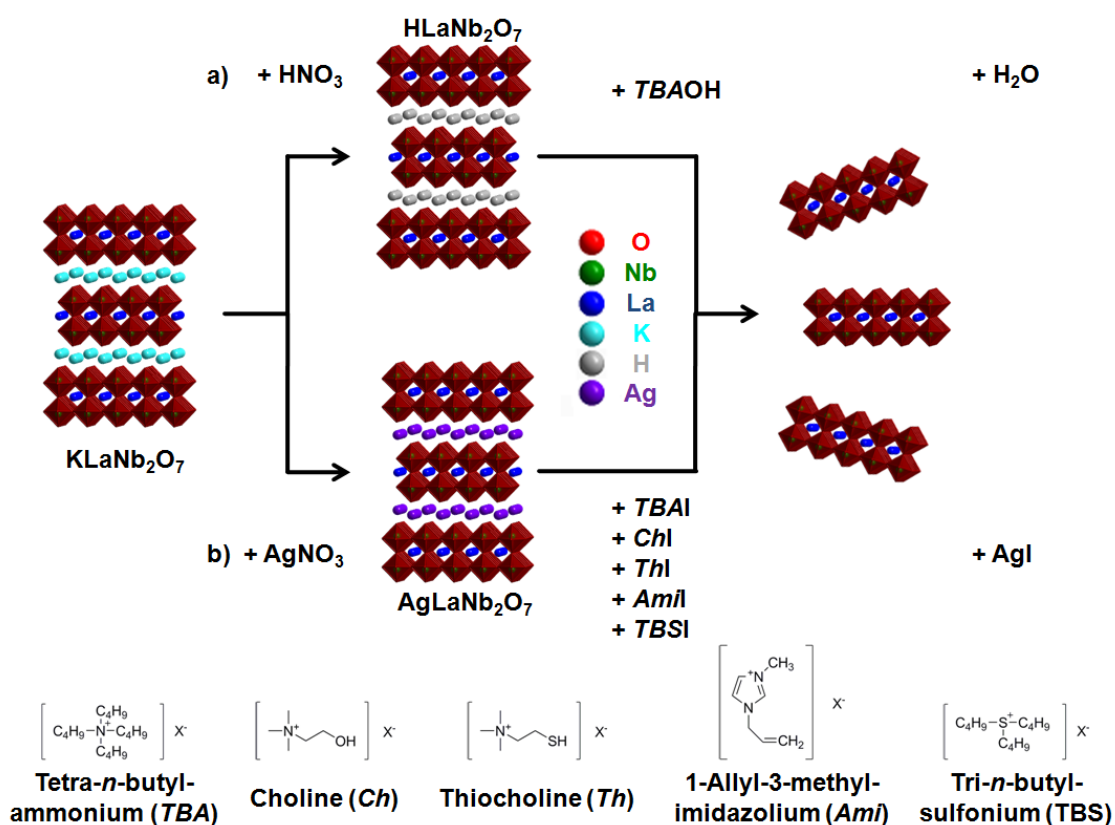


**Figure 3.3.2:** Schematic overview of the exfoliation of  $\text{KLaNb}_2\text{O}_7$  via a)  $\text{HLaNb}_2\text{O}_7$  through addition of bulky organic hydroxides or b)  $\text{AgLaNb}_2\text{O}_7$  through addition of bulky organic iodides into unilamellar nanosheets  $\text{LLaNb}_2\text{O}_7$  ( $L = \text{TBA}, \text{Ch}, \text{Th}, \text{Ami}, \text{TBS}$ ).

TEM and AFM images of  $\text{TBALaNb}_2\text{O}_7$  nanosheets derived from  $\text{AgLaNb}_2\text{O}_7$  and *TBAI* are compared to  $\text{TBALaNb}_2\text{O}_7$  nanosheets derived from  $\text{HLaNb}_2\text{O}_7$  and *TBAOH* in Figure 3.3.3, and likewise for  $\text{TBA}\text{Ca}_2\text{Nb}_3\text{O}_{10}$  in Figure 3.3.4. The corresponding atomic ratios determined by EDX spectroscopy are listed in Table S3.3.3 and match with the ratios of the perovskite layers found for the precursors. Hence, Ag intercalation into the perovskite layer during the cation-silver exchange can largely be excluded.

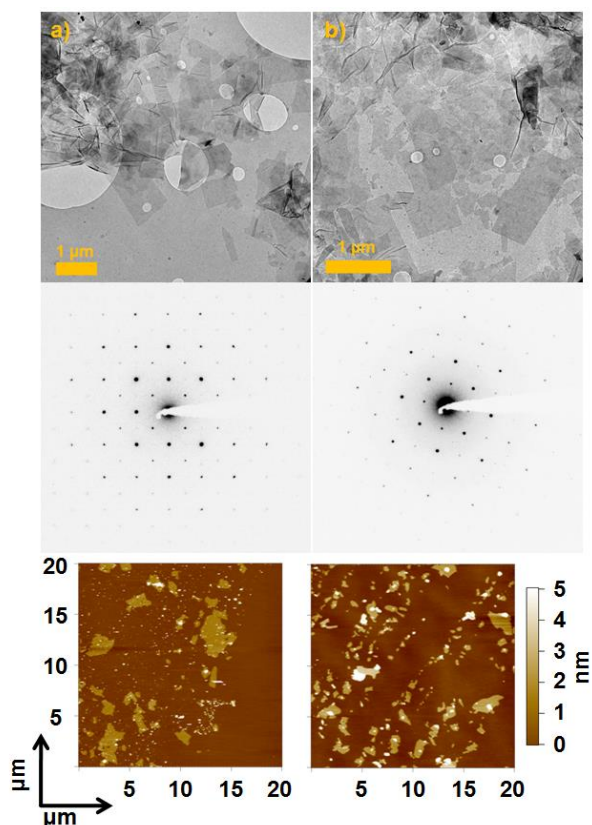


**Figure 3.3.3:** TEM overview images (top), corresponding SAED patterns of single nanosheets along the [001] direction (middle) and AFM overview images of  $TBALaNb_2O_7$  nanosheets (bottom) derived from a)  $AgLaNb_2O_7$  /  $TBAI$  and b)  $HLaNb_2O_7$  /  $TBAOH$ .

For the lanthanum niobate the two exfoliation pathways yielded nanosheets with different lateral sizes ranging from 50 nm-2.5 μm that are randomly distributed over the Si wafer or lacey carbon grid, respectively. Random AFM screening experiments of 3 different 20 μm x 20 μm nanosheet containing areas after a 1 day, 3 days, 5 days and 8 days exfoliation period revealed a similar trend for both methods. After 1 day only a few nanosheets with an initial height of 2.1 nm were observed. Regions with plenty of nanosheets deposited on the Si wafer were obtained after 5 days exfoliation for the silver and 3 days for the proton pathway, pointing towards a somewhat faster separation in the common H-based approach. After 8 days the average height of nanosheets was 2.7 nm in all experiments. Thus, for both materials the height is significantly higher than the crystallographic thickness of the double perovskite layer (~1.05 nm).<sup>22</sup> This is caused by the adsorption of water and the ligand shell surrounding the nanosheet under ambient measurement conditions.<sup>23</sup> In an earlier publication, we showed that subsequent dilution of the colloidal nanosheet suspension can lead to a replacement of  $TBA^+$  cations by  $H^+$  that causes a decrease of the height in the AFM measurements (see Chapter 4.1).<sup>24</sup> Accordingly, in the present case the increase in height with longer exfoliation is consistent with a larger amount of  $TBA^+$  cations attached to the nanosheet surface. As  $TBA^+$  is too large in size to

compensate one negative charge per unit cell, this observation might point towards the attachment of a second  $TBA^+$  layer on the nanosheet surface.<sup>25</sup> SAED patterns and the resulting  $d$ -values are the same within the margin of error (Table S3.3.4) for both unilamellar nanosheets and in accordance with the ones found for the bulk materials along stacking direction.

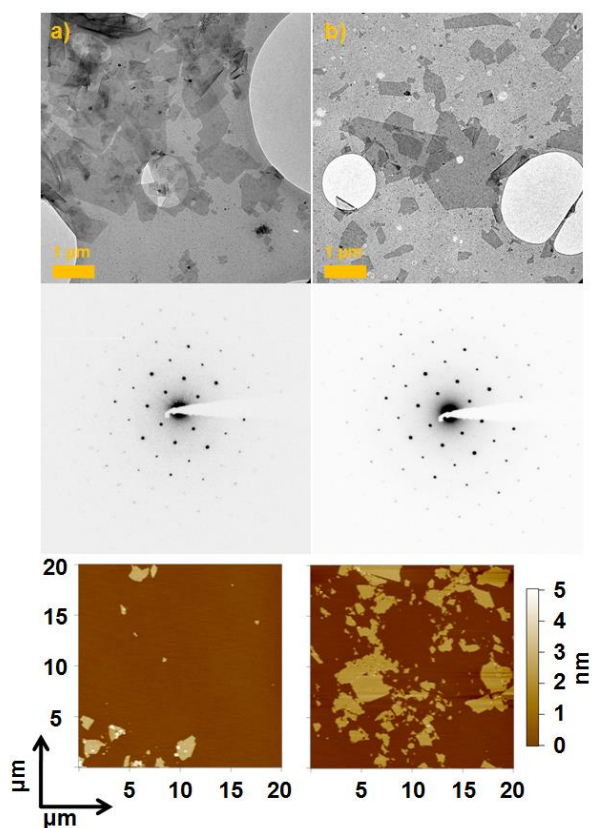


**Figure 3.3.4:** TEM overview images, corresponding SAED patterns of single nanosheets along [001] direction and AFM overview images of  $TBACa_2Nb_3O_{10}$  nanosheets derived from a)  $AgCa_2Nb_3O_{10}$  /  $TBAI$  and b)  $HCa_2Nb_3O_{10}$  /  $TBAOH$ .

Similar observations are made for  $TBACa_2Nb_3O_{10}$  nanosheets derived from  $AgCa_2Nb_3O_{10}$  and  $TBAI$  on the one hand and from  $HCa_2Nb_3O_{10}$  and  $TBAOH$  on the other hand. Nanosheets with lateral dimensions between 50 nm and 2.5 μm are randomly distributed for both exfoliation pathways. For the proton-based approach even slightly larger nanosheets up to 5 μm are found. After 1 day of exfoliation nanosheets with an average height of 2.7 nm are obtained in the beginning that grow to a height around 3.3 nm to 3.5 nm for longer exfoliation periods. The relative difference in height compared to  $TBALaNb_2O_7$  is caused by the larger crystallographic thickness of the triple perovskite layer (~1.44 nm) as compared to the double layer (~1.05 nm).<sup>22</sup> Comparing the changes for both nanosheet types, the absolute difference in height after a 1 day and 8 days exfoliation period is around 0.6 nm in both cases, thus further pointing to the attachment of an additional  $TBA^+$  layer after longer exfoliation periods.

Again, the  $H^+$  approach (3 days) to quantitative exfoliation into  $TBACa_2Nb_3O_{10}$  nanosheets seems to be slightly faster than the  $Ag^+$  (5 days) approach. The extracted  $d$ -values from the SAED patterns are the same within the margin of error for both exfoliation pathways and listed in Table S3.3.4.

Although both exfoliation procedures seem to yield similar results for lanthanum and calcium niobate nanosheets, we like to mention two findings we made for the structurally related tantalate nanosheets  $TBALaTa_2O_7$  and  $TBACa_2Ta_3O_{10}$ . Powder XRD patterns of bulk  $RbLaTa_2O_7$  ( $P4/mmm$ , No. 123) and  $RbCa_2Ta_3O_{10}$  ( $P4/mmm$ , No. 123), their cation proton-exchanged forms  $HLaTa_2O_7$  and  $HCa_2Ta_3O_{10}$ , as well as their cation-silver exchanged forms  $AgLaTa_2O_7$  ( $I4/mmm$ , No. 139) and  $AgCa_2Ta_3O_{10}$  ( $P4/mmm$ , No. 123) are displayed in Figure S3.3.2 along with their EDX quantification data in Table S3.3.5. The bulk structures are similar to those reported in the literature.<sup>26</sup> No reference data was available for comparison of the cation-proton exchanged materials. Judging from EDX data the interlayer  $Rb^+$  cations were completely exchanged for protons in  $HCa_2Ta_3O_{10}$ , but ~30%  $Rb^+$  remained in  $HLaTa_2O_7$ . For both cation-silver exchanged materials the  $Rb^+$  cations can be completely exchanged for  $Ag^+$ , but additional reflections in the XRD may point towards the formation of a minor impurity phase.<sup>27</sup> Exfoliation experiments on the tantalates were conducted in a similar fashion as those of the niobates. AFM images of  $TBALaTa_2O_7$  and  $TBACa_2Ta_3O_{10}$  are compared in Figure S3.3.3. For both exfoliation pathways we did not succeed to produce large amounts of unilamellar nanosheets. Still, despite similarities with the niobate systems we found two main differences for the tantalate systems: First, while the proton approach yielded some nanosheets for  $TBALaTa_2O_7$ , we did not find any after silver based exfoliation. Second, for  $TBACa_2Ta_3O_{10}$  both approaches yielded nanosheets, but with the  $Ag$  route it was possible to isolate unilamellar nanosheets, whilst nanosheets seemed still to be linked together with the  $H$  route. Thus, depending on the layer composition one route might give advantages over the other route.

In the next step, we tested various organic iodides on the silver-exchanged lanthanum and calcium niobates. Choline iodide ( $ChI$ ) was the first iodide investigated.  $Ch^+$  and the  $N,N,N$ -trimethylethanolammonium cations are quarternary ammonium cations like  $TBA^+$ , but instead feature a hydroxyl group at one end. The TEM overview images and corresponding SAED patterns along with AFM images of single  $ChLaNb_2O_7$  and  $ChCa_2Nb_3O_{10}$  nanosheets are depicted in Figure 3.3.5. TEM reveals nanosheets with sharp edges and lateral dimensions of a few hundred nanometers up to ~1.5  $\mu m$  per edge. Their composition and SAED patterns match with those of their  $TBA$ -analogues (Table S3.3.6 and Table S3.3.7). Additionally, we observed the prescence of crystalline silver particles attached to the surface of the nanosheets, as shown for  $ChLaNb_2O_7$  in Figure S3.3.4. The main  $d$ -spacing of 2.34 Å found in the particles belongs to the (111) plane of elemental  $Ag$ . This can be explained as

follows. During exfoliation the interlayer  $\text{Ag}^+$  reacts with the  $\text{I}^-$  to form a yellow  $\text{AgI}$  precipitate that is afterwards removed without nanosheets *via* low-speed centrifugation. A XRD of the dried precipitate is shown in Figure S3.3.4, where the reflections can be assigned to  $\text{AgI}$ . When exfoliation is carried out under light the highly photosensitive  $\text{AgI}$  decomposes to  $\text{Ag} + \frac{1}{2} \text{I}_2$  and the formed silver particles attach to the nanosheet surface. Thus the silver-based exfoliation should be carried out under exclusion of light. On the other hand the silver route might be useful for photochemical labeling, where the exfoliation and photochemical labeling are performed in one step rather than in two steps.<sup>28</sup> Photochemical labeling can be employed to probe charge separation and the distribution of redox-active sites on the surface of nanosheets.

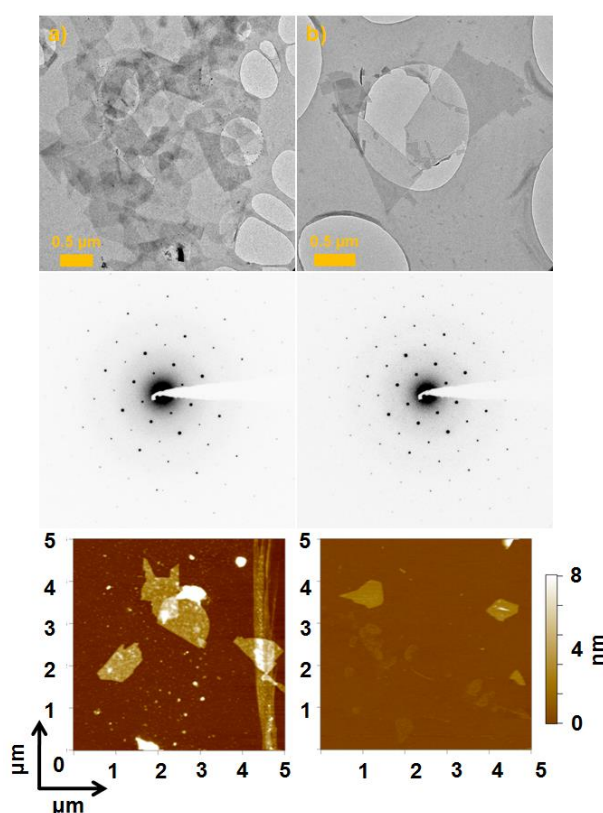


**Figure 3.3.5:** TEM overview images, corresponding SAED patterns of single nanosheets along [001] and AFM overview images of a)  $\text{ChLaNb}_2\text{O}_7$  nanosheets and b)  $\text{ChCa}_2\text{Nb}_3\text{O}_{10}$  nanosheets after silver based exfoliation.

Contrary to the TEM observations, only a few nanosheets are found in the AFM. They exhibit rather round edges and are mostly found on some rough surface. Thus, niobate nanosheets with  $\text{Ch}^+$  attached seem to have a weaker interaction with the Si wafer than those with  $\text{TBA}^+$ , and choline tends to form some kind of organic film on the surface. This film makes assignment of an absolute height difficult. For the  $\text{ChLaNb}_2\text{O}_7$  we found relative heights down to 2.4 nm and for  $\text{ChCa}_2\text{Nb}_3\text{O}_{10}$  down to 2.0 nm proving the formation of unilamellar



nanosheets. At this point we note that the silver exfoliation route was based on the Pearson acid - base concept and thus the formation of AgI instead of  $\text{H}_2\text{O}$ .<sup>14</sup> Our attempts to synthesize  $\text{ChLaNb}_2\text{O}_7$  nanosheets *via* exfoliation of  $\text{AgLaNb}_2\text{O}_7$  with choline chloride ( $\text{ChCl}$ ) or choline hydroxide ( $\text{ChOH}$ ) did not give any evidence for the presence of nanosheets in TEM and AFM analysis, which is in line with the expected higher propensity of  $\text{Ag}^+$  and  $\text{I}^-$  to form insoluble precipitates.

As an alternative exfoliation agent we chose thiocholine iodide ( $\text{ThI}$ ) which exhibits the same structure as choline, but features a thiol group instead of the hydroxyl group. Figure 3.3.6 shows an overview TEM image and the SAED pattern of a single  $\text{ThLaNb}_2\text{O}_7$  nanosheet, the corresponding  $d$ -values are listed in Table S3.3.7 and match with those for lanthanum niobate nanosheets. The EDX plot for  $\text{ThLaNb}_2\text{O}_7$  is given in Figure S3.3.5 showing the presence of all anticipated elements. The S  $\text{K}_\alpha$  signal overlaps with the Nb  $\text{L}_\alpha$  signal, but its maximum is clearly distinguishable proving the successful attachment of  $\text{Th}^+$  to the nanosheet. The nanosheets are similar in size to the previous ones. A height determination *via* AFM was not possible, as the thiocholine forms an organic film worse than choline on the Si wafer making the detection of single nanosheets impossible under the applied conditions. Further, it has to be mentioned that the colloidal  $\text{ThLaNb}_2\text{O}_7$  suspension is only stable for a few days before a precipitate begins to settle down. This might be due to the formation of disulfide bridges, which could explain why we did not obtain  $\text{ThCa}_2\text{Nb}_3\text{O}_{10}$  nanosheets but instead a precipitate at the bottom of the reaction vessel. Addition of e.g. sodium thiosulfate or others along with different solvents have to be tested in future experiments to stabilize colloidal suspensions.<sup>29</sup>

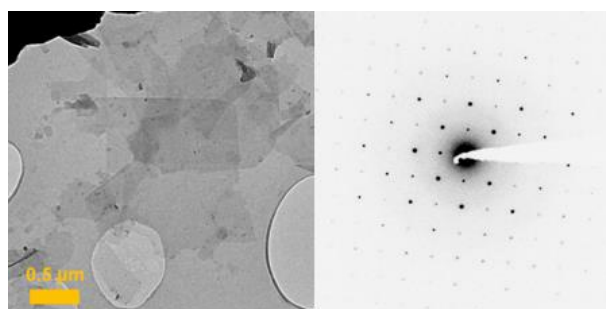


**Figure 3.3.6:** TEM overview image and corresponding SAED pattern of  $\text{ThLaNb}_2\text{O}_7$  nanosheets exfoliated from  $\text{AgLaNb}_2\text{O}_7$  /  $\text{ThI}$ .

As third exfoliation agent we chose 1-allyl-3-methylimidazolium iodide ( $\text{AmI}$ ) as it features a double bond attached to the methylimidazolium ring. In addition to the niobates a phosphatotantalate was tested as a non-perovskite model system. The bulk material  $\text{KTaP}_2\text{O}_8$  crystallizes in the monoclinic space group  $C2/m$  (No. 12) and is isotypic to  $\text{KFe}(\text{SO}_4)_2$ . This compound exhibits a layered structure composed of  $\text{TaP}_2\text{O}_8^-$  layers

separated by  $K^+$  layers and is known for its proton exchange ability. TEM overview images and corresponding SAED patterns along with AFM images of single  $AM/LaNb_2O_7$ ,  $AM/Ca_2Nb_3O_{10}$  and  $AM/TaP_2O_8$  nanosheets are displayed in Figure 3.3.7. TEM images show nanosheets for all materials and the elemental composition along with the SAED patterns match with the theoretical values (Table S3.3.8 and Table 3.3.9). The niobate nanosheets furnished using  $AmI$  are similar in size to those obtained in the other exfoliation experiments. The phosphatotantalate shows significantly larger nanosheets that are hard to distinguish due to the overlap of the nanosheets. While  $AM/LaNb_2O_7$  nanosheets have a height around 2.1 nm,  $AM/Ca_2Nb_3O_{10}$  did not deposit on the Si wafer and  $AM/TaP_2O_8$  was only detectable on a rough surface, exhibiting a relative height of  $\sim 2.5$  nm. Hence, the silver route can be extended to other ionic layered structures as well.

The last exfoliation agent investigated was tri-*n*-butylsulfonium iodide ( $TBSI$ ), which again demonstrates that like earlier mentioned for the tantalates an exfoliation route might work for one system, but fail for the other. Figure S3.3.6 shows a TEM image of successfully exfoliated  $TBSTaP_2O_8$  nanosheets, whilst for the niobates no nanosheets were obtained with  $TBSI$ .

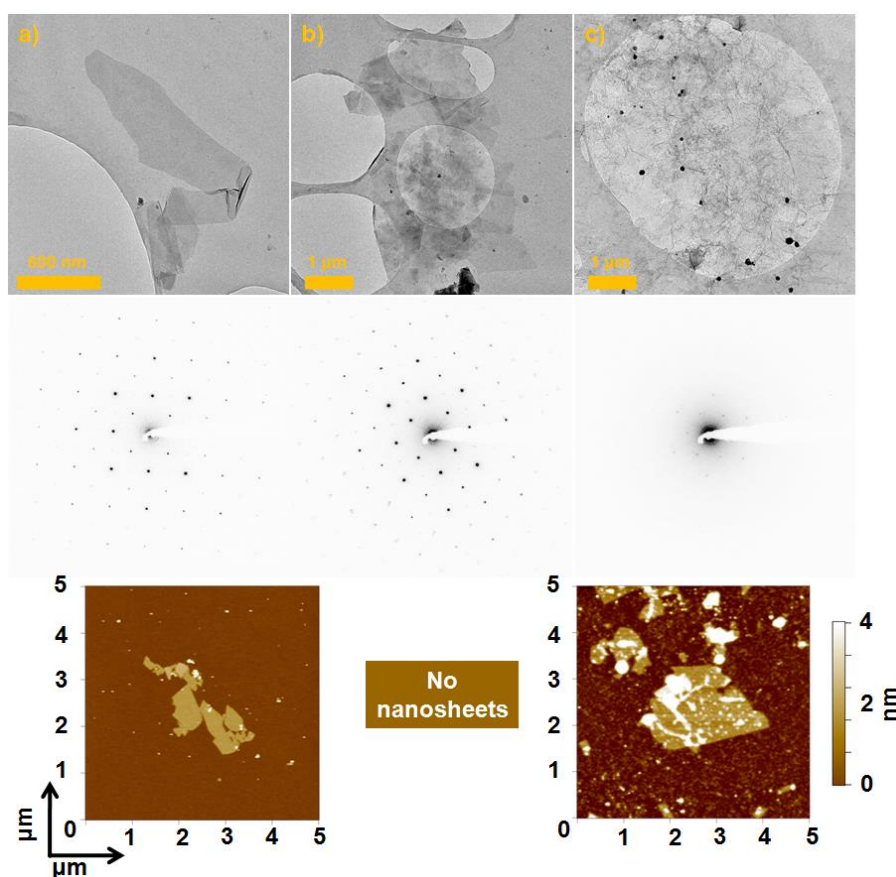


**Figure 3.3.7:** TEM overview images, corresponding SAED patterns and AFM images of a)  $AM/LaNb_2O_7$ , b)  $AM/Ca_2Nb_3O_{10}$  and c)  $AM/TaP_2O_8$  nanosheets.



### 3.3.3 Conclusion

In conclusion, we established an alternative exfoliation pathway for layered TMOs that relies on silver-exchange of the interlayer ions followed by treatment with bulky organic iodides in aqueous solution. The nanosheets obtained with *TBAI* as exfoliation agent are similar in size and quality compared to those achieved by the common route *via* cation-proton exchange and treatment with *TBAOH* for the lanthanum and calcium niobates. The silver based exfoliation route allows for an easy attachment of ligands with functional groups onto the nanosheet surface, which we have shown for hydroxyl groups (*Ch*), thiol groups (*Th*) and double bonds (*Am*), that in this form have not been reported by the proton based exfoliation route as yet. This functional groups can be imagined to be beneficial in various ways, e.g. for the specific binding of nanoparticles onto the nanosheet surface, which can be useful for catalysis purposes; to improve the surface coverage in LBL approaches; or to allow for a denser packing in heterostructures like the one we achieved with tetra-*n*-butylphosphonium (*TBP*<sup>+</sup>) ligands shown in Chapter 4.3. Another major advantage would be to bridge the gap between inorganic and organic synthesis e.g. by performing click-chemistry between the double bond and the thiol group on a substrate that would allow for an enhanced portfolio in the fabrication of hybrid nanostructures.

Our preliminary comparison of various materials suggests that depending on their composition and structure, exfoliation can be possible *via* one route, whilst it is not possible *via* the other. A theory to explain the exfoliation trends needs to be established in the future based on e.g. size and charge of ligand and nanosheet, synthesis properties like pH, concentration and other factors.

### 3.3.4 Bibliography

- [1] K. G. Sanjaya Ranmohotti, E. Josepha, J. Choi, J. Zhang, J. B. Wiley, *Adv. Mater. (Weinheim, Ger.)* **2011**, 23, 442-460.
- [2] R. E. Schaak, T. E. Mallouk, *Chem. Mater.* **2002**, 14, 1455-1471.
- [3] M. A. Hayward, *Semicond. Sci. Technol.* **2014**, 29, 064010.
- [4] M. Osada, T. Sasaki, *Adv. Mater. (Weinheim, Ger.)* **2012**, 24, 210-228.
- [5] R. Ma, T. Sasaki, *Adv. Mater. (Weinheim, Ger.)* **2010**, 22, 5082-5104.
- [6] L. Wang, T. Sasaki, *Chem. Rev. (Washington, DC, U. S.)* **2014**, 114, 9455-9486.
- [7] R. Ma, T. Sasaki, *Acc. Chem. Res.* **2015**, 48, 136-143.
- [8] S. Shori, P. J. Pellechia, H.-C. zur Loye, H. J. Ploehn, *J. Colloid Interface Sci.* **2015**, 437, 97-110.
- [9] J. Y. Kim, F. E. Osterloh, H. Hiramatsu, R. K. Dumas, K. Liu, *J. Phys. Chem. B* **2005**, 109, 11151-11157.

- [10] O. C. Compton, C. H. Mullet, S. Chiang, F. E. Osterloh, *J. Phys. Chem. C* **2008**, *112*, 6202-6208.
- [11] D. Mochizuki, K. Kumagai, M. M. Maitani, Y. Wada, *Angew. Chem., Int. Ed. Engl.* **2012**, *51*, 5452-5455.
- [12] D. Mochizuki, K. Kumagai, M. M. Maitani, E. Suzuki, Y. Wada, *J. Phys. Chem. C* **2014**, *118*, 22968-22974.
- [13] F. Kishimoto, D. Mochizuki, K. Kumagai, M. M. Maitani, E. Suzuki, Y. Wada, *Phys. Chem. Chem. Phys.* **2014**, *16*, 872-875.
- [14] R. G. Pearson, *J. Am. Chem. Soc.* **1963**, *85*, 3533-3539.
- [15] M. Sato, J. Abo, T. Jin, M. Ohta, *Solid State Ionics* **1992**, *51*, 85-89.
- [16] T. Tokumitsu, K. Toda, T. Aoyagi, D. Sakuraba, K. Uematsu, M. Sato, *J. Ceram. Soc. Jpn.* **2006**, *114*, 795-797.
- [17] M. Sato, J. Abo, T. Jin, M. Ohta, *J. Alloys Compd.* **1993**, *192*, 81-83.
- [18] Y. Chen, X. Zhao, H. Ma, S. Ma, G. Huang, Y. Makita, X. Bai, X. Yang, *J. Solid State Chem.* **2008**, *181*, 1684-1694.
- [19] M. Sato, J. Watanabe, K. Uematsu, *J. Solid State Chem.* **1993**, *107*, 460-470.
- [20] J. Boltersdorf, P. A. Maggard, *ACS Catalysis* **2013**, *3*, 2547-2555.
- [21] N. S. P. Bhuvanesh, P. M. Woodward, *J. Am. Chem. Soc.* **2002**, *124*, 14294-14295.
- [22] L. Li, R. Ma, Y. Ebina, K. Fukuda, K. Takada, T. Sasaki, *J. Am. Chem. Soc.* **2007**, *129*, 8000-8007.
- [23] S. Ida, C. Ogata, M. Eguchi, W. J. Youngblood, T. E. Mallouk, Y. Matsumoto, *J. Am. Chem. Soc.* **2008**, *130*, 7052-7059.
- [24] C. Ziegler, S. Werner, M. Bugnet, M. Wörsching, V. Duppel, G. A. Botton, C. Scheu, B. V. Lotsch, *Chem. Mater.* **2013**, *25*, 4892-4900.
- [25] Y. Song, N. Iyi, T. Hoshide, T. C. Ozawa, Y. Ebina, R. Ma, N. Miyamoto, T. Sasaki, *Chem. Commun. (Cambridge, U. K.)* **2015**.
- [26] K. Toda, M. Sato, *J. Mater. Chem.* **1996**, *6*, 1067-1071.
- [27] K. Toda, T. Suzuki, M. Sato, *Solid State Ionics* **1996**, *93*, 177-181.
- [28] E. M. Sabio, M. Chi, N. D. Browning, F. E. Osterloh, *Langmuir* **2010**, *26*, 7254-7261.
- [29] D. Bordo, F. Forlani, A. Spallarossa, R. Colnaghi, A. Carpen, M. Bolognesi, S. Pagani, in *Biol. Chem., Vol. 382*, **2001**, p. 1245.

### 3.3.5 Supporting Information

#### EXPERIMENTAL PROCEDURES:

**Chemicals.**  $\text{K}_2\text{CO}_3$  (>99%) and  $\text{KNO}_3$  (99%) was purchased from Merck;  $\text{CaCO}_3$  (99%) from Grüssing;  $\text{AgNO}_3$  (99.8%+), tetra-*n*-butylammonium iodide (*TBAI*,  $\text{C}_{16}\text{H}_{36}\text{IN}$ , 99%) and tetra-*n*-butylammonium hydroxide 30-hydrate (*TBAOH*,  $\text{C}_{16}\text{H}_{37}\text{NO}\cdot 30 \text{ H}_2\text{O}$ , 98%) 1-allyl-3-methylimidazolium iodide (*AmI*,  $\text{C}_7\text{H}_{11}\text{IN}_2$  98%) from Aldrich;  $\text{Rb}_2\text{CO}_3$  (99.8%),  $\text{La}(\text{OH})_3$  (99.95%),  $\text{Nb}_2\text{O}_5$  (99.5%),  $\text{Ta}_2\text{O}_5$  (99%), choline iodide (*ChI*,  $\text{C}_5\text{H}_{14}\text{INO}$ , 98%), choline hydroxide (*ChOH*,  $\text{C}_5\text{H}_{15}\text{NO}_2$ , 46% w/w aqueous solution) from Alfa Aesar;  $\text{NH}_4\text{H}_2\text{PO}_4$  (98%) from Acros Organics, choline chloride (*ChCl*,  $\text{C}_5\text{H}_{14}\text{ClNO}$ , 99%+) from Fluka, acetylthiocholine iodide (*AcI*,  $\text{C}_7\text{H}_{16}\text{INOS}$ , 99%+) from Roth, and tri-*n*-butylsulfonium iodide (*TBSI*,  $\text{C}_{12}\text{H}_{27}\text{IS}$  >96%) from TCI. All chemicals were used as purchased.

**Bulk materials.** Layered Dion-Jacobson (DJ) phases  $\text{KLaNb}_2\text{O}_7$ ,  $\text{KCa}_2\text{Nb}_3\text{O}_{10}$ ,  $\text{RbLaTa}_2\text{O}_7$ , and  $\text{RbCa}_2\text{Ta}_3\text{O}_{10}$  were synthesized similar to procedures known from literature.<sup>1-3</sup> All bulk materials were synthesized by thoroughly mixing of stoichiometric amounts of respective carbonates, oxides and/or hydroxides. 20% excess of  $\text{K}_2\text{CO}_3$  or 40% excess of  $\text{Rb}_2\text{CO}_3$  were used to compensate for the loss due to volatilization of the alkali source.  $\text{KLaNb}_2\text{O}_7$  and  $\text{KCa}_2\text{Nb}_3\text{O}_{10}$  were obtained by heating starting materials at 1200 °C for 60 h,  $\text{RbLaTa}_2\text{O}_7$  at 1100 °C for 12 h and  $\text{RbCa}_2\text{Ta}_3\text{O}_{10}$  at 1150 °C for 60 h. For synthesis of  $\text{KTaP}_2\text{O}_8$  stoichiometric amounts of  $\text{KNO}_3$ ,  $\text{Ta}_2\text{O}_5$  and  $\text{NH}_4\text{H}_2\text{PO}_4$  were preheated at 250 °C for 16 h, grinded and finally fired up to 950 °C for 24 h.<sup>4-5</sup>

**Cation-proton exchange.**  $\text{HLaNb}_2\text{O}_7$ ,  $\text{HCa}_2\text{Nb}_3\text{O}_{10}$ ,  $\text{HLaTa}_2\text{O}_7$  and  $\text{HCa}_2\text{Ta}_3\text{O}_{10}$  were obtained through a common acid exchange.<sup>6-7</sup> In general, 2 g of the bulk material was stirred in 200-250 mL acid for 5-7 days with several replacements of the acid in between. All DJ bulk materials were treated with 5M  $\text{HNO}_3$  and  $\text{KTaP}_2\text{O}_8$  with 8M  $\text{HCl}$ . Afterwards all materials were filtrated, washed with distilled water or ethanol and dried at 60 °C over night.

**Cation-silver exchange.**  $\text{AgLaNb}_2\text{O}_7$ ,  $\text{AgCa}_2\text{Nb}_3\text{O}_{10}$ ,  $\text{AgLaTa}_2\text{O}_7$  and  $\text{AgCa}_2\text{Ta}_3\text{O}_{10}$  and  $\text{AgTaP}_2\text{O}_8$  were prepared similar to routes reported in the literature.<sup>8-10</sup> Therefore, bulk materials were treated with a 4x molar excess of molten  $\text{AgNO}_3$  at 260 °C for 12-24 h. After the reaction, cation-silver exchanged materials were washed with distilled water and dried at 60 °C over night.

**Thiocholine iodide.** Thiocholine iodide (*ThI*) was synthesized through deacetylation of acetylthiocholine according to Peng *et al.*<sup>11</sup> Acetylthiocholine (1000 mg, 3.46 mmol) was suspended in 30 mL ethanol. After adding 8 mL hydrochloric acid the weakly yellow suspension was refluxed for seven hours. The yellow suspension was allowed to cool down and distilled to remove the ethanol. A small amount of ethanol was added to the oily liquid and distilled again. The colorless crystals of thiocholine iodide were washed with ethanol and

allowed to dry at 60°C. The product was verified *via* mass spectroscopy, elemental analysis and NMR analysis.

NMR:  $^1\text{H}$ - $\delta$  (MetOH- $d_3$ ): 2.8 ( $\text{CH}_2\text{-S}$ ); 3.16 ( $(\text{Me})_3\text{N}$ ); 3.4 ( $\text{CH}_2\text{-N}$ )

MS (FAB.): calculated for I: 126.9; measured: 127.1

MS (FAB $^+$ ): calculated for  $\text{C}_5\text{H}_{14}\text{NS}^+$ : 120.2; measured: 120.2

EA:  $\text{C}_5\text{H}_{14}\text{NSI}$  calculated: N: 5.67; C: 24.30; H: 5.71; S: 12.97; measured: N: 5.76; C: 24.42; H: 5.53; S: 12.84

**Exfoliation.** For exfoliation experiments 250 mg of silver- or proton-exchanged materials were mixed in a 1:1 molar ratio with the exfoliation agent in 40 mL of aqueous solution and shaken for several days in the dark. Silver-exchanged compounds were treated with *TBAI*, *ChI*, *ChCl*, *ChOH*, *ThI*, *AmI* and *TBSI*, while proton-exchanged compounds were treated with *TBAOH*. For further characterization, the suspensions were centrifuged at 3000 rpm for 30 min in order to remove non-exfoliated material.

#### CHARACTERIZATION:

**XRD.** Powder X-ray diffraction (XRD) patterns of bulk materials, cation- or silver-exchanged materials were recorded on a Huber G670 Guinier Imaging Plate diffractometer (HUBER X-Ray Diffraction Equipment, Rimsting;  $\text{Cu K}\alpha_1$ -radiation,  $\lambda = 154.051$  pm,  $\text{Ge}(111)$ -monochromator, external standard  $\text{SiO}_2$ ).

**EDX.** Composition of bulk materials, cation- or silver-exchange materials was determined by scanning electron microscopy (SEM) coupled with energy dispersive X-ray spectroscopy (EDX) on a JSM-6500F electron microscope (JEOL Ltd., Tokyo) equipped with a 7418 EDX detector (Oxford Instruments, Abingdon).

**ICP-AES.** Inductively coupled plasma and atomic emission spectroscopy (ICP-AES) was performed on a VISTA RL CCD and ICP-AES analyzer system (Agilent Technologies, Waldbronn) to ascertain complete cation-silver exchange.

**AFM.** Atomic force microscopy (AFM) topography measurements of nanosheets were performed after deposition of a colloidal suspension centrifuged at 3000 rpm for 15-30 min on a Si wafer with (100) orientation after ultrasonication in 5%  $\text{HNO}_3$  (Silchem, Freiberg). A MFP-3D Stand alone AFM (Asylum Research, Santa Barbara) operated in tapping-mode was used with OMCL-AC160TS-R3 (Olympus, Tokyo) cantilevers with a resonant frequency of 300 kHz.

**TEM.** Transmission electron microscopy (TEM) samples were prepared by dropping a diluted colloidal nanosheet suspension onto a copper or gold grid coated with a lacey and holey carbon film, respectively. A Philips CM30 ST microscope (300 kV,  $\text{LaB}_6$  cathode,  $\text{CS} = 1.15$  mm, Royal Philips Electronics, Amsterdam) was used for imaging of nanosheets and determining their elemental composition *via* EDX measurements.

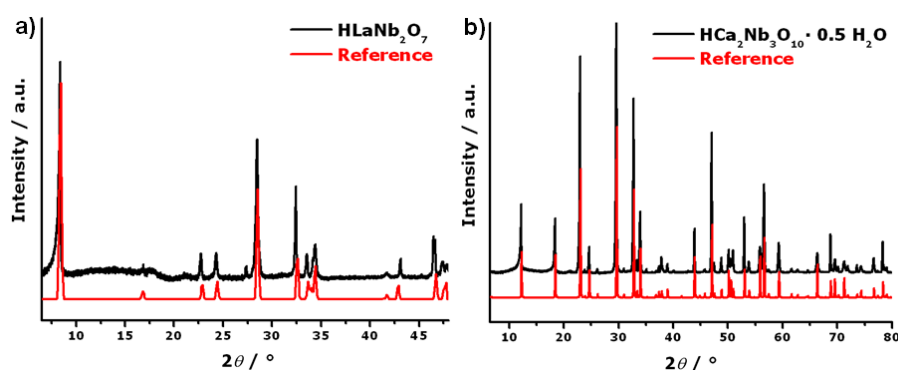


**Figure S3.3.1:** Powder XRD patterns of a)  $\text{HLaNb}_2\text{O}_7$  and b)  $\text{HCa}_2\text{Nb}_3\text{O}_{10} \cdot 0.5\text{H}_2\text{O}$  in comparison with the respective simulated patterns taken from the ICSD data base.<sup>6-7</sup> Note that the broad reflections around  $18^\circ 2\theta$  and  $23^\circ 2\theta$  are due to the polyester mounting foil in the XRD setup.

**Table S3.3.1:** SEM-EDX quantification data of bulk, cation-proton and cation-silver exchanged lanthanum niobates or calcium niobates, respectively. The theoretical formula is compared to the experimental formula determined by the element specific signals given in at%.

Theoretical formula						Experimental formula
	K K $\alpha$	Ag L $\alpha$	La L $\alpha$	Nb L $\alpha$	O K $\alpha$	
KLaNb <sub>2</sub> O <sub>7</sub>	8.6	-	8.0	16.6	66.8	KLaNb <sub>2</sub> O <sub>8</sub>
HLaNb <sub>2</sub> O <sub>7</sub>	0.3	-	7.2	14.9	77.6	(H)LaNb <sub>2</sub> O <sub>10.4</sub>
AgLaNb <sub>2</sub> O <sub>7</sub>	-	6.2	6.0	13.4	74.4	Ag <sub>0.9</sub> La <sub>0.9</sub> Nb <sub>2</sub> O <sub>11.1</sub>
	K K $\alpha$	Ag L $\alpha$	Ca K $\alpha$	Nb L $\alpha$	O K $\alpha$	
KCa <sub>2</sub> Nb <sub>3</sub> O <sub>10</sub>	5.6	-	10.9	16.9	66.6	KCa <sub>2</sub> Nb <sub>3</sub> O <sub>10.7</sub>
HCa <sub>2</sub> Nb <sub>3</sub> O <sub>10</sub>	-	-	11.9	18.2	69.9	(H)Ca <sub>2</sub> Nb <sub>3</sub> O <sub>11.5</sub>
AgCa <sub>2</sub> Nb <sub>3</sub> O <sub>10</sub>	-	5.3	11.0	17.1	66.6	Ag <sub>0.9</sub> Ca <sub>1.9</sub> Nb <sub>3</sub> O <sub>11.7</sub>

**Table S3.3.2:** ICP-AES data after cation-silver exchange of  $\text{KLaNb}_2\text{O}_7$  and  $\text{KCa}_2\text{Nb}_3\text{O}_{10}$  showing complete exchange of K after cation-silver exchange.

Sample	Ag [ $\mu\text{g/g}$ ]	Ca [ $\mu\text{g/g}$ ]	La [ $\mu\text{g/g}$ ]	Nb [ $\mu\text{g/g}$ ]	K [ $\mu\text{g/g}$ ]
$\text{AgLaNb}_2\text{O}_7$	132.1	-	105.8	304.0	-
$\text{AgCa}_2\text{Nb}_3\text{O}_{10}$	146.5	115.5	-	390.5	-

**Table S3.3.3:** Comparison of TEM-EDX data of  $TBALaNb_2O_7$  and  $TBACa_2Nb_3O_{10}$  nanosheets after exfoliation via the silver or proton route. All values are given in at%.

Theoretical formula						Experimental formula
	K K $_{\alpha}$	Ag L $_{\alpha}$	La L $_{\alpha}$	Nb L $_{\alpha}$	O K $_{\alpha}$	
Ag: <i>TBALa</i> Nb <sub>2</sub> O <sub>7</sub>	-	-	7.8	21.0	71.2	( <i>TBA</i> )La <sub>0.7</sub> Nb <sub>2</sub> O <sub>6.8</sub>
H: <i>TBALa</i> Nb <sub>2</sub> O <sub>7</sub>	-	-	6.5	16.6	76.9	( <i>TBA</i> )La <sub>0.8</sub> Nb <sub>2</sub> O <sub>9.3</sub>
	K K $_{\alpha}$	Ag L $_{\alpha}$	Ca K $_{\alpha}$	Nb L $_{\alpha}$	O K $_{\alpha}$	
Ag: <i>TBACa</i> <sub>2</sub> Nb <sub>3</sub> O <sub>10</sub>	-	-	8.9	14.3	76.8	( <i>TBA</i> )Ca <sub>1.9</sub> Nb <sub>3</sub> O <sub>16.1</sub>
H: <i>TBACa</i> <sub>2</sub> Nb <sub>3</sub> O <sub>10</sub>	-	-	12.4	21.5	66.1	( <i>TBA</i> )Ca <sub>1.7</sub> Nb <sub>3</sub> O <sub>9.2</sub>

**Table S3.3.4:** Most prominent  $d$ -spacings and corresponding ( $hkl$ ) values observed by SAED of  $TBALaNb_2O_7$  and  $TBACa_2Nb_3O_{10}$  nanosheets after exfoliation via the silver or proton route. The values are given in Å and the margin of error is  $\pm 0.3$  Å.

	(001)	(101)	(002)	(201)	(202)
Ag: $TBALaNb_2O_7$	3.88	2.73	1.94	1.72	1.37
H: $TBALaNb_2O_7$	3.92	2.75	1.96	1.74	1.38
	(200)	(220)	(400)	(420)	(440)
Ag: $TBACa_2Nb_3O_{10}$	3.88	2.76	1.94	1.73	1.38
H: $TBACa_2Nb_3O_{10}$	3.85	2.72	1.92	1.73	1.36

**Table S3.3.5:** SEM-EDX quantification data of bulk, cation-proton and cation-silver exchanged lanthanum tantalates or calcium tantalates, respectively. The theoretical formula is compared to the experimental formula determined by the element specific signals given in at%.

	Rb $K_{\alpha}$	Ag $L_{\alpha}$	La $L_{\alpha}$	Ta $L_{\alpha}$	O $K_{\alpha}$	
RbLaTa <sub>2</sub> O <sub>7</sub>	6.1	-	7.3	14.5	72.1	Rb <sub>0.8</sub> LaTa <sub>2</sub> O <sub>9.9</sub>
HLaTa <sub>2</sub> O <sub>7</sub>	2.2	-	8.5	17.6	71.7	Rb <sub>0.3</sub> LaTa <sub>2</sub> O <sub>8.1</sub>
AgLaTa <sub>2</sub> O <sub>7</sub>	-	7.3	13.0	6.6	73.1	Ag <sub>1.1</sub> LaTa <sub>2</sub> O <sub>11.3</sub>
	Rb $K_{\alpha}$	Ag $L_{\alpha}$	Ca $K_{\alpha}$	Ta $L_{\alpha}$	O $K_{\alpha}$	
RbCa <sub>2</sub> Ta <sub>3</sub> O <sub>10</sub>	4.2	-	9.8	14.4	71.6	Rb <sub>0.9</sub> Ca <sub>2</sub> Ta <sub>3</sub> O <sub>14.9</sub>
HCa <sub>2</sub> Ta <sub>3</sub> O <sub>10</sub>	-	-	8.4	13.8	77.8	(H)Ca <sub>1.8</sub> Ta <sub>3</sub> O <sub>16.9</sub>
AgCa <sub>2</sub> Ta <sub>3</sub> O <sub>10</sub>	-	5.0	10.7	19.7	64.6	Ag <sub>0.8</sub> Ca <sub>1.6</sub> Ta <sub>3</sub> O <sub>9.8</sub>

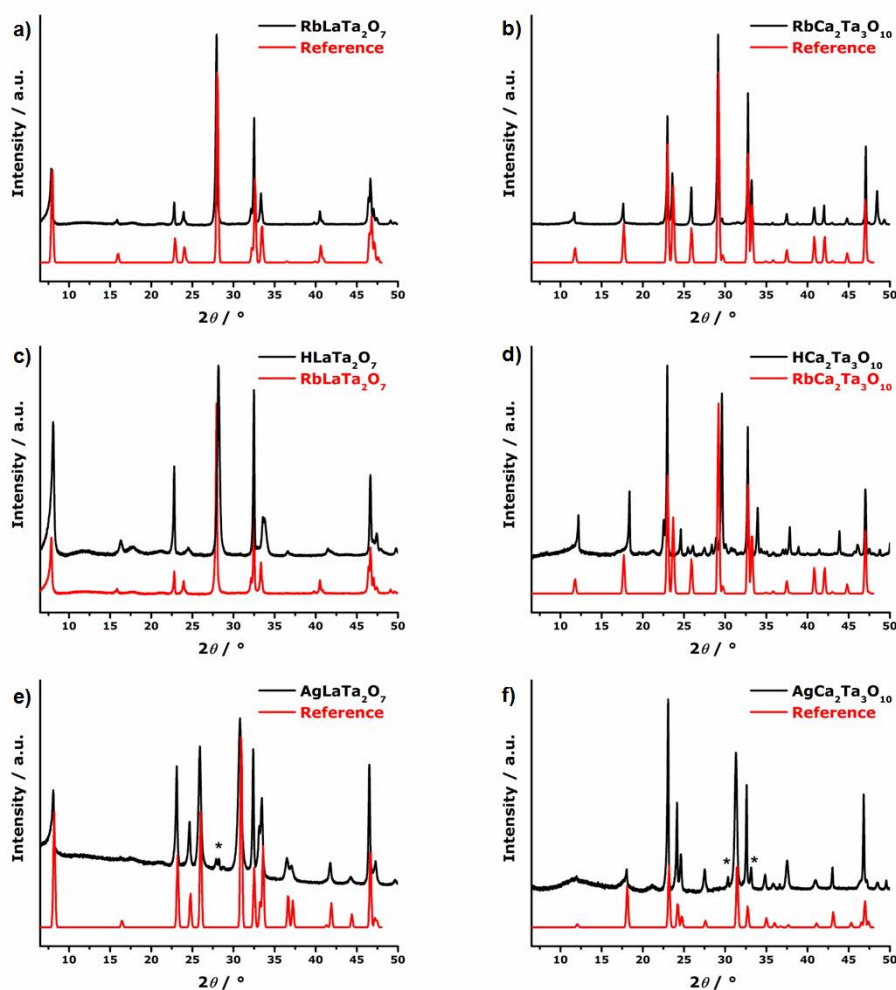


**Figure S3.3.2:** Powder XRD patterns of a)  $\text{RbLaTa}_2\text{O}_7$  and b)  $\text{RbCa}_2\text{Ta}_3\text{O}_{10}$  bulk materials, c)  $\text{HLaTa}_2\text{O}_7$  + d)  $\text{HCa}_2\text{Ta}_3\text{O}_{10}$  after cation-proton exchange, and e)  $\text{AgLaTa}_2\text{O}_7$  + f)  $\text{AgCa}_2\text{Ta}_3\text{O}_{10}$  after cation-silver exchange of the bulk material in comparison with the respective simulated patterns taken from the ICSD data base.<sup>3, 10</sup> Note that for both cation-proton exchanged forms no references were available, and the XRD patterns are therefore compared to the bulk patterns. The asterisks mark additional reflections found in the cation-silver exchanged forms that might arise from minor impurities. The broad reflections around  $18^\circ 2\theta$  and  $23^\circ 2\theta$  are due to the polyester mounting foil in the XRD setup.

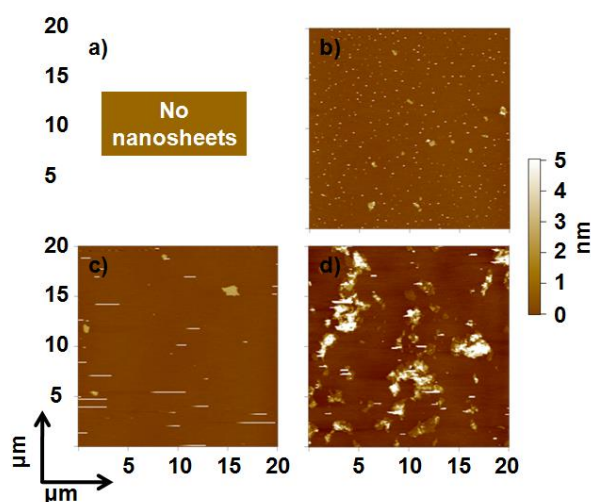


**Figure S3.3.3:** AFM overview images of  $TBLaTa_2O_7$  nanosheets derived from a)  $AgLaTa_2O_7$  /  $TBAI$  and b)  $HLaTa_2O_7$  /  $TBAOH$  as well as  $TBACa_2Ta_3O_{10}$  nanosheets derived from c)  $AgCa_2Ta_3O_{10}$  /  $TBAI$  and d)  $HCa_2Ta_3O_{10}$  /  $TBAOH$ . Note that for a) we did not find any evidence for a successful exfoliation after investigation of 3 wafers and ~25 different regions per wafer.

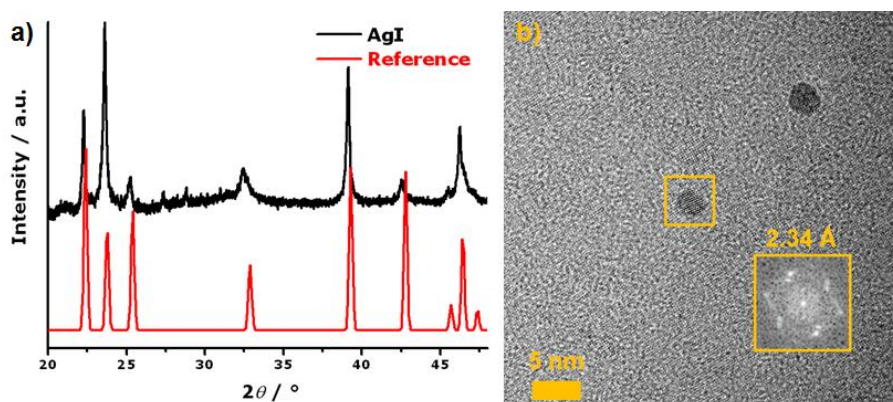


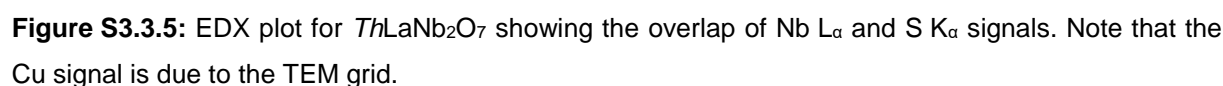
**Figure S3.3.4:** a) XRD of isolated yellow precipitate after Ag exfoliation belonging to AgI and b) TEM image of  $ChLaNb_2O_7$  nanosheets after exfoliation of  $AgLaNb_2O_7$  /  $ChI$  showing crystalline particles on the surface. The inset shows the FFT of the marked particle, the found distance belongs to the distance of the (111) plane of Ag.

**Table S3.3.6:** Comparison of TEM-EDX data of  $ChLaNb_2O_7$  and  $ChCa_2Nb_3O_{10}$  nanosheets after exfoliation via the silver or proton route. All values are given in at%.

Theoretical formula	Experimental formula				
	K K $\alpha$	Ag L $\alpha$	La L $\alpha$	Nb L $\alpha$	O K $\alpha$
$TBLaNb_2O_7$	-	-	7.0	14.4	78.6
	$(TBA)LaNb_2O_{10.9}$				
	K K $\alpha$	Ag L $\alpha$	Ca K $\alpha$	Nb L $\alpha$	O K $\alpha$
$TBACa_2Nb_3O_{10}$	-	-	8.1	17.9	74.0
	$(TBA)Ca_{1.4}Nb_3O_{12.4}$				



	(001)	(101)	(002)	(201)	(202)
<i>ChLaNb<sub>2</sub>O<sub>7</sub></i>	3.92	2.73	1.96	1.73	1.36
<i>ThLaNb<sub>2</sub>O<sub>7</sub></i>	3.90	2.74	1.95	1.72	1.37
	(200)	(220)	(400)	(420)	(440)
<i>ChCa<sub>2</sub>Nb<sub>3</sub>O<sub>10</sub></i>	3.85	2.71	1.93	1.73	1.35



Theoretical formula					Experimental formula	
<i>Am</i> LaNb <sub>2</sub> O <sub>7</sub>	K K <sub>α</sub>	Ag L <sub>α</sub>	La L <sub>α</sub>	Nb L <sub>α</sub>	O K <sub>α</sub>	<i>(Am)</i> La <sub>1.1</sub> Nb <sub>2</sub> O <sub>9.8</sub>
	-	-	8.3	15.5	76.2	
<i>Am</i> Ca <sub>2</sub> Nb <sub>3</sub> O <sub>10</sub>	K K <sub>α</sub>	Ag L <sub>α</sub>	Ca K <sub>α</sub>	Nb L <sub>α</sub>	O K <sub>α</sub>	<i>(Am)</i> Ca <sub>2</sub> Nb <sub>3</sub> O <sub>8.9</sub>
	-	-	14.3	21.6	64.1	
<i>Am</i> TaP <sub>2</sub> O <sub>8</sub>	K K <sub>α</sub>	Ag L <sub>α</sub>	P K <sub>α</sub>	Ta L <sub>α</sub>	O K <sub>α</sub>	<i>(Am)</i> TaP <sub>1.4</sub> O <sub>8.8</sub>
	-	-	13.2	8.9	77.9	

	(001)	(101)	(002)	(201)	(202)
<i>Ami</i> LaNb <sub>2</sub> O <sub>7</sub>	3.90	2.74	1.95	1.74	1.37
	(200)	(220)	(400)	(420)	(440)
<i>Ami</i> Ca <sub>2</sub> Nb <sub>3</sub> O <sub>10</sub>	3.87	2.73	1.94	1.73	1.36
	(110)		(020)		(220)
<i>Ami</i> TaP <sub>2</sub> O <sub>8</sub>	4.38		2.59		2.27

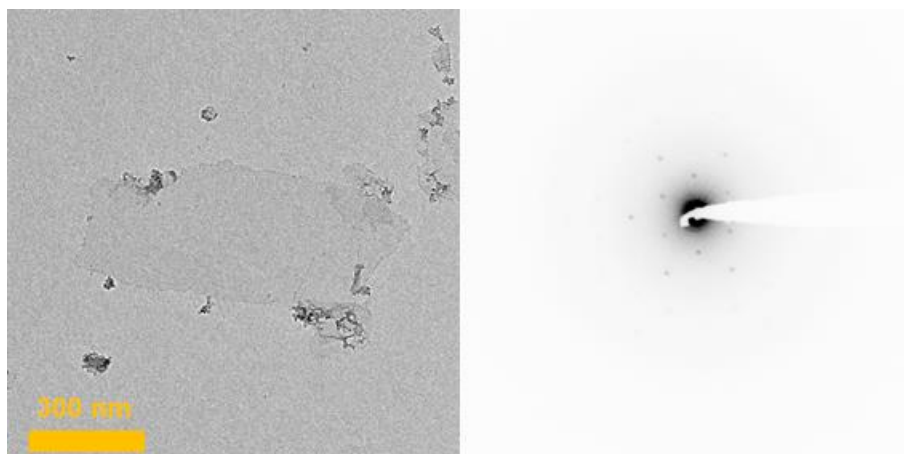


**Figure S3.3.6:** TEM image and corresponding SAED pattern of a  $TBSTaP_2O_8$  nanosheet.

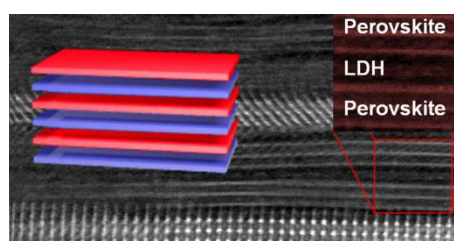
- [1] M. Sato, J. Abo, T. Jin, M. Ohta, *Solid State Ionics* **1992**, 51, 85-89.
- [2] T. Tokumitsu, K. Toda, T. Aoyagi, D. Sakuraba, K. Uematsu, M. Sato, *J. Ceram. Soc. Jpn.* **2006**, 114, 795-797.
- [3] K. Toda, M. Sato, *J. Mater. Chem.* **1996**, 6, 1067-1071.
- [4] S. Oyetola, A. Verbaere, Y. Piffard, M. Tournoux, *Eur. J. Solid State Inorg. Chem.* **1988**, 25, 259-278.
- [5] S. Oyetola, A. Verbaere, D. Guyomard, Y. Piffard, M. Tournoux, *Eur. J. Solid State Inorg. Chem.* **1989**, 26, 175-191.
- [6] M. Sato, J. Abo, T. Jin, M. Ohta, *J. Alloys Compd.* **1993**, 192, 81-83.
- [7] Y. Chen, X. Zhao, H. Ma, S. Ma, G. Huang, Y. Makita, X. Bai, X. Yang, *J. Solid State Chem.* **2008**, 181, 1684-1694.
- [8] M. Sato, J. Watanabe, K. Uematsu, *J. Solid State Chem.* **1993**, 107, 460-470.
- [9] J. Boltersdorf, P. A. Maggard, *ACS Catalysis* **2013**, 3, 2547-2555.
- [10] K. Toda, T. Suzuki, M. Sato, *Solid State Ionics* **1996**, 93, 177-181.
- [11] L. Peng, G. Zhang, D. Zhang, J. Xiang, R. Zhao, Y. Wang, D. Zhu, *Org. Lett.* **2009**, 11, 4014-4017.

## 4 Nanosheet Based Heterostructures

### 4.1 Artificial Solids by Design: Assembly and Electron Microscopy Study of Nanosheet-Derived Heterostructures

Christian Ziegler,<sup>^</sup> Stephan Werner,<sup>^</sup> Matthieu Bugnet, Matthias Wörsching, Viola Duppel, Gianluigi A. Botton, Christina Scheu, Bettina V. Lotsch

PUBLISHED IN: Adapted with permission from *Chem. Mater.* **2013**, 25, 4892-4900.  
DOI: <http://dx.doi.org/10.1021/cm402950b>  
Copyright: ©2013 American Chemical Society



**ABSTRACT:** Two-dimensional materials do not only attract interest owing to their anisotropic properties and quantum confinement effects, but also lend themselves as well-defined building blocks for the rational design of 3D materials with custom-made structures and, hence, properties. Here, we present the bottom-up fabrication of an artificial superlattice derived from positively charged layered double hydroxide (LDH) and negatively charged perovskite layers sequentially assembled by electrostatic layer-by-layer deposition. In contrast to previously employed bulk methods averaging out the elemental distribution within such stacks, we use a combination of HRTEM, STEM and EEL spectroscopy to elucidate the structure and composition of the multilayer stack with a high spatial resolution on the subnanometer scale. Atomic column resolved STEM coupled with EELS line-scans confirms the periodic arrangement of individual nanosheets by evaluation of the Ca  $L_{2,3}$  and Mn  $L_{2,3}$  edges. Furthermore, HRTEM confirms the formation of up to 100 double layer thick films, thus demonstrating the transition from ultrathin nanosheet assemblies to artificial bulk solids with engineered structures and, hence, property profiles. We ascertain the formation of densely packed stacks with a well-ordered layered morphology, while non-idealities such as lack of in-plane layer registry, layer terminations, sheet bending and contamination by residual ligands are side effects of the solution-based deposition process. In addition, we demonstrate that the packing density of the multilayer system can be tuned by changing the LDH dispersing agent from formamide to water, resulting in porous stacks containing about eight-times less LDH and featuring significantly increased interlayer distances.

### 4.1.1 Introduction

The rational design of solids with tailor-made properties has been a hallmark of soft chemistry and a major driving force of modern materials science. In principle, high temperature solid-state synthesis is governed by thermodynamic principles and is therefore inherently constrained with respect to the compositions and structures that can be realized. In contrast, kinetically controlled soft chemistry protocols, relying on the use of pre-formed building blocks and operating at low temperatures, open up pathways to unconventional solids with large compositional scope, albeit often at the expense of stability. Driven by the rise of nanochemistry and the ability to sculpture well-defined nanoscale building blocks such as two-dimensional (2D) nanosheets, the modular assembly of preformed nano-objects into hierarchical superlattices has taken shape in recent years, based on the pioneering work by Mallouk<sup>1-6</sup> and by Sasaki<sup>7-10</sup>. As a prerequisite for designing complex solids from nanosheet building blocks, the successful isolation of graphene, along with the identification of its unique properties, has sparked the quest for inorganic 2D materials with extraordinary physical characteristics.<sup>11-17</sup> Given the rapidly increasing number of nanosheets such as LDHs,<sup>18</sup> transition metal oxides,<sup>19</sup> metal disulfides<sup>20</sup> and other layered materials<sup>21</sup> at hand, we envision the rational synthesis of complex, multifunctional solids by combining different types of nanosheets into precisely arranged heterostructures with unique property profiles. The design of artificial solids with custom-made properties, which are otherwise inaccessible due to thermodynamic constraints under high temperature conditions, will be useful in a range of applications, including spintronics, optoelectronics and catalysis.<sup>1, 4, 7-8, 22</sup> For example, vertical heterojunctions composed of photoactive layers may be engineered to optimize charge separation and transport, and miniaturized versions of photocatalytic donor-acceptor systems are accessible using the 2D building block approach. To achieve maximum control over the layer sequence, we use an electrostatic layer-by-layer (LBL) procedure (also known as electrostatic self-assembly deposition, ESD). Alternative deposition protocols that have been employed by other groups include the Langmuir-Blodgett (LB) method<sup>23-29</sup> or flocculation<sup>30-35</sup> of oppositely charged nanosheets, although the former lacks scalability and the latter typically yields disordered assemblies. In LBL, multilayer films form due to electrostatic and hydrophobic forces between positively and negatively charged nanosheets in a self-limiting fashion, thus allowing for a high level of control over the layer sequence at the (sub)nanoscale.<sup>6</sup> In previous works, anionic inorganic nanosheets were stacked with cationic polymers such as poly(diallyldimethylammonium chloride) (PDDA),<sup>4, 7-8, 36</sup> whereas cationic inorganic nanosheets can be assembled with anionic polymers such as poly(sodium styrene-4-sulfonate) (PSS).<sup>37</sup> Recent approaches have delineated routes to obtain polymer-free films after ultraviolet-visible (UV) irradiation of the hybrid films, leading to the photoinduced decomposition of the polycations forming the organic substructure.<sup>23-26</sup> In

contrast, only very few studies have been dedicated to the direct combination of positively and negatively charged inorganic nanosheets. An important advantage of using charged nanosheets to assemble multilayer structures instead of organic polyelectrolytes is that sequentially grown layers do not necessarily interpenetrate, thus giving rise to more rigid, structurally well-defined superlattices.<sup>38</sup> Li *et al.* reported a successful LBL assembly of anionic  $\text{Ti}_{0.91}\text{O}_2^{0.36-}$  or  $\text{Ca}_2\text{Nb}_3\text{O}_{10}^-$  with cationic  $\text{Mg}_{0.67}\text{Al}_{0.33}(\text{OH})_2^{0.33+}$  nanosheets with up to 10 bilayers.<sup>39</sup> Other examples are  $\text{Ni}_{0.8}\text{Fe}_{0.2}(\text{OH})_2/\text{MnO}_2$ ,<sup>40</sup>  $\text{Mg}_{0.67}\text{Al}_{0.33}(\text{OH})_2/\text{MnO}_2$ ,<sup>41</sup>  $\text{Co}_{0.67}\text{Al}_{0.33}(\text{OH})_2/\text{montmorillonite}$ ,<sup>42</sup>  $\text{Co}_{0.67}\text{Al}_{0.33}(\text{OH})_2/\text{polyvinyl alcohol}/\text{graphene oxide}$ <sup>43</sup> and  $\text{Ni}_{0.66}\text{Al}_{0.33}(\text{OH})_2/\text{TaS}_2$ ,<sup>44</sup> which were assembled into hybrid thin films by exfoliation-restacking experiments. Ida *et al.* developed a synergistic LBL system exhibiting a drastic change in photoluminescence, using  $\text{Ti}_{1.81}\text{O}_4$  as an “antenna” for UV-light harvesting and  $\text{Eu}(\text{OH})_{3-x}$  as an emissive layer in  $\text{Eu}(\text{OH})_{3-x}/\text{Ti}_{1.81}\text{O}_4$  nanocomposites. This system, similar to the others, was only composed of 1-4 layers.<sup>45</sup>

All of these studies, however, monitor the assembly process only indirectly, implicitly assuming the alternate stacking of oppositely charged and fully delaminated monolayers. Thus, ultimate evidence of the alternate layer stacking by means of high-resolution analytical techniques is still elusive. Furthermore, the transition from ultrathin films to artificial solids with bulk dimensions has yet to be demonstrated.

To fill this gap, we present a locally resolved, precise elemental and structural analysis of a novel artificial solid composed of perovskite and layered double hydroxide nanosheets. We use high-resolution TEM (HRTEM) as well as scanning TEM (STEM) combined with energy-dispersive X-ray spectroscopy (EDX) and electron energy loss spectroscopy (EELS) to elucidate both the composition and structure of the hybrid system with ultrahigh resolution to yield insights into the interfacial quality, real structure and morphology of the stack. The thickness of the 200-layer system approaches the bulk level, thus demonstrating the feasibility of the modular, rational synthesis of new solids from 2D building blocks by soft chemistry. In addition, our analysis adds to the understanding and improvement of the colloidal interactions and interfacial integrity determining the overall quality of the resulting superlattices.

#### 4.1.2 Results and Discussion

We assembled a multilayer film composed of nanosheet building blocks by sequentially adsorbing cationically charged  $[\text{Mn}_2\text{Al}(\text{OH})_6]^+[\text{ES}]^-$  nanosheets (abbreviated as  $\text{Mn}_2\text{Al}(\text{OH})_6^+$  in the following;  $\text{ES}^-$ : ethylbenzenesulfonate) suspended in either formamide or water and anionically charged  $[(\text{TBA})_{1-x}\text{H}_x]^+[\text{Ca}_2\text{Nb}_3\text{O}_{10}]^-$  nanosheets (abbreviated as  $\text{Ca}_2\text{Nb}_3\text{O}_{10}^-$  in the following;  $\text{TBA}^+$ : tetra-*n*-butylammonium) suspended in water on a planar Si/SiO<sub>2</sub> substrate. Before we consider the multilayer stacks, the building blocks -  $\text{Mn}_2\text{Al}(\text{OH})_6^+$  and  $\text{Ca}_2\text{Nb}_3\text{O}_{10}^-$

nanosheets – will be briefly discussed in the following. LDHs are described by the general formula  $[M^{II}_{1-x}M^{III}_x(OH)_2][A^{n-}_{x/n} \cdot m H_2O]$ , where  $M^{II}$  and  $M^{III}$  represent di- and trivalent metal ions within the Brucite-like layers (here  $Mn^{II}$  and  $Al^{III}$ ), and  $A^{n-}$  is an organic or inorganic interlayer anion (e.g.  $ES$ ).<sup>46</sup> The structure of a LDH is depicted in Figure 4.1.1 (red). Attractive electrostatic forces between the cationic layers and the interlayer anions stabilize the structure. To overcome these forces and exfoliate the layered structure, the LDH is typically swollen with formamide and exfoliated by ultrasonication, yielding positively charged nanosheets.<sup>47</sup> The empirical formula of the synthesized LDH was determined to be  $[Mn_{2.1}Al(OH)_6][ES \cdot 1.3 H_2O]$  by ICP-AES and elemental analysis.

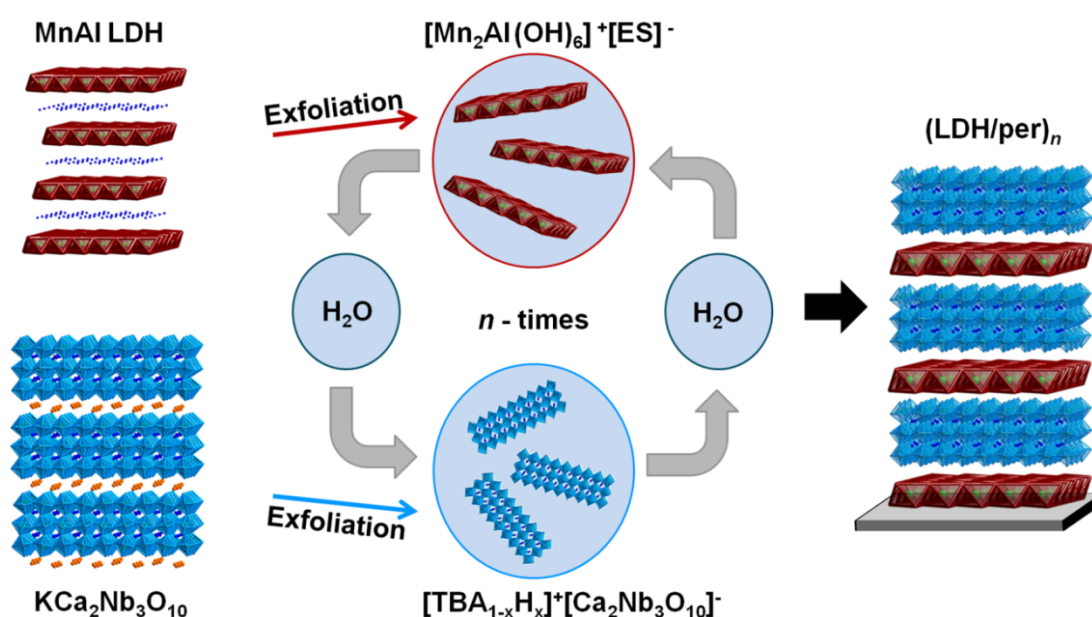
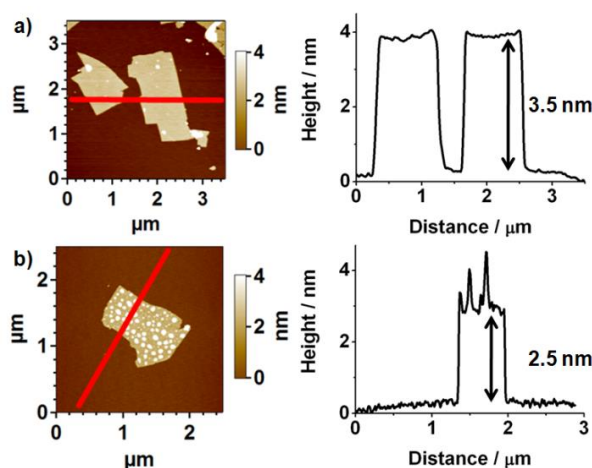
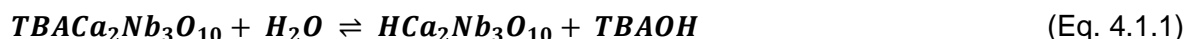


**Figure 4.1.1:** Schematic drawing of the liquid-phase process, employed to construct hybrid superlattices. Exfoliation of the layered bulk materials into  $Mn_2Al(OH)_6^+$  and  $Ca_2Nb_3O_{10}^-$  nanosheets is followed by electrostatic LBL assembly with intermediate washing steps in order to achieve 3D  $(LDH/per)_n$  heterostructures immobilized on a substrate.

Dion-Jacobson-type layered perovskites can be described by the general formula  $M[A_{n-1}B_nO_{3n+1}]$  ( $A = Ca, Sr, La$  etc.  $B = Ti, Nb, Ta$  etc.), where the negatively charged  $[A_{n-1}B_nO_{3n+1}]^-$  layers composed of blocks of  $n$  corner-sharing  $BO_6$  octahedra are interleaved with exchangeable monovalent cations  $M^+$  ( $M = H, K, Rb$  etc.).<sup>6</sup> In the monoclinic structure of  $KCa_2Nb_3O_{10}$  the corner sharing  $BO_6$  octahedra are distorted from the ideal cubic structure as shown in Figure 4.1.1 (blue). Both types of nanosheets were synthesized by intercalation – exfoliation protocols according to established procedures, which are detailed in the Supporting Information.<sup>48-50</sup> Atomic force microscopy (AFM) typically reveals  $Mn_2Al(OH)_6^+$  nanosheets with a height around 1.5-1.7 nm and lateral dimensions of several hundreds of nanometers (Figure S4.1.3, Figure S4.1.4), when exfoliated in formamide or water,

respectively.  $\text{Ca}_2\text{Nb}_3\text{O}_{10}^-$  nanosheets were determined with a typical height of 3.5 nm and lateral sizes around 1-2  $\mu\text{m}$  (Figure 4.1.2 a). Note that the nanosheet thicknesses are higher than the crystallographic thicknesses or those determined experimentally under ultra-high vacuum conditions (0.48 nm<sup>51</sup> to 0.81 nm<sup>18</sup> for  $\text{Mn}_2\text{Al}(\text{OH})_6^+$  and 1.44 nm<sup>39</sup> to 1.80 nm<sup>28</sup> for  $\text{Ca}_2\text{Nb}_3\text{O}_{10}^-$ ), which is rationalized by the presence of the ligand shell and adsorption of water, as AFM measurements were carried out under ambient rather than vacuum conditions.<sup>52</sup> To prove this hypothesis, the contribution of the  $\text{TBA}^+$  ligand shell to the overall height of the  $\text{Ca}_2\text{Nb}_3\text{O}_{10}^-$  nanosheets was established. (Figure 4.1.2).

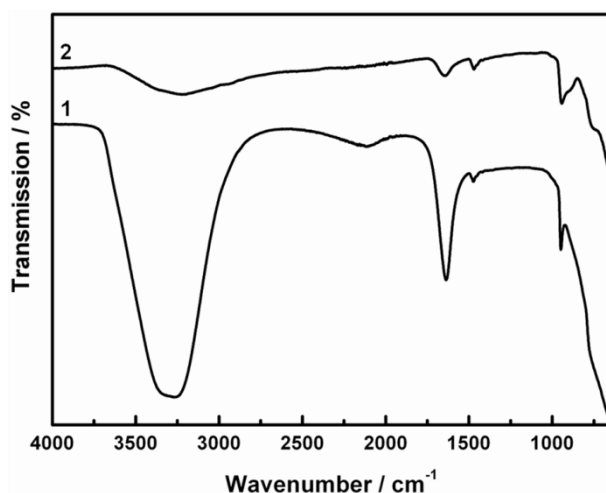
First, the amount of  $\text{TBA}^+$  in  $[(\text{TBA})_{1-x}\text{H}_x]^+[\text{Ca}_2\text{Nb}_3\text{O}_{10}]^-$  was determined to be 0.84 ( $x = 0.16$ ) by elemental analysis (see Table S4.1.1) In the second step, the nanosheet suspension was subjected to a 1:2 dilution with water, since the comparatively high amount of  $\text{TBA}^+$  suggests a relatively dense packing of  $\text{TBA}^+$  on the nanosheet surface.<sup>4</sup> Figure 4.1.2 displays AFM measurements of the undiluted (top) and diluted samples (bottom) with the corresponding height profiles. The undiluted sample shows an almost flat surface of the nanosheet with an initial height of 3.5 nm, whereas the diluted sample exhibits the formation of spots on the surface, along with a decrease of the initial height to around 2.5 nm. With higher dilution the spots vanish almost completely. We attribute these observations to the reversible proton –  $\text{TBA}^+$  exchange between  $[(\text{TBA})_{1-x}\text{H}_x]^+[\text{Ca}_2\text{Nb}_3\text{O}_{10}]^-$  and water:



**Figure 4.1.2:** AFM images and corresponding height profiles of  $\text{Ca}_2\text{Nb}_3\text{O}_{10}^-$  nanosheets after a) synthesis and b) 1:2 dilution of the sample shown in (a) with water.

Our assumption that  $\text{TBA}^+$  is washed away by diluting with water was further confirmed by IR spectroscopy (Figure 4.1.3). While the spectrum of  $\text{TBA}_{0.84}\text{H}_{0.16}\text{Ca}_2\text{Nb}_3\text{O}_{10}$  shows strong absorption bands due to the organic ligand, the intensity of these bands at 3300 and 1638  $\text{cm}^{-1}$  are strongly decreased compared to the Nb-O stretching band just below

1000  $\text{cm}^{-1}$  in the spectrum of the nanosheets diluted with water. Therefore, taking into account the thickness calculated from crystallographic data of one perovskite block in the  $\text{KCa}_2\text{Nb}_3\text{O}_{10}$  bulk material (1.44 nm) and the coverage of the nanosheets with  $\text{TBA}^+$  (top and bottom,  $\approx 2 \cdot 0.2 \text{ nm}^{28}$ ), as well as the presence of surface-adsorbed water, we can ascertain the formation of single  $\text{Ca}_2\text{Nb}_3\text{O}_{10}^-$  nanosheets.<sup>39</sup>



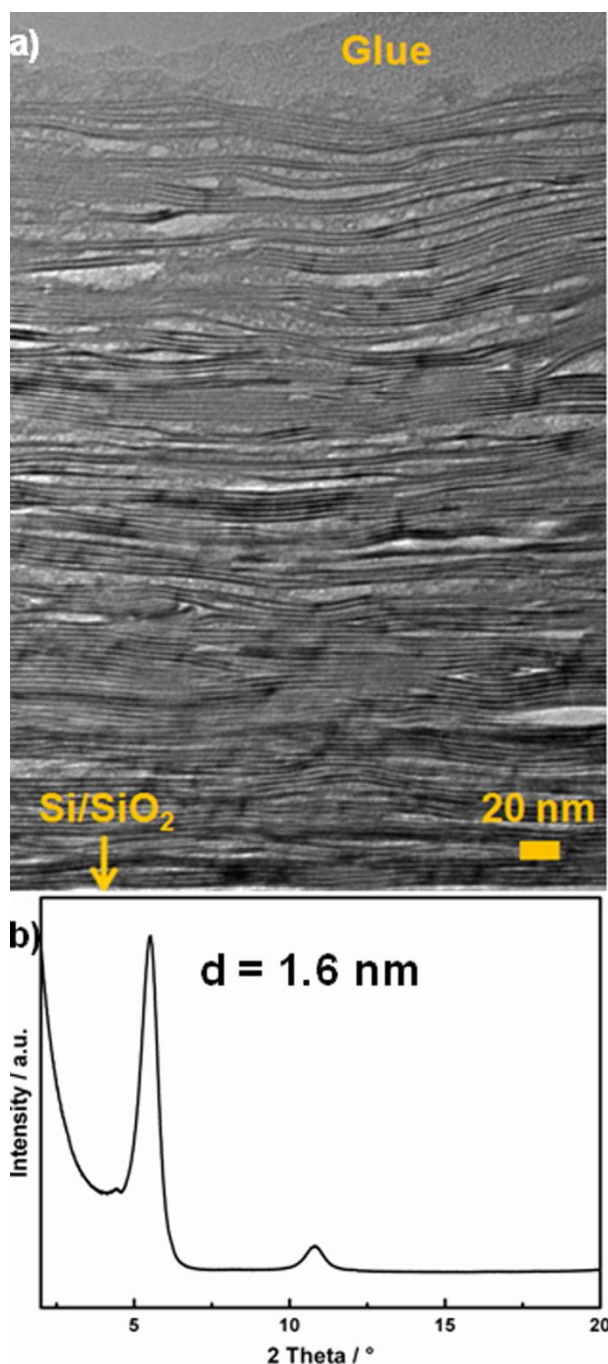
**Figure 4.1.3:** IR spectra of  $\text{TBA}_{0.84}\text{H}_{0.14}\text{Ca}_2\text{Nb}_3\text{O}_{10}$  before 1 and after 2 dilution with water.

Figure 4.1.1 schematically depicts the formation of  $(\text{LDH}_{\text{fa/aq}}/\text{per})_n$  multilayer films (fa = LDH exfoliated in formamide, aq = LDH exfoliated in water,  $n$  = number of bilayers).  $\text{Mn}_2\text{Al}(\text{OH})_6^+$  and  $\text{Ca}_2\text{Nb}_3\text{O}_{10}^-$  are alternately adsorbed on a  $\text{Si}/\text{SiO}_2$  substrate with washing steps in between to remove excess material and avoid flocculation of the colloidal suspensions. All protocols in the literature relying on positively charged LDH nanosheets use sheets suspended in formamide in order to avoid contamination with carbonate dissolved in water through contact with air. This measure accounts for the fact that the cationic LDH layers have a high affinity to divalent carbonate anions, which are difficult to exchange for monovalent anions and could therefore influence the LBL assembly.<sup>39</sup> In the present study  $\text{Ca}_2\text{Nb}_3\text{O}_{10}^-$  was dispersed in water rather than formamide, since no signs of agglomeration of  $\text{Mn}_2\text{Al}(\text{OH})_6^+$  during the LBL process was observed.

Figure 4.1.4 a shows an overview HRTEM image of a cross-section sample of a multilayer  $(\text{LDH}_{\text{fa}}/\text{per})_{100}$  film. The layers are grown in an ordered fashion on the  $\text{Si}/\text{SiO}_2$  substrate, yet “real structure” effects as opposed to an ideally ordered structure composed of infinitely extended sheets are clearly visible. The layers show a significant degree of flexibility and bending around defects such as sheet terminations, which leads to voids and overlaps in the assembly. Hence, displacements and small holes are visible in the cross-section sample, which can also arise from mechanical forces acting on the sample during the TEM cross-section preparation. Accordingly, the XRD pattern of a  $(\text{LDH}/\text{per})$  multilayer stack shows two (00 $\ell$ ) reflections around 5.5 and 11.0° 2 theta, pointing to a double layer thickness of



$\approx 1.6$  nm (Figure 4.1.4 b). The reflections are broadened due to sheet bending and different layer packing densities as seen in the TEM cross-section images of the stack. The number of counted bilayers ( $100 \pm 5$ ) and the effective thickness of the stack (250 nm) roughly correspond to that expected for a 100 bilayer film ( $100 \cdot (1.44 \text{ nm} + 0.48 \text{ nm}) = 192 \text{ nm}$ ), taking holes and irregularities into account. A plot of the number of bilayers, determined by AFM, vs. thickness of the stack shows a linear progression of the layer thickness (Figure S4.1.5).



**Figure 4.1.4:** a) Bright field HRTEM micrograph of the cross-section of a 100 bilayer  $(\text{LDH}_{\text{tal}}/\text{per})_{100}$  film obtained by electrostatic LBL assembly. b) XRD pattern of  $(\text{LDH}/\text{per})_{80}$  measured in reflection mode.

The presence of both components –  $\text{Mn}_2\text{Al}(\text{OH})_6^+$  and  $\text{Ca}_2\text{Nb}_3\text{O}_{10}^-$  – in the assembly was verified based on an EDX mapping of the LDH- and perovskite-specific elements, respectively (Figure 4.1.5). The signal of the Al  $K_\alpha$ , Mn  $K_\alpha$ , Ca  $K_\alpha$ , Nb  $L_\alpha$ , and O- $K_\alpha$  peaks from EDX maps shows evidence of a homogeneous distribution throughout the multilayer, thus confirming the formation of a hybrid nanostructure featuring layered components intimately mixed at the nanoscale. The observed carbon signal either arises from the remaining organic counterions ( $\text{TBA}^+$  and  $\text{ES}^-$ ) or from the glue used for TEM sample preparation. EDX quantification confirms that the amount of  $\text{Ca}_2\text{Nb}_3\text{O}_{10}^-$  is 2-3 times higher than that of  $\text{Mn}_2\text{Al}(\text{OH})_6^+$ . Individual spectra and related quantification data are shown in Figure S4.1.7 and Table S4.1.3. In order to draw further conclusions on the local structure of the stack and to ascertain the sequential assembly of nanosheets (rather than the formation of a disordered nanocomposite as obtained by flocculation), atomic column resolved high-angle annular dark field (HAADF)-STEM measurements were performed.

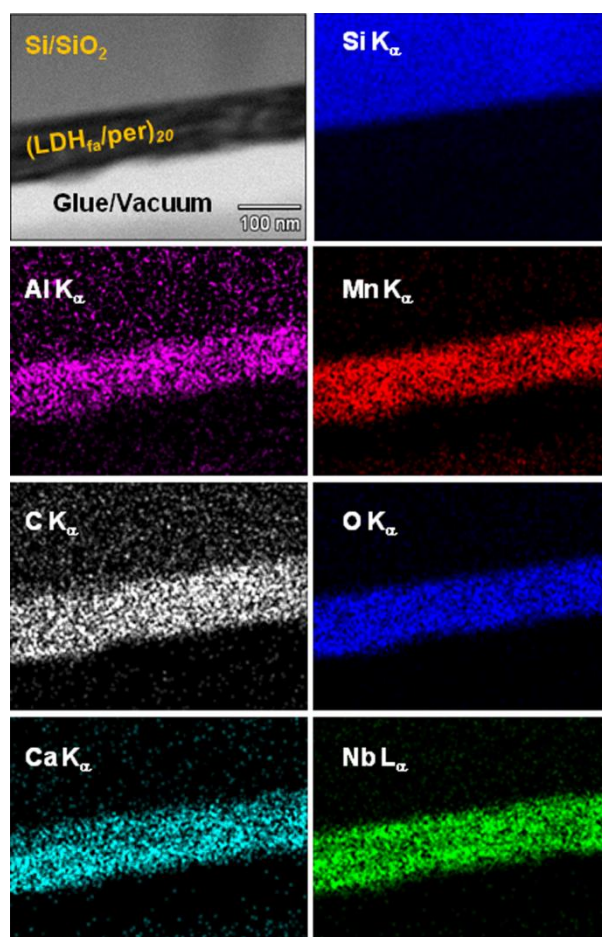


**Figure 4.1.5:** EDX mapping of a  $(\text{LDH}_{\text{tal}}/\text{per})_{20}$  stack on Si showing homogeneous distribution of all elements. Si  $K_\alpha$ , C  $K_\alpha$ , O  $K_\alpha$ , Al  $K_\alpha$ , Mn  $K_\alpha$ , Ca  $K_\alpha$  and Nb  $L_\alpha$  signals were measured.

The HAADF image (Figure 4.1.6 a) shows an alternating sequence of three bright columns/planes with one broad dark layer in between. Given the sensitivity to the atomic

number in HAADF imaging, we attribute the dark slabs to the LDH as will be discussed below. Nevertheless, STEM measurements reveal rapid disintegration under the electron beam, which might explain why no crystalline signature was obtained in these regions. The bright columns/planes arranged in regular “triplets” originate from the heavy niobium atoms and hence can be related to the perovskite layer composed of three edge-sharing  $\text{NbO}_6$  octahedra as fundamental structural motif. These layers are not always oriented along the zone axis as expected for the bulk material, but tilted with respect to each other within the plane of the sheets (i.e. by rotation around a common axis perpendicular to the substrate); thus, the atomic columns can appear as lines in the off-axis orientation. This is clear evidence of the presence of individual delaminated perovskite sheets rather than non-exfoliated bulk material. Some of the perovskite sheets are brighter than others; this is likely related to their orientation with respect to the electron beam. Indeed, it can be observed that brighter layers are atomically resolved, whereas the darker layers are not.

Besides the stacking disorder due to sheet terminations and corrugations owing to varying amounts of adsorbed LDH between the perovskite layers, another observation should be pointed out: In Figure 4.1.6 a the white ellipse marks an area where additional niobium columns seem to be present. This can result from inhomogeneous adsorption of LDH and, hence, formation of wedges causing a tilting of the perovskite layers in the projection of the TEM foil.

Figure 4.1.6 b shows the corresponding intensity profile taken along the orange bar (Figure 4.1.6 a). This intensity profile yields Nb-Nb distances inside a perovskite layer of 3.6-4.2 Å and shows Nb-Nb distances between two different layers starting from 6-9 Å. Figure 4.1.7 a shows the atomic distances of Nb-Nb and Ca-Ca within a perovskite layer in horizontal and vertical directions. In Table S4.1.4 these distances are listed and compared to the values obtained from the perovskite layer in the bulk materials  $\text{KCa}_2\text{Nb}_3\text{O}_{10}$  (monoclinic, space group  $P2_1/m$ ) and  $\text{HCa}_2\text{Nb}_3\text{O}_{10} \cdot 0.5 \text{H}_2\text{O}$  (tetragonal, space group  $P4/mbm$ ). The values are significantly different and can therefore not be considered an imaging artifact. All experimental values are in agreement with the distances found in the bulk materials. The inset of Figure 4.1.6 b displays a smaller distance marked with a blue circle next to a larger distance marked with a green cross between two perovskite layers, which is also highlighted in the intensity profile. This observation confirms that the distances between the perovskite layers are not constant due to different amounts of adsorbed LDH. The smaller distance is close to the distances found between two perovskite layers in the  $\text{HCa}_2\text{Nb}_3\text{O}_{10} \cdot 0.5 \text{H}_2\text{O}$  bulk material and might suggest deposition of multiple layers of  $\text{HCa}_2\text{Nb}_3\text{O}_{10}$  upon partial  $\text{TBA}^+$  – proton exchange during the LBL process. To test this possibility and its impact on the multilayer formation, we attempted to assemble  $\text{Ca}_2\text{Nb}_3\text{O}_{10}^-$  without  $\text{Mn}_2\text{Al}(\text{OH})_6^+$  under otherwise identical experimental conditions and found that this leads to a random

accumulation of sheets without a defined multilayer structure. Similarly, the addition of  $\text{Mn}^{2+}$  and  $\text{Al}^{3+}$  ions in solution does not lead to multilayer structures but rather to the deposition of a few layers of  $\text{Ca}_2\text{Nb}_3\text{O}_{10}^-$  on the substrate (Figure S4.1.6). Hence, as expected and in line with the TEM results, oppositely charged nanosheets are crucial for the fabrication of such heterostructures and multilayer stacking of  $\text{HCa}_2\text{Nb}_3\text{O}_{10}$  without the presence of LDH can be excluded (Figure 4.1.7a).

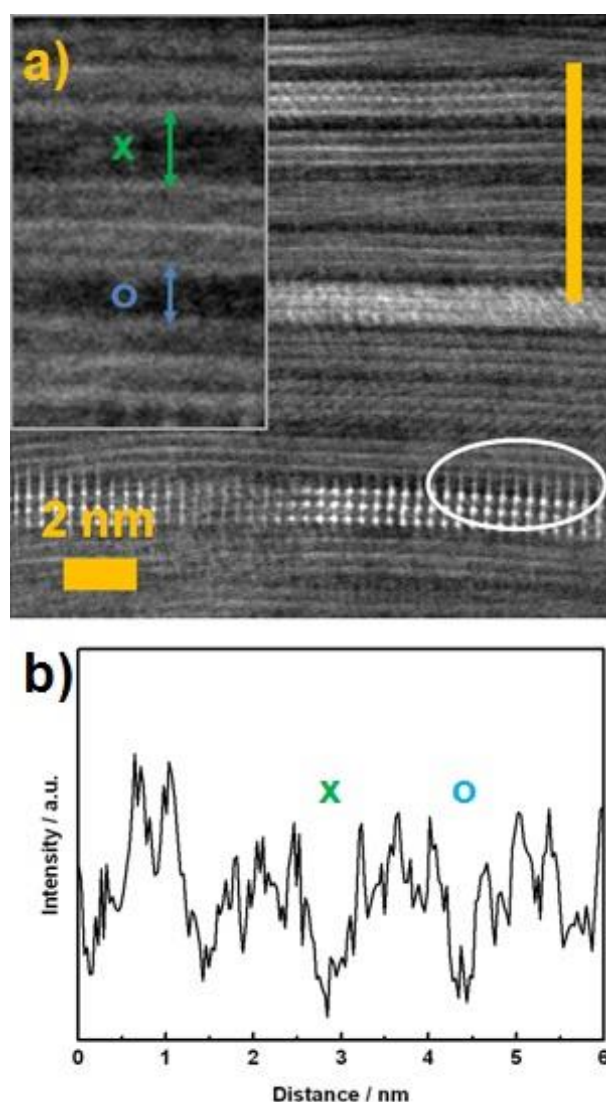


**Figure 4.1.6:** a) High-resolution HAADF-STEM image of a  $(\text{LDH}_{\text{fa}}/\text{per})_{100}$  film and b) intensity profile taken along the orange bar with the green cross marking a large and the blue circle a smaller distance between individual perovskite layers, as shown in the inset. The white ellipse highlights a region where additional columns are visible due to a projection effect.

Another factor already evident from the EDX data is that less  $\text{Mn}_2\text{Al}(\text{OH})_6^+$  than  $\text{Ca}_2\text{Nb}_3\text{O}_{10}^-$  is present throughout the sample. Hence, the signal for the Mn  $L_{2,3}$  edge is weak. In addition, elements tend to have a low inelastic scattering cross-section at high energy losses. Figure 4.1.7 c shows enlarged the extracted and normalized signal of Ca  $L_{2,3}$  and Nb  $M_{2,3}$ ,

whereas the Mn L<sub>2,3</sub> and the O K edge are depicted in Figure 4.1.7 d with the individual spectra of the bright perovskite layer (blue line) and the dark LDH layer (red line), respectively. Note that the signal of the Ca L<sub>2,3</sub> and Nb M<sub>2,3</sub> edges decreases, but does not totally vanish. This can be explained by a slight tilt of the measured multilayer region with respect to the incident beam and the finite resolution of the experimental technique, giving rise to signal contributions from layer regions deeper in the stack. Furthermore, a change of the O K near-edge fine structures is visible, indicating a change of the environment of the oxygen atoms when comparing the pristine perovskite with the hybrid superlattice. An intensity profile of the extracted Ca L<sub>2,3</sub>, Mn L<sub>2,3</sub> and O K edges is shown in Figure 4.1.7 e (for details see Supporting Information).

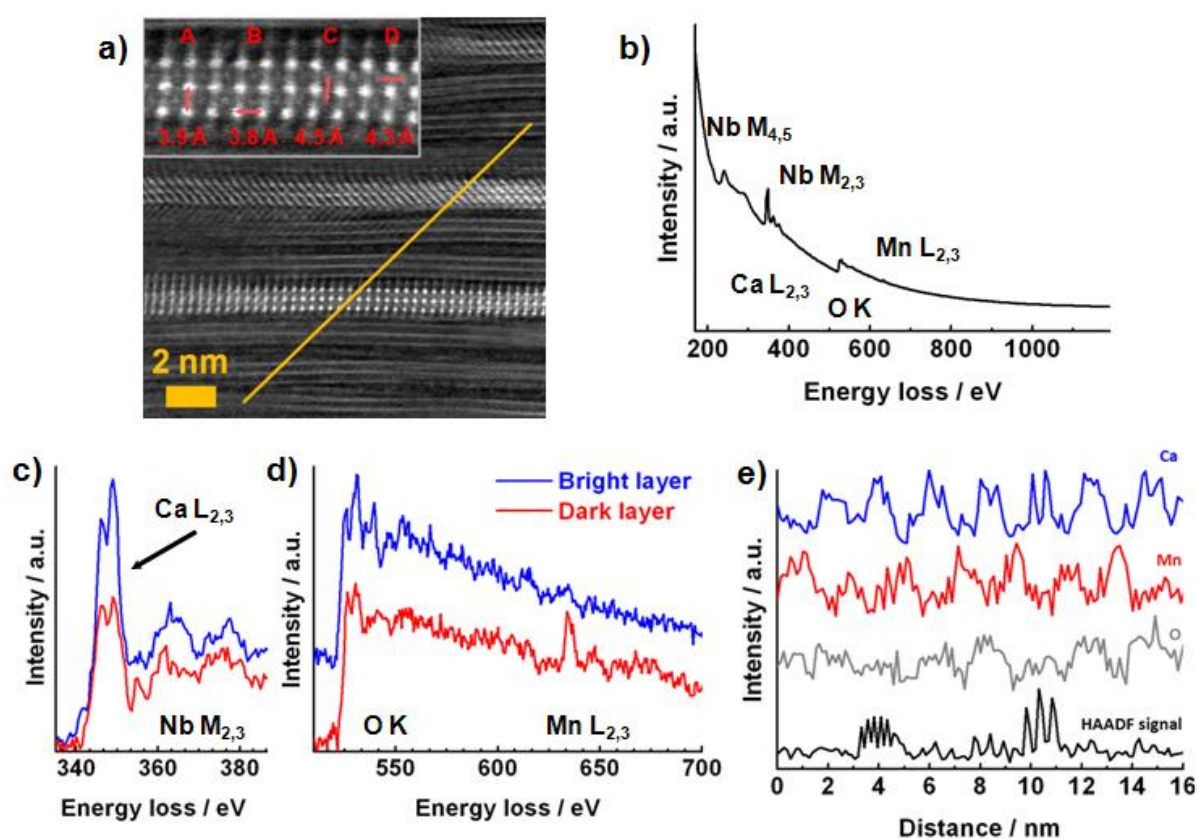


**Figure 4.1.7:** a) STEM cross-section image of a (LDH<sub>fa</sub>/per)<sub>100</sub> film. The inset shows the vertical (vert) and horizontal (horiz) distances between A) Nb-Nb<sub>horiz</sub>, B) Nb-Nb<sub>vert</sub>, C) Ca-Ca<sub>vert</sub>, D) Ca-Ca<sub>horiz</sub>. The orange line corresponds to an EELS line-scan, where b) shows the corresponding summed up EEL spectra, c) the individual EEL spectra of the Ca L<sub>2,3</sub> and Nb M<sub>2,3</sub> edges without shift and d) the individual EEL spectra of the O K and Mn L<sub>2,3</sub> edge with a vertical shift of the blue spectra. In c) and d) the spectra from the bright layer (perovskite) are shown in blue, those from the dark layer (LDH) in red. e) Extracted intensity profiles of Ca L<sub>2,3</sub>, Mn L<sub>2,3</sub>, O K, and the HAADF signal taken along the orange line in (a).

Figure 4.1.7a shows a HR-STEM image where an EELS line-scan was performed along the orange line. 128 EEL spectra were taken along a distance of 16.3 nm with a dispersion of 0.5 eV/channel. In the range from 169 to 1193 eV most major ionization edges of interest are visible: the Nb-M<sub>4,5</sub> with an onset at 205 eV and a delayed maximum, the Ca-L<sub>2,3</sub> with two white-lines at 346 eV and 350 eV, the Nb-M<sub>2,3</sub> at 363 eV and 378 eV with a sharp threshold peak, the O-K at 532 eV, and the Mn-L<sub>2,3</sub> at 640 eV and 651 eV. Figure 4.1.6b depicts all EEL spectra integrated over the full set of data with the energy scale calibrated based on the Ca-L<sub>3</sub> edge in the dataset. The Mn-L<sub>2,3</sub> edge is only visible in the dark layer, whereas the Ca-L<sub>2,3</sub> is always present, but with significantly decreased intensity in the dark layer. This is different to measurements known from literature performed on (LaNb<sub>2</sub>O<sub>7</sub>/Ca<sub>2</sub>Nb<sub>3</sub>O<sub>10</sub>)<sub>n</sub> multilayer stacks, where the perovskite layers are less sensitive to electron irradiation and the signals can clearly be distinguished.<sup>28</sup>

The maximum of the Mn L<sub>2,3</sub> signal consistently lies in the minimum of the Ca L<sub>2,3</sub> signal, thus proving the alternate stacking of individual Mn<sub>2</sub>Al(OH)<sub>6</sub><sup>+</sup> nanosheets with Ca<sub>2</sub>Nb<sub>3</sub>O<sub>10</sub><sup>-</sup> nanosheets at the nanometer scale. Notably, this finding implies full delamination of the LDH and perovskite sheets in solution or upon interaction with the respective oppositely charged top nanosheet layer.

The O K signal is more dominant in the perovskite region, but less pronounced than the Ca L<sub>2,3</sub> signal showing the additional existence of oxygen atoms between the layers, which can be attributed to the Mn<sub>2</sub>Al(OH)<sub>6</sub><sup>+</sup> layers. The Al L<sub>2,3</sub> edge (73 eV) is influenced by the rising background from the Nb N<sub>2,3</sub>(34 eV), Ca M<sub>2,3</sub> (25 eV) and Mn M<sub>2,3</sub> (49 eV) edges. In addition, the amount of aluminum present in the sample is low, which makes the detection of the Al L<sub>2,3</sub> edge difficult. Also, the Al K edge is located at much higher energy-losses (~1560 eV) and hence shows a weaker signal for the same acquisition time. However, an increased exposure time quickly leads to contamination and therefore to an enhanced background of the C K edge, which renders the detection of the Al K edge challenging and rather unreliable under the present conditions and nature of the sample.

The above analysis yields insights into the structure and morphology of the multilayer stack both on the atomic and nanoscale. In line with the solution-based stepwise “growth” process, epitaxial layer stacking is neither expected nor observed.

Nevertheless, the adsorption process generates densely packed regions with little defects next to regions with major stacking faults and locally aggregated organic residues, which likely stem from residual, non-exchanged ligands.

Along these lines, it is instructive to probe the influence of the assembly conditions on the structure and interfacial quality of the resulting heterostructures. Therefore, in addition to the (LDH<sub>fa</sub>/per)<sub>100</sub> multilayer film assembled with formamide as dispersing solvent for the LDH, a



(LDH<sub>aq</sub>/per)<sub>90</sub> stack using aqueous suspensions throughout was synthesized. Accordingly, exfoliation of the LDH was carried out in H<sub>2</sub>O rather than formamide.

A low-resolution cross-sectional STEM image of both samples is shown in Figure 4.1.8 for comparison. In contrast to the (LDH<sub>fa</sub>/per)<sub>100</sub> film, the (LDH<sub>aq</sub>/per)<sub>90</sub> film is less densely stacked and apparently exhibits larger distances between the perovskite layers. The amount of LDH attached to the perovskite sheets appears to be less than in the (LDH<sub>fa</sub>/per)<sub>100</sub> stack and the space between the perovskite layers is not as homogeneously filled. EDX analysis suggests that approximately ten times less Mn<sub>2</sub>Al(OH)<sub>6</sub><sup>+</sup> is present in the (LDH<sub>aq</sub>/per)<sub>90</sub> stack than in the (LDH<sub>fa</sub>/per)<sub>100</sub> film. In agreement with its porous and less ordered structure, the (LDH<sub>aq</sub>/per)<sub>90</sub> film is less stable under the electron beam, making EELS line-scans unfeasible under the given circumstances.

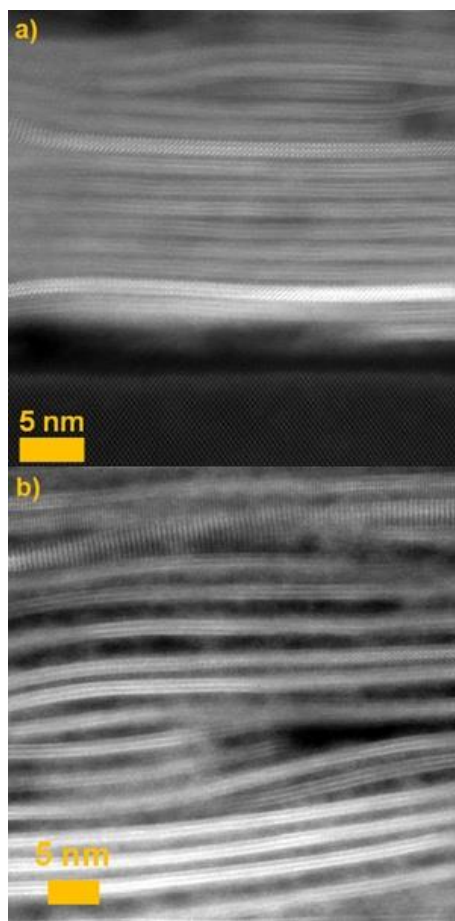


**Figure 4.1.8:** Comparison of STEM cross-section images taken from a (LDH<sub>fa</sub>/per)<sub>100</sub> film assembled with the LDH being dispersed in formamide (a), and a (LDH<sub>aq</sub>/per)<sub>90</sub> film with the LDH dispersed in water (b).

Figure 4.1.9 displays an overall EEL spectrum for the (LDH<sub>aq</sub>/per)<sub>90</sub> stack, similar to the one shown for (LDH<sub>fa</sub>/per)<sub>100</sub>. All edges are less pronounced and the signal for the Mn L<sub>2,3</sub> edge is further decreased, with only a small peak visible as shown in the inset (marked with a red

circle). We attribute the lower amount of LDH in the water-based sample to the equilibrium reaction described above (Eq. 4.1.1), which is visualized schematically in Figure 4.1.10. During the LDH deposition, the outer  $[(TBA)_{1-x}H_x]^+[Ca_2Nb_3O_{10}]^-$  layer of the stack is exposed to water. According to Eq. 4.1.1, the equilibrium is shifted to the right, thus increasing the degree of protonation (larger  $x$ ) for the  $[(TBA)_{1-x}H_x]^+[Ca_2Nb_3O_{10}]^-$  nanosheets whilst diluting the suspension with water. Hence, less  $TBA^+$  is present on the nanosheets, thus reducing the apparent layer charge density on the nanosheet surface when assuming only minimal dissociation of the protons in contrast to  $TBA^+$ . Therefore, the fraction of cations at the nanosheet surface exchangeable with LDH is reduced, giving rise to an overall higher amount of protons along with a lower amount of LDH in the final heterostructure. This is further substantiated by monitoring the pH whilst adding HCl to an aqueous  $TBA_{0.84}H_{0.16}Ca_2Nb_3O_{10}$  suspension. Figure S4.1.8 shows the pH plotted versus the molar fraction of  $TBA^+$  in  $TBA_xH_{1-x}Ca_2Nb_3O_{10}$ . Similar to the titration of  $TBA_xH_{1-x}TiNbO_5$  with  $HCl^3$  two equivalent points were found.

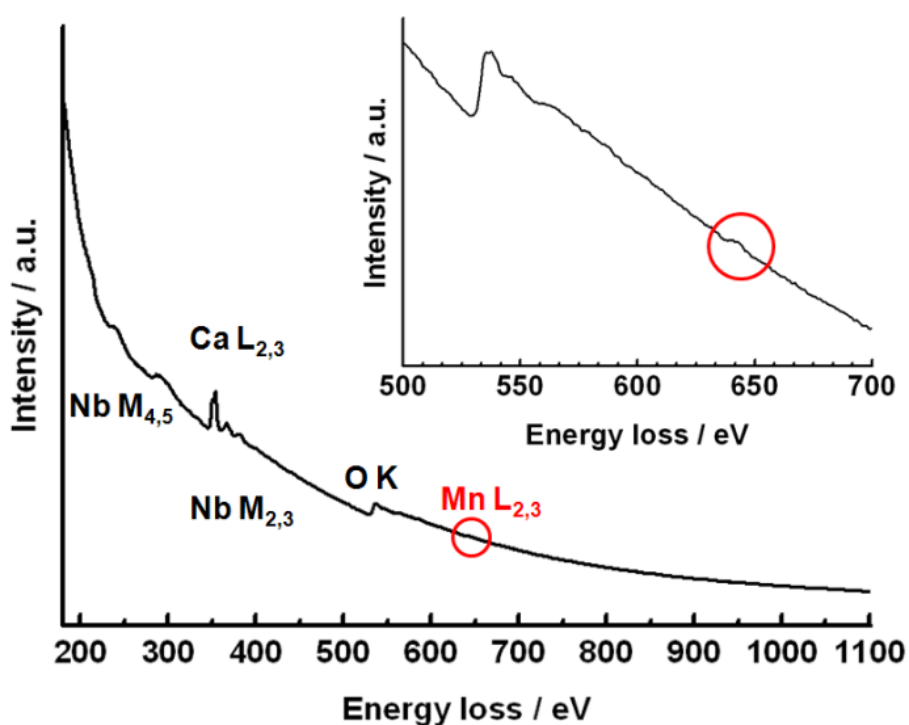


**Figure 4.1.9:** EELS line-scan of a  $(LDH_{aq}/per)_{90}$  film showing all spectra summed in black and the O K and Mn  $L_{2,3}$  edge (marked in red) enlarged in the inset.

The relevant one for the LbL assembly is the equivalent point at pH 8.7. Above this pH a single phase unilamellar colloid exists, which is necessary for a successful LbL deposition. Just below pH 5.5 solid  $TBA_xH_{1-x}Ca_2Nb_3O_{10}$  with a proton fraction of more than 50% starts precipitating. We infer from these results that the change of solvents employed for the dispersion of the nanosheets apparently has a major impact on the structure and



composition of the resulting superlattices. Although the choice of solvent is limited by the limited dispersability of the nanosheets in many solvents, this finding nevertheless points out an important design criterion in the assembly of nanosheets, which is governed by colloidal stability, ionic strength, composition of the Helmholtz double layer and solution equilibria influenced by the pH.

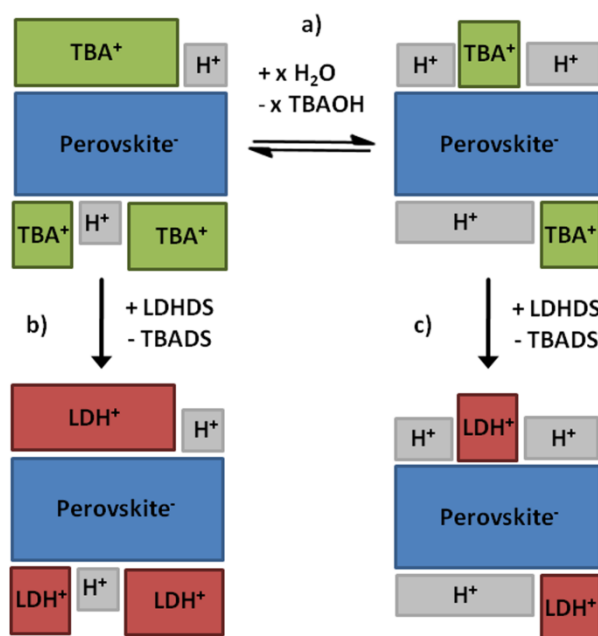


**Figure 4.1.10:** Scheme depicting the proposed formation mechanism of a (LDH/per)<sub>n</sub> film as a function of the equilibrium reaction (a). Densely packed (LDH<sub>fd</sub>/per)<sub>n</sub> films are obtained in step (b), while in step (c) less dense (LDH<sub>aq</sub>/per)<sub>n</sub> films are generated due to a shift of the equilibrium reaction of TBAOH and water.

### 4.1.3 Conclusion

We have demonstrated the rational synthesis of a complex two-component solid composed of Mn<sub>2</sub>Al(OH)<sub>6</sub><sup>+</sup> and Ca<sub>2</sub>Nb<sub>3</sub>O<sub>10</sub><sup>-</sup> nanosheets by means of electrostatic layer-by-layer assembly, which highlights the feasibility of the “rational design” of complex solids through judicious combination of nanosheet building blocks. For the first time, we have been able to map out the structure and elemental distribution within the stacks locally resolved by HRTEM, STEM and EELS analysis, and ascertained the presence of alternating, compositionally distinct LDH and perovskite layers of consistent and reproducible minimum thickness, i.e. single sheets. While the perovskite layers are highly crystalline and stable, no crystalline signature of the LDH layers was obtained owing to their rapid damage under the electron beam. The morphology of the multilayer films can be modified by selection of different nanosheet dispersing solvents, which was demonstrated by fabricating dense stacks from LDH dispersed in formamide, whilst suspension in water leads to less dense

stacks containing a smaller overall amount of LDH. This feature will be helpful as a future design criterion to tune the composition and porosity of the stacks.

In addition, we demonstrated that multilayer films composed of 100 double layers (and possibly more) can easily be obtained by ESD, which is a first step towards the synthesis of tailor-made bulk solids rather than ultrathin films from individual 2D building blocks. Finally, with this study we add evidence to the notion that solids can in fact be “designed” in a rational way by taking advantage of soft chemistry routes to new solids, rather than relying on traditional explorative solid-state synthesis which is largely driven by thermodynamic principles.

#### **ACKNOWLEDGEMENT:**

This work was supported by the cluster of excellence Nanosystems Initiative Munich (NIM), the Fonds der Chemischen Industrie (FCI) and the Center for Nanoscience (CeNS). Part of the electron microscopy work was performed at the Canadian Centre for Electron Microscopy (CCEM), a Canadian national facility supported by NSERC and McMaster University. G.A.B. is grateful to the NSERC of Canada for partially supporting this work through a Discovery Grant.

We thank Kulpreet S. Viridi for initial microscopy studies, T. Holzmann and A. Schwarze for cross-section TEM sample preparation, C. Minke for SEM/EDX measurements, H. Hartl and M.-L. Schreiber for ICP measurements, R. Eicher for CHNS analysis as well as Stephan Hug and Christine Stefani for additional XRD measurements.

#### **4.1.4 Bibliography**

- [1] S. W. Keller, H.-N. Kim, T. E. Mallouk, *J. Am. Chem. Soc.* **1994**, *116*, 8817-8818.
- [2] H.-N. Kim, S. W. Keller, T. E. Mallouk, J. Schmitt, G. Decher, *Chem. Mater.* **1997**, *9*, 1414-1421.
- [3] M. Fang, C. H. Kim, G. B. Saupe, H.-N. Kim, C. C. Waraksa, T. Miwa, A. Fujishima, T. E. Mallouk, *Chem. Mater.* **1999**, *11*, 1526-1532.
- [4] R. E. Schaak, T. E. Mallouk, *Chem. Mater.* **2000**, *12*, 2513-2516.
- [5] R. E. Schaak, T. E. Mallouk, *Chem. Mater.* **2000**, *12*, 3427-3434.
- [6] R. E. Schaak, T. E. Mallouk, *Chem. Mater.* **2002**, *14*, 1455-1471.
- [7] T. Sasaki, Y. Ebina, M. Watanabe, G. Decher, *Chem. Commun. (Cambridge, U. K.)* **2000**, 2163-2164.
- [8] T. Sasaki, Y. Ebina, T. Tanaka, M. Harada, M. Watanabe, G. Decher, *Chem. Mater.* **2001**, *13*, 4661-4667.
- [9] T. Tanaka, K. Fukuda, Y. Ebina, K. Takada, T. Sasaki, *Adv. Mater. (Weinheim, Ger.)* **2004**, *16*, 872-875.

- [10] M. Osada, Y. Ebina, K. Takada, T. Sasaki, *Adv. Mater. (Weinheim, Ger.)* **2006**, *18*, 295-299.
- [11] K. S. Novoselov, A. K. Geim, S. V. Morozov, D. Jiang, Y. Zhang, S. V. Dubonos, I. V. Grigorieva, A. A. Firsov, *Science* **2004**, *306*, 666-669.
- [12] A. K. Geim, K. S. Novoselov, *Nat. Mater.* **2007**, *6*, 183-191.
- [13] A. K. Geim, *Science* **2009**, *324*, 1530-1534.
- [14] R. F. Service, *Science* **2009**, *324*, 875-877.
- [15] M. J. Allen, V. C. Tung, R. B. Kaner, *Chem. Rev. (Washington, DC, U. S.)* **2010**, *110*, 132-145.
- [16] D. R. Cooper, B. D'Anjou, N. Ghattamaneni, B. Harack, M. Hilke, A. Horth, N. Majlis, M. Massicotte, L. Vandsburger, E. Whiteway, V. Yu, *ISRN Condens. Matter. Phys.* **2012**, *2012*, 56.
- [17] K. S. Novoselov, A. H. C. Neto, *Phys. Scr.* **2012**, *T146*, 014006.
- [18] L. Li, R. Ma, Y. Ebina, N. Iyi, T. Sasaki, *Chem. Mater.* **2005**, *17*, 4386-4391.
- [19] T. Sasaki, M. Watanabe, H. Hashizume, H. Yamada, H. Nakazawa, *J. Am. Chem. Soc.* **1996**, *118*, 8329-8335.
- [20] P. Joensen, R. F. Frindt, S. R. Morrison, *Mater. Res. Bull.* **1986**, *21*, 457-461.
- [21] R. Mas-Balleste, C. Gomez-Navarro, J. Gomez-Herrero, F. Zamora, *Nanoscale* **2011**, *3*, 20-30.
- [22] T. Tanaka, S. Nishimoto, Y. Kameshima, M. Miyake, *Mater. Lett.* **2011**, *65*, 2315-2318.
- [23] K. Saruwatari, H. Sato, J. Kameda, A. Yamagishi, K. Domen, *Chem. Commun. (Cambridge, U. K.)* **2005**, 1999-2001.
- [24] K. Saruwatari, H. Sato, T. Idei, J. Kameda, A. Yamagishi, A. Takagaki, K. Domen, *J. Phys. Chem. B* **2005**, *109*, 12410-12416.
- [25] M. Muramatsu, K. Akatsuka, Y. Ebina, K. Wang, T. Sasaki, T. Ishida, K. Miyake, M.-a. Haga, *Langmuir* **2005**, *21*, 6590-6595.
- [26] B.-W. Li, M. Osada, T. C. Ozawa, R. Ma, K. Akatsuka, Y. Ebina, H. Funakubo, S. Ueda, K. Kobayashi, T. Sasaki, *Jpn. J. Appl. Phys.* **2009**, *48*, 2009.
- [27] M. Osada, K. Akatsuka, Y. Ebina, H. Funakubo, K. Ono, K. Takada, T. Sasaki, *ACS Nano* **2010**, *4*, 5225-5232.
- [28] B.-W. Li, M. Osada, T. C. Ozawa, Y. Ebina, K. Akatsuka, R. Ma, H. Funakubo, T. Sasaki, *ACS Nano* **2010**, *4*, 6673-6680.
- [29] B.-W. Li, M. Osada, K. Akatsuka, Y. Ebina, T. C. Ozawa, T. Sasaki, *Jpn. J. Appl. Phys.* **2011**, *50*, 09NA10.
- [30] J. L. Gunjekar, T. W. Kim, H. N. Kim, I. Y. Kim, S.-J. Hwang, *J. Am. Chem. Soc.* **2011**, *133*, 14998-15007.

- [31] U. Unal, Y. Matsumoto, N. Tanaka, Y. Kimura, N. Tamoto, *J. Phys. Chem. B* **2003**, *107*, 12680-12689.
- [32] U. Unal, Y. Matsumoto, N. Tamoto, M. Koinuma, M. Machida, K. Izawa, *J. Solid State Chem.* **2006**, *179*, 33-40.
- [33] S. Ida, U. Unal, K. Izawa, C. Ogata, T. Inoue, Y. Matsumoto, *Mol. Cryst. Liq. Cryst.* **2007**, *470*, 393-402.
- [34] L. Wang, D. Wang, X. Y. Dong, Z. J. Zhang, X. F. Pei, X. J. Chen, B. Chen, J. Jin, *Chem. Commun. (Cambridge, U. K.)* **2011**, *47*, 3556-3558.
- [35] Z. Gao, J. Wang, Z. Li, W. Yang, B. Wang, M. Hou, Y. He, Q. Liu, T. Mann, P. Yang, M. Zhang, L. Liu, *Chem. Mater.* **2011**, *23*, 3509-3516.
- [36] J. Huang, R. Ma, Y. Ebina, K. Fukuda, K. Takada, T. Sasaki, *Chem. Mater.* **2010**, *22*, 2582-2587.
- [37] J. Han, Y. Dou, M. Wei, D. G. Evans, X. Duan, *Angew. Chem., Int. Ed. Engl.* **2010**, *49*, 2171-2174.
- [38] P. G. Hoertz, T. E. Mallouk, *Inorg. Chem.* **2005**, *44*, 6828-6840.
- [39] L. Li, R. Ma, Y. Ebina, K. Fukuda, K. Takada, T. Sasaki, *J. Am. Chem. Soc.* **2007**, *129*, 8000-8007.
- [40] H. Li, L. Deng, G. Zhu, L. Kang, Z.-H. Liu, *Mater. Sci. Eng., B* **2012**, *177*, 8-13.
- [41] X. Zhang, Y. Wang, X. Chen, W. Yang, *Mater. Lett.* **2008**, *62*, 1613-1616.
- [42] S. Huang, X. Cen, H. Peng, S. Guo, W. Wang, T. Liu, *J. Phys. Chem. B* **2009**, *113*, 15225-15230.
- [43] D. Chen, X. Wang, T. Liu, X. Wang, J. Li, *ACS Appl. Mater. Interfaces* **2010**, *2*, 2005-2011.
- [44] E. Coronado, C. Marti-Gastaldo, E. N. Navarro-Moratalla, A. Ribera, S. J. Blundell, P. J. Baker, *Nature Chem.* **2010**, *2*, 1031-1036.
- [45] S. Ida, Y. Sonoda, K. Ikeue, Y. Matsumoto, *Chem. Commun. (Cambridge, U. K.)* **2010**, *46*, 877-879.
- [46] R. Ma, T. Sasaki, *Adv. Mater. (Weinheim, Ger.)* **2010**, *22*, 5082-5104.
- [47] T. Hibino, *Chem. Mater.* **2004**, *16*, 5482-5488.
- [48] S. Werner, V. W.-h. Lau, S. Hug, V. Duppel, H. Clausen-Schaumann, B. V. Lotsch, *Langmuir* **2013**, *29*, 9199-9207.
- [49] M. Dion, M. Ganne, M. Tournoux, *Mater. Res. Bull.* **1981**, *16*, 1429-1435.
- [50] Y. Ebina, T. Sasaki, M. Watanabe, *Solid State Ionics* **2002**, *151*, 177-182.
- [51] M. J. Hudson, S. Carlino, D. C. Apperley, *J. Mater. Chem.* **1995**, *5*, 323-329.
- [52] S. Ida, C. Ogata, M. Eguchi, W. J. Youngblood, T. E. Mallouk, Y. Matsumoto, *J. Am. Chem. Soc.* **2008**, *130*, 7052-7059.

#### 4.1.5 Supporting Information

##### EXPERIMENTAL PROCEDURES:

**Chemicals.** All chemicals and solvents were purchased from commercial suppliers and used without further purification: 4-ethylbenzenesulfonic acid (Sigma-Aldrich, 95%), manganese nitrate ( $\text{Mn}(\text{NO}_3)_2 \cdot 4 \text{H}_2\text{O}$ , Sigma-Aldrich, 97%), aluminum nitrate ( $\text{Al}(\text{NO}_3)_3 \cdot 9 \text{H}_2\text{O}$ , Fluka, 99%), sodium hydroxide (NaOH, AppliChem, 97%), formamide (Fluka, 98%), potassium carbonate ( $\text{K}_2\text{CO}_3$ , Merck KGaA, 99%), calcium carbonate ( $\text{CaCO}_3$ , Grüssing, 99%), niobium pentoxide ( $\text{Nb}_2\text{O}_5$ , Alfa Aesar, 99.5%), tetra-*n*-butylammonium hydroxide 30-hydrate (*TBAOH*, Sigma-Aldrich, 98%). Deionized water was used throughout all procedures.

**$\text{Mn}_2\text{Al}(\text{OH})_6^+$  Synthesis.** The LDH bulk compounds were synthesized by a typical coprecipitation method according to the literature.<sup>1</sup>  $\text{Mn}(\text{NO}_3)_2 \cdot 4 \text{H}_2\text{O}$  (3.33 mmol, 835 mg) and  $\text{Al}(\text{NO}_3)_3 \cdot 9 \text{H}_2\text{O}$  (1.67 mmol, 626 mg) were dissolved in 100 mL water. An aqueous solution of 4-ethylbenzenesulfonic acid (1 mM, 100 mL) was added to the metal nitrate solution. Under Argon atmosphere (to avoid absorption of ambient  $\text{CO}_2$ ) 1 M NaOH was added dropwise to the solution to adjust the pH to 9.0. The brown precipitate was recovered by filtration, washed with water and acetone and dried under vacuum for 24 h. Exfoliation of  $\text{MnAl}$  ethylbenzenesulfonate (*ES*) LDH in formamide was carried out by dispersing 25 mg of the bulk material in 50 mL formamide and subsequent sonication for 30 min. The resulting colloidal suspensions were centrifuged at 1,000 rpm for 10 min to remove possible non-exfoliated particles. The supernatant was used for further synthesis. Exfoliation of the LDH in water was done by dispersing 25 mg bulk LDH in 50 mL water and subsequent sonication for 5 min.

**$\text{Ca}_2\text{Nb}_3\text{O}_{10}^-$  Synthesis.**  $\text{KCa}_2\text{Nb}_3\text{O}_{10}$  was synthesized in a modified procedure according to Dion *et al.*<sup>2</sup>  $\text{K}_2\text{CO}_3$ ,  $\text{CaCO}_3$  and  $\text{Nb}_2\text{O}_5$  were mixed and thoroughly grinded in the molar ratio 1.2 : 4 : 3. The mixture was then fired up to a temperature of 1200 °C for 60 h. 1 g of the as-synthesized powder was stirred in 40 mL 5M  $\text{HNO}_3$  for 5 days to achieve cation-proton exchange. The acid was replaced every day.<sup>3</sup> For exfoliation 0.2 g of the proton-exchanged form  $\text{HCa}_2\text{Nb}_3\text{O}_{10} \cdot 0.5 \text{H}_2\text{O}$  were dispersed with tetra-*n*-butylammonium hydroxide 30-hydrate (*TBAOH*) at a molar ratio of 1:1 in 50 mL aqueous solution. The suspension was shaken for 4 weeks and non-exfoliated particles were removed by centrifugation at 3,000 rpm for 30 min. The supernatant with a nanosheet concentration of ~2mg/mL was used for further synthesis.

**Multilayer assembly.** The multilayer films composed of  $\text{Mn}_2\text{Al}(\text{OH})_6^+$  and  $\text{Ca}_2\text{Nb}_3\text{O}_{10}^-$  were assembled using a StratoSequence 6 LBL robot (nanoStrata Inc., Tallahassee). After exfoliation, a Si (100) wafer terminated with a native  $\text{SiO}_2$  layer ( $\text{Si}/\text{SiO}_2$ ) was first immersed into the LDH nanosheet suspension in formamide for 10 min, then rinsed in water for 1 min,

immersed in the perovskite nanosheet suspension in water for 10 min and rinsed in water again for 1 min. This procedure was repeated  $n$  times in order to obtain multilayer films depicted as  $(\text{LDH}_{\text{fa}}/\text{per})_n$ . The washed film was dried under  $\text{N}_2$  gas flow for 1 min after each cycle. Multilayer films based on LDH suspended in water instead of formamide were assembled in the same way and are labelled as  $(\text{LDH}_{\text{aq}}/\text{per})_n$ .

**Cross-section preparation.** For transmission electron microscopy (TEM) characterizations a sandwich structure was prepared by gluing two Si/SiO<sub>2</sub> wafers together on the side of the multilayers and subsequently cutting the sandwich structure into discs. The discs were grinded, dimpled and ion-thinned.

#### CHARACTERIZATION:

X-ray diffraction (XRD) analysis, scanning electron microscopy (SEM) coupled with energy-dispersive X-ray (EDX) analysis, inductively coupled plasma atomic emission spectroscopy (ICP-AES), elemental analysis, atomic force microscopy (AFM) and transmission electron microscopy (TEM) were used to monitor starting and intermediate compounds as well as the obtained nanosheets.

**XRD.** XRD data of powders were collected using a Huber G670 (Huber, Rimsting; Cu K $\alpha_1$ -radiation,  $\lambda = 154.051$  pm, Ge(111)-monochromator, external standard SiO<sub>2</sub>) Guinier Imaging Plate diffractometer. XRD of multilayer stacks was performed on a Bruker D8 Advance diffractometer (Bruker, Billerica, Cu K $\alpha_1$ -radiation,  $\lambda = 154.051$  pm).

**SEM-EDX.** SEM was conducted on a JSM-6500F electron microscope (JEOL Ltd., Tokyo). The microscope was equipped with a 7418 EDX detector (Oxford Instruments, Abingdon).

**ICP-AES.** ICP-AES was done using a VISTA RL CCD and ICP-AES analyzer system (Agilent Technologies, Waldbronn).

**Elemental Analysis.** An Elementar vario EL (Elementar Analysensysteme, Hanau) was employed for elemental analysis (EA). To this end, nanosheets were isolated by centrifugation and the carbon, hydrogen and nitrogen mass fraction measured. The excess hydrogen content not attached to the  $\text{TBA}^+$  was calculated and used for the determination of  $x$ .

**AFM.** AFM measurements were performed on a MFP-3D Stand alone AFM (Asylum Research, Santa Barbara). Tapping-mode was applied using OMCL-AC160TS-R3 (Olympus, Tokio) cantilevers with a resonant frequency of 300 kHz.

**(S)TEM-EDX.** A Philips CM30 ST microscope (300 kV, LaB<sub>6</sub> cathode, CS = 1.15 mm, Royal Philips Electronics, Amsterdam) was used for EDX mapping. The HAADF STEM imaging, and STEM-EDX/EELS investigations were performed in a FEI Titan 80-300 Cubed (S)TEM (FEI, Hillsboro) operated at 300 kV, equipped with a high brightness X-FEG, two aberration

correctors for the probe and the image forming lenses, and a Gatan GIF (model 866) spectrometer.

**EELS.** The EELS line-scan was performed taking 128 spectra along a distance of 16.3 nm with a dispersion of 0.5 eV/channel. Exposure time was 0.4 s. Energy-windows of 353.0-366 eV for Ca  $L_{2,3}$ , 533.0-581 eV for O K and 640.0-652 eV for Mn  $L_{2,3}$  were used for the signal extraction along the measured distance.

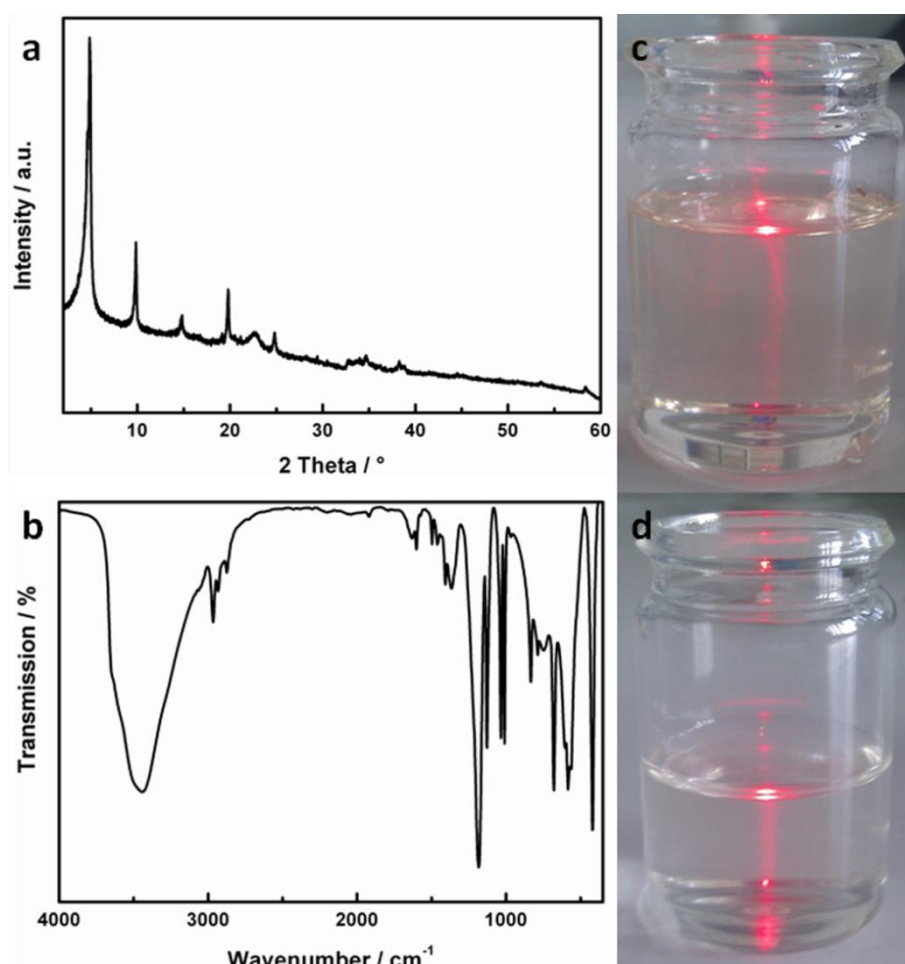


**Figure S4.1.1:** a) XRD and b) IR of MnAl *ES* LDH, c) and d) photographs of  $\text{Mn}_2\text{Al}(\text{OH})_6^+$  nanosheets suspended in formamide and water, respectively.

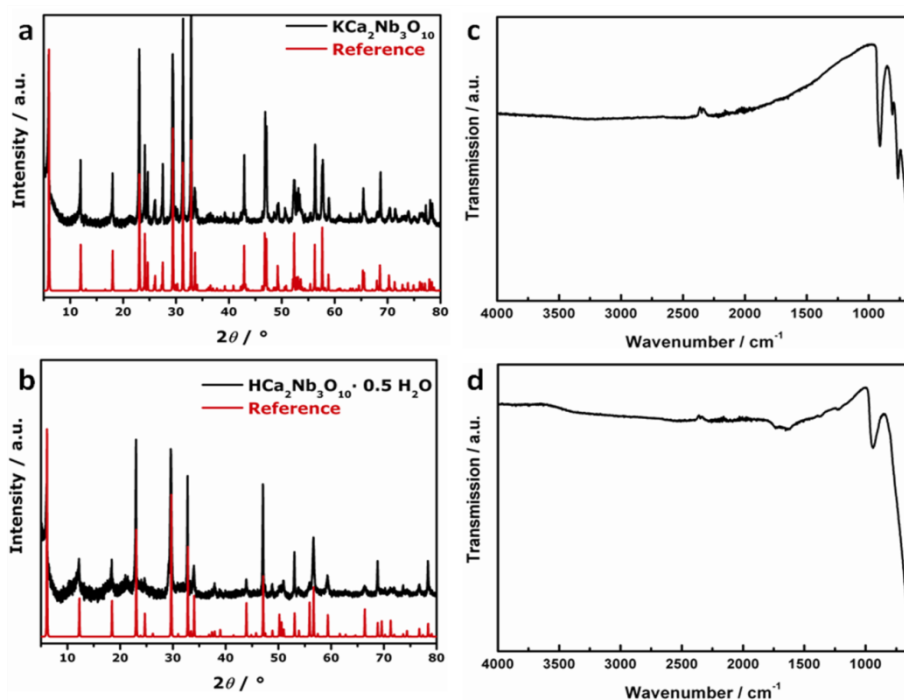


**Figure S4.1.2:** Left: XRD patterns of a)  $\text{KCa}_2\text{Nb}_3\text{O}_{10}$ , b)  $\text{HCa}_2\text{Nb}_3\text{O}_{10} \times 0.5 \text{H}_2\text{O}$  with the respective simulated patterns<sup>4,5</sup> taken from the ICSD data base; right: IR of c)  $\text{KCa}_2\text{Nb}_3\text{O}_{10}$  and d)  $\text{HCa}_2\text{Nb}_3\text{O}_{10}$ .

**Table S4.1.1:** EDX quantification data for  $\text{KCa}_2\text{Nb}_3\text{O}_{10}$ ,  $\text{HCa}_2\text{Nb}_3\text{O}_{10} \cdot 0.5 \text{H}_2\text{O}$  and  $\text{Ca}_2\text{Nb}_3\text{O}_{10}^-$

Element (atomic%)	K $K_\alpha$	Ca $K_\alpha$	Nb $L_\alpha$	O $K_\alpha$
<b>Compound</b>				
$\text{KCa}_2\text{Nb}_3\text{O}_{10}$	5.7	11.0	19.0	64.4
$\text{HCa}_2\text{Nb}_3\text{O}_{10}^*$	-	11.7	20.6	67.8
$\text{Ca}_2\text{Nb}_3\text{O}_{10}^-$	-	12.2	19.0	67.4

\*ICP-AES yielded  $\text{HCa}_{2.2}\text{Nb}_3\text{O}_{10} \times n \text{H}_2\text{O}$  without traces of K.

**Table S4.1.2:** Elemental analysis (C, H, N) of  $\text{Ca}_2\text{Nb}_3\text{O}_{10}^-$ . The values are given in weight-%

N	C	H	Formula
0.79 %	10.05 %	2.18 %	$\text{TBA}_{0.84}\text{H}_{0.16}\text{Ca}_2\text{Nb}_3\text{O}_{10}$



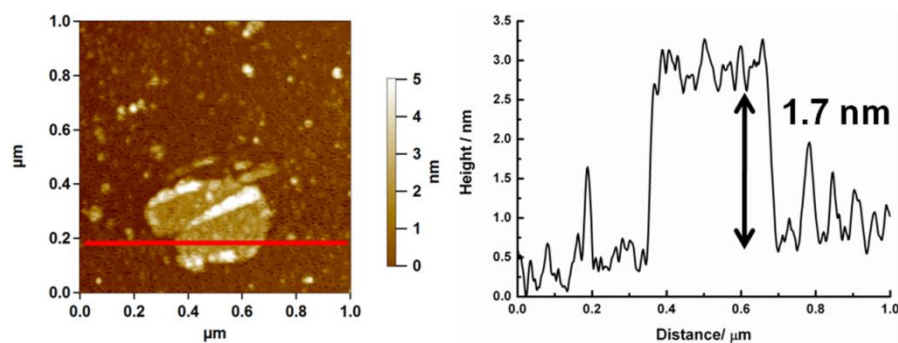


**Figure S4.1.3:** AFM image and corresponding height profile of a  $[\text{Mn}_{0.67}\text{Al}_{0.33}(\text{OH})_2]^{0.33+}[\text{ES}_{0.33}]^{0.33-}$  (ES: ethylbenzenesulfonate) nanosheet exfoliated in formamide.

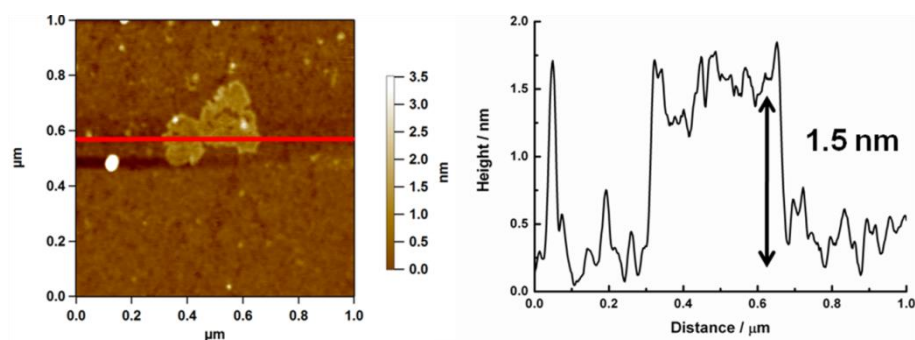


**Figure S4.1.4:** AFM image and corresponding height profile of a  $[\text{Mn}_{0.67}\text{Al}_{0.33}(\text{OH})_2]^{0.33+}[\text{ES}_{0.33}]^{0.33-}$  (ES: ethylbenzenesulfonate) nanosheet exfoliated in water.

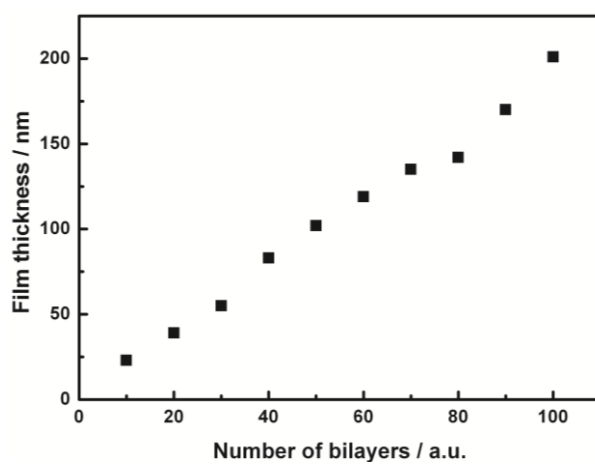


**Figure S4.1.5:** Number of bilayers vs. film thickness.

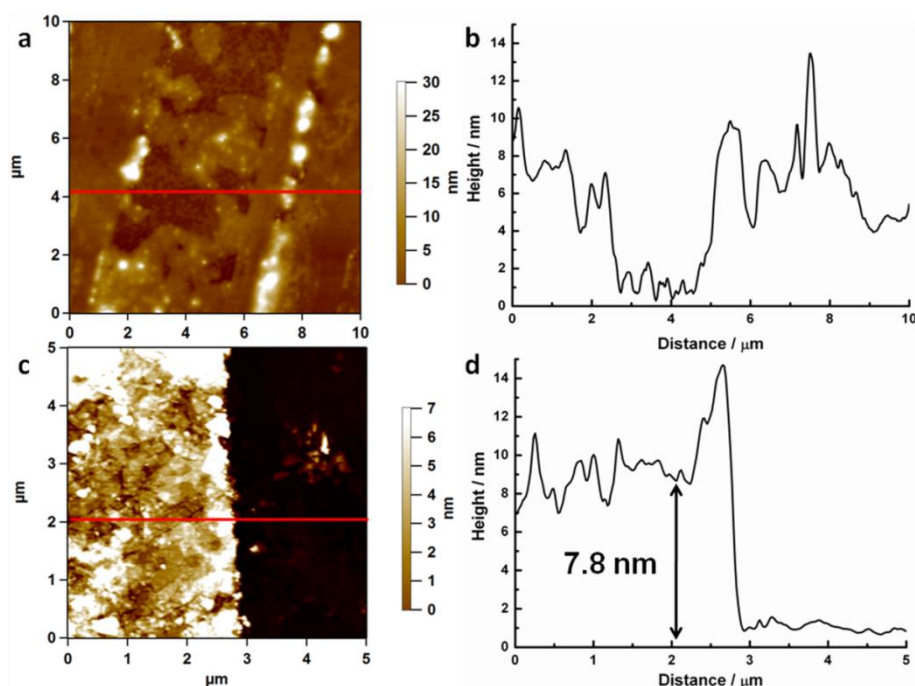


**Figure S4.1.6:** a) AFM image of 100 layers of  $\text{Ca}_2\text{Nb}_3\text{O}_{10}^-$  nanosheets and b) its corresponding height profile. c) AFM image of 60 layers of  $\text{Ca}_2\text{Nb}_3\text{O}_{10}^-$  nanosheets and  $\text{MnCl}_2/\text{AlCl}_3$  dissolved in formamide. The images show that perovskite nanosheets stacked without positively charged counterparts and perovskite nanosheets stacked with  $\text{Mn}^{2+}$  and  $\text{Al}^{3+}$  ions do not form thick multilayer films.

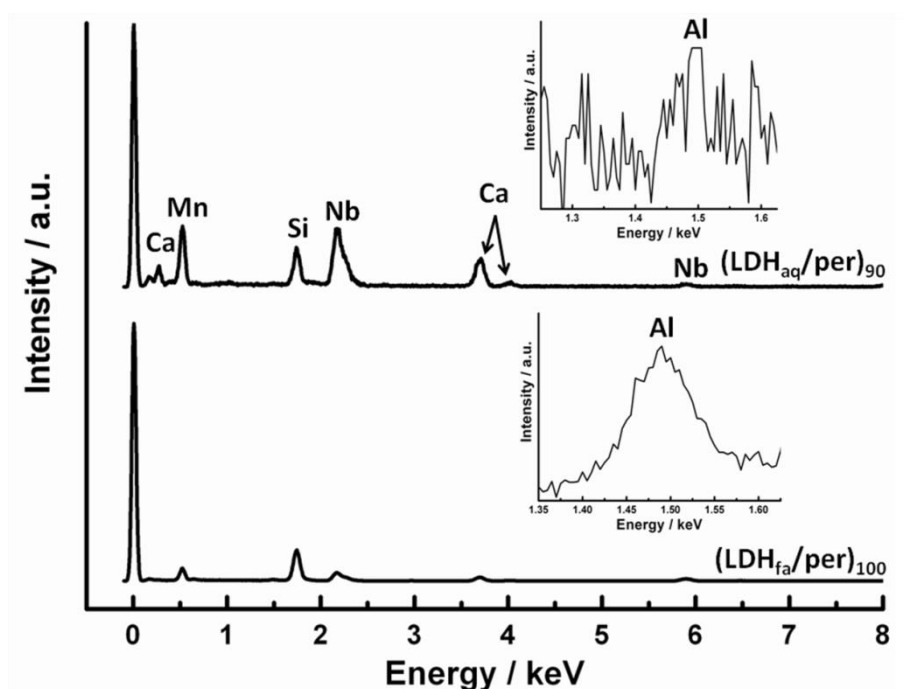


**Figure S4.1.7:** EDX spectra of  $(\text{LDH}_{\text{fa}}/\text{per})_{100}$  and  $(\text{LDH}_{\text{aq}}/\text{per})_{90}$ .

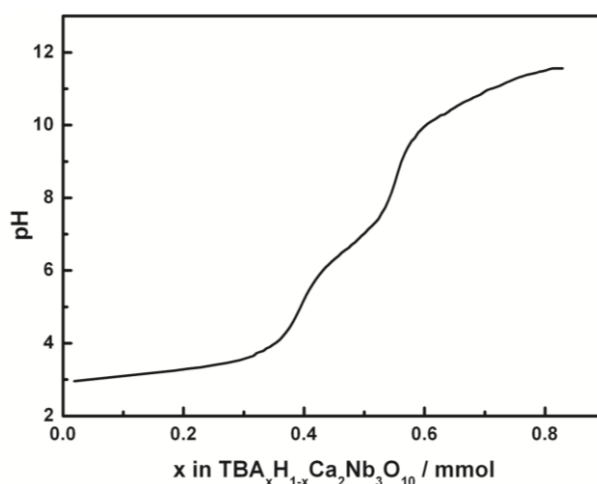


**Figure S4.1.8.** HCl titration curve of  $TBA_xH_{1-x}Ca_2Nb_3O_{10}$ .

**Table S4.1.3:** EDX quantification data for the spectra shown in Figure S4.1.7.

Stack/Element (atomic%)	Mn K $_{\alpha}$	Al K $_{\alpha}$	Ca K $_{\alpha}$	Nb L $_{\alpha}$	O K $_{\alpha}$	C K $_{\alpha}$	Si K $_{\alpha}$	Cu K $_{\alpha}$
(LDH <sub>fa</sub> /per) <sub>100</sub>	2.4	0.9	3.9	9.0	45.3	2.4	36.0	0.1
(LDH <sub>aq</sub> /per) <sub>90</sub>	0.6	0.3	6.5	13.0	45.7	25.1	8.4	0.4

**Table S4.1.4:** Comparison of Nb-Nb and Ca-Ca distances in the perovskite layer found in the bulk materials  $KCa_2Nb_3O_{10}$  and  $HCa_2Nb_3O_{10} \cdot 0.5 H_2O$ , along with the experimentally obtained values.  $KCa_2Nb_3O_{10}$ , shows a larger distribution of interatomic distances owing to its lower (monoclinic) symmetry.

	$KCa_2Nb_3O_{10}$	$HCa_2Nb_3O_{10} \cdot 0.5 H_2O$	Experimental
<b>Nb-Nb<sub>vert</sub></b>	4.2/4.3 Å	4.2 Å	$3.9 \pm 0.1$ Å
<b>Nb-Nb<sub>horiz</sub></b>	3.8/3.9 Å	3.9 Å	$3.8 \pm 0.1$ Å
<b>Ca-Ca<sub>vert</sub></b>	4.1/4.5 Å	4.3 Å	$4.5 \pm 0.1$ Å
<b>Ca-Ca<sub>horiz</sub></b>	3.5/3.7/4.0/4.3 Å	3.9 Å	$4.3 \pm 0.1$ Å

#### BIBLIOGRAPHY:

- [1] Werner, S.; Lau, V. W.-h.; Hug, S.; Duppel, V.; Clausen-Schaumann, H.; Lotsch, B. V. *Langmuir* **2013**, 29, 9199.
- [2] Dion, M.; Ganne, M.; Tournoux, M. *Mater. Res. Bull.* **1981**, 16, 1429.
- [3] Hata, H.; Kobayashi, Y.; Bojan, V.; Youngblood, W. J.; Mallouk, T. E. *Nano Lett.* **2008**, 8, 794.
- [4] Tokumitsu, T.; Toda, K.; Aoyagi, T.; Sakuraba, D.; Uematsu, K.; Sato, M. *J. Ceram. Soc. Jpn.* **2006**, 114, 795.
- [5] Chen, Y.; Zhao, X.; Ma, H.; Ma, S.; Huang, G.; Makita, Y.; Bai, X.; Yang, X. *J. Solid State Chem.* **2008**, 181, 1684.

## 4.2 Thermal Behavior of Layered Perovskite and Layered Double Hydroxide Heterostructures

Christian Ziegler, Stephan Werner, Katarina Marković, Teresa Dennenwaldt, Viola Duppel,  
Christina Scheu, Bettina V. Lotsch

*Manuscript to be submitted.*

**ABSTRACT:** The construction of vertical heterostructures out of 2D building blocks has become a promising route to rationally design complex multilayer systems with intriguing properties at mild synthesis conditions. Here, we present the thermal post-treatment of such a multilayer stack (LDH/per)<sub>n</sub> consisting of anionic calcium niobate perovskite nanosheets and cationic manganese aluminium layered double hydroxide (LDH) nanosheets. Cross-sections were prepared and high-resolution transmission electron microscopy (HRTEM) coupled with energy-dispersive X-ray spectroscopy (EDX) was used to monitor structural changes in the range of 300-1000°C under ambient conditions. The (LDH/per)<sub>n</sub> stack shows diffusion of elements up to 500°C and starts to transform to other crystalline phases at temperatures ≥ 600°C. For annealing temperatures of 1000°C crystalline particles of different compositions were obtained. We present evidence for the formation of unknown Al-Mn-Nb-O phases that have not been reported to be accessible by means of conventional synthesis routes. Besides, the formation of known Al<sub>x</sub>Mn<sub>2-x</sub>O<sub>3</sub> and MnNb<sub>2</sub>O<sub>6</sub> compounds was verified with EDX and selected area electron diffraction (SAED).

### 4.2.1 Introduction

Tremendous research efforts have been directed to the development of miniature, hierarchical functional systems through the controlled organization of two-dimensional (2D) nanosheets utilized as building blocks for these hybrid structures.<sup>1</sup> For example, a miniaturized all-nanosheet capacitor has been synthesized out of (Ru<sub>0.95</sub>O<sub>2</sub><sup>0.2-</sup>/Ca<sub>2</sub>Nb<sub>3</sub>O<sub>10</sub><sup>-</sup>/Ru<sub>0.95</sub>O<sub>2</sub><sup>0.2-</sup>) nanosheet assemblies where the ruthenium oxide sheets operate as electrodes and the calcium niobate sheets act as dielectrics.<sup>2</sup> Due to its ultrathin size, the multilayer assembly showed a nearly 10 times higher capacitance than the state-of-the-art HfO<sub>2</sub>-based capacitor and may hence find use in the fabrication of high-density dynamic random access memory devices (DRAM) in the future. Another example is the alternate stacking of (LaNb<sub>2</sub>O<sub>7</sub>/Ca<sub>2</sub>Nb<sub>3</sub>O<sub>10</sub><sup>-</sup>)<sub>n</sub> nanosheet layers, which showed ferroelectric behavior despite the fact that both types of nanosheets and stacks made out of only one type of nanosheets are paraelectric.<sup>3</sup> Combination of Zn-Cr layered double hydroxides (LDHs) with layered titanates or polyoxometalates leads to a remarkably enhanced photocatalytic activity for water

oxidation compared to the pristine Zn-Cr-LDH.<sup>4-5</sup> As the list goes on, a lot of reviews have been devoted to monitor the rapid process in this emerging field of nanoarchitectonics.<sup>1, 6-13</sup>

For the fabrication of electrostatically assembled heterostructures three major techniques, namely flocculation, Langmuir-Blodgett (LB) transfer and layer-by-layer (LBL) assembly are applied. Flocculation is the simplest method and achieved by destabilization of (a) colloidal suspension(s), yielding large amounts of precipitated nanosheets or heterostructures thereof. The LB technique uses self-assembled and compressed monolayers floating at the air-solvent interface, which are transferred onto a substrate by horizontal or vertical lifting of the substrate, producing densely packed films. Whereas flocculation lacks control over the layer structure and registry, LB is a time-consuming process which is rather difficult to scale up. The LBL approach combines both techniques and heterostructures are built up by an alternate immersion of a substrate into oppositely charged suspensions with extensive washing steps in between to remove excess material. Independent of the technique, most works focus on the synthesis and properties of ultrathin multilayers up to a maximum of 25-30 layers. In a recent study, we have demonstrated the rational synthesis of a complex (LDH/per)<sub>n</sub> heterostructure composed of up to 100 bilayers of perovskite  $TBA_{1-y}H_yCa_2Nb_3O_{10}$  and LDH  $ES[Mn_2Al(OH)_6]$  ( $TBA$  = tetra-*n*-butylammonium,  $ES$  = ethylbenzenesulfonate) nanosheets, aiming for the directed synthesis of functional bulk materials rather than ultrathin films (see Chapter 4.1).<sup>14</sup> A detailed TEM study coupled with several spectroscopic techniques has proven the formation of densely packed stacks on the one hand side, but also demonstrated non-idealities and real structure effects that need to be overcome in future approaches on the other side. Thermal annealing of such heterostructures can be one route to reduce such non-idealities as organic residues incorporated into the heterostructures can be completely decomposed, which should lead to a compression of the complete stack. Exceeding a certain temperature the different nanosheets might arrange to form smooth interfaces or for even higher temperatures exhibit the formation of metastable phases due to the arrangement of materials at the nanometer scale that cannot be achieved *via* common synthesis protocols.

In the following, we investigate the thermal behavior of these (LDH/per)<sub>n</sub> stacks upon annealing them in the temperature range between 300°C-1000°C under ambient conditions. Cross-sections of the stacks were analyzed with HRTEM coupled with EDX spectroscopy and SAED. While recent studies focus on the thermal stability of solely perovskite stacks, our analysis monitors, for the first time, the thermal transformation of a mixed perovskite / LDH heterostructure and shows the possibility to construct new “3D” compounds that may not be accessible by common solid-state methods.<sup>15</sup>

## 4.2.2 Results and Discussion

Cross-section HRTEM images of (LDH/per)<sub>n</sub> multilayers heated at temperatures of 300°C-500°C are shown in Figure 4.2.1. Different crystalline, amorphous and intermediate layers are visible for all stacks and labeled with (A)-(D) to facilitate comparison in the following.

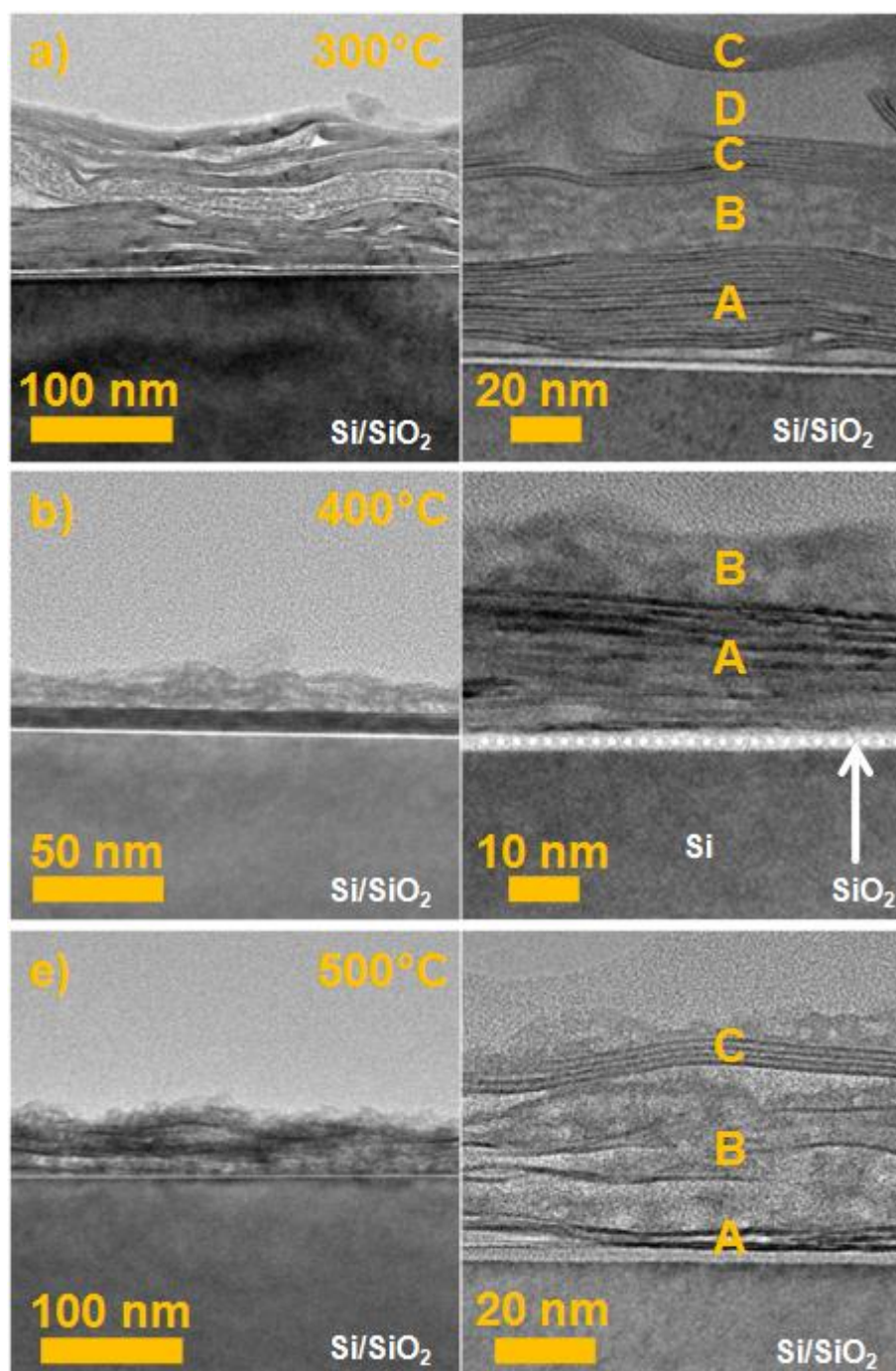


**Figure 4.2.1:** HRTEM overview images at two different magnifications of (LDH/per)<sub>n</sub> multilayer stacks annealed at a) 300°C ( $n = 40$ ), b) 400°C ( $n = 30$ ) and c) 500°C ( $n = 50$ ). (A) denotes a alternatingly stacked layer close to the substrate, (B) a LDH enriched layer, (C) a perovskite enriched layer and (D) an amorphous region. Note that the bright SiO<sub>2</sub> layer on top of the Si wafer increases successively for higher temperatures and longer heating rates as all experiments are performed under ambient conditions, i.e. in the presence of oxygen.

Assignments of regions (A)-(D) are based on EDX measurements (Table 4.2.1) and TEM investigations. Region (A) is always located close to the substrate and displayed at higher magnification in Figure S4.2.1. For the 300°C annealed sample, features similar to those without heating are present.<sup>14</sup> We conclude, that crystalline layers of perovskite nanosheets  $[\text{Ca}_2\text{Nb}_3\text{O}_{10}]^-$  are stacked in a homogeneous fashion and interleaved with amorphous LDH nanosheets  $[\text{Mn}_2\text{Al}(\text{OH})_6]^+$  of various thicknesses, because elements of both, perovskite and LDH, are present in ratios similar to those of the non-annealed sample. The LDH nanosheets are crystalline in the beginning of the experiment but rapidly disintegrate under electron beam irradiation so that only amorphous regions remain, as we have shown for the room-temperature prepared heterostructures.<sup>14</sup> The different thicknesses of the amorphous LDH layers arise from the exfoliation process as not all LDH nanosheets are exfoliated down to a single layer and sometimes double or triple layers can be deposited. This is exemplary highlighted in Figure S4.2.1. Region (A) is followed by a sponge-like region (B) that will be discussed later and region (C) which shows more densely packed layers of the perovskite that exhibit the same findings as discussed for region (A). The amorphous region (D) is most likely related to intercalated, carbon-based glue used for TEM sample preparation, which is sometimes found in the outer layers. For region (C) as well as region (A) at higher temperatures an average thickness of around 1.46 nm for the crystalline layers is observed. This is close to the crystallographic thickness of 1.44 nm for a  $[\text{Ca}_2\text{Nb}_3\text{O}_{10}]^-$  layer in the  $\text{KCa}_2\text{Nb}_3\text{O}_{10}$  bulk compound measured between the outer oxygen atoms.<sup>16</sup> We have shown with XRD and TEM that the average  $([\text{Ca}_2\text{Nb}_3\text{O}_{10}]^-/[\text{Mn}_2\text{Al}(\text{OH})_6]^+)$  bilayer is around 1.6 nm, but can be smaller or larger depending on the packing density and other effects like sheet bending, sheet terminations etc.<sup>14</sup> As heating of the heterostructure leads to decomposition of organic residues related to the ligands of both nanosheets, it is most likely that we find more densely packed regions. As mentioned for region (A), EDX measurements were performed to verify an alternating stacking of both nanosheets and the results are listed for all samples heated between 300°C-600°C in Table 4.2.1. Note that the EDX values should be interpreted qualitatively rather than quantitatively as we measured larger areas to enhance the signal to noise ratio and thus adjacent layers might contribute to the signal. For all regions (A) and (C), signals of Ca and Nb from the perovskite along with Mn and Al from the LDH are detected and point towards an alternating stacking sequence of both for all these regions as we observe a regular stacking in the TEM. For the denser regions we observe a relative decrease of Ca as well as a relative decrease of Mn along with increasing temperatures, compared to the room temperature stoichiometry. For all regions (B) the LDH signal is drastically increased compared to the perovskite signal and thus explains the sponge-like appearance where sometimes individual perovskite layers are included. We did not obtain such areas for the  $(\text{LDH/per})_n$  stack at room temperature and thus attribute this

LDH enrichment to an effect caused by the heating of the stack. At room temperature perovskite and LDH layers are deposited alternately by electrostatic layer by layer assembly driven by the strong interaction of the oppositely charged nanosheets, while excess nanosheets with the same charge show weak interaction among themselves and are removed by the washing step. Hence, at higher temperatures we find that complete nanosheets and/or ions out of nanosheets seem to migrate during the heating of the stack, such that phase separation occurs. This is different to stacks fabricated out of  $[\text{Ca}_2\text{Nb}_3\text{O}_{10}]^-$  nanosheets only, which exhibit thermal stability up to 700°C.<sup>15</sup> Note that these stacks are synthesized with the LB technique where the organic  $\text{TBA}^+$  ligand is decomposed with UV light after each step to enable deposition of the next layer, where the formed stack is most likely similar to “bulk”  $\text{HCa}_2\text{Nb}_3\text{O}_{10}$ .

**Table 4.2.1:** EDX data of  $(\text{LDH/per})_n$  multilayers heated at temperatures between 300°C-600°C at various regions found on the sample.

T / °C	Region	Ca / at%	Nb / at%	Mn / at%	Al / at%	O / at%
300	(A)	11.85	26.29	6.88	2.85	52.13
	(B)	3.76	11.04	27.81	17.78	39.61
	(C)	13.28	27.91	6.40	2.89	49.52
400	(A)	6.39	16.54	4.90	2.89	69.28
	(B)	0.42	6.49	15.12	13.03	64.94
500 (3 h)	(A)	3.13	12.10	7.57	5.93	71.27
500 (10 h)	(A)	7.54	21.72	9.23	7.46	54.05
	(B)	5.76	16.02	13.97	10.44	53.81
	(C)	8.64	21.32	5.70	2.42	61.92
	(B)	5.09	15.08	14.07	9.16	56.61
600	(A)	3.89	14.60	10.73	9.54	60.20

To visualize these observations, EDX line-scans of  $(\text{LDH/per})_n$  multilayers heated at maximum temperatures of 300°C-500°C are displayed in Figure 4.2.2. Where for 300°C annealing the LDH enriched region (B) was formed between two alternately stacked regions to give an A-B-C stacking, this layer (B) seems to migrate to the outer boundary surface with increased annealing temperatures so that we only observe an A-B stacking in the end. Note that it is also possible that the outer layer (C) was removed during ion thinning where usually the glue as “weakest” part is removed first. Weak interaction between e.g. region (B) and region (C) might also lead to a removal of the layer instead of thinning of the material. Overall, annealing between 300°C-500°C leads to a separation of a perovskite rich and a LDH rich region, whereas the LDH rich region seems to move away from the substrate.



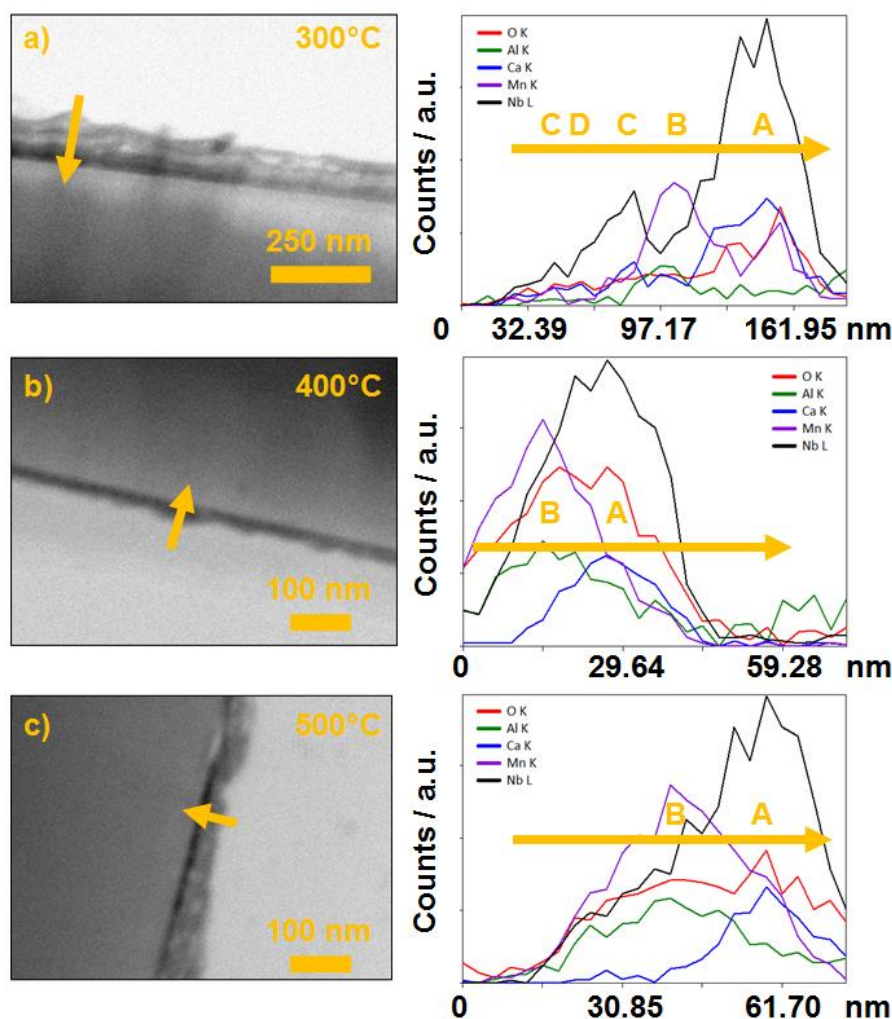


**Figure 4.2.2:** TEM images and corresponding EDX line-scans of  $(\text{LDH/per})_n$  multistacks annealed at a) 300°C ( $n = 40$ ), b) 400°C ( $n = 30$ ) and c) 500°C ( $n = 50$ ). (A) denotes an alternately stacked layer close to the substrate, (B) a LDH enriched layer, (C) a perovskite enriched layer and (D) an amorphous region.

In the next step, the effects of a change in heating rate were studied. The results for a stack annealed at 500°C for 6 h are displayed in Figure 4.2.3, where the time to reach the maximum temperature has been increased from 3 h to 10 h. The HRTEM image for this slowly heated sample clearly displays the formation of a phase-separated darker (crystalline) (A)+(C) and a sponge-like brighter region (B), alternating for three periods. The EDX line-scan shows that the darker area is perovskite-rich, whereas the brighter region is LDH dominated. Hence, instead of one LDH-rich layer, several layers are formed in which the perovskite and LDH nanosheets are clustered, respectively, which might point towards an intermediate step before all layers migrate to the outer boundary and completely separate. According to the EDX data given in Table 4.2.1, the loss of Ca is clearly reduced compared to the faster heated stack. No significant change for the LDH was observed. Thus, a slower heating rate might suppress the Ca loss and have a direct influence on the formation of new structures at higher temperatures.

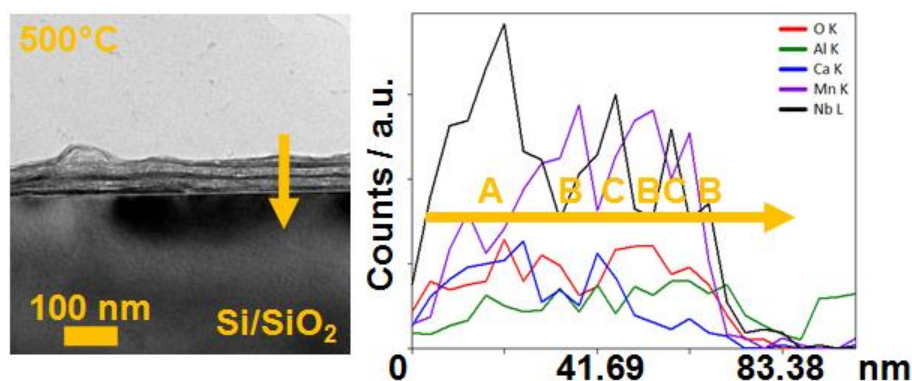


**Figure 4.2.3:** TEM image and corresponding EDX line-scans of a (LDH/per)<sub>40</sub> multilayer stack annealed at 500°C with a slower heating and cooling rate (50°C/h). (A)+(C) denote a perovskite enriched layer, (B) a LDH enriched layer.

At temperatures of 600°C no distinct lamellar nanoscale structures are visible anymore and the whole stack appears amorphous, as can be seen in Figure 4.2.4. Only a slight difference in contrast is apparent. The brighter outer region shows a relatively higher amount of LDH-related elements as compared to the darker inner region where the heavier Nb atoms of the perovskite are present. Overall, 600°C seems to be a transition point where the whole layered structure collapses and thermally rearranges, forming new structures.

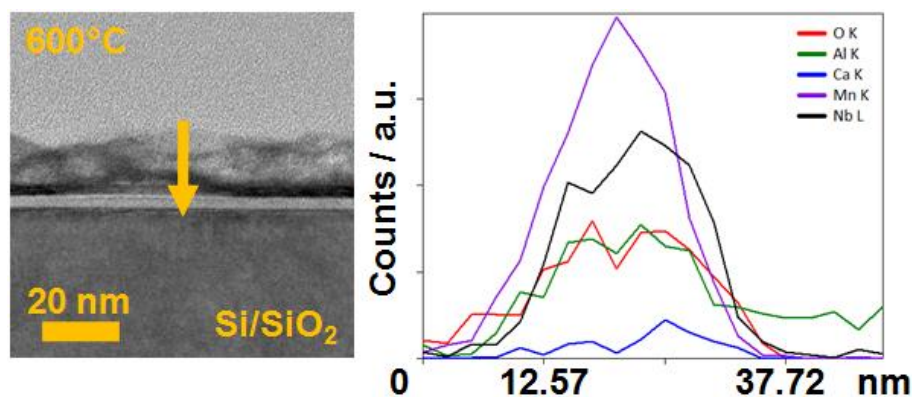


**Figure 4.2.4:** TEM image and corresponding EDX line-scans of a (LDH/per)<sub>30</sub> multilayer stack annealed at 600°C.

Figure S4.2.2 shows HRTEM images at various magnifications for the samples heated at 700°C. The increased temperature leads to the formation of some crystalline domains. Interestingly, a large Mn-oxide particle was found as shown in Figure S4.2.3. Since we can exclude that this particle was brought in as an impurity, the Al must have been diffused out into e.g. the perovskite region, leaving a crystalline Mn oxide behind. Since we did not find Ca enriched regions for this sample nor for the following ones, we hypothesize that Ca concomitantly moved towards the Si where it possibly formed a calcium silicate. As regions

get thicker towards the substrate - making TEM investigations impossible - we cannot provide evidence for this assumption at this point. Another possibility would be that Ca is removed into the gas phase.

1000°C was chosen as the maximum heating temperature. An overview TEM image is shown in Figure 4.2.5. While at temperatures of 700°C crystalline domains were still in close vicinity and overlapping, at 1000°C crystalline particles are now separately embedded into a thick SiO<sub>2</sub> matrix. The dark region below the particle on the right is due to a thickness effect and EDX showed no elements besides Si and O. EDX data of 22 particles are listed in Table S4.2.2. As apparent from these data, the local difference in chemical composition is very large and hence, we categorized the particles into different groups. The most prominent group has a higher atomic ratio of Nb to the sum of Mn+Al+(Ca); the second group possesses an elemental content of Mn>Nb>Al>(Ca), while we identified Al<sub>x</sub>Mn<sub>2-x</sub>O<sub>3</sub> as a third and MnNb<sub>2</sub>O<sub>6</sub> as a fourth group, and, finally, we list those regions whose composition was found only once. All these compounds do not have any Si present and hence do not show any reaction with the substrate at this temperature. In the following we focus on the analysis of the first, third and fourth group.

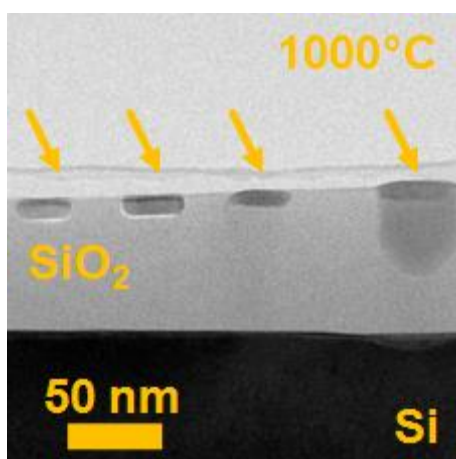


**Figure 4.2.5:** Overview TEM image of a (LDH/per)<sub>20</sub> multilayer stack annealed at 1000°C. The orange arrows point towards the embedded particles.

Al<sub>x</sub>Mn<sub>2-x</sub>O<sub>3</sub> was identified to be one motif that is formed out of the (LDH/per)<sub>n</sub> stack under the applied synthesis conditions. Figure 4.2.6 displays a HRTEM image of a crystalline particle along with the corresponding SAED pattern. The corresponding *d*-values are 9.22 Å, 4.61 Å, 4.18 Å, 3.09 Å, 2.31 Å etc. and the measured angle between two independent planes in the present orientation is 90°. The composition according to EDX is Al<sub>0.2</sub>Mn<sub>1.8</sub>O<sub>x</sub> and similar to a compound known from literature, Al<sub>0.2</sub>Mn<sub>1.8</sub>O<sub>3</sub>. Al<sub>0.2</sub>Mn<sub>1.8</sub>O<sub>3</sub> crystallizes in the cubic space group *Ia* $\bar{3}$  (no. 206) with cell parameters *a* = 0.94 nm and  $\alpha = \beta = \gamma = 90^\circ$ .<sup>17</sup> This or similar compositions were found for 4 out of 22 particles. Occasionally, a slight amount of Ca and

Nb was present. The reason for this “impurity” could either be a doping of the elements into the structure or too quick embedding into the SiO<sub>2</sub> matrix, so that elements did not have enough time to diffuse and phase-separate.

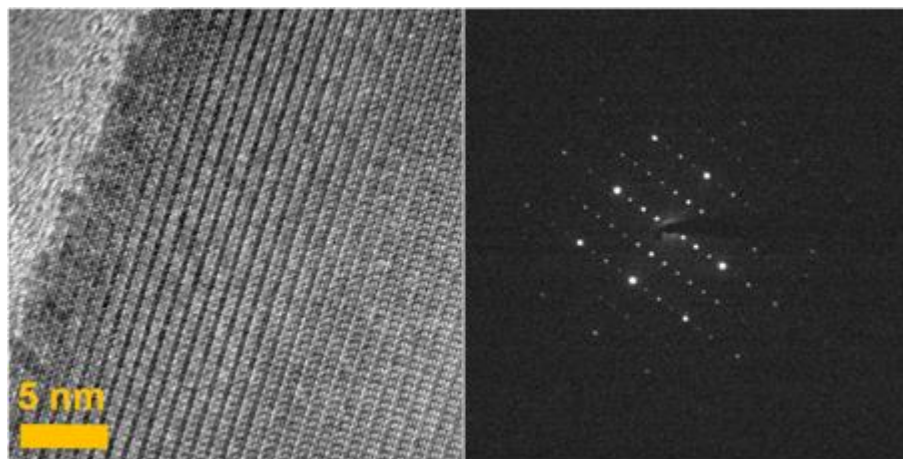


**Figure 4.2.6:** HRTEM image and corresponding SAED pattern of an  $\text{Al}_x\text{Mn}_{2-x}\text{O}_3$  particle formed from a  $(\text{LDH/per})_{100}$  multilayer stack annealed at 1000°C.

The second structural motif we found was  $\text{MnNb}_2\text{O}_6$  which we obtained 3 out of 22 times. The HRTEM image along with the SAED pattern is displayed in Figure 4.2.7.  $\text{MnNb}_2\text{O}_6$  crystallizes in the orthorhombic space group  $Pbcn$  (no. 60) with lattice parameters  $a = 1.44376(3)$  nm,  $b = 0.57665(1)$  nm,  $c = 0.50841(1)$  nm and  $\alpha = \beta = \gamma = 90^\circ$ .<sup>18</sup> The particle is oriented along the  $b$  axis and SAED reflections of 7.19 Å along one direction as well as 2.52 Å in the orthogonal direction match well with 7.22 Å for (200) and 2.54 Å for the (002) planes.

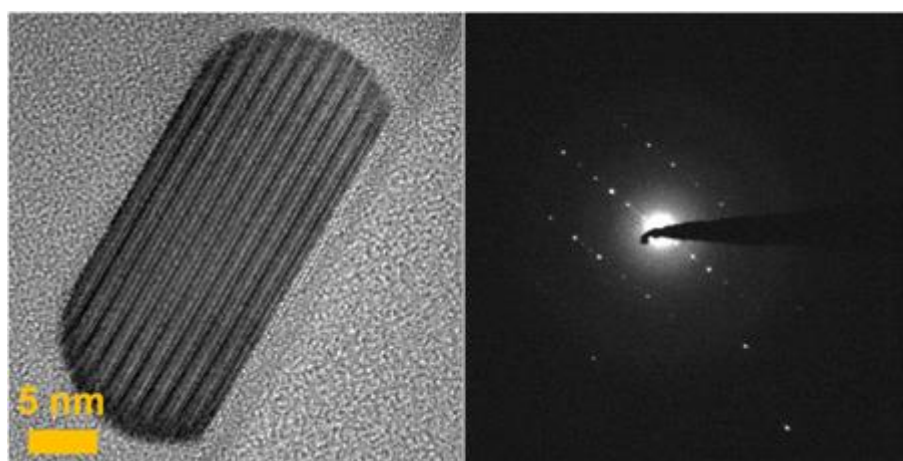


**Figure 4.2.7:** HRTEM image and corresponding SAED pattern of a  $\text{MnNb}_2\text{O}_6$  particle formed from a  $(\text{LDH/per})_{100}$  multilayer stack annealed at 1000°C.



Last, 7 out of 22 times we obtained phases where the atomic Nb content exceeds the sum of the other elements. However, the obtained ratios vary greatly and the corresponding particles also exhibit different morphologies. Figure 4.2.8 exemplarily shows the HRTEM image and corresponding SAED pattern of a particle with composition  $\text{Al}_{0.9}\text{Mn}_{1.2}\text{Nb}_3\text{O}_x$ . Table 4.2.2 lists the obtained  $d$ -values in comparison with the ones found for  $\text{KCa}_2\text{Nb}_3\text{O}_{10}$ . To our knowledge, no compounds based on the elements Al-Mn-Nb-O are known yet; thus, irrespective of their exact composition all 7 particles might belong to new compounds, assuming phase-pure materials. As mentioned for the perovskite layers found for lower temperatures close to the substrate (A), it seems that Ca diffuses out of the perovskite structure, while Al and the remaining Mn compensate the charge.

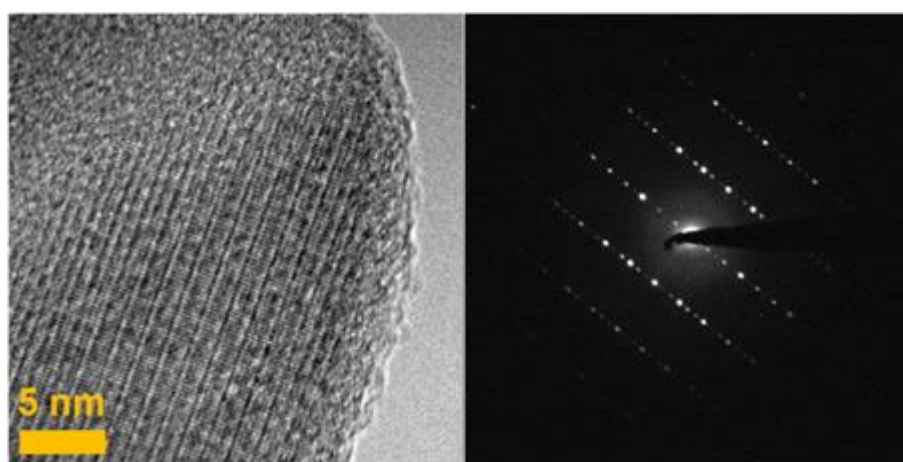


**Figure 4.2.8:** HRTEM image and corresponding SAED pattern of an Al-Mn-Nb-O particle formed from a  $(\text{LDH/per})_{20}$  multilayer stack annealed at  $1000^\circ\text{C}$ .

**Table 4.2.2:**  $d_{hkl}$ -values of the particle  $\text{Al}_{0.9}\text{Mn}_{1.16}\text{Nb}_3\text{O}_{15.56}$  in comparison to the Dion-Jacobson (DJ) phase  $\text{KCa}_2\text{Nb}_3\text{O}_{10}$ .

$d / \text{\AA}$	$d (\text{KCa}_2\text{Nb}_3\text{O}_{10})$	$(hkl)$
7.18		
3.59	3.78	(200)
	3.44	(210)
	2.74	(220)
	2.68	(024)
2.54	2.54	(300)
2.40		
2.24	2.17	(230)
1.80	1.84	(410)
	1.61	(028)
1.44	1.46	(430)

### 4.2.3 Conclusion

In conclusion, we have investigated the thermal behavior of  $([\text{Ca}_2\text{Nb}_3\text{O}_{10}]/[\text{Mn}_2\text{Al}(\text{OH})_6])^+_n$  multilayer systems in the temperature range between 300°C and 1000°C. The initial alternately stacked nanosheets begin to phase segregate at temperatures between 300 and 500°C into a crystalline perovskite dominated layer and an amorphous LDH layer. The perovskite-dominated layer shows a significant loss of Ca and Mn with increasing annealing temperatures and thus gives rise to the formation of an unknown phase with approximate composition  $\text{Al}_{0.9}\text{Mn}_{1.2}\text{Nb}_3\text{O}_x$  at 1000°C, which to our knowledge has not been synthesized by conventional solid-state routes yet. The LDH rich layer, on the contrary, migrates to the outer boundary and may act there as a crystallization nucleus for the formation of  $\text{Al}_x\text{Mn}_{2-x}\text{O}_3$  as well as  $\text{MnNb}_2\text{O}_6$  at 1000°C, which we could identify by SAED and EDX analysis. Besides this, several other compositions have been obtained that highlight the possibility to use the LBL assembly scheme with subsequent annealing for the fabrication of nanostructures with compositions that are not accessible by conventional solid-state synthesis in the thermodynamic regime. Although this might be considered a preliminary study, we like to emphasize our results as a “proof-of-principle” and are aware of the fact that in order to aim for a controlled synthesis of new materials the multilayer arrangement has first to be well-controlled and, as importantly, increased numbers of multilayers have to be obtained in order to target true bulk-scale synthesis. For thicker samples, XRD could then be used to monitor reaction products faster than by means of TEM cross-sections and reaction parameters may then be adjusted accordingly.

### 4.2.4 Bibliography

- [1] R. Ma, T. Sasaki, *Annu. Rev. Mater. Res.* **2015**, *45*, 111-127.
- [2] C. Wang, M. Osada, Y. Ebina, B.-W. Li, K. Akatsuka, K. Fukuda, W. Sugimoto, R. Ma, T. Sasaki, *ACS Nano* **2014**, *8*, 2658-2666.
- [3] B.-W. Li, M. Osada, T. C. Ozawa, Y. Ebina, K. Akatsuka, R. Ma, H. Funakubo, T. Sasaki, *ACS Nano* **2010**, *4*, 6673-6680.
- [4] J. L. Gunjekar, T. W. Kim, H. N. Kim, I. Y. Kim, S.-J. Hwang, *J. Am. Chem. Soc.* **2011**, *133*, 14998-15007.
- [5] J. L. Gunjekar, T. W. Kim, I. Y. Kim, J. M. Lee, S.-J. Hwang, *Sci. Rep.* **2013**, *3*.
- [6] R. Ma, T. Sasaki, *Adv. Mater. (Weinheim, Ger.)* **2010**, *22*, 5082-5104.
- [7] K. S. Novoselov, A. H. C. Neto, *Phys. Scr.* **2012**, *2012*, 014006.
- [8] M. Osada, T. Sasaki, *Adv. Mater. (Weinheim, Ger.)* **2012**, *24*, 210-228.
- [9] K. Ariga, Y. Yamauchi, G. Rydzek, Q. Ji, Y. Yonamine, K. C. W. Wu, J. P. Hill, *Chem. Lett.* **2014**, *43*, 36-68.

- [10] J. L. Gunjakar, I. Y. Kim, J. M. Lee, Y. K. Jo, S.-J. Hwang, *J. Phys. Chem. C* **2014**, *118*, 3847-3863.
- [11] I. Y. Kim, Y. K. Jo, J. M. Lee, L. Wang, S.-J. Hwang, *J. Phys. Chem. Lett.* **2014**, *5*, 4149-4161.
- [12] M. Osada, T. Sasaki, *Polym. J.* **2015**, *47*, 89-98.
- [13] B. V. Lotsch, *Annu. Rev. Mater. Res.* **2015**, *45*, 85-109.
- [14] C. Ziegler, S. Werner, M. Bugnet, M. Wörsching, V. Duppel, G. A. Botton, C. Scheu, B. V. Lotsch, *Chem. Mater.* **2013**, *25*, 4892-4900.
- [15] B.-W. Li, M. Osada, Y. Ebina, K. Akatsuka, K. Fukuda, T. Sasaki, *ACS Nano* **2014**, *8*, 5449-5461.
- [16] L. Li, R. Ma, Y. Ebina, K. Fukuda, K. Takada, T. Sasaki, *J. Am. Chem. Soc.* **2007**, *129*, 8000-8007.
- [17] E. Banks, E. Kostiner, *J. Appl. Phys.* **1966**, *37*, 1423-1424.
- [18] S. C. Tarantino, M. Zema, F. Maglia, M. C. Domeneghetti, M. A. Carpenter, *Phys. Chem. Miner.* **2005**, *32*, 568-577.

## 4.2.5 Supporting Information

### EXPERIMENTAL PROCEDURES:

**Chemicals.** All chemicals and solvents were purchased from commercial suppliers and used without further purification: Potassium carbonate ( $K_2CO_3$ , Merck KGaA, >99%), calcium carbonate ( $CaCO_3$ , Grüssing, 99%), niobium(V) oxide ( $Nb_2O_5$ , Alfa Aesar, 99.5%), sodium hydroxide (NaOH, AppliChem, 97%), tetra-*n*-butylammonium hydroxide (*TBAOH*,  $[CH_3(CH_2)_3]_4NOH \cdot 30 H_2O$ , Sigma-Aldrich, 98%), manganese nitrate ( $Mn(NO_3)_2 \cdot 4H_2O$ , Sigma-Aldrich, 97%), 4-ethylbenzenesulfonic acid (Sigma-Aldrich, 95%) aluminum nitrate ( $Al(NO_3)_3 \cdot 9H_2O$ , Fluka, 99%), and formamide (Fluka, 98%).

**Nanosheets.**  $TBA_{1-y}H_yCa_2Nb_3O_{10}$  nanosheets were synthesized in a 3-step procedure. First, the bulk material was synthesized by mixing stoichiometric amounts of  $K_2CO_3$ ,  $CaCO_3$  and  $Nb_2O_5$ , and subsequent heating of the material at 1200°C for 60 h. 20% excess of  $K_2CO_3$  was added to compensate for volatilization losses. Second, 1 g of  $KCa_2Nb_3O_{10}$  was stirred in 40 mL 5M  $HNO_3$  for 5 days to exchange the cation for a proton to yield  $HCa_2Nb_3O_{10}$ . To ensure complete cation-exchange, the acid was renewed on a daily basis. Last, for exfoliation 0.2 g of  $HCa_2Nb_3O_{10}$  were mixed with *TBAOH* at a molar ratio of 1:1 and 50 mL water was added. The suspension was shaken for 2-4 weeks and non-exfoliated particles were removed by centrifugation at 3000 rpm for 30 min. The supernatant with a concentration of 2mg/mL was used for the LBL assembly.

$ES[Mn_2Al(OH)_6]$  nanosheets were synthesized in a 2-step procedure. The LDH bulk compound was synthesized by a typical co-precipitation method where  $Mn(NO_3)_2 \cdot 4H_2O$  (3.33 mmol, 835 mg) and  $Al(NO_3)_3 \cdot 9H_2O$  (1.67 mmol, 626 mg) were dissolved in 100 mL water and an aqueous solution of 4-ethylbenzenesulfonic acid (1 mM, 100 mL) was added to the solution. The pH was then adjusted to 9.0 with 1 M NaOH under an Argon atmosphere and the brown precipitate recovered by filtration. After a washing step with water and acetone, the filtrate was dried under vacuum for 24 h. Exfoliation of  $ES[Mn_2Al(OH)_6]$  was performed by dispersing 25 mg of the bulk material in 50 mL formamide and subsequent sonication for 30 min. The resulting colloidal suspension was centrifuged at 3000 rpm for 30 min to remove possible non-exfoliated particles and used for LBL assembly.

**LBL.**  $(LDH/per)_n$  ( $n = 20-100$ ) multilayer films were fabricated with a StratoSequence 6 LBL robot (nanoStrata Inc., Tallahassee) on a Si (100) substrate. Wafers were cleaned with ethanol and dried under nitrogen prior to use and then placed into the sample holder. First, the Si wafer was immersed into the colloidal  $ES[Mn_2Al(OH)_6]$  nanosheet suspension for 10 min and excess material removed by 1 min rinsing and spinning of the wafer in  $H_2O$ . The same procedure was then applied for the  $TBA_{1-y}H_yCa_2Nb_3O_{10}$  deposition. After each layer the



substrate was dried under nitrogen flow for 1 min. The procedure was repeated  $n$ -times to obtain  $(\text{LDH/per})_n$  multilayer films.

**Calcination.**  $(\text{LDH/per})_n$  ( $n = 20$ -100) multilayer stacks were heated applying two different programs in a muffle furnace under ambient conditions. For 300-700°C the samples were heated up for 3 h, the maximum temperature kept for 6 h and the stack cooled down within 3 h. Additionally, the 500°C and the 1000°C samples were heated up for 10 h, the maximum temperature kept for 6 h and the stack cooled down within 10 h. The detailed temperature programs are listed in Table S4.2.1.

**Cross-section.** In order to characterize the multilayer assemblies by TEM, cross-section samples were prepared. Two halves of a Si wafers were glued together using a two-component adhesive creating a sandwich structure with the lamellar multilayer film in the middle. Subsequently, the sandwich was inserted into a Cu-tube and cut into thin discs. After a grinding and dimpling step and subsequent polishing with two different diamond pastes, the sample was ion-thinned until a small hole was visible.

#### CHARACTERIZATION:

**TEM.** A Philips CM30 ST microscope (300 kV,  $\text{LaB}_6$  cathode,  $\text{CS} = 1.15$  mm, Royal Philips Electronics, Amsterdam) was used for TEM investigations and EDX analysis of  $(\text{LDH/per})_n$  cross-section samples.

**Table S4.2.1:** Temperature programs and number of bilayers used for the heating study.

Temperature program	Bilayers / $n$
RT – 3 h – 300°C – 6 h – 300°C – 3 h – RT	40
RT – 3 h – 400°C – 6 h – 400°C – 3 h – RT	30
RT – 3 h – 500°C – 6 h – 500°C – 3 h – RT	50
RT – 10 h – 500°C – 6 h – 500°C – 10 h – RT	40
RT – 3 h – 600°C – 6 h – 600°C – 3 h – RT	30
RT – 3 h – 700°C – 6 h – 700°C – 3 h – RT	50
RT – 10 h – 1000°C – 6 h – 1000°C – 10 h – RT	20
RT – 10 h – 1000°C – 6 h – 1000°C – 10 h – RT	100

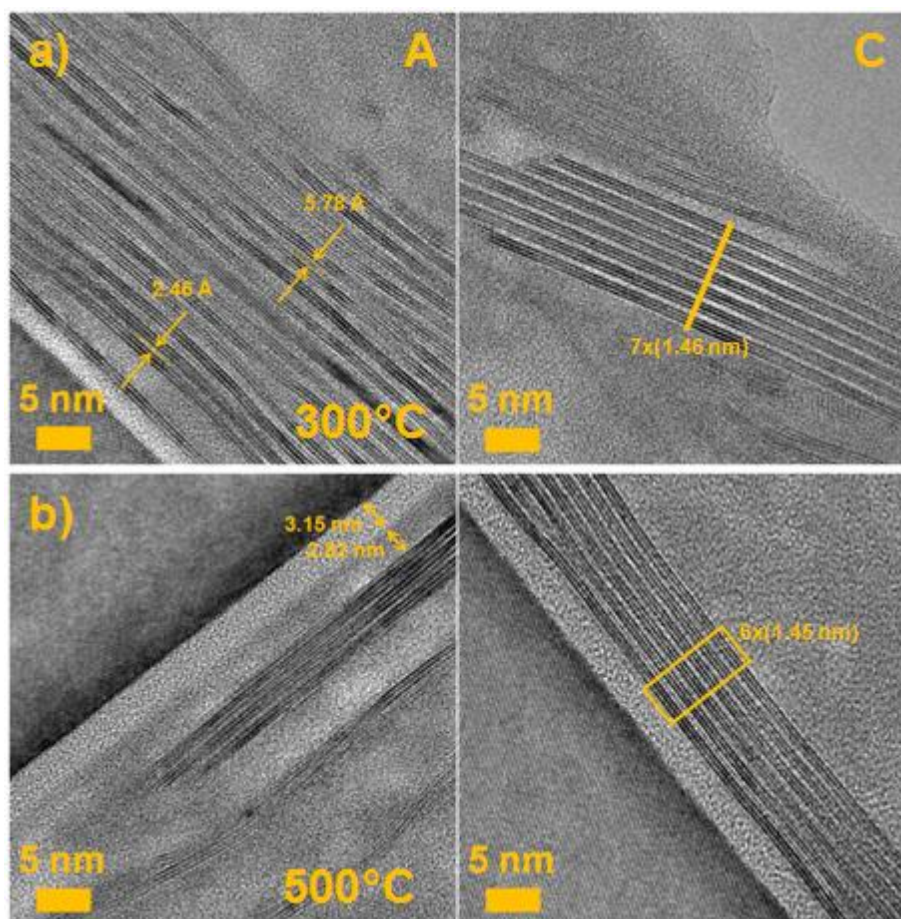


**Figure S4.2.1:** HRTEM images of (LDH/per)<sub>n</sub> multilayer stacks annealed at a) 300°C ( $n = 40$ ), and b) 500°C ( $n = 50$ ). (A) denotes a homogeneous, alternately stacked layer close to the substrate, (C) a perovskite enriched layer.

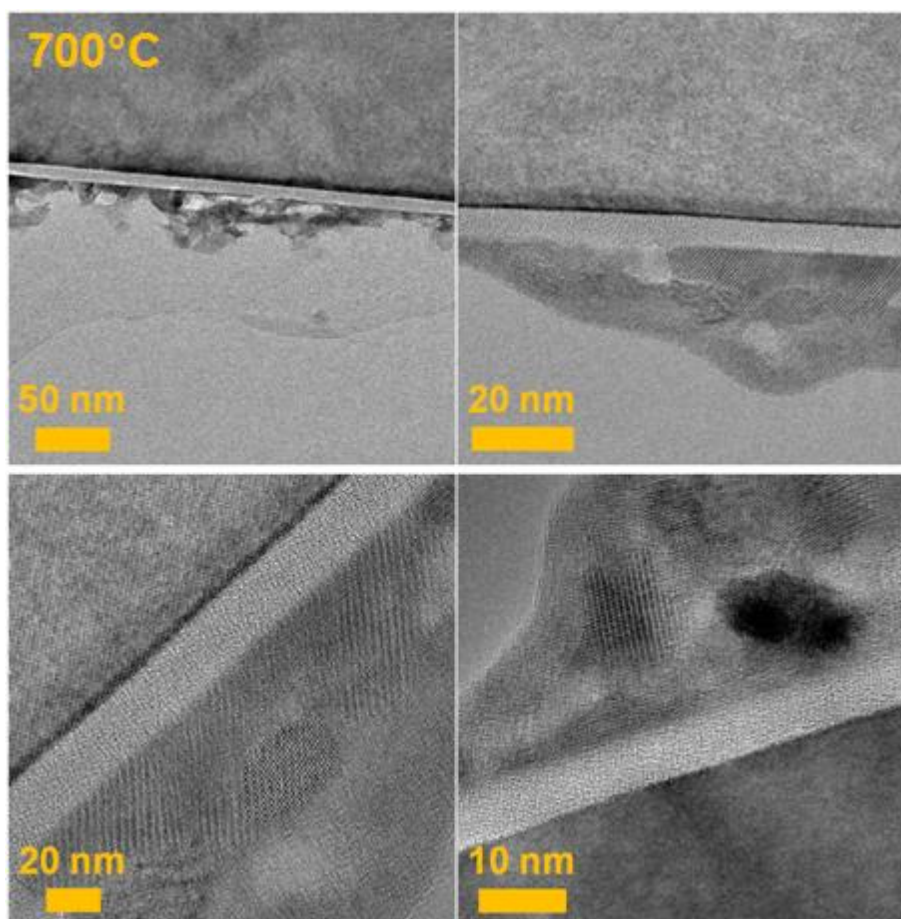


**Figure S4.2.2:** HRTEM images of a (LDH/per)<sub>50</sub> multilayer stack annealed at 700°C, showing different regions at various magnifications.

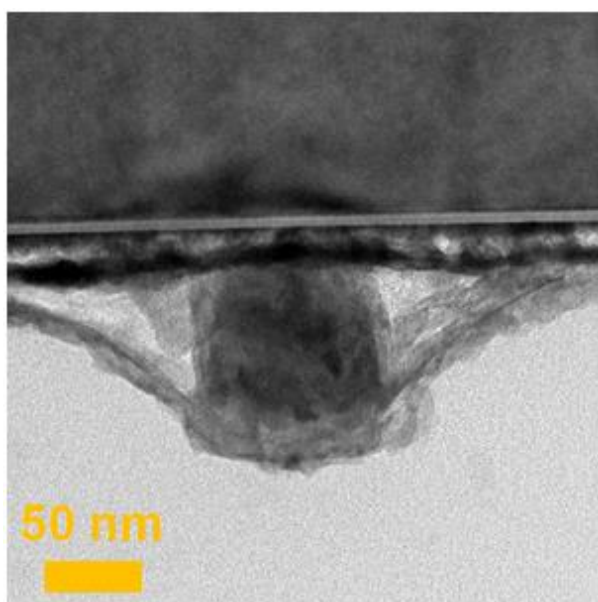


**Figure S4.2.3:** HRTEM image of a Mn-oxide particle formed out of a (LDH/per)<sub>50</sub> multilayer stack annealed at 700°C.

**Table S4.2.2:** EDX data for 22 crystalline particles obtained after heating (LDH/per)<sub>n</sub> multilayers at temperatures of 1000°C, sorted according their composition.

No°	Ca / at%	Nb / at%	Mn / at%	Al / at%	O / at%
Nb > Mn+Al+(Ca)					
1	0.19	11.20	5.32	1.32	81.96
2	0.17	12.44	6.45	2.85	78.10
3	-	8.12	3.72	1.72	86.44
4	0.09	26.11	9.58	1.29	62.94
5	0.23	13.75	5.52	0.85	79.65
6	0.19	15.74	5.29	1.88	76.89
7	2.91	19.92	7.57	6.32	63.28
Mn > Nb > Al > (Ca)					
8	-	6.99	10.84	1.62	80.54
9	1.11	5.33	25.31	5.96	62.30
10	1.32	8.17	17.16	6.66	66.69
11	0.41	7.07	26.86	4.00	61.67
12	0.41	15.63	18.99	1.70	63.27
Al <sub>x</sub> Mn <sub>2-x</sub> O <sub>3</sub>					
13	0.26	0.19	17.29	3.21	79.06
14	0.10	0.09	17.12	6.69	76.00
15	-	-	28.46	4.39	67.16
16	-	1.04	27.60	3.83	67.52
MnNb <sub>2</sub> O <sub>6</sub>					
17	0.79	16.30	9.16		73.76
18	0.89	15.56	5.31		78.25
19	1.37	21.91	6.86		69.86
Various					
20	0.26	10.59	9.01	13.15	66.99
21	1.80	1.49	0.86	5.16	90.69
22	-	17.32	17.25	1.96	63.46

### 4.3 Nanoarchitectonics of Calcium Niobate Nanosheets

Christian Ziegler, Annekathrin Ranft, Maximilian Lamoth, Katarina Marković, Stephanie Linke, Matthias Wörsching, Christina Scheu, Bettina V. Lotsch

*Unpublished results.*

**ABSTRACT:** Two-dimensional (2D) transition metal oxide (TMO) nanosheets have remarkable potential as building blocks for hierarchically structured assemblies. We present the construction of several nanoarchitectures based on  $A_{1-y}H_yCa_2Nb_3O_{10}$  ( $A^+ = TBA^+$ ,  $TBP^+$ ;  $TBA^+$  = tetra-*n*-butylammonium,  $TBP^+$  = tetra-*n*-butylphosphonium) perovskite nanosheets and evaluate specific nanosheet properties that enable these architectures. For the first time we investigate an artificial layer-by-layer (LBL) heterostructure of  $TBA_{1-y}H_yCa_2Nb_3O_{10}$  and poly(diallyldimethyl ammonium chloride) (PDDA) with up to 80 bilayers by transmission electron microscopy (TEM) and propose improvements for bottom-up synthesized bulk materials. The influence of the ligand is discussed for a similar approach where  $TBP_{1-y}H_yCa_2Nb_3O_{10}$  nanosheets were combined with layered double hydroxide (LDH)  $[Mn_2Al(OH)_6]^+$  nanosheets. Transferable multilayers of  $TBA_{1-y}H_yCa_2Nb_3O_{10}$  were achieved by evaporation induced self-assembly (EISA) of the nanosheets on a Si substrate and mixing with polystyrene (PS) spheres lead to a macroporous morphology after calcination of the as-deposited material. Finally, a multilayer material was fabricated by an alternate stacking of spin-coated nanosheets and melted PS spheres that were deposited on the nanosheet layer by a “self-assembly on water surface” (SAWS) approach. All morphologies were investigated by atomic force microscopy (AFM), scanning electron microscopy (SEM) or TEM and highlight possibilities and drawbacks in the fabrication of functional materials based on 2D TMO nanosheets in the context of nanoarchitectonics.

#### 4.3.1 Introduction

Complex next-generation nanomaterials with precisely controlled architectures and interfaces demand new synthetic innovations in order to aim for a targeted functionality in such hybrid materials.<sup>1</sup> Among all types of 2D inorganic nanosheets, TMO nanosheets offer a large variety of layered precursors with intriguing functional properties that can be exfoliated into unilamellar layers under mild solution-based processes at room temperature.<sup>2-6</sup> Such nanosheets show potential to be used as insulators, semiconductors and even conductors depending on their stoichiometry, and can be imagined as part of future high-performance devices for energy conversion, nanoelectronic or optoelectronic applications.<sup>7</sup> TMO nanosheets possess an extremely high 2D anisotropy with a thickness down to 1 nm, lateral

sizes of  $\sim 1\ \mu\text{m}$  and offer a well-defined composition and structure as 2D single crystal. These features make them perfect candidates for the fabrication of specific hierarchical nanoarchitectures.

$TBA_{1-y}H_yCa_2Nb_3O_{10}$  nanosheets are a prominent member of this material class and have for example proven capable of photocatalytic water splitting, to be used as electron transport material for solution-processed multi-junction polymer solar cells or as part of ultrathin capacitors.<sup>8-10</sup>  $TBA_{1-y}H_yCa_2Nb_3O_{10}$  nanosheets are derived from a Dion-Jacobson-type layered perovskite  $KCa_2Nb_3O_{10}$ , where negatively charged  $[Ca_2Nb_3O_{10}]^-$  perovskite layers consisting of corner-sharing  $NbO_6$  octahedra and  $Ca^{2+}$  in the A-site position of the perovskite are interleaved with exchangeable  $K^+$  ions.<sup>11-12</sup> In a two-step soft-chemical reaction monovalent  $K^+$  can be exchanged against  $H^+$  and then against  $TBA^+$  or other bulky organic cations to yield colloidal suspensions of unilamellar nanosheets. Starting from this point several approaches are known to form nanosheet architectures with different morphologies. Note that an overview scheme for all applied synthesis routes is given in Figure 1.6 in Chapter 1. For  $TBA_{1-y}H_yCa_2Nb_3O_{10}$  main fabrication routes focused on layer-by-layer (LBL) assembly *via* electrostatic sequential deposition (ESD) or Langmuir-Blodgett (LB) procedures. In the first approach, negatively charged  $[Ca_2Nb_3O_{10}]^-$  nanosheets are stacked with positively charged materials like poly(allylamine hydrochloride) (PAH) or poly(diallyldimethyl ammonium chloride) (PDDA),<sup>13-14</sup> layered double hydroxides,<sup>15-16</sup> or organic dyes.<sup>17</sup> This procedure can also be used to synthesize core-shell structures.<sup>18</sup> In the latter, amphiphilic ammonium cations are used to form a floating nanosheet monolayer that can be transformed by vertical or horizontal dipping and lifting.<sup>19-25</sup> For both, the number of multilayers is still limited and additional experiments are necessary to evaluate the critical step from ultrathin layers back to 3D bulk materials. Tuning of the layer thickness, modification of the morphology, as well as transfer of the achieved nanostructures are other factors that need to be investigated for each individual nanosheet itself. Here we present several approaches that show the flexibility and at the same time limitations for nanoarchitectures based on  $[Ca_2Nb_3O_{10}]^-$  nanosheet building blocks.

### 4.3.2 Experimental Section

#### EXPERIMENTAL PROCEDURES:

**Chemicals.** Water was purified by a Milli-Q purification system (Milli-Q Academic A10) and millipore water (M-H<sub>2</sub>O) was used throughout all procedures. All chemicals and solvents were purchased from commercial suppliers and used without further purification: Potassium carbonate ( $K_2CO_3$ , Merck KGaA, >99%), calcium carbonate ( $CaCO_3$ , Grüssing, 99%), niobium(V) oxide ( $Nb_2O_5$ , Alfa Aesar, 99.5%), tetra-*n*-butylammonium hydroxide ( $TBAOH$ ,

[CH<sub>3</sub>(CH<sub>2</sub>)<sub>3</sub>]<sub>4</sub>NOH•30 H<sub>2</sub>O, Sigma-Aldrich, 98%), tetra-*n*-butylphosphonium hydroxide (*TBPOH*, Sigma-Aldrich, 40 wt%), 4-ethylbenzenesulfonic acid (*ES*, Sigma-Aldrich, 95%), manganese nitrate (Mn(NO<sub>3</sub>)<sub>2</sub>•4H<sub>2</sub>O, Sigma-Aldrich, 97%), aluminum nitrate (Al(NO<sub>3</sub>)<sub>3</sub>•9H<sub>2</sub>O, Fluka, 99%), sodium hydroxide (NaOH, AppliChem, 97%), formamide (Fluka, 98%), (3-Aminopropyl)triethoxysilane (APTES, C<sub>9</sub>H<sub>23</sub>NO<sub>3</sub>Si, Alfa Aesar, 98%), polyethyleneimine (PEI, (C<sub>2</sub>H<sub>5</sub>N)<sub>*n*</sub>, 50 wt% in H<sub>2</sub>O, Sigma-Aldrich), poly(diallyldimethylammonium chloride) (PDDA, (C<sub>8</sub>H<sub>16</sub>NCl)<sub>*n*</sub>, 20 wt% in H<sub>2</sub>O, Sigma-Aldrich), sodium dodecyl sulfate (SDS, NaC<sub>12</sub>H<sub>25</sub>SO<sub>4</sub>, Acros, 99%) and polystyrene spheres (PS, (C<sub>8</sub>H<sub>8</sub>)<sub>*n*</sub>, 5% dispersion in M-H<sub>2</sub>O, diameter *d* = 0.172 μm, 0.617 μm, Microparticles GmbH).

**A<sub>1-y</sub>H<sub>y</sub>Ca<sub>2</sub>Nb<sub>3</sub>O<sub>10</sub> (A<sup>+</sup> = *TBA*<sup>+</sup>, *TBP*<sup>+</sup>).** KCa<sub>2</sub>Nb<sub>3</sub>O<sub>10</sub> was synthesized according to procedures known from literature.<sup>16, 26</sup> Stoichiometric amounts of K<sub>2</sub>CO<sub>3</sub>, CaCO<sub>3</sub> and Nb<sub>2</sub>O<sub>5</sub> were mixed and thoroughly grinded. 20% excess of K<sub>2</sub>CO<sub>3</sub> was added to compensate for volatilization losses. The mixture was fired up to a temperature of 1200°C for 60 h. 1 g of the bulk material was stirred in 40 mL 5M HNO<sub>3</sub> for 5 days to completely exchange the cation for a proton with daily renewal of the acid. For exfoliation 0.2 g of HCa<sub>2</sub>Nb<sub>3</sub>O<sub>10</sub> were dispersed with *TBAOH* or *TBPOH*, respectively, at a molar ratio of 1:1 in 50 mL aqueous solution. The suspension was shaken for 2-4 weeks and non-exfoliated particles were removed by centrifugation at 3000 rpm for 30 min. The supernatant with a nanosheet concentration of ~2 mg/mL was used for further synthesis and investigations. Stability of nanosheets was tested by ultrasonication and heating of the material. *TBA* ratios, concentration influence, dipping time and modifications of the Si wafer as pretreatment with 5% HNO<sub>3</sub>, H<sub>2</sub>SO<sub>5</sub> or pre-functionalization with PEI, PDDA and APTES were tested to optimize surface coverage.

**ES[Mn<sub>2</sub>Al(OH)<sub>6</sub>].** The layered double hydroxide (LDH) bulk compound was synthesized by a typical coprecipitation method.<sup>27</sup> Mn(NO<sub>3</sub>)<sub>2</sub>•4H<sub>2</sub>O (3.33 mmol, 835 mg) and Al(NO<sub>3</sub>)<sub>3</sub>•9H<sub>2</sub>O (1.67 mmol, 626 mg) were dissolved in 100 mL water and an aqueous solution of 4-ethylbenzenesulfonic acid (1 mM, 100 mL) was added to the metal nitrate solution. 1 M NaOH was added dropwise to the solution under an Argon atmosphere to adjust the pH to 9.0. The brown precipitate was recovered by filtration, washed with water and acetone and dried under vacuum for 24 h. Exfoliation of ES[Mn<sub>2</sub>Al(OH)<sub>6</sub>] in formamide was performed by dispersing 25 mg of the bulk material in 50 mL formamide and subsequent sonication for 30 min. The resulting colloidal suspensions were centrifuged at 3000 rpm for 30 min to remove possible non-exfoliated particles.

**Layer-by-Layer assembly (LBL).** Si wafers were dipped in 5% HNO<sub>3</sub> and sonicated for 30 min at 30°C. Afterwards, they were thoroughly rinsed with distilled H<sub>2</sub>O and dried at 60°C. The wafers were stored in EtOH and dried with N<sub>2</sub> before usage. Wafer functionalization with APTES was performed by dipping the wafer into a 1 mM solution of APTES in EtOH for 30 min at room temperature. Afterwards, the wafers were thoroughly rinsed with H<sub>2</sub>O and

EtOH for 30 min and dried with N<sub>2</sub>. The LBL assembly was then performed on a StratoSequence 6 LBL robot (nanoStrata Inc., Tallahassee). For the best quality stack the wafer was placed into the holder and first dipped for 20 min into a  $TBA_{1-y}H_yCa_2Nb_3O_{10}$  perovskite nanosheet suspension where the pH was adjusted to 11 with 1M NaOH, then rinsed and spinned in water for 5 min, immersed in a diluted 5 wt% PDDA solution, rinsed and spinned in water for 5 min again. This procedure was repeated 80 times in order to obtain multilayer films (Per/PDDA)<sub>80</sub>. The washed film was dried under N<sub>2</sub> gas flow for 1 min after each layer. For the (LDH/per)<sub>50</sub> stack,  $ES[Mn_2Al(OH)_6]$  and  $TBP_{1-y}H_yCa_2Nb_3O_{10}$  were used and the dipping time for the perovskite and LDH suspensions reduced to 10 min.

**Cross-section preparation.** For transmission electron microscopy (TEM) characterizations a sandwich structure was prepared by gluing two Si wafers together on the side of the multilayers and subsequently cutting the sandwich structure into discs. The discs were grinded, dimpled and ion-thinned. A part of the TEM lamellae was prepared by focused ion beam (FIB) using the lift-out technique.

**Evaporation induced self-assembly (EISA) and macroporous solids.** EISA was performed based on studies of Kuroda *et al.*<sup>28</sup> To achieve thick  $TBA_{1-y}H_yCa_2Nb_3O_{10}$  films, the colloidal nanosheet suspension was filled into a glass vial and a Si (100) wafer of 1 cm x 1.5 cm was vertically dipped into the suspension. The suspension was slowly evaporated at temperatures of 30°C, 60°C or 80°C in a muffle furnace. For the fabrication of macroporous solids the nanosheet suspension was mixed with PS bead suspensions with various diameters at various ratios of 1:4, 1:10, 1:15, 1:20, 1:25 and 1:30. The deposited material was then calcined at various temperatures between 300°C-700°C to remove the PS beads.

**Spin-coating and self-assembly on water surface (SAWS).** Multilayers of  $TBA_{1-y}H_yCa_2Nb_3O_{10}$  and melted PS layers were formed by a combination of spin-coating and SAWS. SAWS is based on protocols of Giersig *et al.* with modifications made by Qi *et al.*<sup>29-30</sup> First, a colloidal nanosheet suspension was spin-coated onto a Si substrate with a speed of 2 k rpm/s and an acceleration speed of 1 k rpm/s. Therefore, one drop of about 0.05 mL was added and spinning was kept on for 2.5 min. The wafer was then calcined for 1 h on a hot-plate at 250°C. For the next layer a plasma cleaned glass of 1 cm<sup>2</sup> was placed in the middle of a glass culture dish with a diameter ~9 cm, which was filled with M-H<sub>2</sub>O in such a way that the substrate was just not covered with water. Afterwards, 20 µL of an equal mixture of EtOH and PS beads ( $d = 0.172 \mu m$ ) was gently dropped on the glass, so that the film spread out on the water surface. To condense the beads in one half of the dish, one drop of SDS solution was added very gently down from the surface of the edge of the dish, so that only a fraction of the SDS got in contact with the water before the rest and further drops were added. To cover the nanosheet substrate surface, the Si wafer was immersed under the water surface



and the monolayers “fished” from the bottom up very slowly. The wafer was dried for 1 h at 120°C and the procedure repeated without a calcination step.

#### CHARACTERIZATION:

SEM coupled with energy-dispersive X-ray (EDX) analysis, ellipsometry, AFM and TEM were used to characterize the obtained nanosheets and the derived structures out of them.

**SEM-EDX.** SEM was conducted on a JSM-6500F electron microscope (JEOL Ltd., Tokyo). The microscope was equipped with a 7418 EDX detector (Oxford Instruments, Abingdon).

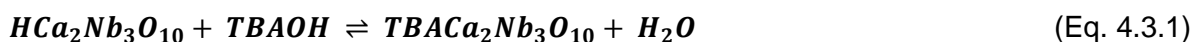
**Ellipsometry.** Ellipsometry was carried out on a M2000D (J.A. Woollam Co, Lincoln) with detection angles of 65°/70°/75°, a spectral range of 190-1000 nm and a fitting range of 350-1000 nm.

**AFM.** AFM measurements were performed on a MFP-3D Stand alone AFM (Asylum Research, Santa Barbara). Tapping-mode was applied using OMCL-AC160TS-R3 (Olympus, Tokio) cantilevers with a resonant frequency of 300 kHz. For statistics at least 3-6 positions of 20 µm x 20 µm were measured depending on the homogeneity of the samples.

**TEM.** A Philips CM30 ST microscope (300 kV, LaB<sub>6</sub> cathode, CS = 1.15 mm, Royal Philips Electronics, Amsterdam) was used for TEM investigations.

### 4.3.3 Results and Discussion

In an earlier study we have shown that the applied synthesis route yields  $TBA_{1-y}H_yCa_2Nb_3O_{10}$  nanosheets with a  $TBA^+$  amount of 0.84 ( $y = 0.16$ ), lateral dimensions around 1-2 µm and a height of 3.5 nm according to AFM measurements under ambient conditions (see Chapter 4.1).<sup>16</sup> The height of the nanosheets is higher than the crystallographic thickness of the perovskite layer (~1.44 nm) due to adsorption of water and also caused by the dense ligand shell surrounding it. Subsequent dilution of the colloidal suspension showed that  $TBA^+$  cations can be replaced by  $H^+$  due to the following equilibrium reaction:



In contrast to this post-treatment a change of the  $TBA^+$  ratio before exfoliation has a different influence as shown in Figure 4.3.1. For a molar ratio of 1:0.1 of  $HCa_2Nb_3O_{10}$  to  $TBAOH$  only a few nanosheets are obtained, which are smaller in size ~0.5 µm and also thinner with a height ~2.6 nm. For a ratio of 1:0.5 nanosheets become larger (~1 µm) and the height increases slightly to ~2.8 nm. For ratios between 1:1-1:4  $TBA_{1-y}H_yCa_2Nb_3O_{10}$  nanosheets show dimensions around 3.5 nm in height and 1-2 µm in size as described in the beginning. Further increase of the  $TBAOH$  amount leads to a successive prevention of exfoliation, which is shown for the extreme case of a ratio of 1:24. This finding is similar to studies on

lepidocrocite-type titanate nanosheets and for lower ratios to an AFM study of  $[\text{Ca}_2\text{Nb}_3\text{O}_{10}]^-$  with various ligands.<sup>31-33</sup> A large excess of aqueous  $\text{TBA}^+$  ions leads to a swelling *via* osmotic hydration of the material in the interlayer region, whereas a 5-fold excess down to an equivalent amount of  $\text{TBA}$  ions favors complete delamination. Below a certain concentration no exfoliation occurs. Note that the solid to solution ratio seems to affect the transition from a swollen phase to exfoliated nanosheets as well as certain other factors such as composition, charge density and the nature of the exfoliating agent or solvent play crucial roles in this process as well.<sup>34</sup>

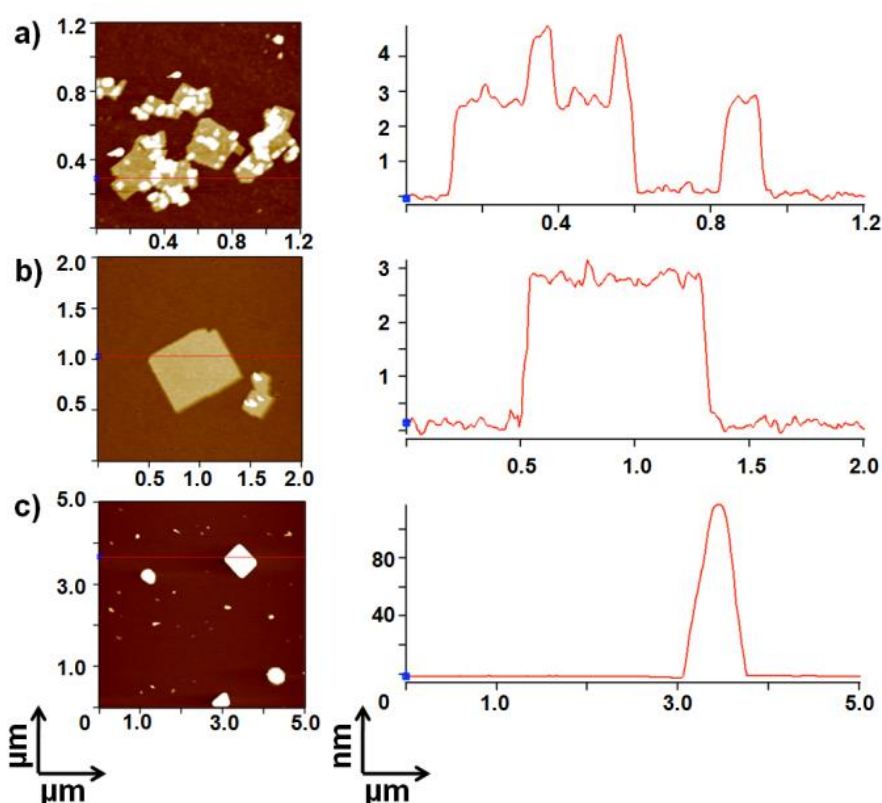


**Figure 4.3.1:** Comparison of AFM images and corresponding height profiles of  $\text{HCa}_2\text{Nb}_3\text{O}_{10}$  exfoliated with a a) 1:0.1, b) 1:0.5, c) 1:24 ratio to  $\text{TBAOH}$ .

Once exfoliated,  $\text{TBA}_{1-y}\text{H}_y\text{Ca}_2\text{Nb}_3\text{O}_{10}$  nanosheets seem to be extremely mechanically stable to ultrasonication compared to other niobate nanosheets. Figure 4.3.2 shows AFM images of nanosheets that were ultrasonicated for 1-12 h. In contrast to nanosheets derived from  $\text{K}_4\text{Nb}_6\text{O}_{17}$  that get smaller with increased ultrasonication duration, no significant change in size was observed for the calcium niobate.<sup>28</sup> Neither did ultrasonication show an influence on the height and hence the  $\text{TBA}^+$  amount present on the sheet. Only small multilayer parts that are sometimes present at the nanosheet surface got removed. Thus, ultrasonication might be exploited to clean the nanosheets from residues. Note that the initial size of the nanosheets is dependent on the crystallite size of the bulk phase and the exfoliation method, e.g.

nanosheets get larger in size for lower shaking or stirring speeds. Regarding thermal stability, we found that individual nanosheets deposited on a Si wafer start to decompose at temperatures  $\geq 300^\circ\text{C}$ .

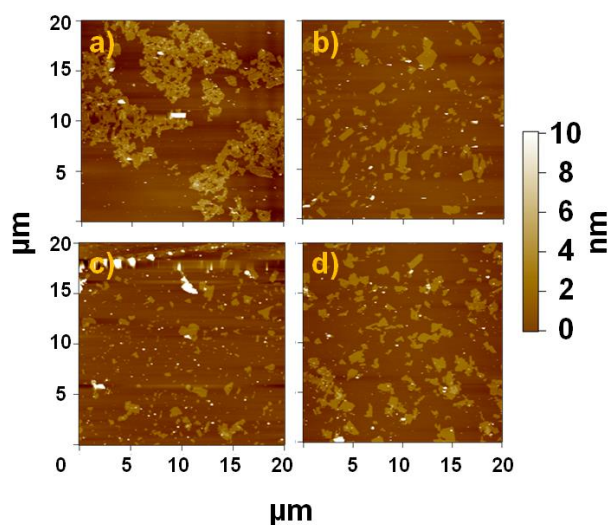


**Figure 4.3.2:** AFM images of  $TBA_{1-y}H_yCa_2Nb_3O_{10}$  nanosheets on a Si substrate after ultrasonication for a) 1 h, b) 2 h, c) 4 h and d) 12 h.

Exfoliation of  $HCa_2Nb_3O_{10}$  with  $TBPOH$  leads to unilamellar  $TBP_{1-y}H_yCa_2Nb_3O_{10}$  nanosheets, which has been up to our knowledge not been demonstrated before. AFM images are shown in Figure 4.3.3 and display slightly smaller nanosheets with a lateral dimension of 500 nm - 1  $\mu\text{m}$ . Contrary to the  $TBA_{1-y}H_yCa_2Nb_3O_{10}$  nanosheets, the wafer had to be washed with water before measurement as  $TBP^+$  samples form some kind of “sticky” film on the Si surface. The height of the nanosheets is around 2.9 nm and thus smaller compared to  $TBA_{1-y}H_yCa_2Nb_3O_{10}$ . This might be due to removal of the ligand during the washing step. Thus,  $TBPOH$  can - similar to titanate nanosheets - also be used for calcium niobates as exfoliation agent.<sup>35</sup>

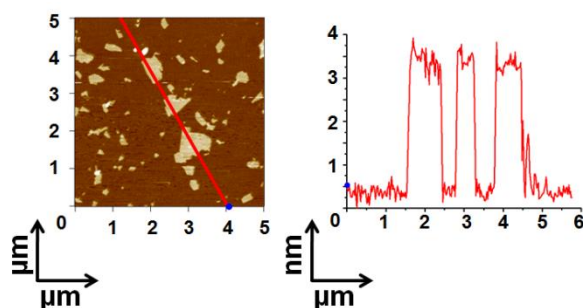


**Figure 4.3.3:** AFM image and corresponding height profile of  $TBP_{1-y}H_yCa_2Nb_3O_{10}$  nanosheets on a Si substrate after washing.

For LBL purposes, surface coverage is one main drawback that needs to be overcome. As simple surface activation by acid treatment of Si wafers with 5% HNO<sub>3</sub> or conc. H<sub>2</sub>SO<sub>5</sub> did not show a significant improvement in surface coverage, we tested several primers for the nanosheets. The AFM images for Si wafer coated with 5 wt% PEI, 20 wt% PDDA or 1 mM APTES after dip-coating in a  $TBA_{1-y}H_yCa_2Nb_3O_{10}$  nanosheet suspension are given in Figure 4.3.4. Similar to the results shown in literature PDDA and PEI can yield an (almost) complete coverage of the substrate depending on the concentration, pH and dipping time.<sup>13,16</sup> Higher concentration, a pH  $\geq 8.4$  and longer dipping times favor complete coverage, but also cause many overlaps and attachment of smaller parts. In contrast, it seems possible to achieve a densely packed monolayer without many overlaps with the aid of APTES. APTES forms thin self-assembled monolayers and does not coil like the polymers.<sup>36</sup> Thus, LBL experiments were performed with APTES functionalized Si wafers.

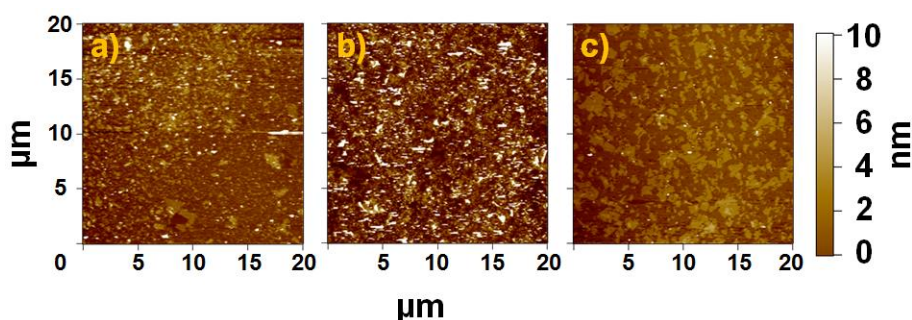


**Figure 4.3.4:** Comparison of Si wafers coated with  $TBA_{1-y}H_yCa_2Nb_3O_{10}$  primed with a) 5 wt% PEI, b) 20 wt% PDDA and c) 1 mM APTES.

TEM images of a (Per/PDDA)<sub>80</sub> stack at various magnifications are shown in Figure 4.3.5. The stack has an average thickness of around 230 nm. This is about half of the sum of crystallographic thickness of  $[Ca_2Nb_3O_{10}]^-$  ( $80 \times 1.44 \text{ nm} = 115.2 \text{ nm}$ ). Mallouk *et al.* have shown with ellipsometric measurements that the increase due to PDDA is around  $0.19 \pm 0.07 \text{ nm}$ , which would yield an overall thickness of around 130 nm for the “theoretical” (Per/PDDA)<sub>80</sub> stack. Thus, we obtain a difference of roughly 100 nm in comparison to the experimental stack in the end.<sup>13</sup> This difference is caused by various factors. As can be seen from Figure 4.3.5 b)-c) the stack is very homogeneous for the first layers, but with increasing bilayer number the arrangement gets inhomogeneous as effects of sheet termination, sheet overlap and inclusion of agglomerates add up. Amorphous gaps form where no sheets are deposited. These gaps get bigger for the outer layers and can be up to 10-15 nm in size. This might also be caused by an agglomeration of the PDDA polymer. Another reason might be the restacking of nanosheets and deposition of multilayer sheets. During optimization of the stacking parameters we encountered one main difficulty, the carryover of the polymer into the  $TBA_{1-y}H_yCa_2Nb_3O_{10}$  suspension that leads to flocculation of the nanosheets. We

found a decrease of the PDDA concentration from 20 wt% down to 5% as most effective way to resolve this problem. An increase of washing time did not show a significant effect. Concentrations  $\leq 1$  wt% lead to no LBL deposition at all. Note that the deposited layers are partly detached from the surface and can easily be removed from the substrate as will be discussed later.

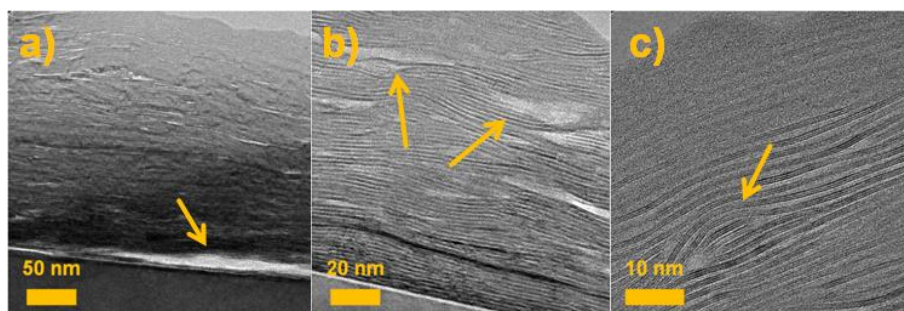


**Figure 4.3.5:** a) Overview TEM image of a (Per/PDDA)<sub>80</sub> stack and b)+c) an enlarged region at higher magnification.

Another possibility to arrange perovskite nanosheets in a LBL-manner is the use of positively charged LDH nanosheets. We have characterized in detail a (LDH/per)<sub>n</sub> stack composed of  $TBA_{1-y}H_yCa_2Nb_3O_{10}$  and  $ES[Mn_2Al(OH)_6]$  nanosheets, as discussed in Chapter 4.1.<sup>16</sup> Applying various analysis methods, we concluded that only  $TBA^+$  can be exchanged against  $[Mn_2Al(OH)_6]^+$  and thus be used to regulate the density of the multilayer arrangement. In the following the difference between  $TBA^+$  and  $TBP^+$  is investigated in more detail. The resulting (LDH/per)<sub>50</sub> stack for  $TBP_{1-y}H_yCa_2Nb_3O_{10}$  and  $ES[Mn_2Al(OH)_6]$  nanosheets is shown in Figure 4.3.6. The stack is similar to the  $TBA^+$  based arrangement and thus very homogeneous. With a height of 70 nm ( $50 \times (1.44 \text{ nm} + 0.48 \text{ nm}) = 96 \text{ nm}$ ) the heterostructure is around 26 nm smaller than expected. Thus, the proposed exchange of  $TBA^+$  against LDH<sup>+</sup> layers might be slower when  $TBP^+$  is used instead. An incomplete exchange would lead to regions where the negatively charged perovskite layer is not covered with a positively charged LDH layer and hence, the next deposited perovskite layer would be washed away due to a weaker bonding force between similar charged layers.<sup>16</sup> According to EDX the ratio of Per:LDH is 3:1 and therefore approximately the same as for the  $TBA$  based multilayer stack. Applying longer dipping time,  $TBP^+$  might be more suitable to form homogeneous LBL structures than  $TBA^+$ .



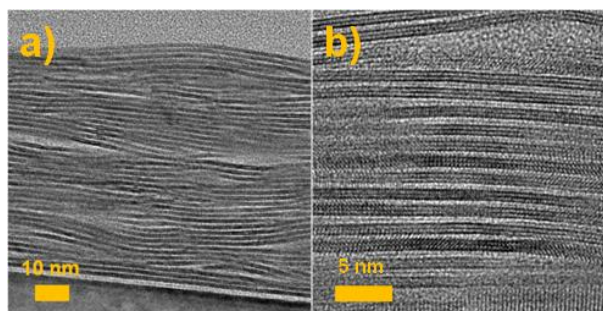


**Figure 4.3.6:** Overview TEM images of a (LDH/per)<sub>50</sub> stack synthesized by alternate stacking of  $TBP_{1-y}H_yCa_2Nb_3O_{10}$  and  $ES[Mn_2Al(OH)_6]$  nanosheets and b) an enlarged region at higher magnification.

An approach to deposit “thick”  $TBA_{1-y}H_yCa_2Nb_3O_{10}$  nanosheet films without any oppositely charged cations is shown in Figure 4.3.7 and is based on EISA, using substrates that were vertically placed in a suspension of nanosheets. According to AFM measurements, slow evaporation of the solvent leads to deposition of 300-600 nm thick restacked nanosheet films. The thickness depends mainly on the concentration of the nanosheet suspension, whereas the homogeneity is governed by the temperature. We found a dilution of the mother nanosheet suspension ( $\sim 2$  mg/mL) of 1:16 and a temperature of 60°C to yield the most uniform films. Still, vibrations and air circulation in the muffle furnace seemed to be the main drawback in order to fabricate homogeneous films and have to be eliminated in future setups. Nevertheless, one main advantage of this assembly is that these films can be separated from the substrate by simply rinsing the wafer in water, and thus they can easily be lifted off and transferred onto another substrate. Thus, no complicated embedding in polymers or stamping procedures are necessary. Once the multilayers are heated above 300°C the decomposition of the ligand leads to an immobilization of the nanosheets onto the wafer surface and harsher conditions like boiling in 6M HCl are necessary to remove the films.



**Figure 4.3.7:** Photographs of a) the experimental EISA setup, b) coated wafers of  $TBA_{1-y}H_yCa_2Nb_3O_{10}$  nanosheets deposited at 60°C at various dilutions of the mother nanosheet suspension with a concentration of  $\sim 2$  mg/mL (1:0, 1:1, 1:2, 1:4 from left to right) and c) nanosheet platelets removed from the wafer.

To demonstrate the viability of this method for the fabrication of more complex films, we used EISA to deposit  $TBA_{1-y}H_yCa_2Nb_3O_{10}$  nanosheets along with PS spheres. Figure 4.3.8 displays SEM images of a deposited film before and after calcination at 300°C. Macroporous solids are formed in good quality, similar to works on  $K_4Nb_6O_{17}$  based nanosheets.<sup>28</sup> As mentioned above, we found that dilution of the stock nanosheet suspension at concentrations down to 0.1 mg/mL gave the most uniform films. Since  $TBA_{1-y}H_yCa_2Nb_3O_{10}$  nanosheet sizes cannot be tuned by ultrasonication, we used larger PS spheres ( $d = 0.617 \mu\text{m}$ ) to achieve a good network where enough but not too many nanosheets are present to wrap around the PS beads. Smaller PS spheres lead to a more densely packed nanosheet film with less pores, as nanosheets do not wrap around the spheres and rather re-stack. From literature it is known, that an additional heating step  $>700^\circ\text{C}$  can be performed to further improve crystallization of the network to form e.g.  $Ca_4Nb_6O_{19}$ .<sup>24</sup> Not that calcination at 300°C is necessary as direct heating at 700°C leads to a collapse of the network.

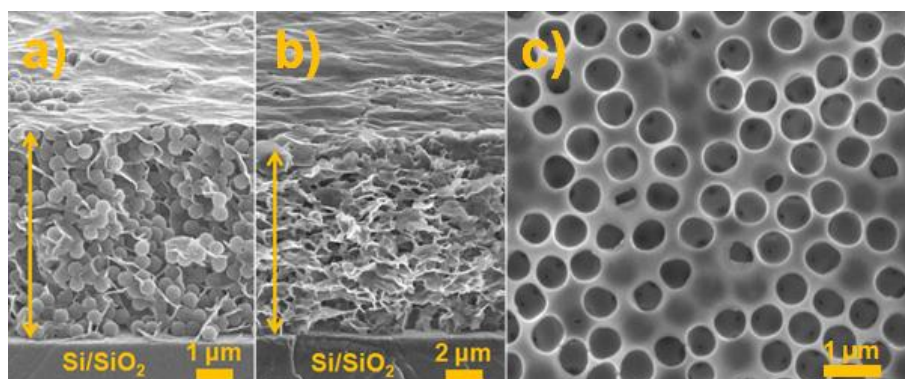


**Figure 4.3.8:** SEM images of a)  $TBA_{1-y}H_yCa_2Nb_3O_{10}$  nanosheets ( $c = 0.1 \text{ mg/mL}$ ) mixed with PS ( $d = 0.617 \mu\text{m}$ ) spheres after EISA deposition at  $60^\circ\text{C}$  and b) side and c) top image ( $c = 0.2 \text{ mg/mL}$ ) after removal of PS spheres.

In the last approach we used the PS spheres to generate a Bragg stack-like material with periodically alternating layers of nanosheets. Figure 4.3.9 shows the SEM image of an alternate stacking of a  $TBA_{1-y}H_yCa_2Nb_3O_{10}$  nanosheet layer with melted PS spheres and unmelted PS spheres on top. Contrary to the EISA approach the layer thickness can be more precisely tuned by spin-coating and yields smoother surfaces. Table 4.3.1 lists the obtained layer thickness for  $TBA_{1-y}H_yCa_2Nb_3O_{10}$  nanosheets ( $c = 6 \text{ mg/mL}$  in 20% M-H<sub>2</sub>O/80% EtOH) at the given spinning conditions. After an initial layer with a thickness of  $\sim 29 \text{ nm}$  each additional drop adds a layer of around  $40 \text{ nm}$ . Note that a calcination step is necessary to decompose the organic ligand layer and hence, to enable interaction of the deposited layer with the new nanosheets. Without the calcination step a maximum thickness of  $\sim 35 \text{ nm}$  independent of the material quantity was reached. The layer can also be decomposed by UV irradiation.<sup>20</sup> This is a crucial point in the utilization of  $TBA_{1-y}H_yCa_2Nb_3O_{10}$  nanosheets as

building blocks. Nanosheets are achieved through a swelling process and the loss of the interaction between neighbouring layer. Once deposited on a substrate the interaction is still weak so that for example only monolayers stay attached on the surface and a LBL approach is possible. Once the ligand is decomposed the bonding increases and multilayers are stabilized. We used this behavior to first immobilize a perovskite multilayer and then added a PS layer that was melted at 120°C. From that point onwards an alternate stacking was possible as can be seen in the SEM image (Figure 4.3.9). The orange arrows point to  $TBA_{1-y}H_yCa_2Nb_3O_{10}$  layers with a thickness of around 30 nm similar to the one observed for the initial layer and the PS spheres on top ( $d = 0.172 \mu\text{m}$ ). The melted PS layer shows a decreased thickness of  $\sim 134$  nm. With this the applicability of perovskite nanosheets in Bragg stack materials is imaginable once more alternating layers are deposited. In future approaches UV irradiation instead of thermal treatment might enable to maintain the PS sphere layers, thus enabling an easy control of the layer thickness in dependence of the sphere diameter.

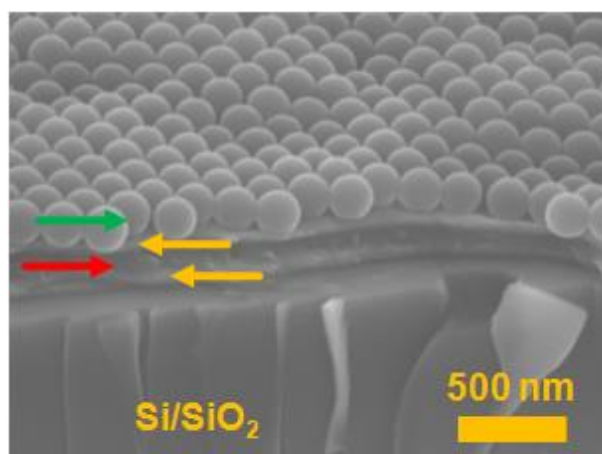


**Figure 4.3.9:** Multilayer stack of  $TBA_{1-y}H_yCa_2Nb_3O_{10}$  nanosheets (orange arrows) with melted PS layer (red) and PS ( $d = 0.172 \mu\text{m}$ ) layer before melting (green).

**Table 4.3.1:** Ellipsometric analysis determining the layer thickness of spin-coated  $TBA_{1-y}H_yCa_2Nb_3O_{10}$  layers ( $c = 6 \text{ mg/mL}$  in 20% M-H<sub>2</sub>O/80% EtOH).

Layer	Thickness	Increase
1	$28.84 \pm 0.09 \text{ nm}$	-
2	$69.58 \pm 0.16 \text{ nm}$	40.74 nm
3	$113.90 \pm 0.41 \text{ nm}$	44.32 nm
4	$152.58 \pm 0.65 \text{ nm}$	38.38 nm



#### 4.3.4 Conclusion

In conclusion, we have shown fabrication of five different heterostructures with perovskite  $A_{1-y}H_yCa_2Nb_3O_{10}$  ( $A^+ = TBA^+, TBP^+$ ) nanosheets that highlight both possibilities and challenges for a controlled design of variable morphologies and hence functionalities. For the first time we have investigated a machine-dip-coated LBL fabrication of (Per/PDDA) heterostacks up to 80 bilayers, exceeding similar multilayer formations by more than 3-fold. As we go from 2D towards 3D materials, several factors like sheet termination/overlap and flocculation lead to more inhomogeneities for higher bilayer numbers, whereas the first multilayers always show a homogeneous stacking. In order to resolve these problems, different solvents and an enhanced washing procedure have to be tested. Additional calcination steps might be beneficial for monolayer homogeneity. Using  $LDH^+$  instead of a polymer we have shown that also the ligand of the nanosheet can have an influence on the stacking quality. We found  $TBP^+$  to exchange more slowly against  $LDH^+$  than  $TBA^+$ , resulting in a more densely packed film. In-depth characterization and monitoring of various ligands (e.g. those shown in Chapter 3.3) in future experiments can be one approach to optimize understanding and synthesis of nanosheet based heterostructures. For the deposition of thick  $TBA_{1-y}H_yCa_2Nb_3O_{10}$  films on a substrate we used EISA where the solvent is slowly evaporated. Both films can easily be separated from the substrate and transferred on top of each other by rinsing off the deposited material in water. Once the perovskite nanosheets are heated above  $300^\circ\text{C}$  this simple separation is not possible anymore, since the nanosheets seem to form a (covalent) bond with the Si surface and possibly also among each other. Adding PS spheres to a  $TBA_{1-y}H_yCa_2Nb_3O_{10}$  suspension we were able to fabricate “macroporous” solids after the mixture was deposited *via* EISA and the PS spheres removed at  $300^\circ\text{C}$ . Since  $TBA_{1-y}H_yCa_2Nb_3O_{10}$  nanosheets have a high mechanical stability, large PS spheres ( $d = 0.617\ \mu\text{m}$ ) had to be used to enable a wrapping of the nanosheets around the spheres, which is the basis of the formation of such porous materials. The deposited porous layer with its cavities might be useful for future photochemical devices. Combination of spin-coating of perovskite nanosheets and deposition of PS spheres with SAWS and subsequent calcination allowed us to form the basis of a 1D Bragg stack like multilayer, that once more layers are deposited may be interesting for certain sensing applications, e.g. as humidity sensor. Overall,  $TBA_{1-y}H_yCa_2Nb_3O_{10}$  nanosheets have proven to be a multifaceted building block for nanoarchitectonics.

### 4.3.5 Bibliography

- [1] M. R. Buck, R. E. Schaak, *Angew. Chem., Int. Ed. Engl.* **2013**, 52, 6154-6178.
- [2] T. Sasaki, *J. Ceram. Soc. Jpn.* **2007**, 115, 9-16.
- [3] M. A. Bizeto, A. L. Shiguihara, V. R. L. Constantino, *J. Mater. Chem.* **2009**, 19, 2512-2525.
- [4] R. Ma, T. Sasaki, *Adv. Mater. (Weinheim, Ger.)* **2010**, 22, 5082-5104.
- [5] M. Osada, T. Sasaki, *Adv. Mater. (Weinheim, Ger.)* **2012**, 24, 210-228.
- [6] M. Osada, T. Sasaki, *Polym. J.* **2015**, 47, 89-98.
- [7] R. Ma, T. Sasaki, *Annu. Rev. Mater. Res.* **2015**, 45, 111-127.
- [8] E. M. Sabio, R. L. Chamousis, N. D. Browning, F. E. Osterloh, *J. Phys. Chem. C* **2012**, 116, 3161-3170.
- [9] L. Chang, M. A. Holmes, M. Waller, F. E. Osterloh, A. J. Moule, *J. Mater. Chem.* **2012**, 22, 20443-20450.
- [10] C. Wang, M. Osada, Y. Ebina, B.-W. Li, K. Akatsuka, K. Fukuda, W. Sugimoto, R. Ma, T. Sasaki, *ACS Nano* **2014**, 8, 2658-2666.
- [11] M. Dion, M. Ganne, M. Tournoux, *Mater. Res. Bull.* **1981**, 16, 1429-1435.
- [12] T. Tokumitsu, K. Toda, T. Aoyagi, D. Sakuraba, K. Uematsu, M. Sato, *J. Ceram. Soc. Jpn.* **2006**, 114, 795-797.
- [13] R. E. Schaak, T. E. Mallouk, *Chem. Mater.* **2000**, 12, 2513-2516.
- [14] M. Fang, C. H. Kim, T. E. Mallouk, *Chem. Mater.* **1999**, 11, 1519-1525.
- [15] L. Li, R. Ma, Y. Ebina, K. Fukuda, K. Takada, T. Sasaki, *J. Am. Chem. Soc.* **2007**, 129, 8000-8007.
- [16] C. Ziegler, S. Werner, M. Bugnet, M. Wörsching, V. Duppel, G. A. Botton, C. Scheu, B. V. Lotsch, *Chem. Mater.* **2013**, 25, 4892-4900.
- [17] S.-H. Bang, Y. Hoshi, T. Ebina, K. Ikegami, *Trans. Mater. Res. Soc. Jpn.* **2011**, 36, 149-152.
- [18] H. Zhou, E. M. Sabio, T. K. Townsend, T. Fan, D. Zhang, F. E. Osterloh, *Chem. Mater.* **2010**, 22, 3362-3368.
- [19] M. Osada, T. Sasaki, *Int. J. Appl. Ceram. Technol.* **2012**, 9, 29-36.
- [20] M. Osada, K. Akatsuka, Y. Ebina, H. Funakubo, K. Ono, K. Takada, T. Sasaki, *ACS Nano* **2010**, 4, 5225-5232.
- [21] L. Bao-Wen, O. Minoru, A. Kosho, E. Yasuo, C. O. Tadashi, S. Takayoshi, *Jpn. J. Appl. Phys.* **2011**, 50, 09NA10.
- [22] M. Osada, T. Sasaki, *ECS Trans.* **2012**, 45, 3-8.
- [23] Y.-H. Kim, H.-J. Kim, M. Osada, B.-W. Li, Y. Ebina, T. Sasaki, *ACS Appl. Mater. Interfaces* **2014**, 6, 19510-19514.

- [24] B.-W. Li, M. Osada, Y. Ebina, K. Akatsuka, K. Fukuda, T. Sasaki, *ACS Nano* **2014**, *8*, 5449-5461.
- [25] K. Yoon-Hyun, D. Lei, O. Minoru, L. Bao-Wen, E. Yasuo, S. Takayoshi, *Nanotechnology* **2015**, *26*, 244001.
- [26] K. S. Virdi, Y. Kauffmann, C. Ziegler, P. Ganter, B. V. Lotsch, W. D. Kaplan, P. Blaha, C. Scheu, *Phys. Rev. B* **2013**, *87*, 115108.
- [27] S. Werner, V. W.-h. Lau, S. Hug, V. Duppel, H. Clausen-Schaumann, B. V. Lotsch, *Langmuir* **2013**, *29*, 9199-9207.
- [28] N. Miyamoto, K. Kuroda, *J. Colloid Interface Sci.* **2007**, *313*, 369-373.
- [29] C. Li, G. Hong, P. Wang, D. Yu, L. Qi, *Chem. Mater.* **2009**, *21*, 891-897.
- [30] J. Rybczynski, U. Ebels, M. Giersig, *Colloids Surf., A* **2003**, *219*, 1-6.
- [31] T. Sasaki, M. Watanabe, *J. Am. Chem. Soc.* **1998**, *120*, 4682-4689.
- [32] T. Maluangnont, K. Matsuba, F. Geng, R. Ma, Y. Yamauchi, T. Sasaki, *Chem. Mater.* **2013**, *25*, 3137-3146.
- [33] H. Gao, S. Shori, X. Chen, H.-C. zur Loye, H. J. Ploehn, *J. Colloid Interface Sci.* **2013**, *392*, 226-236.
- [34] R. Ma, T. Sasaki, *Acc. Chem. Res.* **2015**, *48*, 136-143.
- [35] F. Geng, R. Ma, Y. Yamauchi, T. Sasaki, *Chem. Commun. (Cambridge, U. K.)* **2014**, *50*, 9977-9980.
- [36] J. Sagiv, *J. Am. Chem. Soc.* **1980**, *102*, 92-98.

## 5 Electronic Structure Investigations

### 5.1 Electronic Structure of $\text{KCa}_2\text{Nb}_3\text{O}_{10}$ as Envisaged by Density Functional Theory and Valence Electron Energy Loss Spectroscopy

Kulpreet Singh Viridi, Yaron Kauffmann, Christian Ziegler, Pirmin Ganter, Bettina V. Lotsch,  
Wayne D. Kaplan, Peter Blaha, Christina Scheu

PUBLISHED IN: Adapted with permission from *Phys. Rev. B* **2013**, 87, 115108.  
DOI: <http://dx.doi.org/10.1103/PhysRevB.87.115108>  
Copyright: ©2013 American Physical Society

**ABSTRACT:**  $\text{KCa}_2\text{Nb}_3\text{O}_{10}$  is a layered Dion-Jacobson-type perovskite important for a number of applications such as photocatalysis and as a building block for heteronanostructures. Despite this, some of its central electronic properties such as the band gap and dielectric function are not well understood. In this report we have attempted to determine the band gap and understand the electronic structure of  $\text{KCa}_2\text{Nb}_3\text{O}_{10}$  using density functional theory. Simultaneously, the band gap and loss function have been determined experimentally using valence electron energy loss spectroscopy. The theoretical results indicate that  $\text{KCa}_2\text{Nb}_3\text{O}_{10}$  is a direct band gap semiconductor with a sparse density of states close to the onset of the conduction band. The calculated band gap value of 3.1 eV is in excellent agreement with the  $3.2 \pm 0.1$  eV measured experimentally. The loss functions computed and experimentally determined show good agreement up to 20 eV, but the theoretical peak positions at higher energy do not agree with the experimental electron energy loss spectrum. These transitions originate from K-3*p*, Ca-3*p*, and Nb-4*p* semicore states and their positions are not well described by Kohn-Sham eigenvalues. After a scissors shift of transitions due to these states by about 2.5 eV to higher energies we obtain good agreement with the experimental loss function and can thus explain the origin of all the features seen in the experimental electron energy loss spectrum.

#### 5.1.1 Introduction

Since first being synthesized nearly three decades ago<sup>1-2</sup>  $\text{KCa}_2\text{Nb}_3\text{O}_{10}$ , a Dion-Jacobson-type perovskite, has constantly attracted the attention of the scientific community for various possibilities it offers. Researchers have reported it to be an interesting material for applications such as ionic conductivity<sup>3</sup> and photocatalysis.<sup>4</sup> Upon intercalation with Li,  $\text{KCa}_2\text{Nb}_3\text{O}_{10}$  has been shown to turn superconducting.<sup>5</sup> Upon doping with  $\text{Eu}^{3+}$  or  $\text{La}^{3+}$  it has been reported to become photoluminescent.<sup>6</sup> In recent years interest in the material has surged again as it has been used as the parent compound for exfoliation into two-

dimensional nanosheets, whereby the  $K^+$  ions of the  $KCa_2Nb_3O_{10}$  have been chemically replaced during exfoliation by bulky organic cations.<sup>7</sup> Possible applications of such nanosheets range from dielectrics to building blocks for layered heterostructures.<sup>8-9</sup> Despite the large interest in pure and doped  $KCa_2Nb_3O_{10}$ , a basic understanding of the electronic structure of this material is lacking. The crystal structure of  $KCa_2Nb_3O_{10}$  was studied using single crystal x-ray diffraction analysis by Fukuoka *et al.*<sup>10</sup> whereby it was suggested to be orthorhombic, space group  $Cmcm$ . However, in this experiment only an average structural model could be obtained with partial occupation of some O sites.<sup>10</sup> Tokumitsu *et al.* argued<sup>11</sup> that as neutron beams interact more strongly with the nuclei than the x-rays, neutron diffraction offered the opportunity to better understand the positions of oxygen atoms. They improved<sup>11</sup> upon the structure model of Fukuoka *et al.*<sup>10</sup> and indicated a monoclinic structure (space group  $P2_1/m$ ) with no partial occupancies. Density functional theory (DFT) has proven to be an invaluable tool for understanding many material properties like bulk moduli, phase diagrams, and crystal structures;<sup>12-13</sup> however, its ability to successfully predict properties relating to excited states (band gaps in particular) has been less successful.<sup>14-15</sup> This is a direct consequence of the fact that the Hohenberg-Kohn theorem<sup>16</sup> is mathematically valid only for ground states.<sup>17</sup> Standard DFT has been infamous in the study of semiconductors for underestimating band gaps and more sophisticated, computationally expensive methods must be used. Recently, progress has been made for calculating band gaps more effectively by using the Tran-Blaha modified Becke Johnson (TB-mBJ) potential.<sup>18</sup> This approach has been successfully demonstrated<sup>18</sup> to predict band gaps of semiconductors (Si, Ge, GaAs, etc.), insulators (LiF, Ne, Kr, etc.), and even correlated transition metal oxides (MnO, NiO). Employing this approach<sup>18</sup> we have attempted to understand the electronic structure of  $KCa_2Nb_3O_{10}$  by obtaining the band structure, density of states (DOS), dielectric function, and loss function.

With the advent of commercially available monochromators on transmission electron microscopes (TEM), determination of band gaps using valence electron energy loss spectroscopy (VEELS) has become an interesting experimental option,<sup>19-22</sup> specifically relating to nanostructures where other methods cannot offer sufficient spatial resolution.<sup>23</sup> In this work we have determined the band gap of  $KCa_2Nb_3O_{10}$  using VEELS. In addition, the loss function  $S$  is determined from VEELS and subsequently compared to the theoretically calculated loss function.

## 5.1.2 Computational and Experimental Methodology

### COMPUTATIONAL DETAILS:

As an input, the structure of  $\text{KCa}_2\text{Nb}_3\text{O}_{10}$  proposed by Tokumitsu *et al.*,<sup>11</sup> determined by powder neutron diffraction, was used for calculations as it offered well defined and fully occupied oxygen sites in contrast to the model of Fukuoka *et al.*<sup>10</sup> In this structure model<sup>11</sup>  $\text{KCa}_2\text{Nb}_3\text{O}_{10}$  crystallizes into a monoclinic crystal, space group  $P2_1/m$  (space group number 11). We have interchanged the crystal axes compared to Ref. 11 by redefining crystal parameters  $a$ ,  $b$ ,  $c$ , and  $\gamma$  to 14.859 Å, 7.7418 Å, 7.7073 Å, and 97.51°, respectively. Density functional theory based calculations were performed on  $\text{KCa}_2\text{Nb}_3\text{O}_{10}$  using an augmented plane wave + local orbitals (APW + lo) approach as incorporated in the WIEN2K code.<sup>24</sup> The atomic spheres used for K, Ca, Nb, and O were 2.42, 2.03, 1.69, and 1.50 a.u. respectively. The wave functions in the atomic spheres were expanded as spherical harmonics up to angular momentum  $l = 10$ . Local orbitals were used for the semicore states (Ca-3s,3p; K-3s,3p; Nb-4s,4p; O-2s). In the interstitial region between the atomic spheres, a plane wave expansion was used, fixing the parameter  $R_{\text{MT}}K_{\text{max}} = 7$ , which is the product of the smallest muffin tin radius and the largest plane wave  $K_{\text{max}}$ . The adequacy of the choice of the plane wave basis set size was checked by additional calculations using  $R_{\text{MT}}K_{\text{max}} = 8$ . The calculated forces on the atoms with this enlarged  $R_{\text{MT}}K_{\text{max}}$  stayed within the convergence criterion used for structure optimization, thereby validating the choice of the size of the plane wave basis set. For optimizing the atomic positions in the unit cell and determining the energy of the system, exchange correlation effects were treated using the generalized gradient approximation as proposed by Perdew, Burke, and Ernzerhof (PBE-GGA).<sup>25</sup> Since it is well known that PBE-GGA underestimates band gaps,<sup>26</sup> the electronic structure calculations (DOS, band structure, and dielectric function) were performed using the TB-mBJ potential<sup>18</sup> which usually predicts band gaps with higher accuracy. The original Becke-Johnson potential<sup>27</sup> is an approximation to the “exact-exchange” optimized effective potential in atoms. Tran and Blaha<sup>18</sup> have introduced a weighing factor for the two terms of this potential (the approximate Slater potential and the response part), which is determined from the average of  $\nabla\rho/\rho$  (where  $\rho$  corresponds to the electron density) of the specific system under investigation. It has been shown in numerous applications<sup>18, 28-30</sup> that the TB-mBJ methodology predicts band gaps in very good agreement with experiment and much more expansive Green’s function based (GW) calculations.

The irreducible Brillouin zone was sampled with a  $[2 \times 4 \times 4]$   $k$ -point mesh for the self-consistency cycle which was taken to be converged when the forces on the atoms fell below 1.0 mRy/a.u. For geometry optimization the structure was optimized by minimizing the forces on the atoms, keeping the overall unit cell parameters constant. The structure was assumed

relaxed when the force components on individual atoms fell below 5.0 mRy/a.u. A denser  $k$  mesh with  $[4 \times 8 \times 8]$   $k$  points was then used to sample the irreducible Brillouin zone to extract the density of states and the optical properties.

Optical properties were determined by employing the OPTIC program<sup>31</sup> of the WIEN2K code, whereby momentum matrix elements were computed in an energy range of  $-5$  to  $5$  Ry. Two different calculations were performed; in the first, no scissor operator was used because of the usage of TB-mBJ potential<sup>18</sup> which models the valence and conduction band states well. However, the TB-mBJ potential does not give correct energy positions of the semicore states (K-3s,3p; Ca-3s,3p; Nb-4p) and in order to determine the dielectric function at higher energies, the transitions due to these states were shifted to a higher energy by an amount  $\Delta E = 2.5$  eV in the  $\epsilon_2$  calculated from the momentum transfer matrix elements.

#### **SYNTHESIS:**

KCa<sub>2</sub>Nb<sub>3</sub>O<sub>10</sub> synthesis was carried out in a way similar to the one performed by Jacobson and co-workers.<sup>2</sup> Commercially available K<sub>2</sub>CO<sub>3</sub> (Merck, 99% purity), CaCO<sub>3</sub> (Grüssing GmbH Germany, 99% purity), and Nb<sub>2</sub>O<sub>5</sub> (Alfa Aesar, 99.5% purity) in a stoichiometric ratio of 1.1:4:3 were thoroughly ground and mixed. A preheating step at 900°C was undertaken before firing up the pelletized compound to 1200°C for 60 h. The purity of the as-synthesized KCa<sub>2</sub>Nb<sub>3</sub>O<sub>10</sub> was checked by means of x-ray diffraction where all reflections obtained were characterized as those of KCa<sub>2</sub>Nb<sub>3</sub>O<sub>10</sub>. For TEM analysis, the KCa<sub>2</sub>Nb<sub>3</sub>O<sub>10</sub> was suspended in ethanol, stirred, and drop coated onto lacy carbon coated copper TEM grids (Plano GmbH Germany), and allowed to dry in air.

#### **VEELS MEASUREMENTS AND DATA ANALYSIS:**

The KCa<sub>2</sub>Nb<sub>3</sub>O<sub>10</sub> TEM samples were investigated using a FEI Titan 80-300 scanning transmission electron microscope equipped with a field emission gun, a Wien-type monochromator, and a Gatan Tridiem 866 energy filter having a 2k CCD camera to obtain the VEEL spectra. A freely suspended particle of KCa<sub>2</sub>Nb<sub>3</sub>O<sub>10</sub> was chosen and checked for thickness by obtaining an electron energy loss spectroscopy (EELS) thickness map which suggested that the thickness of the particle investigated was about 0.3 times the inelastic mean-free-path length. The sample was oriented into a random orientation such that it was not in a zone axis for a high-symmetry plane. Measurements for band gap and loss function extraction were performed in scanning transmission electron microscopy (STEM) mode with a stationary spot using convergence and collection angles of 9.5 mrad each. A spectrometer dispersion of 0.02 eV/channel was used for acquiring the VEEL spectra. Additionally, to obtain the core loss excitations Ca M<sub>2,3</sub> and Nb N<sub>2,3</sub> EEL spectrum was acquired in TEM mode from a different region using parallel illumination, collection angle (governed by the

objective lens aperture and the spectrometer entrance aperture in TEM mode<sup>32</sup>) of 9.5 mrad, and a dispersion of 0.2 eV/channel. The chosen collection angle resulted in a momentum transfer of  $\sim 3 \text{ \AA}^{-1}$ , due to which the contribution of dipole-forbidden transitions<sup>32-34</sup> to the EELS signal was reduced.

The VEEL spectra of  $\text{KCa}_2\text{Nb}_3\text{O}_{10}$  were acquired in a two-step process. In the first step, 50 spectra were acquired with acquisition times of 0.14 s each, such that the spectra spanned across the tail of the zero-loss peak (ZLP) on the negative side up to the valence loss features of importance (-6 to +34 eV). Next, 50 spectra were acquired with an acquisition time of 1.12 s each, where the spectra spanned from the tail of the ZLP on the positive side of the energy loss until the features of interest (+1 to +41 eV). The spectra in the first set containing the complete ZLP were aligned to get the maximum overlap between all ZLPs and were then added, to get a single spectrum, using EELS tools routines<sup>35</sup> implemented in the commercially available software package Digital Micrograph (Gatan Inc., Pleasanton California). The 50 spectra in the second set were also added to get a single spectrum. These two spectra were calibrated in the following way. The maximum of the ZLP in the first spectrum was defined to be zero energy loss. Then the uncalibrated second spectrum containing the valence loss features with a better signal-to-noise ratio was superimposed on the first spectrum and then calibrated such that the positions of valence loss excitations in both spectra overlapped. The calibrated spectra were then spliced to form a single spectrum which was used for subsequent analyses. The energy resolution, as governed by the full width at half maximum of the ZLP, was 0.2 eV and was achieved for settings where the ZLP was not symmetric. Due to this, the method of subtracting the mirrored negative side of ZLP<sup>19, 22</sup> was not used for removing the ZLP contribution from the spectra. Instead a power-law function was used to describe the tail of the ZLP as has been used by Erni and Browning<sup>36</sup> and then subtracted from the spectrum to obtain the loss function. However, we did not use a Lorentzian fit of the first derivative like Erni and Browning<sup>36</sup> to determine the conduction band onset.

### 5.1.3 Results and Discussion

#### DFT CALCULATIONS:

The crystal structure of  $\text{KCa}_2\text{Nb}_3\text{O}_{10}$  is shown in Figure 5.1.1. It consists of two-dimensional (2D) planes containing K, Ca, or Nb atoms parallel to the crystallographic (100) plane. There are two different  $\text{NbO}_2$  planes in the structure, one located between the  $\text{KO}_2$  and  $\text{CaO}$  planes (Nb atoms referred to subsequently as Nb3 and Nb4), the other located in the crystallographic (200) plane between two  $\text{CaO}$  planes (Nb atoms referred to subsequently as Nb1 and Nb2). Geometry optimization of the  $\text{KCa}_2\text{Nb}_3\text{O}_{10}$  structure changed the fractional



atomic positions (see Table 5.1.1) up to 0.03 Å (Ca3) as compared to the experimental structure proposed by Tokumitsu *et al.* The Nb1(2)-O octahedra are not significantly modified; the corresponding Nb-O distances change by less than 0.02 Å. Overall the Nb1(2)O<sub>2</sub> plane is less buckled. On the other hand the Nb3(4)-O octahedra rotate slightly and the Nb-O distances change up to 0.07 Å. This makes the Nb3-O and Nb4-O octahedra more similar. Partly due to these rotations, but in particular due to large movements of the Ca ions, some Ca-O bond lengths change by up to 0.3 Å, thereby increasing the shortest Ca-O distances and making the complex Ca-O polyhedra more isotropic. The large changes around Ca also change the bond valence sums from 2.44-1.90-1.65-2.34 to 2.33-2.16-1.81-2.02 (Ca1-Ca2-Ca3-Ca4), making them much closer to the formal valence of Ca. Some K-O distances change by up to 0.2 Å which makes the K1-O2-K2 distances much more similar.

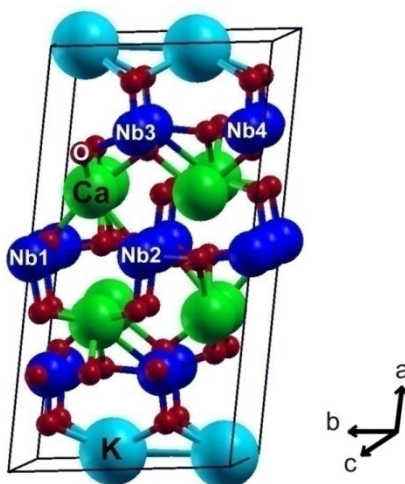


**Figure 5.1.1:** (Color online) Unit cell of  $\text{KCa}_2\text{Nb}_3\text{O}_{10}$  indicating the planes of K, Ca and Nb atoms; Nb atoms in the median plane have been labeled Nb1 and Nb2 whereas the ones in the planes between K and Ca planes are labeled as Nb3 and Nb4.

The total density of states obtained using modified Becke-Johnson potential<sup>18</sup> showed the valence band having a width of about 5 eV separated from the conduction band by a band gap value of 3.1 eV (Figure 5.1.2). At the conduction band onset the DOS is fairly low up to 4.3 eV, after which there is a sudden increase up to 6 eV, where another gap separates the conduction bands into two regions. The low-energy part of the DOS can be attributed to the semicore states as follows: Between -30.9 and -30.3 eV are the Nb-4*p* states (which incidentally are spin-orbit split by about 0.2 eV); between -28.6 and -27.9 eV K-3*s* states; between -20.2 and -19.0 eV Ca-3*p* states; between -18.4 and -16.2 eV O-2*s* states; between -11.3 and -10.8 eV K-3*p* states. Transitions from these semicore states into the conduction band should be delineated in the imaginary part of the dielectric function  $\epsilon_2$ .

**Table 5.1.1:** Theoretically optimized (top row) and experimental (bottom row) atomic positions in  $\text{KCa}_2\text{Nb}_3\text{O}_{10}$ .

Ca 1	0.6495	0.7855	0.75
	0.653	0.78	0.75
Ca 2	0.3405	0.7023	0.75
	0.346	0.717	0.75
Ca 3	0.6384	0.2893	0.75
	0.628	0.322	0.75
Ca 4	0.3480	0.1969	0.75
	0.351	0.201	0.75
K 1	0.0203	0.6302	0.25
	0.035	0.616	0.25
K 2	0.0071	0.1226	0.25
	0.008	0.132	0.25
Nb 1	0.5	0	0
	0.5	0	0
Nb 2	0.5	0.5	0
	0.5	0.5	0
Nb 3	0.7900	0.5778	0.9960
	0.7848	0.571	0.004
Nb 4	0.7889	0.0733	0.9943
	0.789	0.075	0.987
O 1	0.6293	0.4998	0.0304
	0.629	0.495	0.033
O 2	0.9091	0.6220	0.9644
	0.905	0.594	0.983
O 3	0.7741	0.3211	0.0136
	0.77	0.316	0.012
O 4	0.7444	0.5503	0.75
	0.749	0.541	0.75
O 5	0.7764	0.5923	0.25
	0.775	0.574	0.25
O 6	0.5226	0.5660	0.75
	0.514	0.576	0.75
O 7	0.5131	0.7536	0.0673
	0.520	0.755	0.053
O 8	0.6286	0.0635	0.0486
	0.630	0.006	0.052
O 9	0.9067	0.0879	0.9530
	0.906	0.081	0.953
O 10	0.7464	0.8139	0.9869
	0.748	0.818	0.974
O 11	0.7389	0.0757	0.75
	0.733	0.065	0.75
O 12	0.7842	0.0504	0.25
	0.782	0.069	0.25
O 13	0.5309	0.9570	0.75
	0.528	0.973	0.75

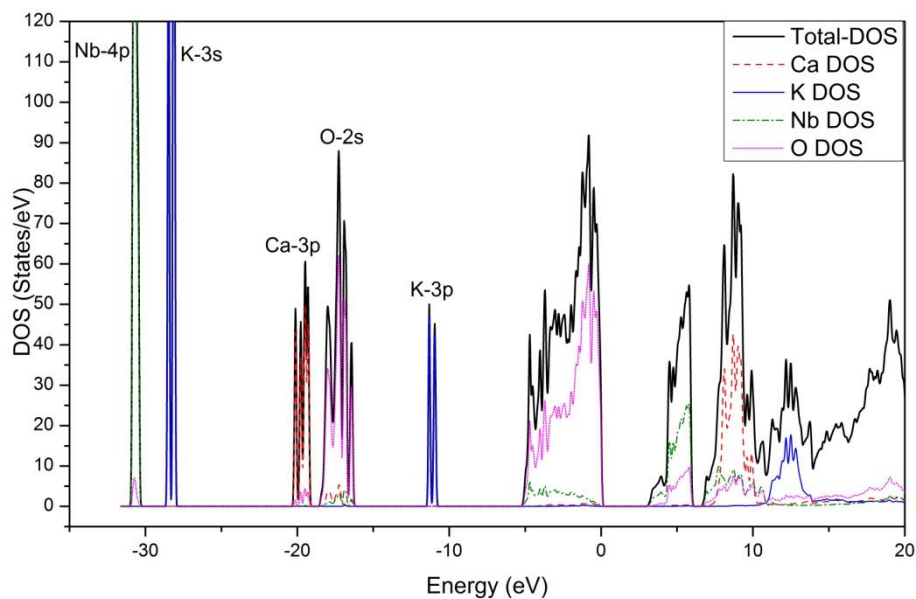


**Figure 5.1.2:** (Color online) Calculated total (full black line) DOS of  $\text{KCa}_2\text{Nb}_3\text{O}_{10}$  showing a band gap of 3.1 eV and sparse availability of conduction band states close to the onset of conduction band. The partial DOS of Ca (red dashed line), K (blue full line), Nb (green dash-dot curve) and O (magenta dotted curve) show the respective partial contributions to the DOS.

As is evident from the partial DOS (PDOS), the valence band is dominated by O-2p states with some admixture of Nb-d states, while in the conduction band Nb-d states dominate and the O-p PDOS is small (Figure 5.1.2). We determined the contributions of  $t_{2g}$ - and  $e_g$ -like Nb orbitals to the conduction band. For this purpose a local coordinate system around each Nb site was introduced such that the axes point as close as possible towards the six O neighbors which form distorted octahedra around the Nb sites. In these local coordinate systems we call the two Nb-4d orbitals pointing towards the O atoms as  $e_g$ -like and the other three Nb-4d orbitals pointing between O atoms as  $t_{2g}$ -like. Of course the  $e_g$ -like and  $t_{2g}$ -like are no irreducible representations for this low-symmetry-point group. The partial DOS due to these Nb  $t_{2g}$ -like and  $e_g$ -like orbitals are shown in Figure 5.1.3. We see that up to 6 eV the conduction band has a predominant  $t_{2g}$ -like character while the  $e_g$ -like orbitals dominate the partial DOS at higher energies.

As mentioned before, the four inequivalent Nb sites group into two different types (Nb1 and Nb2 in the central layer between two Ca layers and Nb3 and Nb4 between a K and Ca layer). The Nb DOS within such pairs is nearly the same, but the partial DOS from the different planes differ significantly (Figure 5.1.4). Interestingly the conduction band onset at 3.1 eV is primarily due to Nb1 and Nb2 states, while Nb3 and Nb4 states are shifted to slightly higher energies. The unoccupied Ca-3d states are about 8-10 eV above the Fermi energy and coincide with the Nb- $e_g$  states, while the K-3d states are shifted even higher up to 12-14 eV.

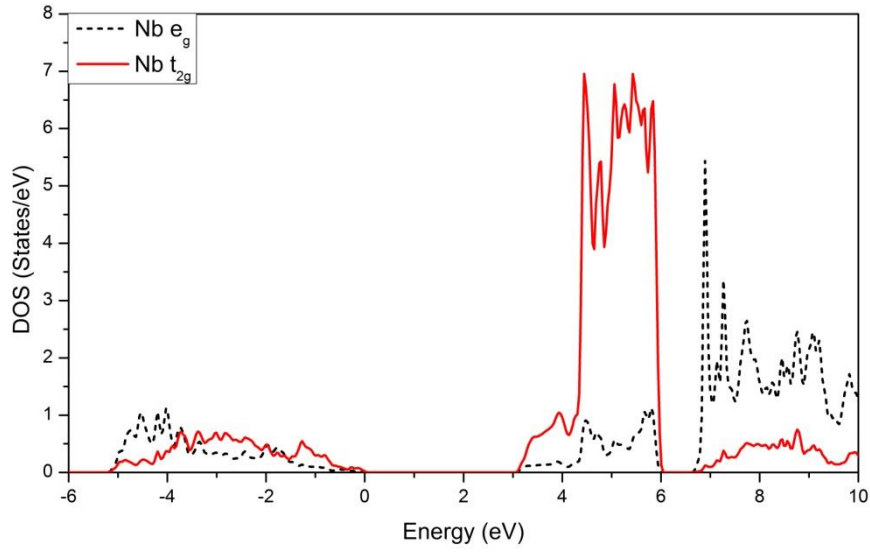


**Figure 5.1.3:** (Color online) Partial DOS contribution of the  $e_g$ -like (dashed black curve) and  $t_{2g}$ -like (full red line) orbitals of Nb to the conduction and valence bands.

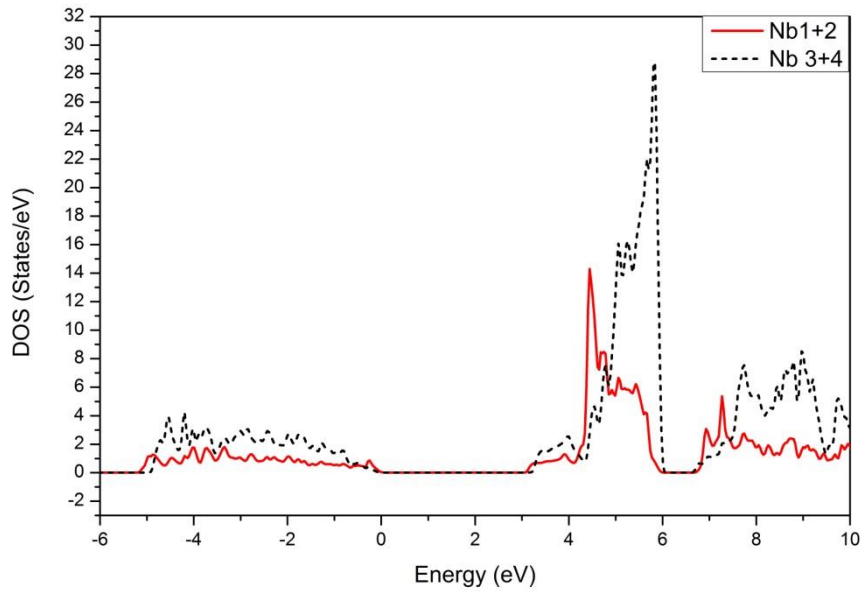


**Figure 5.1.4:** (Color online) The partial DOS contribution shows two distinct varieties of Nb atoms, Nb1 and Nb2 (full red line) and Nb3 and Nb4 (dashed black curve) with the conduction band onset contributed by the Nb1, Nb2 atoms.

The band structure of  $\text{KCa}_2\text{Nb}_3\text{O}_{10}$  is shown in Figure 5.1.5. One observes a large number of fairly flat bands at the top of the valence band (within 2 eV from the valence band maximum), while for the lower valence bands some dispersion is evident. Specifically, the top of the valence band is nearly degenerate at several high-symmetry points in  $k$  space ( $\Gamma$ , A, B, and C). On the contrary the conduction band onset at 3.1 eV is constituted by two strongly

dispersive bands whose energy minima occur at the  $\Gamma$  and A points, thereby showing that  $\text{KCa}_2\text{Nb}_3\text{O}_{10}$  is a direct band gap semiconductor. The conduction band states in the energy range 3.1-4.4 eV are quite dispersed, while bands in the energy range of 5.5-6.0 eV are less dispersed. As expected from the short  $\Gamma$ -A direction (large periodicity in direct space) and the 2D nature of  $\text{KCa}_2\text{Nb}_3\text{O}_{10}$  where the Nb-O perovskitelike layers (with fairly localized wave functions) are completely decoupled in the  $a$  direction by the K layers, all bands in this direction are very flat.

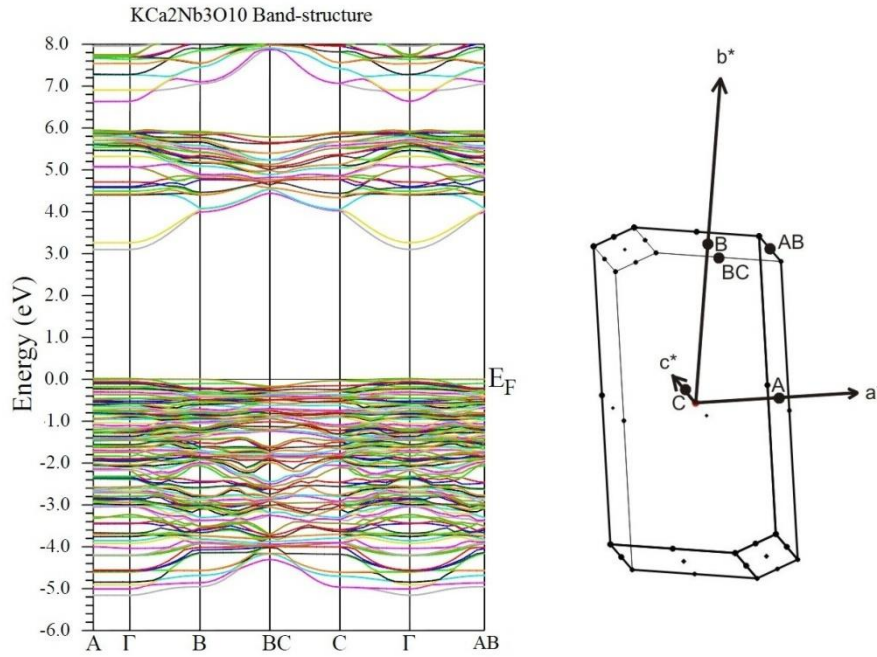


**Figure 5.1.5:** (Color online) Band structure of  $\text{KCa}_2\text{Nb}_3\text{O}_{10}$  (along with the shape of the Brillouin zone) indicating it to be a direct band gap semiconductor.

The optical properties, namely the real and imaginary parts of the dielectric function  $\epsilon$  and the loss function, were computed by the OPTIC program.<sup>31</sup> All these properties are in principle tensors of the order  $3 \times 3$ ; however, simplifications were made for easier interpretation. While in monoclinic systems, the dielectric tensor contains nonzero off-diagonal elements,<sup>31, 37</sup> we have neglected such (small) terms in our analysis. In addition the average dielectric function  $\epsilon$  was defined as the average of the three diagonal elements  $\epsilon_{xx}$ ,  $\epsilon_{yy}$ ,  $\epsilon_{zz}$  (Equation 5.1.1) for simplicity.

$$\epsilon = \frac{(\epsilon_{xx} + \epsilon_{yy} + \epsilon_{zz})}{3} \quad (\text{Eq. 5.1.1})$$

The dielectric function is a complex function ( $\epsilon = \epsilon_1 + \epsilon_2$ ) and its imaginary part  $\epsilon_2$  is obtained<sup>31</sup> from the joint density of states including the momentum matrix elements  $p$  between occupied and empty states (Equation 5.1.2).

$$\epsilon_{ij} \approx \frac{1}{\omega^2} \sum_{o,e} \int_k p_{i;o,e,k} p_{j;o,e,k} \delta(E_{e,k} - E_{o,k} - \omega) \quad (\text{Eq. 5.1.2})$$

The real part  $\epsilon_1$  has been extracted using the Kramers-Kronig transformation.<sup>38</sup> In addition, the loss function  $S$ , which is related to dielectric function<sup>32</sup> as described by Equation 5.1.3, has also been calculated:

$$S = \text{Im} \left[ -\frac{1}{\epsilon} \right] \frac{\epsilon_2}{(\epsilon_1^2 + \epsilon_2^2)} \quad (\text{Eq. 5.1.3})$$

The average dielectric function is shown in Figure 5.1.6. From the complex dielectric function the refractive index and the extinction coefficient could be extracted.<sup>39</sup> In addition from the real part, one could ascertain the position of plasmon excitation  $E_p$  as points where  $\epsilon_1(E)$  is zero and has a positive slope with respect to energy.<sup>39-41</sup> At three values of energy (11.3, 30.0, and 37.0 eV) these two conditions are satisfied, indicating plasmon excitation of valence electrons at these energy values. It is worth noting that close to  $E = 24$  eV the value of  $\epsilon_1$  comes very close to zero but still does not cross the energy axis. From the real part of the dielectric function we have determined the ion clamped (high frequency) macroscopic dielectric constant  $\epsilon^\infty$  of  $\text{KCa}_2\text{Nb}_3\text{O}_{10}$  as 0.77.<sup>38</sup>

It is worth mentioning that Li and co-workers<sup>42</sup> have determined the dielectric constant of  $\text{KCa}_2\text{Nb}_3\text{O}_{10}$  in the low-frequency regime ( $10^1$ - $10^6$  Hz) to be varying between 500 and 1800. A comparison of our calculated dielectric function to their measurements would rather be inappropriate, because electronic transitions calculated in our methodology constitute the predominant dielectric response only at very high frequencies ( $10^{13}$  Hz and higher).<sup>39</sup>

The imaginary part of the dielectric function offers insight into the interband transitions. A closer look at the partial density of states and the character of the corresponding bands enables us to analyze the features observed in  $\epsilon_2$ . The initial set of transitions occurring between 4.5 and 7.0 eV is due to transitions from the valence band into the Nb- $t_{2g}$  bands, whereas the one between 7.0 and 11.0 eV is due to excitations of valence electrons into the Nb- $e_g$  states. The transitions depicted close to 25 eV are due to excitations from the K-3p bands into the K-3d states (located more than 12 eV above the valence band maximum), while the sharp peak around 28 eV corresponds to the promotion of electrons from Ca-3p states to the Ca-3d states in the upper conduction bands. Finally Nb-4p semicore electrons constitute the transitions starting at 35 eV.

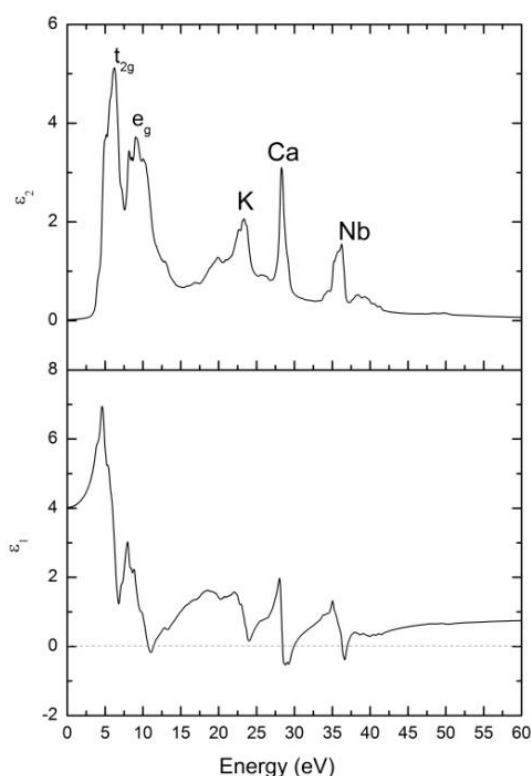


**Figure 5.1.6:** Computed real and imaginary parts of the dielectric function of  $\text{KCa}_2\text{Nb}_3\text{O}_{10}$ . From the real part one would establish 11.3, 30.0 and 37.0 eV to be plasmon excitations.

#### VEELS AND BAND GAP EXTRACTION:

VEEL spectrum of  $\text{KCa}_2\text{Nb}_3\text{O}_{10}$  in the energy loss range 0-10 eV is shown in Figure 5.1.7. One can establish that the onset of the conduction band is  $3.2 \pm 0.1$  eV which confirms our calculated value of 3.1 eV and the value of 3.35 eV experimentally determined<sup>4</sup> by Domen and co-workers. The error in our measurement is governed by the calibration method and the signal-to-noise ratio. Improving the quality of data with regard to the onset of the conduction band is difficult. On one hand, one could improve the signal-to-noise ratio by increasing the exposure time, but then one risks increasing the chances of contamination, beam damage, and detector damage, which are common limitations in STEM and VEELS. Another possible alternative is choosing a thicker region for investigations, thereby increasing the scattering cross section. However, the chances of Cerenkov radiation causing an artifact for band gap extraction in the VEEL spectra increase for thicker samples.<sup>19</sup> Rafferty and Brown<sup>43</sup> proposed that for direct band gap semiconductors in the VEEL spectrum, the region close to the band onset could be described by  $(E - E_g)^{0.5}$ , where  $E_g$  is the band gap. Knowing from our calculations that  $\text{KCa}_2\text{Nb}_3\text{O}_{10}$  is a direct band gap semiconductor, we avoid fitting such a function to the onset. Clearly a function of the form  $(E - E_g)^{0.5}$  would indicate an abrupt onset;

however, we observe a very gentle onset. The very gentle onset observed by us conforms well to the fact that only a few conduction band states are available below 4 eV.

It is necessary to highlight that we have not applied deconvolution to the acquired VEELS for removal of multiple scattering, a method which has been used regularly.<sup>44-46</sup> The justification lies in the fact that we have acquired VEEL spectra from a thin region (thickness  $\sim 0.3$  mean-free-path length) in which the scattering cross section for multiple scattering events is negligible.

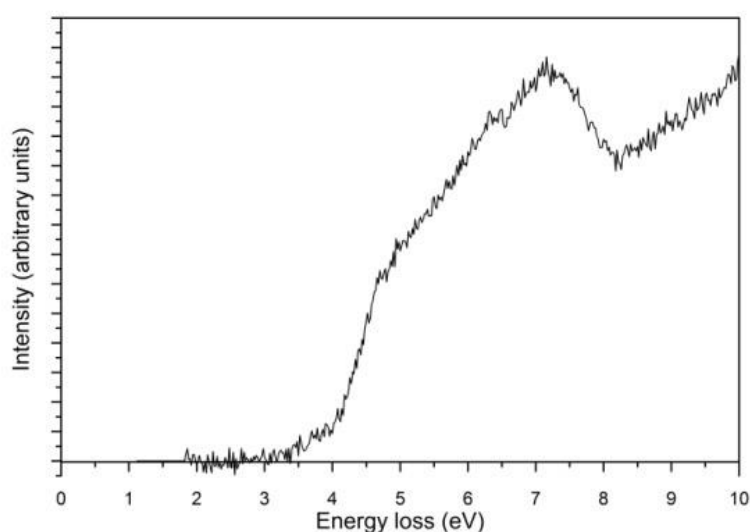


**Figure 5.1.7:** Onset of the conduction band at  $3.2 \pm 0.1$  eV indicated by ZLP subtracted VEELS of  $\text{KCa}_2\text{Nb}_3\text{O}_{10}$ .

The surface plasmon is an important loss mechanism, for thin samples when probed in the transmission electron microscope, especially in the valence loss region. It has been suggested that for thin samples<sup>44</sup> this excitation can superimpose on other valence excitation, thereby making it hard to extract the band gap. Therefore it is necessary to understand if such an excitation is interfering in our measurements. The surface plasmon becomes an important loss mechanism only in cases where the thickness of the material is less than 20 nm<sup>32</sup> or when the loss spectrum is acquired in aloof conditions (i.e., the beam is placed just outside the edge of the sample).<sup>47</sup> From EELS thickness maps we have estimated the thickness of the region investigated to be around 0.3 times the inelastic mean-free-path length. Using the model for calculating mean-free-path length proposed by Malis and co-workers<sup>48</sup> we estimate the thickness of our material to be about 42 nm. As such the chances for a surface plasmon signal making a significant contribution to the loss spectrum are negligible.



Cerenkov losses are another pitfall which can hinder<sup>44</sup> the identification of the conduction band onset from VEELS. When the velocity of an electron passing through a medium exceeds the phase velocity of light in that medium, Cerenkov radiation is generated.<sup>19, 32, 49</sup> Clearly, for electrons with an energy of 300 keV Cerenkov radiation would be generated in  $\text{KCa}_2\text{Nb}_3\text{O}_{10}$  whose  $\epsilon_1$  varies between 4 and 7 in the energy range 0-5 eV. As such it is necessary to discuss the possible chances of such losses interfering with our measurements. It has been known<sup>50-51</sup> that Cerenkov radiation has an angular distribution such that most of the radiation is confined within an angular width of the order of 0.1 mrad. This implies that for a conventionally used collection angle of about a few milliradians, nearly all Cerenkov radiation generated would be collected for an on-axis spectrometer entrance aperture.<sup>21</sup> One way of limiting the contribution of Cerenkov radiation would be using a dedicated dark-field spectrometer entrance aperture (for details see Ref. 19); however, that was not possible using our apparatus.

Cerenkov radiation generation can, however, be strongly damped when the thickness of the material probed is less than about 100 nm.<sup>19, 51-54</sup> Erni and Browning showed<sup>54</sup> that there are negligible Cerenkov losses for thickness below 100 nm in materials with normalized emission rate below 0.9. The normalized emission rate<sup>54</sup> for  $\text{KCa}_2\text{Nb}_3\text{O}_{10}$  can be determined on the basis of the computed maximum value of  $\epsilon_1$  (6.95) to be 0.76. Therefore on the basis of the analysis of Erni and Browning,<sup>54</sup> it can be deduced that in a VEELS measurement from a 42-nm-thick region of  $\text{KCa}_2\text{Nb}_3\text{O}_{10}$ , the Cerenkov radiation generation is heavily damped and as such does not contribute significantly to the scattering cross section.

van Benthem and co-workers determined<sup>45</sup> the optical properties of  $\text{SrTiO}_3$  using VEELS (STEM mode, 6.5 mrad convergence and collection angles, respectively) and vacuum ultraviolet spectroscopy. They found<sup>45</sup> good agreement between the two methods and concluded that Cerenkov losses did not contribute to the VEELS signal in any significant manner.

In light of these results<sup>19, 21, 45, 50-54</sup> and the fact that our calculated and experimentally determined loss function show good agreement (Figure 5.1.8), it can be assumed that Cerenkov losses on account of damping do not contribute significantly to the VEEL spectra acquired.

The band gap values determined using VEELS ( $3.2 \pm 0.1$  eV) and DFT (3.1 eV) compare well with the band gap value of 3.35 eV measured by Domen and co-workers<sup>4</sup> using photocatalysis. This shows the success in usage of VEELS and modified Becke-Johnson potentials<sup>18</sup> for ascertaining the band gaps with reasonable accuracy.

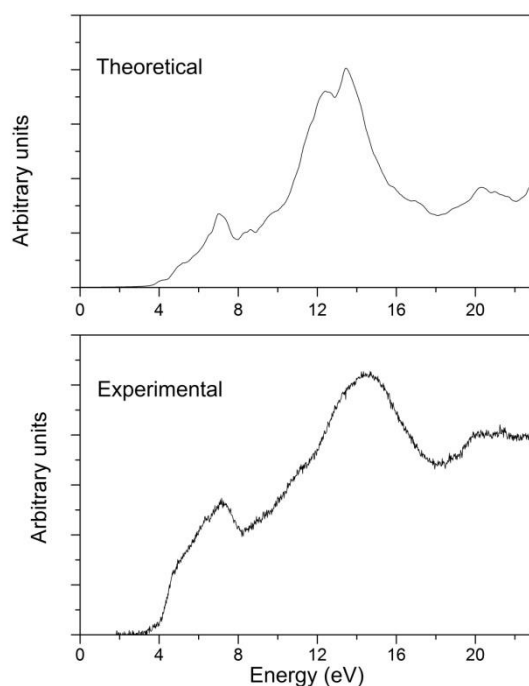


**Figure 5.1.8:** Theoretically computed and experimentally determined loss functions.

#### LOSS FUNCTION COMPARISON:

In an electron energy loss spectrum, the double differential scattering cross section<sup>32</sup> is directly proportional to the loss function  $S$ . Therefore the intensity measured in EELS experiments is directly related to the loss function. A big advantage of this technique is the easy identification of plasmon excitations,<sup>39</sup> which in thicker samples would dominate the EELS. Moreover it serves as a good method of comparing the agreement between theory and experiments. To this end the loss function of  $\text{KCa}_2\text{Nb}_3\text{O}_{10}$  was extracted from experimental VEELS and theoretically computed dielectric function and plotted for comparison in Figure 5.1.8. When one compares the experimental and calculated loss functions one sees good agreement in the regime  $E < 20$  eV.

#### LOSS FUNCTION AT HIGHER ENERGIES:

In order to better understand the semicore states, we acquired EELS in TEM mode with a larger dispersion (0.2 eV/channel). The EEL spectrum is shown in Figure 5.1.9. There are two distinct features visible, namely the peaks at 35 and 45.5 eV. A comparison with the literature<sup>55-56</sup> helps in identifying the feature with a maximum at 35 eV to be the Ca  $M_{2,3}$  edge. Bach and co-workers have shown<sup>57</sup> that Nb in an oxidation state of +5 yields a Nb  $N_{2,3}$  edge at 46 eV; hence we designate the peak at 45.5 eV as that due to Nb  $N_{2,3}$  excitation.

In the calculated imaginary part of the dielectric function, shown in Figure 5.1.6, we had designated the transitions at 28 and 37 eV to electrons from the Ca-3*p* and Nb-4*p* states. The excitations due to the corresponding energy levels (Ca-3*p* and Nb-4*p*) in EEL spectrum occur at higher energies (35 eV Ca  $M_{2,3}$  edge and 46 eV Nb  $N_{2,3}$  edge). Even taking into

account that peaks in loss function are usually a few eV higher in energy than the peaks in  $\epsilon_2$ , because low values (zeroes) in  $\epsilon_1$  appear usually a few eV after peaks in  $\epsilon_2$ , the positions of excitations due to Ca-3*p* and Nb-4*p* electrons are not optimal. This points to shortcomings in our computational methodology specifically for semicore states. It has been shown previously<sup>58</sup> that DFT based methods predict the semicore states at higher energies than the ones that are experimentally measured. This is related to the fact that these methods cancel the self-interaction incompletely,<sup>59</sup> and also the TB-mBJ method cannot cure the problems for these low-lying states. In addition, such localized excitations are known<sup>60</sup> to produce large excitonic effects which cannot be modeled by single particle approaches.

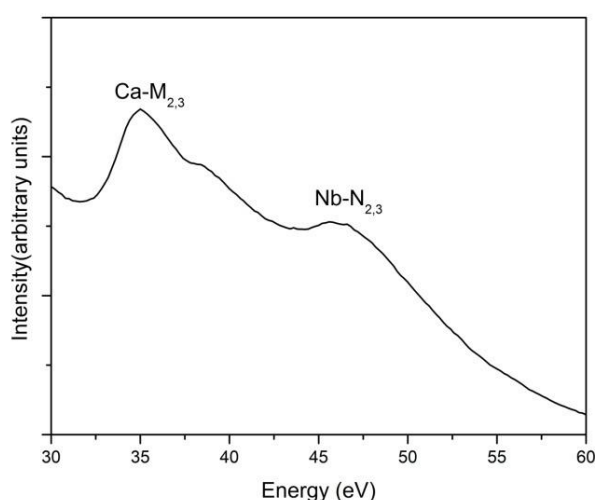


**Figure 5.1.9:** EELS acquired in TEM mode indicating Ca  $M_{2,3}$  and Nb  $N_{2,3}$  edges.

In order to model the high energy loss function in a more realistic manner, we computed  $\epsilon_2$  due to valence and semicore states separately. The momentum transfer matrix was computed, first using all the electrons and then using only the valence band electrons ( $E > -5.3$  eV). Then the  $\epsilon_2$  calculated for valence band electrons was subtracted from the  $\epsilon_2$  calculated for all electrons to get  $\epsilon_2$  for the semicore states. This  $\epsilon_2$  due to the semicore electrons was shifted by energy  $\Delta E$  where  $\Delta E > 0$  because the semicore states are located at energies lower than what were computed. Then the partial  $\epsilon_2$  due to the valence electrons and the semicore states after the shift were added to get the corrected  $\epsilon_2$ . Then the Kramers-Kronig analysis was applied on this corrected  $\epsilon_2$  to get the real part of the dielectric function and the loss function.

This procedure was undertaken for different values of  $\Delta E$  until a good agreement was reached between the theoretical and experimental loss functions with regard to the positions of Ca  $M_{2,3}$  and Nb  $N_{2,3}$  edges. We found the best agreement using a  $\Delta E$  value of 2.5 eV. The calculated  $\epsilon_1$ ,  $\epsilon_2$ , and loss function, after correction, are shown in Figure 5.1.10. In the corrected loss function, the feature at 29 eV stems from the excitation of K-3*p* electrons, the

peak around 34 eV from Ca-3*p* electrons, and the broad Nb N<sub>2,3</sub> edge is between 40 and 47 eV. These energies agree well with the experimental EEL spectrum (Figure 5.1.9).

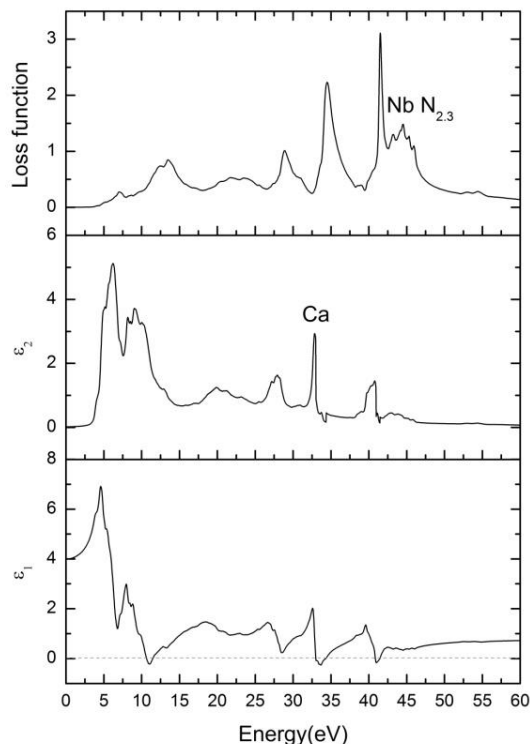


**Figure 5.1.10:** The corrected dielectric function and loss function obtained by shifting the transitions due to semicore states by 2.5 eV towards higher energies.

### 5.1.4 Conclusions

Density functional theory based calculations show that the  $\text{KCa}_2\text{Nb}_3\text{O}_{10}$  structure is more symmetric than the experimental structure previously proposed and some bond distances (in particular Ca-O) differ by as much as 0.3 Å. The central  $\text{NbO}_2$  plane is less buckled.  $\text{KCa}_2\text{Nb}_3\text{O}_{10}$  is a direct band gap semiconductor with a calculated band gap of 3.1 eV. The conduction band onset is dominated by Nb1, Nb2  $t_{2g}$ -like states (in the central plane between two Ca layers), whereas the Nb3, Nb4 (between K and Ca layers) states are shifted upwards. The large crystal field separates the empty Nb  $t_{2g}$  and  $e_g$  states by a small gap. On the other hand the valence band is dominated by O-2*p* states. The Ca-3*d* (and even more the K-3*d*) states start only at more than 8 eV above the valence band maximum. The band gap value of  $3.2 \pm 0.1$  eV extracted from the STEM-VEELS measurement matches well with the theoretical results and a value reported in the literature. The loss function shows good agreement between theory and experiment up to about 20 eV but large deviations occur at higher energies. This comes about because the position of the semicore states predicted

DFT calculations is higher than in reality, and for a proper modeling of the loss function at such high energies one needs to manually shift the position of the transitions due to these states.

#### ACKNOWLEDGEMENTS:

This work was partially supported through the financial endowment of the German Science Foundation through the cluster of excellence Nanosystems Initiative Munich (NIM) and the Center for Nanoscience (CeNS). K.S.V. is grateful to the Elite Network of Bavaria for financial support. P.B. was supported by the SFB-F41 (ViCoM) project of the Austrian Science Funds (FWF). We thank Professor Ray Egerton for fruitful discussions and insightful comments.

#### 5.1.5 Bibliography

- [1] M. Dion, M. Ganne, M. Tournoux, *Mater. Res. Bull.* **1981**, 16, 1429-1435.
- [2] A. J. Jacobson, J. W. Johnson, J. T. Lewandowski, *Inorg. Chem.* **1985**, 24, 3727-3729.
- [3] V. Thangadurai, W. Weppner, *J. Mater. Chem.* **2001**, 11, 636-639.
- [4] K. Domen, J. Yoshimura, T. Sekine, A. Tanaka, T. Onishi, *Catal. Lett.* **1990**, 4, 339-343.
- [5] H. Fukuoka, T. Isami, S. Yamanaka, *Chem. Lett.* **1997**, 26, 703-704.
- [6] M. A. Bizeto, V. R. L. Constantino, H. F. Brito, *J. Alloys Compd.* **2000**, 311, 159-168.
- [7] Y. Ebina, T. Sasaki, M. Watanabe, *Solid State Ionics* **2002**, 151, 177-182.
- [8] M. Osada, T. Sasaki, *Adv. Mater. (Weinheim, Ger.)* **2012**, 24, 210-228.
- [9] B.-W. Li, M. Osada, T. C. Ozawa, Y. Ebina, K. Akatsuka, R. Ma, H. Funakubo, T. Sasaki, *ACS Nano* **2010**, 4, 6673-6680.
- [10] H. Fukuoka, T. Isami, S. Yamanaka, *J. Solid State Chem.* **2000**, 151, 40-45.
- [11] T. Tokumitsu, K. Toda, T. Aoyagi, D. Sakuraba, K. Uematsu, M. Sato, *J. Ceram. Soc. Jpn.* **2006**, 114, 795-797.
- [12] E. Kaxiras, *Atomic and Electronic Structure of Solids*, Cambridge University Press, **2003**.
- [13] J. Hafner, *Acta Mater.* **2000**, 48, 71-92.
- [14] A. Seidl, A. Görling, P. Vogl, J. A. Majewski, M. Levy, *Phys. Rev. B* **1996**, 53, 3764-3774.
- [15] W. Ku, A. G. Eguiluz, *Phys. Rev. Lett.* **2002**, 89, 126401.
- [16] P. Hohenberg, W. Kohn, *Physical Review* **1964**, 136, B864-B871.
- [17] A. S. Bamzai, B. M. Deb, *Rev. Mod. Phys.* **1981**, 53, 95-126.
- [18] F. Tran, P. Blaha, *Phys. Rev. Lett.* **2009**, 102, 226401.

- [19] L. Gu, V. Srot, W. Sigle, C. Koch, P. van Aken, F. Scholz, S. B. Thapa, C. Kirchner, M. Jetter, M. Rühle, *Phys. Rev. B* **2007**, 75, 195214.
- [20] J. Park, S. Heo, J.-G. Chung, H. Kim, H. Lee, K. Kim, G.-S. Park, *Ultramicroscopy* **2009**, 109, 1183-1188.
- [21] M. Stöger-Pollach, H. Franco, P. Schattschneider, S. Lazar, B. Schaffer, W. Grogger, H. W. Zandbergen, *Micron* **2006**, 37, 396-402.
- [22] S. Lazar, G. A. Botton, M. Y. Wu, F. D. Tichelaar, H. W. Zandbergen, *Ultramicroscopy* **2003**, 96, 535-546.
- [23] T. Kuykendall, P. Ulrich, S. Aloni, P. Yang, *Nat. Mater.* **2007**, 6, 951-956.
- [24] P. Blaha, K. Schwarz, G. Madsen, D. Kvasnicka, J. Luitz, *WIEN2K, an augmented plane wave+ local orbitals program for calculating crystal properties*, **2001**.
- [25] J. P. Perdew, K. Burke, M. Ernzerhof, *Phys. Rev. Lett.* **1996**, 77, 3865-3868.
- [26] J. Heyd, J. E. Peralta, G. E. Scuseria, R. L. Martin, *J. Chem. Phys.* **2005**, 123, 174101.
- [27] A. D. Becke, E. R. Johnson, *J. Chem. Phys.* **2006**, 124, 221101.
- [28] D. J. Singh, S. S. A. Seo, H. N. Lee, *Phys. Rev. B* **2010**, 82, 180103.
- [29] W. Feng, D. Xiao, J. Ding, Y. Yao, *Phys. Rev. Lett.* **2011**, 106, 016402.
- [30] D. Koller, F. Tran, P. Blaha, *Phys. Rev. B* **2011**, 83, 195134.
- [31] C. Ambrosch-Draxl, J. O. Sofo, *Comput. Phys. Commun.* **2006**, 175, 1-14.
- [32] R. Egerton, *Electron Energy-Loss Spectroscopy in the Electron Microscope*, Springer US, **2011**.
- [33] J. M. Auerhammer, P. Rez, *Phys. Rev. B* **1989**, 40, 2024-2030.
- [34] H. Ma, S. H. Lin, R. W. Carpenter, O. F. Sankey, *J. Appl. Phys.* **1990**, 68, 288-290.
- [35] D. R. G. Mitchell, B. Schaffer, *Ultramicroscopy* **2005**, 103, 319-332.
- [36] R. Erni, N. D. Browning, *Ultramicroscopy* **2007**, 107, 267-273.
- [37] Y. Abraham, N. A. W. Holzwarth, R. T. Williams, *Phys. Rev. B* **2000**, 62, 1733-1741.
- [38] H. Fröhlich, *Theory of dielectrics: dielectric constant and dielectric loss*, Clarendon Press, **1958**.
- [39] M. Fox, *Optical Properties of Solids*, OUP Oxford, **2010**.
- [40] V. Gallegos-Orozco, R. Martínez-Sánchez, F. Espinosa-Magaña, *Phys. Rev. B* **2008**, 77, 045128.
- [41] V. J. Keast, A. J. Scott, M. J. Kappers, C. T. Foxon, C. J. Humphreys, *Phys. Rev. B* **2002**, 66, 125319.
- [42] B.-W. Li, M. Osada, Y. Ebina, T. C. Ozawa, R. Ma, T. Sasaki, *Appl. Phys. Lett.* **2010**, 96, 182903.
- [43] B. Rafferty, L. M. Brown, *Phys. Rev. B* **1998**, 58, 10326-10337.
- [44] M. Stöger-Pollach, *Micron* **2008**, 39, 1092-1110.

- [45] K. van Benthem, C. Elsässer, R. H. French, *J. Appl. Phys.* **2001**, 90, 6156-6164.
- [46] Dorneich, French, Mülleians, Loughin, Rühle, *J. Microsc.* **1998**, 191, 286-296.
- [47] M. R. S. Huang, R. Erni, H.-Y. Lin, R.-C. Wang, C.-P. Liu, *Phys. Rev. B* **2011**, 84, 155203.
- [48] T. Malis, S. C. Cheng, R. F. Egerton, *J. Electron Microsc. Tech.* **1988**, 8, 193-200.
- [49] F. J. García de Abajo, *Rev. Mod. Phys.* **2010**, 82, 209-275.
- [50] C. v. Festenberg, *Z. Phys.* **1968**, 214, 464-471.
- [51] C. v. Festenberg, *Z. Phys.* **1969**, 227, 453-481.
- [52] E. Kröger, *Z. Phys.* **1968**, 216, 115-135.
- [53] F. J. García de Abajo, A. Rivacoba, N. Zabala, N. Yamamoto, *Phys. Rev. B* **2004**, 69, 155420.
- [54] R. Erni, N. D. Browning, *Ultramicroscopy* **2008**, 108, 84-99.
- [55] K. S. Katti, M. Qian, D. W. Frech, M. Sarikaya, *Microsc. Microanal.* **1999**, 5, 358-364.
- [56] C. C. Ahn, O. L. Krivanek, R. Burger, M. M. Disko, P. Swann, *EELS atlas: a reference collection of electron energy loss spectra covering all stable elements*, HREM Facility, Center for Solid State Science, Arizona State University, **1983**.
- [57] D. Bach, R. Schneider, D. Gerthsen, J. Verbeeck, W. Sigle, *Microsc. Microanal.* **2009**, 15, 505-523.
- [58] M. Arai, S. Kohiki, H. Yoshikawa, S. Fukushima, Y. Waseda, M. Oku, *Phys. Rev. B* **2002**, 65, 085101.
- [59] T. Miyake, P. Zhang, M. L. Cohen, S. G. Louie, *Phys. Rev. B* **2006**, 74, 245213.
- [60] R. Laskowski, P. Blaha, *Phys. Rev. B* **2010**, 82, 205104.

## 5.2 Band Gap Extraction from Individual Two-dimensional Perovskite Nanosheets using Valence Electron Energy Loss Spectroscopy

Kulpreet S. Viridi,<sup>^</sup> Yaron Kauffmann,<sup>^</sup> Christian Ziegler,<sup>^</sup> Pirmin Ganter, Peter Blaha, Bettina V. Lotsch, Wayne D. Kaplan, Christina Scheu

*Manuscript submitted.*

**ABSTRACT:** Rapid progress in the synthesis of nanostructures with tailor-made morphologies necessitates adequate analytical tools to unravel their physical properties. In our study, we investigate, on the nanometer scale, the band gap of individual  $[TBA_xH_{1-x}]^+[Ca_2Nb_3O_{10}]^-$  nanosheets obtained through intercalation – exfoliation of the layered bulk phase  $KCa_2Nb_3O_{10}$  with tetra-*n*-butylammonium hydroxide (TBAOH) using valence electron energy loss spectroscopy (VEELS) in the scanning transmission electron microscope (STEM). The nanosheets consist of an anionically charged perovskite layer with cationic organic ligands surrounding it. Due to the hybrid nature, a careful acquisition and analysis protocol is required since the nanosheets disintegrate easily under electron beam irradiation. The VEELS data reveal a fundamental band gap of an individual freely suspended perovskite nanosheet to be  $3.0 \pm 0.2$  eV and optically allowed transitions above  $3.8 \pm 0.2$  eV (“optical band gap”). The spatial resolution of the measurements is about 9 nm, taking into account 50% of the excitations when illuminating with an incident electron beam of 1 nm diameter. Our investigations reveal that the band gap of an individual nanosheet is not changed significantly compared to the bulk phase, which is confirmed by UV-Vis data. This is rationalized by the quasi 2D electronic structure of the bulk material being preserved upon delamination.

### 5.2.1 Introduction

Since the discovery of graphene<sup>1</sup> the scientific community has paid considerable attention to apply the principles of two-dimensional (2D) synthesis to other families of materials. A viable approach to various classes of inorganic 2D-nanostructures has been the solution-mediated delamination of layered bulk materials down to the single sheet level. This has led to the synthesis of 2D-nanosheets based on e.g. oxides,<sup>2</sup> boron nitride,<sup>3</sup> metal dichalcogenides,<sup>4</sup> and metal disulphides<sup>5</sup>. One prominent class of such materials is derived from the Dion-Jacobson family of layered perovskites, with the prototypic member  $KCa_2Nb_3O_{10}$ <sup>6,7</sup>. This perovskite was delaminated into 2D-nanostructures consisting of monolayer sheets for the first time about two decades ago.<sup>8</sup> A systematic study of the synthesis procedure and corresponding characterization of the sheets was made by Schaak and Mallouk.<sup>9</sup>



$[TBA_xH_{1-x}]^+[Ca_2Nb_3O_{10}]^-$  nanosheets have a structure similar to the layered Dion-Jacobson perovskite  $KCa_2Nb_3O_{10}$  shown in Figure 5.2.1a. The  $K^+$  ions of  $KCa_2Nb_3O_{10}$  are chemically replaced during the intercalation process by the bulky  $TBA^+$  cation. This replacement is accompanied by the introduction of a large amount of water and causes significant reduction in the interaction between adjacent  $[Ca_2Nb_3O_{10}]^-$  perovskite blocks to the extent that the blocks become independent of each other. In contrast to the structure of other types of nanosheets<sup>3</sup> such as BN or  $MoS_2$  where the delaminated structure is charge neutral,  $[TBA_xH_{1-x}]^+[Ca_2Nb_3O_{10}]^-$  nanosheets have a “two component” structure with the delaminated sheet consisting of a  $[Ca_2Nb_3O_{10}]^-$  block with a layer of charge compensating cationic ligands around it (Figure 5.2.1b). These nanosheets have been suggested as possible candidates for various types of applications.<sup>2, 9-18</sup> Sasaki and co-workers proposed the use of them as ultrathin dielectrics.<sup>2, 13, 18,10,17,16</sup> The group of Osterloh has demonstrated the photochemical water splitting capability of  $[TBA_xH_{1-x}]^+[Ca_2Nb_3O_{10}]^-$  nanosheets<sup>11</sup> and investigated the redoxactive sites by photolabeling.<sup>19</sup> They also showed that high angle annular dark field - scanning transmission electron microscopy (HAADF-STEM) is an excellent tool for characterizing the nanosheets loaded with metal and metal oxide nanoparticles.<sup>19</sup> In addition, they used the sheets as an electron transport layer in solution-processed multi-junction polymer solar cells.<sup>14</sup> The group of Ishihara showed a high photocatalytic activity of Rh-doped calcium niobate nanosheets for  $H_2$  production from the water / methanol system without catalyst loading,<sup>12</sup> while a co-catalyst was necessary for their N-doped nanosheets which than also exhibited excellent photocatalytic properties<sup>20</sup>. In other research studies, several functional multilayers and superlattices were constructed by sequential deposition of  $[TBA_xH_{1-x}]^+[Ca_2Nb_3O_{10}]^-$  and other nanosheets.<sup>10, 15</sup>

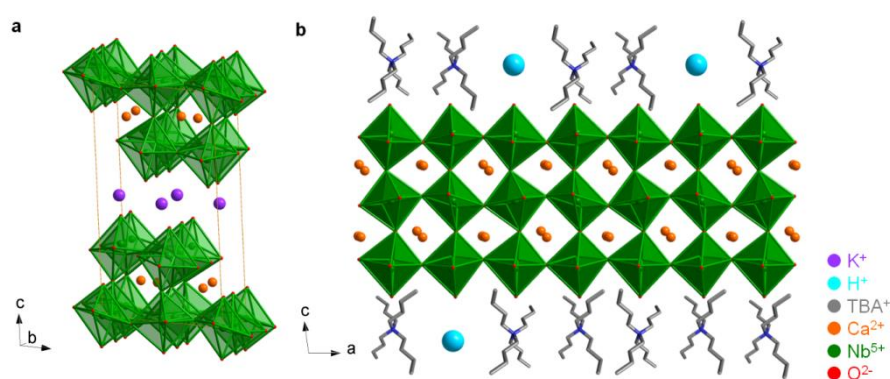


**Figure 5.2.1:**  $KCa_2Nb_3O_{10}$  has a layered structure (a) with parallel planes of  $K^+$  ions sandwiched between perovskite blocks consisting of corner-sharing  $NbO_6$  octahedra (illustrated in green with red oxygen atoms at the apex and Nb atoms in the centre), filled with  $Ca^{2+}$  ions on the A site positions.  $[TBA_xH_{1-x}]^+[Ca_2Nb_3O_{10}]^-$  nanosheets (b) have a structure derived from  $KCa_2Nb_3O_{10}$  where the  $K^+$  ions are replaced by bulky  $TBA^+$  and protons for charge balance.

In light of such intense research activities, it is important to understand the electronic properties of these nanosheets, the band gap in particular. Compton *et al.*<sup>11</sup> determined the optical band gap and found a value of 3.53 eV, whereby the exfoliated material was dried and studied by means of diffuse reflectance measurements. Akatsuka *et al.* investigated<sup>21</sup> the electronic structure of  $[TBA_xH_{1-x}]^+[Ca_2Nb_3O_{10}]^-$  nanosheet films (number of layers between 1 and 10) deposited on an indium-tin-oxide coated glass. They determined an optical band gap of 3.44 eV for the nanosheets using photocurrent measurements upon ultraviolet illumination and assuming an indirect semiconducting character.<sup>21</sup> In both studies the obtained optical band gap values were determined macroscopically and found to be larger than the one reported in literature for the parent bulk  $KCa_2Nb_3O_{10}$  phase of 3.35 eV which was determined in an early study *via* diffuse reflectance spectroscopy.<sup>22</sup> Thus, to facilitate a better comparison of the obtained band gap values it would be beneficial to use a technique that allows for the detection of individual nanosheets and to use the same technique and ideally same equipment for the nanosheet and bulk measurements in order to minimize e.g. systematic calibration artefacts. One of such techniques can be VEELS in STEM.<sup>23,24</sup>

With the development of commercially available monochromators in recent years, VEELS has become an interesting approach for determining band gaps in S/TEM with a high spatial resolution.<sup>25-28,29,30,31</sup> Gu and co-workers have demonstrated<sup>25</sup> the applicability of this method for bulk Si and GaN thin films. Erni and Browning<sup>28</sup> successfully used the technique to determine the size-dependent band gap of CdSe quantum dots. Park *et al.*<sup>26</sup> and Dennenwaldt *et al.*<sup>30</sup> measured the band gap of amorphous  $SiO_2$  thin films and nanotubes, respectively. Kuykendall *et al.*<sup>27</sup> applied the technique for measuring the band gaps of individual InGaN nanowires with different atomic ratios while Keller *et al.* studied  $Cu(In,Ga)Se_2$  thin solar cells<sup>29</sup>. Jiang and Spence investigated  $ZrSiO_4$  and  $ZrO_2$  bulk ceramics and discussed the effect of surface excitations on band gap values determined by VEELS.<sup>31</sup> In the present work, we demonstrate that we can determine the band gap of beam sensitive  $[TBA_xH_{1-x}]^+[Ca_2Nb_3O_{10}]^-$  nanosheets using VEELS which we shall compare with our findings about bulk  $KCa_2Nb_3O_{10}$ .<sup>32</sup> We describe in detail the acquisition procedure which is necessary to prevent artefacts due to radiation damage. Similar to King *et al.*<sup>33</sup> who used optical absorption data to calculate the band gap of bulk  $In_2O_3$ , we distinguish in the following between the “fundamental gap” (which is the energy position where the first transition occurs) and the “optical gap” (where a significant intensity is measured in the VEELS or the UV-Vis data). The results obtained by VEELS are discussed in light of the band structure and compared to the results of UV-Vis measurements performed on a macroscopic scale. An important finding is that for our calcium niobate perovskite the fundamental as well as optical band gap values are not changed significantly when going from the 3D to the 2D structure.

## 5.2.2 Experimental Section

### EXPERIMENTAL PROCEDURES:

**Synthesis of  $[TBA_xH_{1-x}]^+ [Ca_2Nb_3O_{10}]^-$  nanosheets.** The parent bulk material  $KCa_2Nb_3O_{10}$  was synthesized in a method similar to that proposed by Jacobson and co-workers<sup>7</sup> whereby a stoichiometric mixture of commercially available  $K_2CO_3$  (Merck, >99% purity),  $CaCO_3$  (Grüssing GmbH Germany, 99 % purity) and  $Nb_2O_5$  (Alfa Aesar, 99.5 % purity) with a 10% molar excess of  $K_2CO_3$  was thoroughly ground, mixed and fired to a temperature of 1200°C for 60 h.  $KCa_2Nb_3O_{10}$  has a layered structure, as shown in Figure 5.2.1a, containing layers of K and Ca atoms along with layers of edge-sharing  $NbO_6$  octahedra. For nanosheet synthesis a methodology similar to that proposed by Ebina *et al.* was used.<sup>18</sup>  $KCa_2Nb_3O_{10}$  (1 g) was treated with 5M  $HNO_3$  (40 cm<sup>3</sup>) for 4 days with daily renewal of the acid for conversion to the protonic oxide  $HCa_2Nb_3O_{10} \cdot 1.5H_2O$ . The product was recovered by filtration, washed with water and air-dried. For exfoliation into nanosheets  $HCa_2Nb_3O_{10} \cdot 1.5H_2O$  (0.2 g) was dispersed in 50 cm<sup>3</sup>  $TBAOH \cdot 30$ -hydrate (Sigma-Aldrich, 98% purity) aqueous solution at a molar ratio of 1:1. The solution was shaken for 4 weeks and non-dispersed solid removed via centrifugation at 3000 rpm.

### CHARACTERIZATION:

**ICP-AES and AFM.** The chemical composition was measured by inductive coupled plasma-atomic emission spectroscopy (ICP-AES) and revealed a value of  $x \approx 0.8$  for  $[TBA_xH_{1-x}]^+ [Ca_2Nb_3O_{10}]^-$ .<sup>15</sup> Atomic force microscopy (AFM) measurements were performed on the diluted suspension of nanosheets allowed to dry on a silicon substrate using an Asylum MFP-3D Stand Alone AFM microscope (Asylum Research, Santa Barbara, CA). A Si micro cantilever (300 Hz resonant frequency and 26.1 N/m spring constant) was used and images taken in tapping mode.

**TEM-(V)EELS.** For TEM studies the resulting colloidal suspension was diluted 4 times with water and drop coated onto lacey carbon coated Cu grids. TEM investigations were performed using a FEI TITAN 80-300 STEM (operated at 300 keV) equipped with a field emission gun, a Wien-type monochromator and Gatan Tridiem 866 energy filter having a 2k x 2k CCD camera. For all spectroscopy measurements, STEM mode was used with convergence and collection angles of 9.5 mrad each. For VEELS measurements a spectrometer dispersion of 0.02 eV/channel was chosen whereas for the core-loss EELS measurements a dispersion of 0.2 eV/channel was used. The full width at half maximum (FWHM) for the VEELS measurements was 0.20 eV.

To obtain a good signal-to-noise ratio (SNR) in the VEELS data we followed a two-fold path reported in literature.<sup>34</sup> Five spectra were acquired within five seconds of irradiation

(acquisition time 0.01 s each) spanning the energy range -5 eV to + 35 eV such that they contained the complete zero-loss peak (ZLP) and also the plasmon excitation. These five spectra were aligned, summed into a single spectrum and the position of the plasmon peak was determined. This procedure was repeated fifteen times to determine the position of the plasmon with an accuracy of  $\pm 0.2$  eV. In the next step, we acquired spectra spanning the energy range +1.5 eV to 41 eV such that they contained the tail of the ZLP on the positive side and also the plasmon excitation. Five spectra acquired in this way within the first five seconds of irradiation (acquisition time 0.64 s each) were summed up to obtain a better SNR. This spectrum was calibrated according to the position of the plasmon peak determined previously. The calibrated spectrum was used for band gap determination. For the fundamental gap the value was taken where the intensity was just above the baseline. To determine the optical gap value, we performed a linear fit to the low loss region with a strong intensity increase and used the value of the first intersection with the baseline.

**UV-Vis.** The optical band gap values of the sheets and the parent bulk material  $\text{KCa}_2\text{Nb}_3\text{O}_{10}$  were also determined on a macroscopic scale by diffuse reflectance spectroscopy. The spectra were acquired at room temperature with a UV-Vis-NIR diffuse reflectance spectrometer (Agilent Technologies, Cary 5000) at a wavelength range of 200-800 nm. Samples were studied as powders using a carrier system with a quartz glass window at the edge of the integrating sphere and using  $\text{BaSO}_4$  as an optical standard. The nanosheets were separated by centrifugation (speed of 20000 rpm), the supernatant removed and the pellet dried at  $100^\circ\text{C}$ . From the reflectance data  $R$  the Kubelka–Munk remission function  $F(R) = (1-R)^2/2R$  was calculated for both the nanosheet as well as the bulk.<sup>35, 36</sup> For a semiconductor with a direct band gap  $F(R)^2 \sim (E-E_g)$  while for an indirect semiconductor  $F(R)^{0.5} \sim (E-E_g)$ .<sup>37</sup> Our density functional theory (DFT) calculations of the parent bulk material  $\text{KCa}_2\text{Nb}_3\text{O}_{10}$  have revealed direct transitions<sup>32</sup> and preliminary DFT results of the sheets indicate that the direct semiconductor character is retained. Thus, Tauc-plots were obtained by plotting  $(F(R)h\nu)^2$  versus the photon energy, the linear part of the curve was extrapolated to the baseline and the optical band gap was extracted from the value of intersection.<sup>38</sup> For the fundamental gap we used the value where  $(F(R)h\nu)^2$  is above the baseline.

### 5.2.3. Results and Discussion

AFM images reveal that the nanosheets are a few hundreds of nanometers to a few microns in lateral dimension and they tend to stack one above the other when dried on the substrate to form regions of multiple sheets (Figure 5.2.2). AFM height profiles indicated jumps in height of about 3.4 nm between the substrate and the single sheet regions. For subsequent steps however, the increase in height is a little less ( $\sim 2.9$  nm) when one moves from one sheet to the next. The thickness of the sheets is larger than the values reported in the

literature which range between 1.85 and 3.0 nm as determined by AFM<sup>19, 21, 39</sup>. Schaak and Mallouk<sup>9</sup> synthesized  $[TBA_xH_{1-x}]^+[Ca_2Nb_3O_{10}]^-$  nanosheets and measured a  $[TBA]^+$  concentration of  $\sim 0.15$ - $0.20$  whereas the  $[TBA]^+$  concentration in our sheets is higher ( $\sim 0.8$ ), as indicated by ICP-AES data.<sup>15</sup> A height of 1.85 nm was observed by Li *et al.*<sup>10</sup> using AFM under vacuum conditions. Okamoto *et al.*<sup>12</sup> synthesized 3% Rh-doped calcium niobate nanosheets (Rh atoms replacing Nb atoms in the nanosheet) and found a height of 2.8-3.0 nm by AFM, which was attributed to adsorption of water and amine on the nanosheet surface.<sup>12</sup> We conclude that the observed higher thickness of our sheets is due to a higher  $[TBA]^+$  concentration as well as hydration under ambient conditions (AFM measurements were carried out in air and at atmospheric pressure).

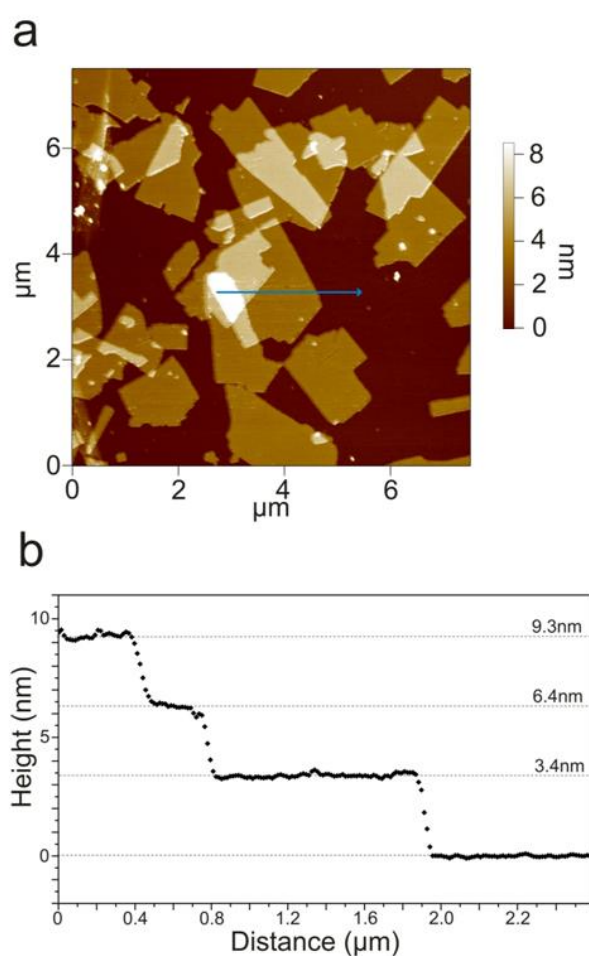


**Figure 5.2.2:** AFM image (a) of the  $[TBA_xH_{1-x}]^+[Ca_2Nb_3O_{10}]^-$  nanosheets dispersed on a Si wafer, which indicates lateral sizes of the order of a few hundred nanometers. Height profile (b) acquired along the arrow shown in (a) depicts the height of a single nanosheet to be 3.4 nm and that of each subsequent sheet in a stack about 2.9 nm.

HAADF-STEM investigations reveal that the perovskite nanosheets are a few hundreds of nanometer up to a few microns in lateral dimension (Figure 5.2.3), which is in agreement with

the AFM measurements. The HAADF-STEM images show dark regions which we classify as vacuum regions (regions without material). This was confirmed by EEL spectra acquired in the dark regions, where the intensity in the low-loss region (1.5-42 eV) was within the noise level indicating absence of any matter.

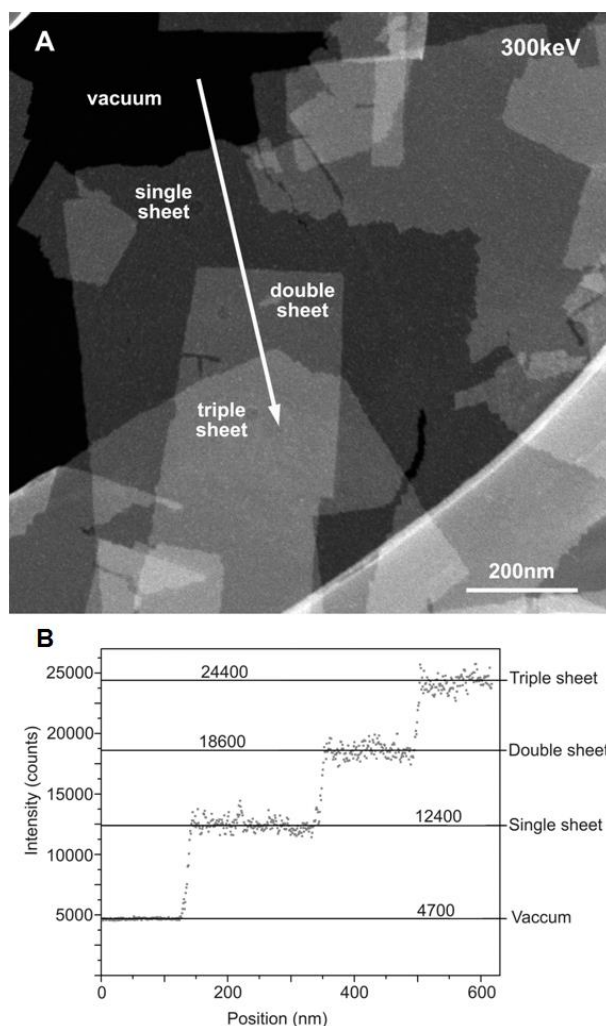


**Figure 5.2.3:** HAADF-STEM image (a) shows dark regions representing vacuum and regions with progressively increasing intensity indicating single, double and triple sheets. The intensity profile (b) along the arrow shown in (a) indicates quantum jumps of intensity when one moves from one sheet to another.

HAADF intensity profiles which are related to mass-thickness contrast<sup>23</sup> show quantum jumps in intensity (Figure 5.2.3), which are attributed to the nanosheets, which are stacked one above the other. Regions where two sheets overlap (labeled double sheets), as well as triple or multiple sheet stacks were observed. The first jump in intensity from vacuum to the region of a single nanosheet (7700 counts) is greater than the following intensity jumps from one sheet to the next sheet (~6000 counts). On the basis of AFM and STEM-HAADF intensity profiles, one can conclude that the ligands in the region between two  $[\text{Ca}_2\text{Nb}_3\text{O}_{10}]^-$

layers are more closely packed compared to the ligand layer shell surrounding a single sheet leading to a larger thickness.

The  $[TBA_xH_{1-x}]^+[Ca_2Nb_3O_{10}]^-$  nanosheets are highly crystalline as observed by high-resolution transmission electron microscopy (HRTEM). An exemplary HR-TEM image from a single sheet along with its fast Fourier transform (FFT) is shown in Figure 5.2.4a. The observed  $d$ -values of about 3.9 Å match well with the interplanar Nb-Nb distances<sup>40</sup> of 3.93 Å and 3.86 Å, respectively, in  $KCa_2Nb_3O_{10}$ . In the case of a double sheet region Moiré fringes appear in the HR-TEM images indicating the presences of two crystals slightly rotated with respect to each other, which is further supported by the corresponding FFT (Figure 5.2.4b). This suggests that two subsequent nanosheets have negligible interaction between them, which is in agreement with the findings by Akatsuka *et al.* based on photocurrent measurements of  $[Ca_2Nb_3O_{10}]^-$  nanosheets.<sup>21</sup>

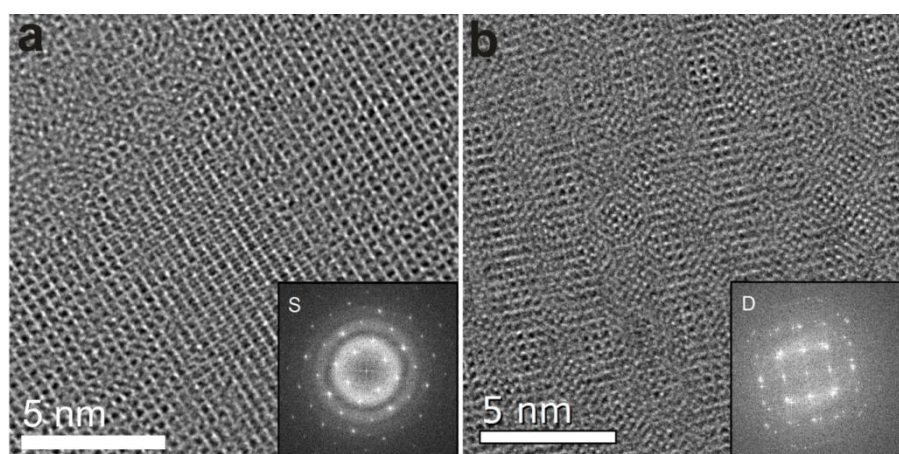


**Figure 5.2.4:** HR-TEM images acquired from a single sheet (a) and double sheet (b) highlight the highly crystalline nature of the sheet as substantiated by the FFTs shown in the insets labeled S for single sheet and D for double sheet.

Core-loss EELS measurements were performed to obtain further insights into the bonding characteristics, oxidation state of the individual atoms and chemical composition of a single nanosheet. The scattering cross section for core-loss excitations is typically several orders of magnitude less than that for the valence loss excitations,<sup>41</sup> hence to obtain a reasonable signal from a very thin specimen region, a larger acquisition time is required. EEL spectra were acquired in STEM mode cumulatively with an overall acquisition time of 10 s. As will be shown below, in that time frame the sheet structure can decay due to irradiation, however the measurements still allowed to obtain compositional information, as decomposition induced loss of crystallinity and carbon contamination, but insignificant changes in the elemental ratios. Core-loss EEL spectra of the parent bulk  $KCa_2Nb_3O_{10}$  phase are used for comparison. The EEL spectrum acquired from a single nanosheet, shown in the top of Figure 5.2.5, illustrates the various edges. A comparison with literature allows identifying the edge onsets



as follows: 240 eV, Nb-M<sub>4,5</sub> edge;<sup>42-43</sup> 284 eV, C-K edge;<sup>42</sup> 346 eV, Ca-L<sub>2,3</sub> edge;<sup>44</sup> 363 eV, Nb-M<sub>2,3</sub> edge;<sup>43</sup> and 532 eV, O-K edge<sup>42</sup>. The [TBA]<sup>+</sup> ions have a composition of [C<sub>16</sub>H<sub>36</sub>N]<sup>+</sup> which implies a very low atomic percentage of N in the overall nanosheet structure. Conforming to this fact, we are hardly able to detect a signal for the N-K edge around 401 eV. The EEL spectrum of bulk KCa<sub>2</sub>Nb<sub>3</sub>O<sub>10</sub> (acquired in diffraction mode<sup>32</sup>) shows the K-L<sub>2,3</sub> edge instead of the C-K edge seen in the nanosheet. This further confirms that during exfoliation nearly all of the K<sup>+</sup> is replaced by [TBA]<sup>+</sup> ions which contribute to the C-K edge signal. We did not observe a chemical shift or change in the shape of the energy loss-near edge structure (ELNES) of the element specific ionization edges of the nanosheet compared to the bulk. This indicates that the valence state and type of bonding within the nanosheet remains similar as in the bulk, e.g Ca<sup>2+</sup> and Nb<sup>5+</sup>.

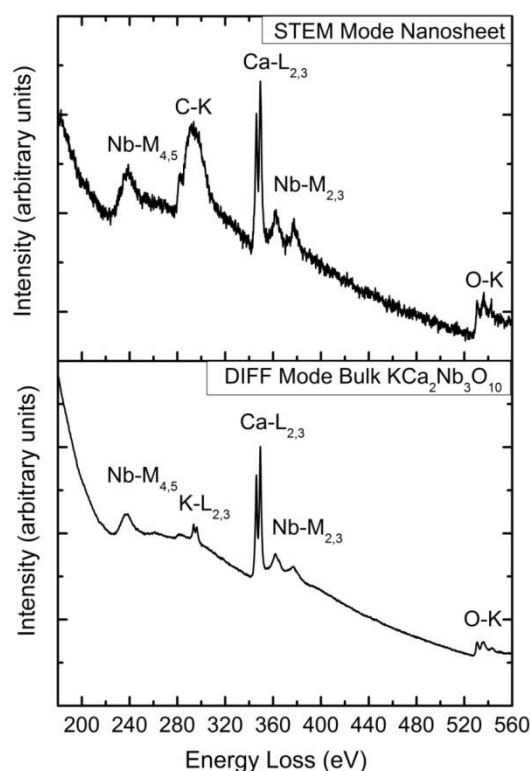


**Figure 5.2.5:** Core-loss EEL spectrum (a) of [TBA<sub>x</sub>H<sub>1-x</sub>]<sup>+</sup>[Ca<sub>2</sub>Nb<sub>3</sub>O<sub>10</sub>]<sup>-</sup> nanosheets acquired in STEM mode and (b) of bulk KCa<sub>2</sub>Nb<sub>3</sub>O<sub>10</sub> acquired in diffraction mode.

To determine the band gap of the nanosheets, it was necessary to identify a single sheet region, which we were able to do by using the STEM-HAADF intensity profile. Second, to obtain high spatial resolution, spectra had to be acquired with a small stationary spot positioned on the nanosheet. However, a hybrid nanostructure when irradiated with 300 kV electrons at a stationary spot of diameter < 1 nm could disintegrate. As such, before making



a comprehensive set of measurements, understanding the possible degradation of the material under the acquisition conditions is crucial. To this end we acquired 50 spectra at a rate of 1 acquisition per second, irradiating a spot on a single sheet region. The successive VEEL spectra are depicted in Figure 5.2.6 and illustrate a change in the state of the sample as it is (carbon) contaminated and damaged due to the electron beam. We found that there is no significant difference between the spectra acquired within the first five seconds; hence we assumed that there was no apparent damage to the nanosheet in the first five seconds of irradiation. Furthermore, we imaged a single sheet region after five seconds of irradiation and found no perceivable damage. As such, all VEEL spectra used for analysis were acquired within the first five seconds of irradiation with a stationary electron beam.

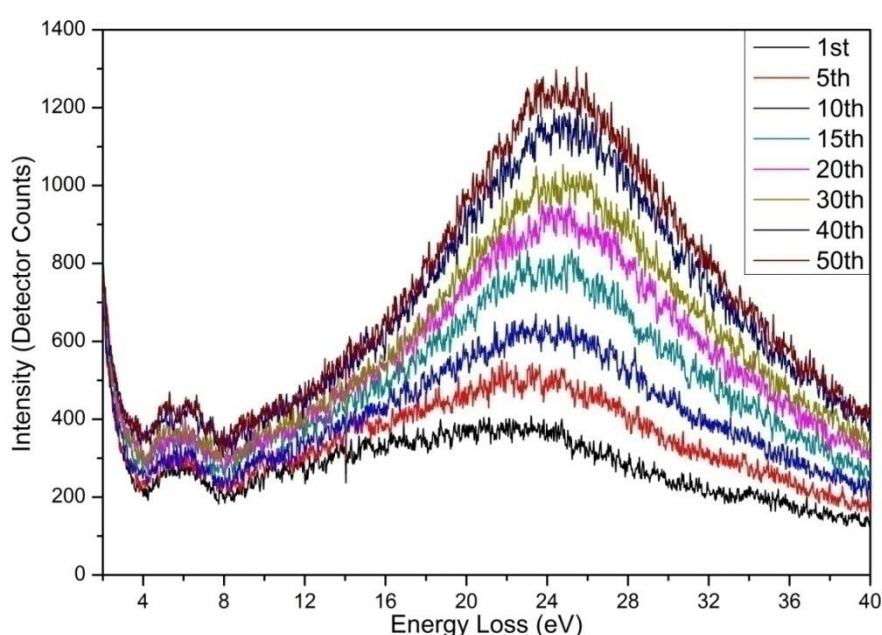


**Figure 5.2.6:** Deterioration of the nanosheets with time is exemplified by the change in the VEEL spectra showing the spectra acquired after one, five, ten, fifteen, twenty, thirty, forty and fifty seconds of irradiation under the electron beam.

Nanostructures by virtue of their small sizes have a very small double differential scattering cross-section, and as such the intensity of their valence loss excitations in the VEEL spectrum is very low (Figure 5.2.7a). A closer look at the valence loss (inset in Figure 5.2.7a) shows that the intensity of the valence loss excitations is three orders of magnitude less than that of the ZLP. Consequentially it was practically impossible to obtain a better SNR when the ZLP and the valence loss excitations are acquired in the same spectrum. Therefore we used the two-fold path<sup>34</sup> as described in detail above. The sum of five spectra acquired with the complete ZLP and the plasmon excitation were used to determine the position of the plasmon peak. The high noise level of the plasmon peak limited the accuracy to  $\pm 0.2$  eV (Figure 5.2.7a). A second set of five spectra were acquired containing the tail of the ZLP on

the positive side and also the plasmon region, summed up and calibrated according to the position of the plasmon peak from the other data set. The resulting spectrum has a good SNR as illustrated in the Figure 5.2.7b and was used for band gap determination for a single sheet region. The process was repeated for acquiring the VEEL spectra from double and triple sheet regions.

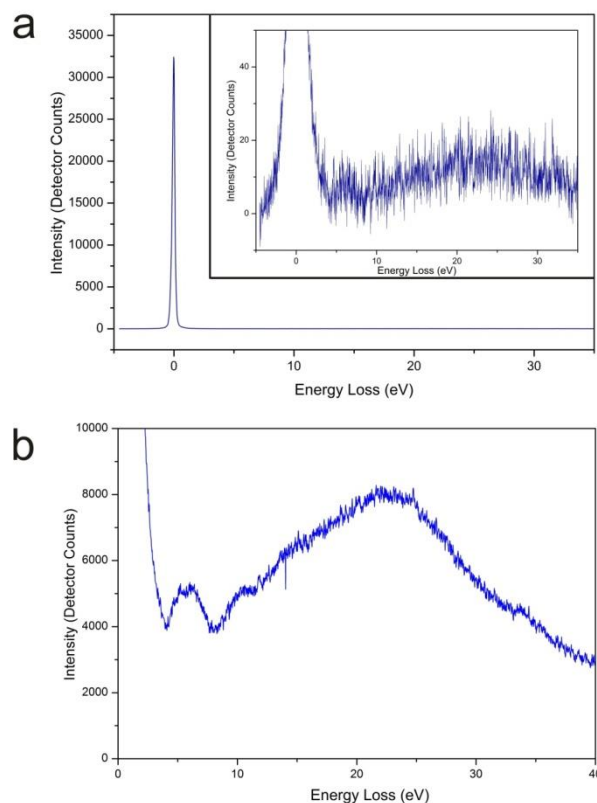


**Figure 5.2.7:** VEEL spectrum acquired from a single sheet (a) show very little signal for valence loss excitations as exemplified by the magnified view in the inset (a). When a separate spectrum is acquired for the valence excitations (b) alone, a better signal to noise ratio can be obtained.

The conduction band onset can be determined from a VEEL spectrum upon careful subtraction of the ZLP.<sup>28, 45</sup> In our data, the tails of the ZLP are noisy, and therefore subtracting a spectrum acquired in vacuum as an approximation to the ZLP could be counterproductive. Hence, instead we subtracted the tail of the ZLP by describing it with a power-law function similar to Erni and Browning.<sup>28</sup> However, we did not use a Lorentzian fit to the first derivative to determine the onset, but rather we determined the fundamental band gap by directly measuring the onset of the ZLP subtracted spectrum. Because of the nano dimensions of the structures investigated, the probability of multiple scattering is negligible; hence we did not apply any deconvolution routine to the VEEL spectrum.

ZLP-subtracted VEEL spectra from the single, double and triple sheets are presented in Figure 5.2.8a. The fundamental conduction band onset for the single, double and triple sheet

regions is the same and amounts to  $3.0 \pm 0.2$  eV whereby the error is governed by the alignment procedure described above, i.e. determining the plasmon peak position in the individual noisy spectra. As can be seen in the close-up in Figure 5.2.8 b, above the fundamental gap a low intensity region occurs followed by a strong increase in intensity. The low intensity at the beginning is related to the low density of states in this regime as revealed in our DFT calculation for the bulk phase<sup>32</sup> and in preliminary calculations of the nanosheets. Dipole forbidden transitions and weak (optical) transition matrix elements are most likely responsible for this low signal, which is also observed for the bulk phase (Figure 5.2.8 d) similar to the results discussed by King *et al.*<sup>33</sup> for bulk  $\text{In}_2\text{O}_3$ . The fundamental gap for the bulk phase is  $3.2 \pm 0.1$  eV as we have reported previously.<sup>32</sup> Besides the fundamental gap remaining essentially unchanged when going from the 3D structure to the nanosheet, the same holds true for the optical gap determined by VEELS, where we found values of  $3.8 \pm 0.2$  eV and  $3.9 \pm 0.1$  eV for the nanosheet and the parent bulk phase  $\text{KCa}_2\text{Nb}_3\text{O}_{10}$ , respectively (see Figure 5.2.8). All values are summarized in Table 5.2.1.

**Table 5.2.1:** Fundamental and optical band gap values determined *via* VEELS and UV-Vis diffuse reflectance data using the Tauc plot method.

	Fundamental gap (eV)		Optical gap (eV)	
	Sheet	Bulk	Sheet	Bulk
<b>VEELS</b>	$3.0 \pm 0.2$	$3.2 \pm 0.1$	$3.8 \pm 0.2$	$3.9 \pm 0.1$
<b>Tauc Plot</b>	$3.4 \pm 0.1$	$3.4 \pm 0.1$	$3.6 \pm 0.1$	$3.6 \pm 0.1$

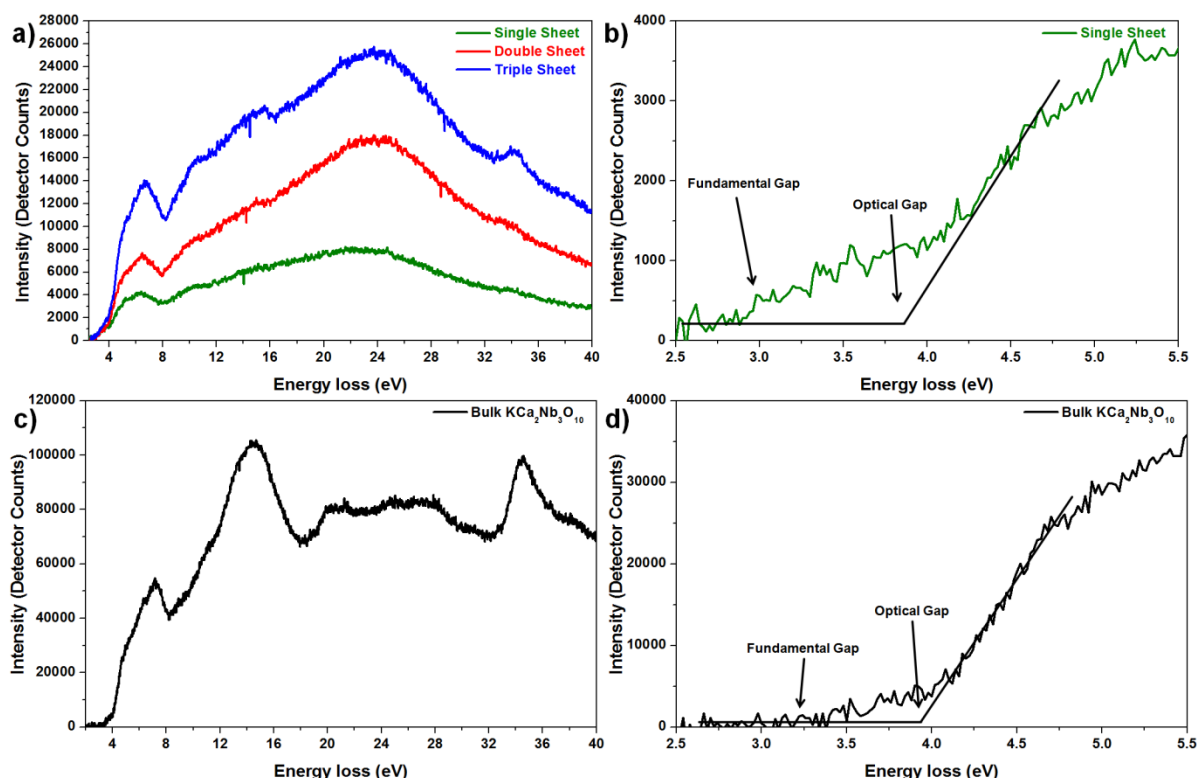


**Figure 5.2.8:** VEEL spectra after ZLP subtraction, acquired from single, double and triple sheet regions (a). (b) The close-up indicates a fundamental gap at  $3.0 \pm 0.2$  eV and a monotonic increase in the scattering cross section. The optical gap is located at  $3.8 \pm 0.2$  eV. The VEEL spectrum (c) of the bulk  $\text{KCa}_2\text{Nb}_3\text{O}_{10}$  after ZLP subtraction<sup>32</sup> shows clear similarities with that of the nanosheets, especially for the single electron valence excitations, while the plasmon region differs strongly. The close-up (d) was used to determine the fundamental and the optical gap.

The fact that the optical and fundamental band gap values are similar for the nanosheets and the bulk is also confirmed by UV-Vis diffuse reflectance measurements which are presented in Figure 5.2.9. The bandgap values estimated *via* Tauc plots (using  $(F(R)h\nu)^2$  as a function of the photon energy) yield a fundamental gap value of  $3.4 \pm 0.1$  eV and an optical gap of  $3.6 \pm 0.1$  eV for both the powder of turbostratically re-stacked nanosheets and the parent bulk phase  $\text{KCa}_2\text{Nb}_3\text{O}_{10}$  (Table 5.2.1). A similar discrepancy of around 0.2 eV for the optical gap values determined by VEELS and UV-Vis data was observed by Erni and Browning.<sup>28</sup> Most likely this is related to the fact that we did not normalize the absorption coefficient, resulting in an underestimation of band gap values using Tauc plots.<sup>35</sup> In addition calibration errors of our energy loss dispersion values can explain the difference between the UV-Vis and VEELS data. The higher value of the fundamental gap determined by UV-Vis diffuse reflectance data might be related to the uncertainties arising from the fact that we do not measure dipole forbidden transitions in the reflectance data but only those with a weak (optical) transition matrix element.<sup>33</sup>

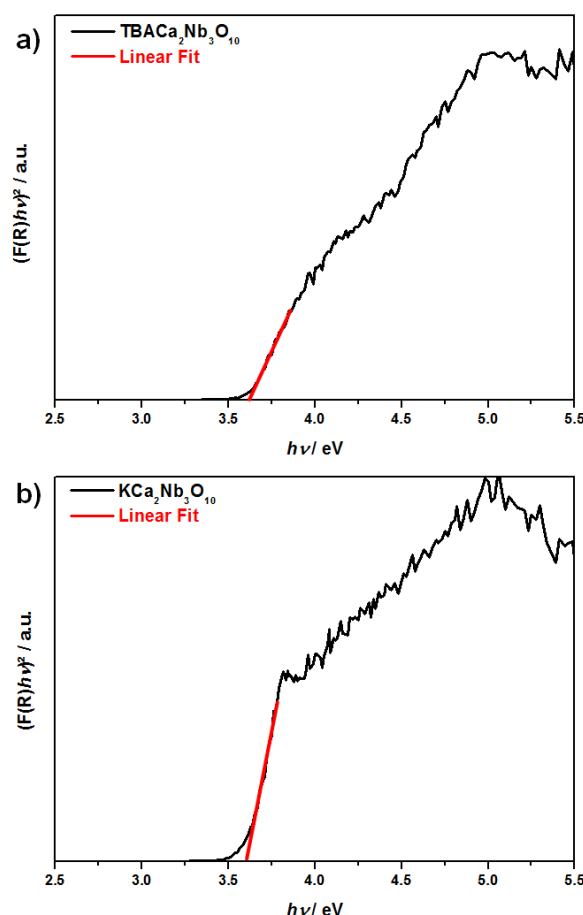


**Figure 5.2.9:** Tauc plots determined from UV-Vis reflectance data for a) dried re-stacked  $[TBA_xH_{1-x}]^+[Ca_2Nb_3O_{10}]^-$  nanosheets and b)  $KCa_2Nb_3O_{10}$  bulk. Assuming a direct semiconductor,  $(F(R)hv)^2$  was plotted against the photon energy. A linear extrapolation was used to determine the optical band gap which is  $3.6 \pm 0.1$  eV for both materials. The fundamental gap is located around  $3.4 \pm 0.1$  eV.

It is worthwhile comparing our band gap values determined by UV-Vis diffuse reflectance spectroscopy to the ones reported in the literature.<sup>11, 21-22</sup> Our optical band gap value for the nanosheets are slightly larger than the values of Compton *et al.*<sup>11</sup> and Akatsu *et al.*<sup>21</sup>. One reason for this is that the determined band gap values depend on the analysis routine and the photon energy region used for doing the linear fit procedure.<sup>33, 36, 38</sup> Furthermore, we assumed a direct semiconducting character as predicted by our DFT calculation, while Akatsu *et al.* assumed an indirect semiconductor for the Tauc plot analysis.<sup>21</sup> Besides this, the studied nanosheets might differ slightly in their chemical composition, as the ligand shell around the nanosheets is a mixture of protons and  $TBA^+$  cations with varying compositions, see above.<sup>11, 21</sup> In particular the different fitting routine and a different experimental setup used by Domen *et al.* might be responsible for the lower optical band gap value which they found for the bulk phase.<sup>22</sup> Since we applied the same type of spectrometer as well as

VEELS on the nanosheet and the bulk material, we are confident to conclude that the band gap is not strongly modified when going from the 3D to the 2D structure.

It is well known that the valence excitations in VEELS are not localized to specific atoms, but span larger regions partly because the valence electrons are delocalized.<sup>46-49</sup> For example, Couillard *et al.* showed that in nanostructured multilayered gate oxides, despite a small local probe confining to a single layer, the excitations due to interband transitions, interface plasmons and Cerenkov radiation due to multiple layers interfere, thereby making it hard to extract the signal due to a single layer from the stack.<sup>49</sup> In light of the above mentioned observation it is worth discussing the possible limit of our experimental methodology with regards to spatial resolution. Egerton described<sup>50</sup> the delocalization of an excitation with a parameter  $d_{50}$  such that 50% of the excitation events occur within a diameter  $d_{50}$ :

$$d_{50} \sim 0.8 \lambda \left[ \frac{E_0}{E} \right]^{3/4} \quad (\text{Eq. 5.2.1})$$

Here  $E_0$  is the energy of the primary electrons,  $E$  the energy at which the excitation occurs and  $\lambda$  the wavelength of the electrons. Using this relation we determine  $d_{50}$  to be about 9 nm. Surface plasmons are a collective excitation mode of the electrons at the surface. They can significantly contribute to the scattering cross-section in the case of nanostructures, as has been shown previously by Nelayah *et al.* for the case of Ag nanoprisms.<sup>51</sup> It has been suggested that surface plasmons can interfere with the valence loss excitations thereby making the extraction of the band gap difficult.<sup>52, 53</sup> As such it is necessary to check the possible implications of surface plasmon excitations to our band gap measurements. Surface plasmons are an important excitation mode when the sample is excited in so-called *aloof* condition, i.e. the beam in STEM mode is placed right outside the edge of the sample.<sup>54</sup> Such *aloof* measurements are often performed for nanostructures.<sup>46, 55-58</sup> The viability of this method is based on the fact that the valence loss excitations are delocalized<sup>46-47</sup> and as such a beam in *aloof* conditions (within a few nm from the edge) is able to trigger low energy valence loss excitations. Despite that, we did not observe a measureable signal above the noise level when we acquired VEEL spectra by placing the beam one nanometer off the sheet. A possible cause for this could be the  $[TBA]^+$  ligands which screen the electric field and hinder its effective penetration into the  $[Ca_2Nb_3O_{10}]^-$  layer. Determining the exact cause of the limited scattering cross section in *aloof* mode excitation for our nanosheets is beyond the scope of the present study and as such was not further investigated.

Cerenkov losses have also been reported<sup>52</sup> to be another hindrance to band gap measurements using VEELS, however, they become dominant only in thicker samples (thickness greater than 0.6 times the mean free path length) or for very small collection angles (few  $\mu$ rad).<sup>25</sup> Given that our measurements were done on regions only a few

nanometers thick using a collection angle of 9.5 mrad, the possibility of strong contributions due to Cerenkov radiation interfering in our measurements can be neglected.

The structural similarity between the  $[TBA_xH_{1-x}]^+[Ca_2Nb_3O_{10}]^-$  nanosheets and  $KCa_2Nb_3O_{10}$  makes it worth comparing the electronic structure between the two materials. Our DFT calculations<sup>32</sup> using the Tran-Blaha modified Becke Johnson potential (which predict band gaps with high accuracy<sup>59</sup>) suggest a fundamental band gap of 3.1 eV for  $KCa_2Nb_3O_{10}$  whereby the partial density of states contribution of K atoms to the valence and conduction bands adjacent to the band gap is negligible. The calculated fundamental gap value is in good agreement with the one obtained by VEELS measurements for bulk  $KCa_2Nb_3O_{10}$  which is  $3.2 \pm 0.1$  eV.<sup>32</sup> This indicates that removal of the K atoms during exfoliation does not change the fundamental band gap value significantly when considering the experimental error ( $3.0 \pm 0.2$  eV for the nanosheet versus  $3.2 \pm 0.1$  eV for the bulk). Similar arguments hold for the optical gap.

The Ca-M<sub>2,3</sub> edge at 34 eV<sup>42</sup> (representing the excitation of Ca-3p electrons into unoccupied levels) can be hardly identified in the VEEL spectra acquired from the single sheet (Figure 5.2.8). In spectra acquired from the triple sheet region, the Ca-M<sub>2,3</sub> edge becomes more pronounced and in the spectra acquired from the bulk  $KCa_2Nb_3O_{10}$  it becomes very intense. Furthermore one sees an increase in the intensity of the plasmon excitation which is expected on the basis of increase in the thickness as one moves from regions of single to double to triple sheet. The most distinguishable difference between the VEELS from nanosheets and the bulk material is the region between 18 and 30 eV. In the  $[TBA_xH_{1-x}]^+[Ca_2Nb_3O_{10}]^-$  nanosheets we observe a broad plasmon in this energy range, which has a greater scattering cross-section than that for single electron excitations. Given the structural similarity between the nanosheet and the bulk materials, the difference in VEELS would imply that the plasmon excitation in the nanosheets is predominantly contributed or modified by the ligand layer.

## 5.2.4 Conclusion

We have successfully demonstrated the use of STEM-VEELS for determining the band gap of  $[TBA_xH_{1-x}]^+[Ca_2Nb_3O_{10}]^-$  nanosheets with a high spatial resolution. These sheets are highly crystalline and have minimal interaction between the individual nanosheets when they stack on each other. The measured fundamental and optical band gap values of individual sheets are close to the band gap values of the bulk  $KCa_2Nb_3O_{10}$  phase and considered invariant within the range of experimental error. This is in accordance to UV-Vis reflectance data and might be also valid for other 2D materials obtained *via* intercalation – exfoliation from anisotropic bulk oxide phases. The measured band gap values provide insight into the electronic structure at high spatial resolution of about 9 nm. The sheets disintegrate within

five seconds under the electron beam bombardment, therefore to effectively determine the band gap fast acquisition is paramount. The valence electron excitations in the nanosheet are similar to that in the bulk  $\text{KCa}_2\text{Nb}_3\text{O}_{10}$  except for the strong plasmon excitation, most likely caused by the ligand layer.

In summary, STEM-VEELS presents a powerful tool for the extraction of local band gaps and as such will be a suitable method for a wide variety of nanostructures which are inaccessible to alternative techniques with typically low spatial resolution. The technique is able to probe also wide band gap semiconductors with thicknesses in the range of a few nanometers and without optical signatures in the visible range.

#### ACKNOWLEDGEMENTS:

This work was partially supported by the German Science Foundation (DFG) through the cluster of excellence Nanosystems Initiative Munich (NIM) and the Center for Nanoscience (CeNS). K.S.V. is grateful to the Elite Network of Bavaria for financial support. P.B. was supported by the SFB-F41 (ViCoM) project of the Austrian Science Funds (FWF). We thank B. Tuffy and K. Schwinghammer for UV-VIS measurements and R. Eicher for CHNS analysis.

#### 5.2.5 Bibliography

- [1] K. S. Novoselov, A. K. Geim, S. V. Morozov, D. Jiang, M. I. Katsnelson, I. V. Grigorieva, S. V. Dubonos, A. A. Firsov, *Nature* **2005**, 438, 197-200.
- [2] R. Ma, T. Sasaki, *Adv. Mater. (Weinheim, Ger.)* **2010**, 22, 5082-5104.
- [3] J. N. Coleman, M. Lotya, A. O'Neill, S. D. Bergin, P. J. King, U. Khan, K. Young, A. Gaucher, S. De, R. J. Smith, I. V. Shvets, S. K. Arora, G. Stanton, H.-Y. Kim, K. Lee, G. T. Kim, G. S. Duesberg, T. Hallam, J. J. Boland, J. J. Wang, J. F. Donegan, J. C. Grunlan, G. Moriarty, A. Shmeliov, R. J. Nicholls, J. M. Perkins, E. M. Grieveson, K. Theuwissen, D. W. McComb, P. D. Nellist, V. Nicolosi, *Science* **2011**, 331, 568-571.
- [4] K. S. Novoselov, D. Jiang, F. Schedin, T. J. Booth, V. V. Khotkevich, S. V. Morozov, A. K. Geim, *Proc. Natl. Acad. Sci. U. S. A.* **2005**, 102, 10451-10453.
- [5] R. J. Smith, P. J. King, M. Lotya, C. Wirtz, U. Khan, S. De, A. O'Neill, G. S. Duesberg, J. C. Grunlan, G. Moriarty, J. Chen, J. Wang, A. I. Minett, V. Nicolosi, J. N. Coleman, *Adv. Mater. (Weinheim, Ger.)* **2011**, 23, 3944-3948.
- [6] M. Dion, M. Ganne, M. Tournoux, *Mater. Res. Bull.* **1981**, 16, 1429-1435.
- [7] A. J. Jacobson, J. W. Johnson, J. T. Lewandowski, *Inorg. Chem.* **1985**, 24, 3727-3729.
- [8] M. M. J. Treacy, S. B. Rice, A. J. Jacobson, J. T. Lewandowski, *Chem. Mater.* **1990**, 2, 279-286.



- [9] R. E. Schaak, T. E. Mallouk, *Chem. Mater.* **2000**, *12*, 2513-2516.
- [10] B.-W. Li, M. Osada, T. C. Ozawa, Y. Ebina, K. Akatsuka, R. Ma, H. Funakubo, T. Sasaki, *ACS Nano* **2010**, *4*, 6673-6680.
- [11] O. C. Compton, E. C. Carroll, J. Y. Kim, D. S. Larsen, F. E. Osterloh, *J. Phys. Chem. C* **2007**, *111*, 14589-14592.
- [12] Y. Okamoto, S. Ida, J. Hyodo, H. Hagiwara, T. Ishihara, *J. Am. Chem. Soc.* **2011**, *133*, 18034-18037.
- [13] M. Osada, T. Sasaki, *Adv. Mater. (Weinheim, Ger.)* **2012**, *24*, 210-228.
- [14] L. Chang, M. A. Holmes, M. Waller, F. E. Osterloh, A. J. Moule, *J. Mater. Chem.* **2012**, *22*, 20443-20450.
- [15] C. Ziegler, S. Werner, M. Bugnet, M. Worsching, V. Duppel, G. A. Botton, C. Scheu, B. V. Lotsch, *Chem. Mater.* **2013**, *25*, 4892-4900.
- [16] Y.-H. Kim, H.-J. Kim, M. Osada, B.-W. Li, Y. Ebina, T. Sasaki, *ACS Appl. Mater. Interfaces* **2014**, *6*, 19510-19514.
- [17] B.-W. Li, M. Osada, Y. Ebina, K. Akatsuka, K. Fukuda, T. Sasaki, *ACS Nano* **2014**, *8*, 5449-5461.
- [18] Y. Ebina, T. Sasaki, M. Watanabe, *Solid State Ionics* **2002**, *151*, 177-182.
- [19] E. M. Sabio, M. Chi, N. D. Browning, F. E. Osterloh, *Langmuir* **2010**, *26*, 7254-7261.
- [20] S. Ida, Y. Okamoto, S. Koga, H. Hagiwara, T. Ishihara, *RSC Advances* **2013**, *3*, 11521-11524.
- [21] K. Akatsuka, G. Takanashi, Y. Ebina, M.-a. Haga, T. Sasaki, *J. Phys. Chem. C* **2012**, *116*, 12426-12433.
- [22] K. Domen, J. Yoshimura, T. Sekine, A. Tanaka, T. Onishi, *Catal. Lett.* **1990**, *4*, 339-343.
- [23] C. B. C. D. B. Williams, *Transmission Electron Microscopy, A Textbook for Materials Science*, Springer Science + Business Media, New York, **2009**.
- [24] D. A. Muller, *Nat. Mater.* **2009**, *8*, 263-270.
- [25] L. Gu, V. Sroog, W. Sigle, C. Koch, P. van Aken, F. Scholz, S. B. Thapa, C. Kirchner, M. Jetter, M. Rühle, *Phys. Rev. B* **2007**, *75*, 195214.
- [26] J. Park, S. Heo, J.-G. Chung, H. Kim, H. Lee, K. Kim, G.-S. Park, *Ultramicroscopy* **2009**, *109*, 1183-1188.
- [27] T. Kuykendall, P. Ulrich, S. Aloni, P. Yang, *Nat. Mater.* **2007**, *6*, 951-956.
- [28] R. Erni, N. D. Browning, *Ultramicroscopy* **2007**, *107*, 267-273.
- [29] D. Keller, S. Buecheler, P. Reinhard, F. Pianezzi, D. Pohl, A. Surrey, B. Rellinghaus, R. Erni, A. N. Tiwari, *Microsc. Microanal.* **2014**, *20*, 1246-1253.
- [30] T. Dennenwaldt, J. Ciston, U. Dahmen, W. Y. Ching, F. J. Pucher, W. Schnick, C. Scheu, *Microsc. Microanal.* **2014**, *20*, 664-670.

- [31] N. Jiang, J. C. H. Spence, *Ultramicroscopy* **2013**, 134, 68-76.
- [32] K. S. Viridi, Y. Kauffmann, C. Ziegler, P. Ganter, B. V. Lotsch, W. D. Kaplan, P. Blaha, C. Scheu, *Phys. Rev. B* **2013**, 87, 115108.
- [33] P. D. C. King, T. D. Veal, F. Fuchs, C. Y. Wang, D. J. Payne, A. Bourlange, H. Zhang, G. R. Bell, V. Cimalla, O. Ambacher, R. G. Egdell, F. Bechstedt, C. F. McConville, *Phys. Rev. B* **2009**, 79, 10.
- [34] H. Müllejans, R. French, *J. Phys. D: Appl. Phys.* **1996**, 29 1751–1760.
- [35] Z. Chen, H. N. Dinh, E. Miller, in *Photoelectrochemical Water Splitting - Standards, Experimental Methods, and Protocols*, Springer, New York Heidelberg Dordrecht London, **2013**.
- [36] S. P. Tandon, J. P. Gupta, *Phys. Status Solidi B* **1970**, 38, 363-367.
- [37] M. S. Dresselhaus, *Solid State Physics Part II Optical Properties of Solids*, **2001**.
- [38] D. L. Wood, J. Tauc, *Phys. Rev. B* **1972**, 5, 3144-3151.
- [39] M. Osada, T. Sasaki, *J. Mater. Chem.* **2009**, 19, 2503-2511.
- [40] T. Tokumitsu, K. Toda, T. Aoyagi, D. Sakuraba, K. Uematsu, M. Sato, *J. Ceram. Soc. Jpn.* **2006**, 114, 795-797.
- [41] R. Brydson, *Electron Energy Loss Spectroscopy*, Tylor and Francis, Oxon, United Kingdom, **2006**.
- [42] O. L. K. C. C. Ahn, R. P. Burgner, M. M. Disko, P. R. Swann *EELS Atlas*, HREM Facility, Arizona State University, Tempe, Arizona, **1983**.
- [43] D. Bach, R. Schneider, D. Gerthsen, J. Verbeeck, W. Sigle, *Microsc. Microanal.* **2009**, 15, 505-523.
- [44] J. Fink, T. Müller-Heinzerling, B. Scheerer, W. Speier, F. U. Hillebrecht, J. C. Fuggle, J. Zaanen, G. A. Sawatzky, *Phys. Rev. B* **1985**, 32, 4899-4904.
- [45] J. Wang, Q. Li, C. Ronning, D. Stichtenoth, S. Müller, D. Tang, *Micron* **2008**, 39, 703-708.
- [46] F. J. García de Abajo, *Rev. Mod. Phys.* **2010**, 82, 209-275.
- [47] R. F. Egerton, *Electron Energy-Loss Spectroscopy in the Electron Microscope*, Springer Science + Business Media, New York, **2011**.
- [48] O. L. Krivanek, M. M. Disko, J. Taftø, J. C. H. Spence, *Ultramicroscopy* **1982**, 9, 249-254.
- [49] M. Couillard, M. Kociak, O. Stéphan, G. A. Botton, C. Colliex, *Phys. Rev. B* **2007**, 76, 165131.
- [50] R. F. Egerton, *Micron* **2003**, 34, 127-139.
- [51] J. Nelayah, M. Kociak, O. Stephan, F. J. Garcia de Abajo, M. Tence, L. Henrard, D. Taverna, I. Pastoriza-Santos, L. M. Liz-Marzan, C. Colliex, *Nat. Phys.* **2007**, 3, 348-353.

- [52] M. Stöger-Pollach, *Micron* **2008**, 39, 1092-1110.
- [53] N. Jiang, J. C. H. Spence, *Ultramicroscopy* **2013**, 134, 68-76.
- [54] M. R. S. Huang, R. Erni, H.-Y. Lin, R.-C. Wang, C.-P. Liu, *Phys. Rev. B* **2011**, 84, 155203.
- [55] R. Arenal, O. Stéphan, M. Kociak, D. Taverna, A. Loiseau, C. Colliex, *Phys.Rev. Lett.* **2005**, 95, 127601.
- [56] M. G. Walls, A. Howie, *Ultramicroscopy* **1989**, 28, 40-42.
- [57] P. M. Echenique, A. Howie, R. H. Ritchie, *Phys. Rev. Lett.* **1999**, 83, 658-658.
- [58] M. A. Itskovsky, H. Cohen, T. Maniv, *Phys. Rev. B* **2008**, 78, 045419.
- [59] F. Tran, P. Blaha, *Phys. Rev. Lett.* **2009**, 102, 226401.

## 6 Summary

A summary and connection of all topics covered in this PhD thesis is schematically depicted in Figure 6.1. Various layered TMOs were synthesized, analyzed and exfoliated into unilamellar nanosheets. The main investigated compound was a DJ type layered perovskite  $\text{KCa}_2\text{Nb}_3\text{O}_{10}$  that was exfoliated into  $[\text{TBA}_{1-y}\text{H}_y]^+[\text{Ca}_2\text{Nb}_3\text{O}_{10}]^-$  nanosheets *via* a common cation-proton exchange and subsequent treatment with *TBAOH* in aqueous solution. Density functional theory calculations showed that  $\text{KCa}_2\text{Nb}_3\text{O}_{10}$  is a direct band gap semiconductor with a fundamental band gap of  $E_g = 3.1$  eV (Chapter 5.1). The conduction band is dominated by the inner Nb  $t_{2g}$ -like states of the central  $\text{NbO}_6$  layer in the triple perovskite block motif and the valence band by the O-2p states. In accordance with these calculations, STEM-VEELS gave a band gap of  $E_g = 3.2 \pm 0.1$  eV for the layered bulk material and was therefore demonstrated to be an alternative analysis method for the determination of the band gap of semiconductor materials. On the basis of these findings, we showed that the band gap of individual  $[\text{TBA}_{1-y}\text{H}_y]^+[\text{Ca}_2\text{Nb}_3\text{O}_{10}]^-$  nanosheets is invariant within the experimental error in STEM-VEELS measurements as the partial density of states contribution of interlayer atoms and ligands to the upper valence and lower conduction band states adjacent to the band gap is negligible (Chapter 5.2).

$\text{KCa}_2\text{Nb}_3\text{O}_{10}$  and structurally related  $\text{RbCa}_2\text{Nb}_3\text{O}_{10}$  were the source for further substitution experiments. On the one hand, replacement of Ca by Pb in the bulk material and subsequent exfoliation lead to a decrease in band gap down to  $E_g = 2.6$  eV. Thus, visible-light sensitization of the material can be useful for photochemical water splitting (Chapter 3.1). The solid-solution  $\text{RbCa}_{2-x}\text{Pb}_x\text{Nb}_3\text{O}_{10}$  was not homogeneous as an additional phase with hypothetical composition “ $\text{RbNb}_3\text{O}_8$ ” started to form along with increasing lead content. HRTEM, SAED, Raman and ssNMR spectroscopy showed that the resulting structure can be seen as an intergrowth structure, where the layered perovskite motif seems to stabilize “ $\text{RbNb}_3\text{O}_8$ ”, which is not accessible *via* common solid-state synthesis methods. The formation of this intergrowth seems to cause a 3D linkage in the former layered perovskite structure and thus, hinders exfoliation for higher Pb contents. As compromise between nanosheet yield and band gap narrowing, nanosheets best suitable for photochemical purposes were achieved for an initial molar ratio of Ca:Pb of 1:1.

On the other hand, a successive replacement of  $\text{K}^+$  and  $\text{Ca}^{2+}$  by rare earth elements showed that nanosheets containing  $\text{Eu}^{3+}$ ,  $\text{Sm}^{3+}$ ,  $\text{Pr}^{3+/4+}$  exhibit red emissions,  $\text{Er}^{3+}$  containing show green emissions and  $\text{Dy}^{3+}$  containing nanosheets exhibit yellow emissions under excitation at  $\lambda = 366\text{nm}$  (Chapter 3.2). Contrary to literature, SEM and TEM coupled with EDX revealed that only up to 20 at% rare earth ions can be incorporated in the  $\text{KCa}_2\text{Nb}_3\text{O}_{10}$  system yielding a maximum  $\text{Ln}^{3+}$  content according to  $\text{K}_{0.8}\text{Ca}_{1.8}\text{Ln}_{0.2}\text{Nb}_3\text{O}_{10}$ . Still, the achieved “diluted”

nanosheets can be considered for future applications in (electro)optical devices and as luminescent probes for chemical and bioanalytical sensors.

In addition to the existing exfoliation protocols we established another route based on a cation-silver-exchange rather than a cation-proton-exchange (Chapter 3.3). Once  $\text{Ag}^+$  is intercalated into the interlayer region of layered materials, bulky organic iodides can be incorporated similarly to the bulky organic bases for materials with  $\text{H}^+$  in the interlayer space. We showed that for exfoliation of  $\text{AgLaNb}_2\text{O}_7$ ,  $\text{AgCa}_2\text{Nb}_3\text{O}_{10}$  and  $\text{AgTaP}_2\text{O}_8$  functional ligands that are otherwise inaccessible as exfoliation agents can be attached to the surface, thus enabling an extension of the “inorganic” nanosheet chemistry to “organic” chemistry.

2D nanosheets can be utilized as 2D building blocks for the fabrication of functional heterostructures. We used  $[\text{TBA}_{1-y}\text{H}_y]^+[\text{Ca}_2\text{Nb}_3\text{O}_{10}]^-$  nanosheets to synthesize a  $[\text{Mn}_2\text{Al}(\text{OH})_6]^+[\text{Ca}_2\text{Nb}_3\text{O}_{10}]^-$  hybrid structure with up to 100 bilayers and verified the alternate stacking of Ca-Nb perovskite and Mn-Al LDH nanosheets with atomically resolved STEM-EELS measurements (Chapter 4.1). Thus, a LBL approach enables the construction of rationally designed bulk materials on a large scale, but still needs to overcome some obstacles as sheet terminations, sheet overlap and stacking faults add up for the increased layer number. Here, the ligand has direct influence on the interlayer distance.  $[\text{TBA}_{1-y}\text{H}_y]^+[\text{Ca}_2\text{Nb}_3\text{O}_{10}]^-$  nanosheets with lower TBA content lead to the formation of less densely packed films. This fine-tuning of the film morphology can be of use for photocatalysis, to enable faster transportation pathways.

In a following approach we evaluated the thermal behavior of the  $[\text{Mn}_2\text{Al}(\text{OH})_6]^+[\text{Ca}_2\text{Nb}_3\text{O}_{10}]^-$  stack at various temperatures to probe the densification of the film with possible formation of cross-layer bonds (Chapter 4.2). In the range of 300°C-500°C a re-arrangement of the layer takes place, where the LDH rich layer moves away from the substrate and the perovskite rich layer shows a loss in the Mn and Ca content. From 700°C a transformation takes place and at temperatures of 1000°C fully crystalline particles of various compositions are formed. We identified  $\text{Al}_x\text{Mn}_{2-x}\text{O}_3$  and  $\text{MnNb}_2\text{O}_6$  and found evidence for formation of an unknown Mn-Al-Nb-O composition. The controlled LBL alignment and subsequent annealing of the stacks can therefore be used for the fabrication of compounds with compositions not accessible *via* common solid-state approaches.

In the last part, the ability of  $[\text{TBA}_{1-y}\text{H}_y]^+[\text{Ca}_2\text{Nb}_3\text{O}_{10}]^-$  nanosheets to form a variety of nanoscale morphologies was shown based on several examples (Chapter 4.3). Using EISA thick nanosheet films were accessible, whereas dip-coating can be used to deposit thin layers. Incorporation of polystyrene spheres PS was exploited to form macroporous materials, whereas an alternate stacking of PS with perovskite nanosheets lead to a Bragg stack-like material. Instead of LDH, PDDA was shown to be an alternative cationic

polyelectrolyte to form ordered perovskite-only bulk materials which are glued together by organic ligands.

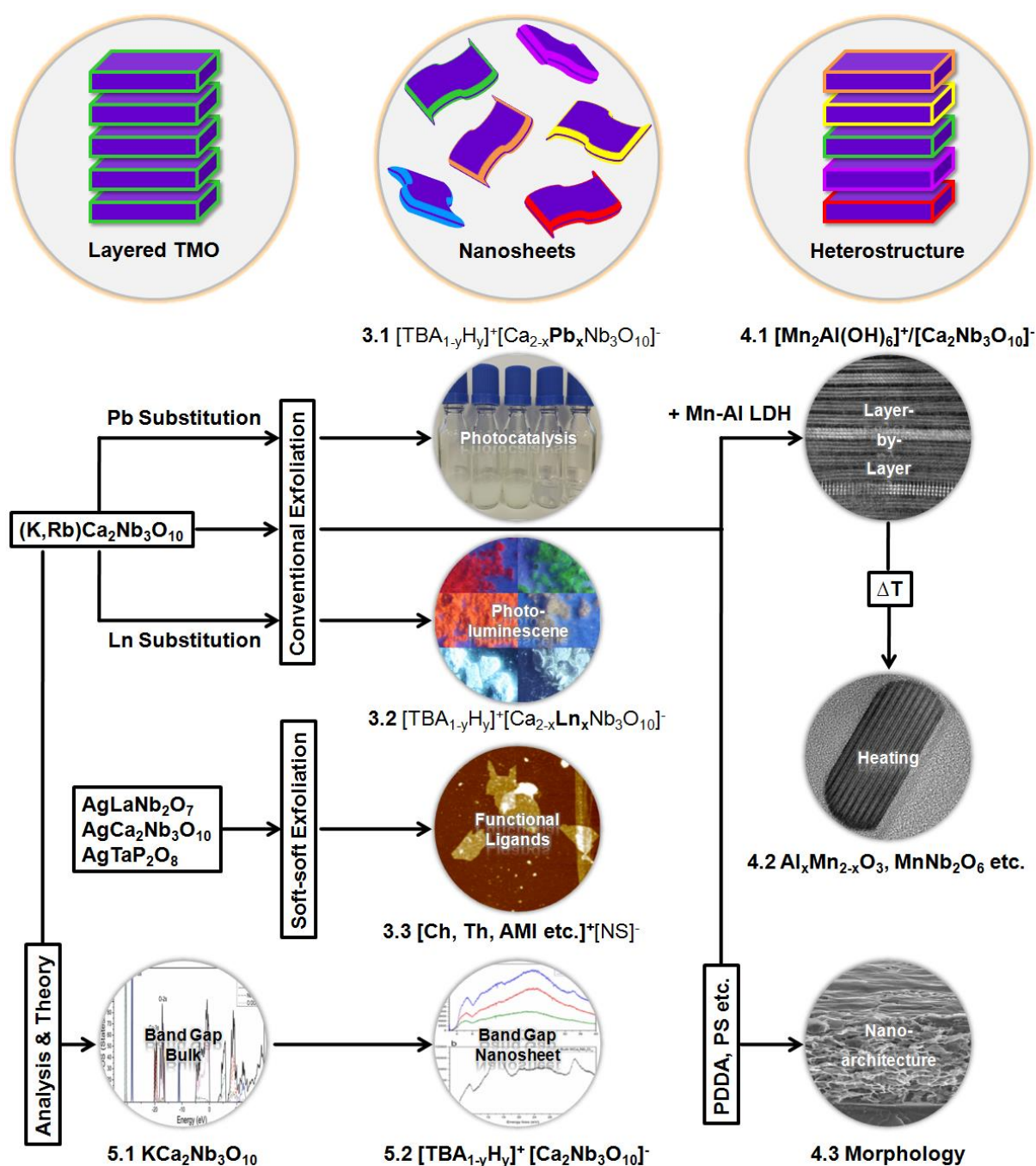


**Figure 6.1:** Schematic overview and connection of topics covered in “Two-dimensional Transition Metal Oxide Nanosheets for Nanoarchitectonics”.

## 7 Conclusion and Outlook

Nanotechnology is still in an early stage regarding characterization methods for multi-component hybrid nanostructures, the (high) level of empiricism in synthesis, and the development of complex nanosystems. 2D nanosheets have shown to be chameleonic materials that do not only have intriguing properties, but also lend themselves as building blocks for the fabrication of functional materials by design. Graphene as the pioneering 2D material has rapidly evolved towards industrial large-scale production and may become part of a broad range of electronic products in the future. This trend will continue for other 2D materials within the next years as complex nanosystems require sophisticated positioning, mutual arrangement, interplay as well as tuning in chemical composition of the processed materials in order to achieve and improve the performance of fabricated devices. Among others, we have shown that TMO nanosheets are excellent candidates for these purposes due to their versatility in composition and their flexibility in the arrangement at the nanometer scale. There are already prototypes for the utilization of TMO nanosheets as ultrathin dielectrics in next-generation nanoelectronics as they exhibit a superior high- $k$  performance. Still, one main hurdle is the current inability to produce large amounts of identical nanostructures with a reasonable lateral size that allows to produce large-scale devices and 3D blocks/solids without defects. Currently the size of TMO nanosheets is mainly determined by the size of the parent bulk material and the applied mechanical force during the exfoliation process. Thus, for large single crystals of layered bulk materials an infinite time for solution-based exfoliation would be necessary. Consequently, bottom-up synthesis of nanosheets rather than the current top-down approach might be the tool of choice to produce high-quality nanosheets in the future. Another approach would be to anneal a thin film of nanosheets after the film has been removed from the substrate. The production of large nanosheets would also help to overcome obstacles we have encountered for the fabrication of bulk materials by means of a LBL assembly.

Another - often overlooked - feature of charged nanoscale materials is the ligand surrounding it. We have shown that the tetra-*n*-butylammonium ligand surrounding calcium niobate nanosheets can be removed due to an equilibrium reaction with water and hence shows only weak interaction with the nanosheet itself. This is an observation that has to be investigated as a function of the nanosheet composition in the future in order to deepen the knowledge of nanosheet chemistry. Furthermore, new exfoliation routes like our soft-soft chemical approach might enable the introduction of ligands with a stronger nanosheet-ligand interaction that can be exploited for targeted deposition or arrangement of individual nanosheets. A different thought is the usage of “functional” nanosheets in catalysis. Market research estimates that nanostructured catalysts will cover 50% of the world market in 2020.

The functional groups of ligands might therefore be used to deposit co-catalysts or to couple other groups like dyes to enhance catalytic activity.

There is and will be a tremendous need in understanding the transition from the nanoscale to the bulk scale, as nanosheets and other nanomaterials find their way into industrial application. Atomic column resolved TEM coupled with several spectroscopies is a powerful but still expensive tool to gather such information. Further improvement of the instrumentation like a decrease of the acceleration voltage whilst maintaining the resolution or an enhancement of the spectroscopy signals will contribute to this knowledge. Other characterization methods such as AFM will be improved as well and new analysis methods will be developed to match the needs of the nano-dimension. As we are still in the beginning of nanotechnology in terms of the complexity in the interplay between individual building blocks, our knowledge is mainly based on distinct examples. In the long run, the creation of an extensive library of nanoscale materials that correlates synthesis of nanomaterials and their properties with their behaviour in composite materials will be realized.

Nanotechnology in the broader context will contribute to breakthrough discoveries and innovation, build materials and systems by nanoscale design, predict the behavior of materials and last but not least will improve the understanding of nature. With this, nanotechnology will contribute to economic and societal progress within the next decades.



## 8 Appendix

### 8.1 List of Publications

Basic results compiled in this thesis were published in scientific journals according to the below-mentioned list. As the scope of the thesis was the synthesis and characterization as well as the assembly of 2D nanosheets, publications beyond this scope are not explicitly listed in prior chapters and are here referred to as not part of this thesis. Talks and posters presentations at scientific conferences as well as workshop participations are summarized separately.

**03      Crystalline Carbon Nitride Nanosheets for Improved Visible-Light Hydrogen Evolution**

Katharina Schwinghammer, Maria B. Mesch, Viola Duppel, Christian Ziegler, Jürgen Senker, Bettina V. Lotsch

*J. Am. Chem. Soc.* **2014**, 136, 1730–1733; DOI: 10.1021/ja411321s

**02      Artificial Solids by Design: Assembly and Electron Microscopy Study of Nanosheet-Derived Heterostructures**

Christian Ziegler,<sup>^</sup> Stephan Werner,<sup>^</sup> Matthieu Bugnet, Matthias Wörsching, Viola Duppel, Gianluigi A. Botton, Christina Scheu, Bettina V. Lotsch

*Chem. Mater.* **2013**, 25, 4892–4900; DOI: 10.1021/cm402950b

**01      Electronic structure of  $\text{KCa}_2\text{Nb}_3\text{O}_{10}$  as envisaged by density functional theory and valence electron energy loss spectroscopy**

Kulpreet Singh Viridi, Yaron Kauffmann, Christian Ziegler, Pirmin Ganter, Bettina V. Lotsch, Wayne D. Kaplan, Peter Blaha, Christina Scheu

*Phys. Rev. B* **2013**, 87(11), 115108; DOI: 10.1103/PhysRevB.87.115108

## 8.2 Chapter Contributions

The following overview lists briefly the main contributions of the authors listed at the beginning of each chapter of this thesis. Note that authors dealing rather with the analysis of the materials and not their interpretation are listed in Chapter 2 and are therefore not repeatedly mentioned.

**Chapter 1, 2, 6, 7:** *For these chapters, writing the manuscript, screening the literature and creating the graphics was done by Christian Ziegler. Christina Scheu and Bettina V. Lotsch revised the manuscript.*

**Chapter 3.1:** *For this chapter, first synthesis of the samples, writing the manuscript, screening the literature, editing the graphics, interpretation and discussion of the analysis was done by Christian Ziegler. Claudia Kamella helped with large-scale synthesis of the materials, Daniel Weber performed the Rietveld refinements and assisted with continuative analysis, Igor Moudrakovski did the main part of the ssNMR interpretation. Daniel Weber, Teresa Dennenwaldt, Christina Scheu and Bettina V. Lotsch revised the manuscript.*

**Chapter 3.2:** *For this chapter, supervision of students Laura Kohout and Stephanie Linke, writing the manuscript, screening the literature, editing the main part of the graphics, interpretation and discussion of the analysis was done by Christian Ziegler. Christina Scheu and Bettina V. Lotsch revised the manuscript.*

**Chapter 3.3:** *For this chapter, supervision of Anne Friedrichs, additional synthesis, writing the manuscript, screening the literature, editing the graphics, interpretation and discussion of the analysis was done by Christian Ziegler. Pirmin Ganter performed synthesis and analysis on phosphotantalates and revised the manuscript with Christina Scheu and Bettina V. Lotsch.*

**Chapter 4.1:** *For this chapter, Stephan Werner and Christian Ziegler equally performed synthesis of the samples, writing of the manuscript, screening of the literature, editing of the graphics, interpretation and discussion of the analysis, Matthias Wörsching was supervised by Christian Ziegler, Viola Duppel and Matthieu Bugnet helped with the TEM analysis. All authors revised the manuscript.*

**Chapter 4.2:** *For this chapter, supervision of Katarina Marković, synthesis of the samples, writing the manuscript, screening the literature, editing the graphics, interpretation and*

*disussion of the analysis was done by Christian Ziegler. Christina Scheu and Bettina V. Lotsch revised the manuscript.*

**Chapter 4.3:** *For this chapter, supervision of Katarina Marković, Stephanie Linke, Matthias Wörsching, writing the manuscript, screening the literature, editing the graphics, interpretation and disussion of the analysis was done by Christian Ziegler. Annekathrin Ranft contributed equally to the supervision of Maximilian Lamoth. Christina Scheu and Bettina V. Lotsch revised the manuscript.*

**Chapter 5.1:** *For this chapter, supervision of Pirmin Ganter, synthesis of the material, assisting discussion of the data was done by Christian Ziegler. Kulpreet S. Viridi did the main part of writing the manuscript, screening the literature, editing the graphics, interpretation and disussion of the analysis. Peter Blaha did the main part of the calculations. All authors revised the manuscript.*

**Chapter 5.2:** *For this chapter, supervision of Pirmin Ganter, synthesis of the materials, editing of some graphics, AFM measurements, analyzing and discussing the optical data, an additional literature survey was done by Christian Ziegler. Kulpreet S. Viridi did the main part of writing the manuscript, screening the literature, editing the graphics, interpretation and disussion of the analysis. All authors revised the manuscript.*

### 8.3 Conference Contributions

- 11**    **“The Postgraphene Area”** (oral presentation)  
13.04.-16.04.2015 Annual Meeting at Deutsches Museum, Munich, Germany
- 10**    **“Synthesis, Characterization and Application of Transition Metal Oxide Nanosheets and Their Utilization as Two-Dimensional Building Blocks”** (oral presentation)  
11.03.2015 Nanosystems Initiative Munich Winter Meeting, Munich, Germany
- 09**    **“Multicomponent Nanostructures: Inorganic Nanosheets and Fabrication of Artificial Solids”** (oral presentation)  
20.01.-23.01.2014 Mechanics meets Energy II Meeting, Winterberg, Germany
- 08**    **“2D Nanosheets as Precursors for the Directed Fabrication of 3D Hybridmaterials”** (poster presentation)  
31.07.-02.08.2013 Nanosystems Initiative Munich Summer Retreat, Fall, Germany
- 07**    **“Layer-by-Layer Assembly and (S)TEM-EDX/EELS Characterization of Layered Perovskites combined with Layered Double Hydroxides”** (poster presentation)  
26.05.-31.05.2013 EDGE conference (*International Electron Energy Loss Spectroscopy Meeting on Enhanced Data Generated by Electrons*), Sainte Maxime, France
- 06**    **“Towards photocatalytically active nanosheets via lead doping”** (poster presentation)  
03.03-09.03.2013 Nanosystems Initiative Munich Winter School, Kirchberg, Austria
- 05**    **“Synthesis and Characterization of new Photoluminescent Layered Perovskites and their Exfoliation”** (poster presentation)  
12.06-15.06.2013 Nanosystems Initiative Munich Summer Retreat, Garmisch-Partenkirchen, Germany
- 04**    **“Nano-Lego: Analysis and Assembly of Nanosheets by Soft Chemistry”** (oral presentation)  
02.05.2012 Joint Departmental Seminar Max Planck Institute for Solid State Research, Stuttgart, Germany

- 03**    **“Assembly and Analysis of Nanosheets used as 2D Building Blocks (using the example of  $\text{KCa}_2\text{Nb}_3\text{O}_{10}$  and  $\text{Mn}^{\text{II}}$   $\text{Al}^{\text{III}}$  Sulfonate)”** (oral presentation)  
20.-24.02.2012 Annual Meeting at Schloss Ringberg, Kreuth, Germany
- 02**    **“Exfoliated layered transition metal oxides used as 2D building blocks”** (poster presentation)  
19.09-23.09.2011 Center for NanoScience Workshop, Venice, Italy
- 01**    **“Exfoliated layered transition metal oxides used as 2D building blocks”** (poster presentation)  
27.07.-29.07.2011 Nanosystems Initiative Munich Summer Retreat, Kampenwand, Germany

## 8.4 Curriculum Vitae

### Personal Information

<b>Name</b>	Christian Ziegler
<b>Date of Birth</b>	18.08.1984
<b>Place of Birth</b>	Munich, Germany
<b>Nationality</b>	German

### Education

#### Postgraduate Education (Chemistry)

since 04/2011	Ludwig Maximilian University Munich and Max Planck Institute for Solid State Research Stuttgart
	PhD thesis (Prof. Dr. Bettina V. Lotsch): "Two-dimensional Transition Metal Oxide Nanosheets for Nanoarchitectonics"

#### Master of Science (Chemistry)

16/02/2011	Master of Science in Chemistry, M. Sc.
10/2008-02/2011	Ludwig Maximilian University Munich
	Master thesis (Prof. Dr. Christina Scheu): "New approaches to exfoliated nanosheets of layered transition metal oxides"

#### Bachelor of Science (Chemistry and Biochemistry)

22/10/2008	Bachelor of Science in Chemistry & Biochemistry, B. Sc.
10/2005-10/2008	Ludwig Maximilian University Munich
	Bachelor thesis (Prof. Dr. Andreas Kornath): ‘

#### Secondary School

25/06/2004	Abitur
09/2002-06/2004	Max-Planck-Gymnasium
09/1995-07/2002	Thomas-Mann Gymnasium

#### Elementary School

09/1994-07/1995	Konrad-Celtis Grundschule
09/1991-07/1994	Gotzmann Grundschule